OCCULTATION ASTRONOMY AND INSTRUMENTATION: STUDIES OF THE URANIAN UPPER ATMOSPHERE

by

RICHARD LEIGH BARON

SUBMITTED TO THE DEPARTMENT OF
EARTH, ATMOSPHERIC & PLANETARY SCIENCES
IN PARTIAL FULFILLMENT OF
THE REQUIREMENTS FOR THE
DEGREE OF
DOCTOR OF PHILOSOPHY

at the
MASSACHUSETTS INSTITUTE OF TECHNOLOGY
August 1989

Signature of Author_____
Department of Earth, Atmospheric & Planetary Sciences
August 1989

Certified by_____
James L. Elliot
Thesis Supervisor

Accepted by _____
Thomas Jordan
Chairman, Committee on Graduate Students

OCCULTATION ASTRONOMY AND INSTRUMENTATION:

STUDIES OF THE URANIAN UPPER ATMOSPHERE

by

RICHARD LEIGH BARON

Submitted to the Department of Earth, Atmospheric & Planetary Sciences
on August 18, 1989 in partial fulfillment of the Degree of
Doctor of Philosophy in Planetary Science

ABSTRACT

Stellar occultations by Uranus between 10 March 1977 and 23 March 1983 have been used to derive the radius and oblateness of Uranus at approximately the 1-μbar level. The atmospheric occultation half-light times and scale heights were used, along with updated ring orbit model parameters, to determine the shape of the planetary limb as projected on the sky. A least squares fit to the limb profile yielded an equatorial radius of $R_e = 26071 \pm 3$ km and an oblateness $\varepsilon = (1 - R_p/R_e)$ of 0.0197 ± 0.0010. The corresponding polar radius was $R_p = 25558 \pm 24$ km. Assuming that the planet is in hydrostatic equilibrium and that J_2 and J_4 are as given by the ring orbit solution of French *et al.* (1988, *Icarus* **73**, 349-378), the inferred rotation period is 17.7 ± 0.6 hr for the latitude range ($-30° < \theta < 26°$) sampled by the observations. This is consistent with Lindal *et al.*'s (1987 *J. Geophys. Res.* **92**, 14987-15001) period of 18.0 ± 0.3 hr at $\theta = +5°$, based on Voyager 2 observations, and with a possible equatorial subrotation predicted by Read (1986 *Quart. J. Roy. Met. Soc.* **112**, 253-272) and supported by the cloud motion studies of Smith *et al.* (1986 *Science* **233**, 43-64).

More than a decade of stellar occultations by Uranus give stratospheric temperatures of about 150 K near the 1-μbar level. In contrast, Voyager UVS stellar and solar occultation observations have been interpreted as showing temperatures as high as 500 K in the region just above the 1-μbar level. Simulated ground-based occultation lightcurves were produced to determine if the interpretations of the two data sets are consistent with each other. Three simulated occultation lightcurves were produced that use number density and temperature profile models determined from Voyager 2 data (Herbert *et al.* 1987 J. Geophys. Res. **92**, 15093-15109). All three simulated lightcurves produce an overall structure consistent with observed ground-based lightcurves. Of the three model lightcurves, the simulated lightcurve derived from the "Best Compromise" parameters of Herbert *et al.* (1987) produced the best match when compared to historical data. Tested against the data from the occultation of 10 March 1977, this simulated lightcurve also produced a lower variance than that of the best fit isothermal model lightcurve for the event.

A modified inversion method is applied to the stellar occultations of KME 15 and KME 17 by Uranus. This method uses Voyager 2 UVS derived Uranian atmosphere conditions above the region probed by earth based occultations (Herbert *et al.* 1987 J. Geophys. Res. **92**, 15093-15109) to establish an atmospheric cap or initial layer for the inversion. This greatly reduces the uncertainty in the upper atmosphere part of the temperature profile. Initial conditions based on extrapolation have been replaced by measured temperatures and density with altitude. We report on the new temperature-pressure atmospheric profiles derived and compare them with previous analyses. The temperatures are substantially

ABSTRACT (CONT.)

higher from the approximate levels of 1.0-μbar to 10.0-μbar, reaching a temperature of 300 K at 1.0-μbar. An average heat flux determination gives a value of nearly 0.5 erg cm^{-2} sec^{-1}. An isothermal layer is discussed that lies directly below the half-light level in three of the four numerically inverted lightcurves. We find this layer to be related to an 8.0-μbar feature reported by Sicardy *et al.* (1985 Icarus **52**, 459-472).

A high performance electronic clock circuit was developed for occultation observations. This clock circuit has been installed into four portable frequency standards and is able to capitalize on the underlying stability of these oscillators. Relative time offsets between clocks may be determined to 0.2 microseconds and are displayed on a liquid crystal display. The clock circuit may be synchronized to submicrosecond accuracy. Circuit function and operation are treated in detail, including a schematic circuit diagram. Performance characteristics are documented for a number of occultation observations.

Thesis Supervisor: Dr. James L. Elliot

Title: Professor, Department of Earth, Atmospheric & Planetary Sciences and Physics

ACKNOWLEDGEMENTS

My thanks go out to my advisor James Elliot for his concern, advice, and opportunities he has presented to me.

My deepest gratitude goes to my Mother, and my two children John and Elizabeth for their continual and unwavering support.

In a class by himself for his attention to detail and continual vigorous encouragement is Richard French- many thanks!

Ted Dunham has been there whenever a need arose and his advice has been great!

TABLE OF CONTENTS

TABLE OF CONTENTS (CONT.)

TABLE OF CONTENTS (CONT.)

LIST OF FIGURES

LIST OF FIGURES (CONT.)

LIST OF FIGURES (CONT.)

LIST OF TABLES

Chapter 1 - Introduction

1.1 Developments in the Study of the Uranian Atmosphere

Uranus is the seventh of the planets from the sun, located at a mean solar distance of 19.18 AU. Discovered in 1781 by the German-English astronomer William Herschell it remained scientifically obscure for nearly 100 years, during which time observations were restricted predominantly to positional information and visual descriptions. In the early 1900s, the advent of modern photometric instrumentation renewed scientific study of Uranus. In 1970, the first high spatial resolution images of the planet in the optical portion of spectrum were made with a 0.9 meter telescope aboard the Stratoscope II. Though clear images were produced, the results were disappointing in that only a uniform disc was discernable. In 1977 rings were discovered and confirmed about the planet by the group of Elliot, Dunham and Mink (Elliot *et al.* 1977). Since approximately 1970, interest has continually grown, reaching a high point with the Voyager 2 flyby in 1986.

The underlying interest in planetary atmospheres derives from a belief that by understanding the atmospheres of other planets we will ultimately be able to better understand the one we live in. Science gives us the means to acquire this understanding. The scientific interest in the gas giants as a whole has been keen since a greater number of sources are becoming available to supply the necessary data. Ground-based spectroscopy and photometry, both disc and spatially resolved, have taken advantage of improvements in detectors (imaging devices) and instrument design. Ground-based occultation observations have also benefitted from lightweight, highly sensitive and photon noise limited portable instrumentation; sensitive high-speed detectors in the infrared portion of the spectrum; and more reliable predictions of the events. Earth satellites have supplied data in regions of the

electromagnetic spectrum (ultraviolet) not available from the ground. In the microwave region of the spectrum, the very large array (VLA) has been providing disc resolved data. The arrival of the Voyager 2 spacecraft at these planets has made available information that serves to give ground-based data a better context in which to be interpreted as well as providing its own unique observations.

1.2 Evidence of a Complex Uranian Atmosphere

A brief summary of relevant observations and the current understanding of the thermal structure and energy balance of the Uranian atmosphere is presented to afford some perspective to the work presented in this thesis. The following outline of data and it's analysis is organized in terms of the three experimental modes in which it has been acquired: analysis of radiation of emission from the planet and surroundings, analysis of radiation in transmission, and analysis of reflected radiation (solar). Wavelengths from ≈10 μm to ≈20 cm (in emission) are used to probe the deepest parts (≈30-mbar to ≈30-bar) of the atmosphere revealing both temperature and composition. Early efforts in observing the short end of this range, including some work as late as 1981, have been found to be useful only in the sense of setting direction due to a variety of deficiencies (Conrath *et al.* 1989). A consistent set of disc integrated data used for detailed analysis in the 10 μm to 4 mm range is composed of data from Rieke *et al.* (1975), Ulich *et al.* (1981), Tokunaga *et al.* (1983), Moseley *et al.* (1984), Hildebrand *et al.* (1985), Orton (1986), Orton *et al.* (1986), Orton *et al.* (1987a, 1987b) plus additional data by Ulich at 3.3 mm. Figure 1-1 shows the various data plotted as a function of brightness temperature and wavelength for Uranus. These measurements and the Voyager 2 IRIS (infrared radiometer and interferometer spectrometer) measurements have been brought into close agreement by

Figure 1-1 Brightness temperature measurements of Uranus in the infrared through near-millimeter spectral region. Crossed circles represent the observations of Tokunaga et al. (1983) at 17.8 and 19.6 μm, as well as those of Orton et al. (1983) at shorter wavelengths. Triangles represent the observations of Moseley et al. (1985), open circles the observations of Hildebrand et al.(1985), filled circles our observations, and the inverted triangle the observation of Ulich (1981). Where larger than the symbols vertical bars represent one standard deviation internal errors only except for Ulich's 3.3-mm datum, where the absolute uncertainty is represented. [After Orton et al. (1986).]

Figure 1-1

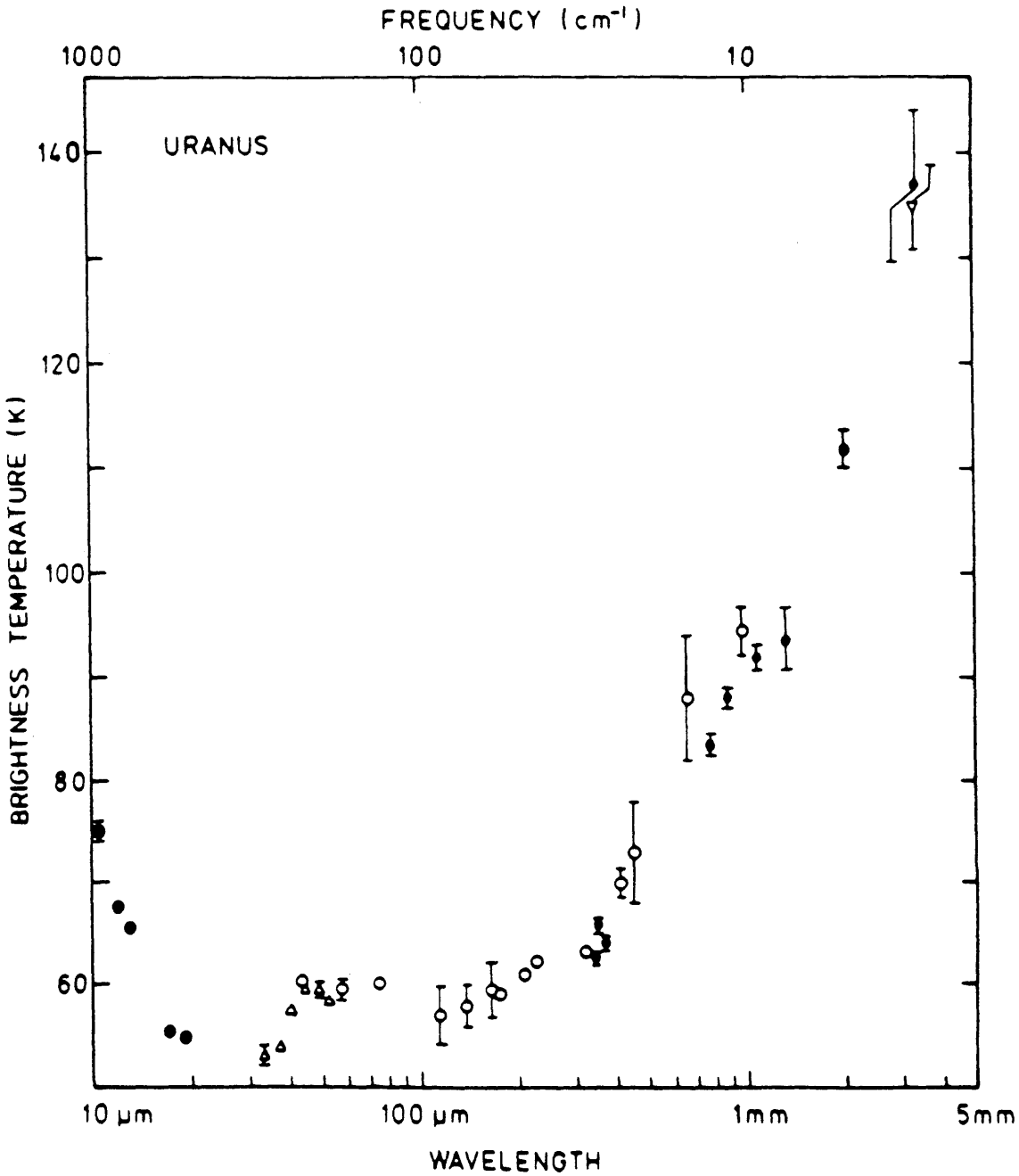
FREQUENCY (cm⁻¹)
1000
100
10
URANUS
140
120
100
80
60
BRIGHTNESS TEMPERATURE (K)
10 μm
100 μm
1mm
5mm
WAVELENGTH

mutual calibration using Mars as a standard. For the data obtained from the very deepest portion of the atmosphere (cm range of wavelengths), the brightness values as a function of wavelength are shown in Figure 1-2 (de Pater and Massie 1985). These data have been interpreted as showing possible ammonia at levels near 10-bar, and also show an apparent secular warming when compared to data taken before.1973. Taken as whole, the data may be inverted (discussed further below) to give an atmospheric temperature-pressure profile under the assumption that the atmospheric emission is due predominantly to collision induced $H_2 - H_2$ transitions. Additional data in the cm wavelength range have been obtained from the VLA. The VLA is able to spatially resolve the planet and thus also give an indication of horizontal thermal structure in the 10-bar to 30-bar region (de Pater and Gulkis 1988).

Data from radiation in transmission come from three sources: Earth-based stellar occultation observations, Voyager 2 based stellar and solar occultation observations, and Earth-based occultation observations of the Voyager 2 spacecraft radio transmissions. The Earth-based observations of stellar occultations by Uranus have been used to retrieve temperature-pressure profiles of the atmosphere along the planet's limb. The observable atmospheric pressures range from less than 1-μbar to ≈30-μbar. The interpretation of this data is discussed in depth by French *et al.* (1983), Elliot (1979), and Sicardy *et al.* (1982). In the portion of the atmosphere probed by this technique, there is no significant absorption. The occultation lightcurve is due only to differential refraction. Stellar and solar occultations made by the Voyager 2 spacecraft cover wavelengths from the vacuum ultraviolet recorded by the ultraviolet spectrometer (UVS) instrument to the near ultraviolet (≈0.25 μm) recorded by the photopolarimeter spectrometer.(PPS) The Voyager 2 stellar and solar occultation observations gave temperature and pressure information (from modeling of absorption profiles) from a pressure of ≈0.5-mbar in the stratosphere to less

Figure 1-2 The spectrum of Uranus with superimposed model calculations. Curve 1 is for a model calculation with 0.90 H_2, 0.02 CH_4, 0.08 He, 1.0 x 10^{-6} H_2O, and 1.5 x 10^{-4} NH_3. Curve 2 is the same but with a NH_3 abundance of 1.0 x 10^{-6}. Curve 3 is similar to curve to curve 2, but with a water abundance equal to the solar value of 1.0 x 10^{-3}. Curve 3 is without and curve 4 with extra opacity due to scattering by the water droplets. Curve 5 (at millimeter wavelength only) is like curve 2, but with a CH_4 abundance equal to 6.0 x 10^{-4} and He of 0.10. Ben Reuven's lineshape was used to calculate the absorption due to NH_3 throughout the entire wavelength range. [After de Pater and Massie (1985).]

Figure 1-2

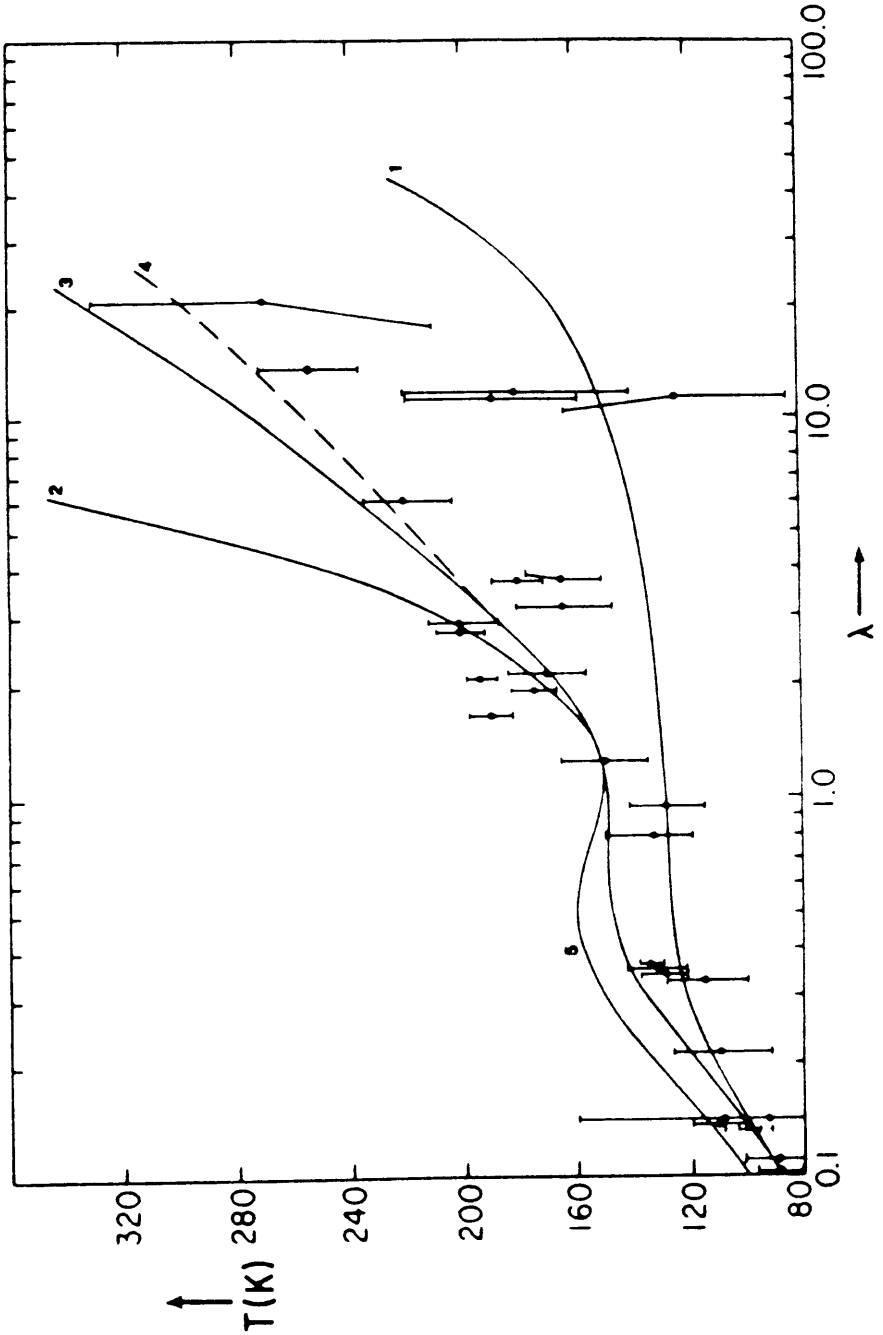

than 10^{-6}-μbars at the outer edges of the atmosphere from the UVS observations (Herbert *et al.* 1987). Essentially one temperature point at 1-mbar was obtained from the PPS data (West *et al.* 1987). The occultation of the Voyager 2 spacecraft (Lindal *et al.* 1987) as it went behind Uranus gave information about the atmosphere from a pressure of ≈0.3-mbar to 2.3-bar for the gas proper and also electron temperatures in the ionosphere. The two microwave wavelengths transmitted by the Voyager were analyzed both individually and differentially to obtain phase and amplitude information during the occultation. This data alone has been used determine the troposphere and lower stratosphere temperatures as function of pressure as shown in Figure 1-3 (Lindal *et al.* 1987).

Data obtained from reflected sunlight are used to determine a geometric albedo, a phase integral and hence a bolometric bond albedo. Measurements from the ground used to determine the phase integral for Uranus cover angles of 3 degrees. Voyager 1 was used to determine the phase integral in the range of 43 to 85 degrees (full disc measurements) and Voyager 2 was used to determine the integral over the range of 15 to 155 degrees in a disc resolved mode (converted to an integrated disc measurement for comparison). A seasonally adjusted Bond albedo of $A = 0.300 \pm 0.049$ was reported by Pearl *et al.* (1987). The IRIS measurements as interpreted by Pearl *et al.* (1987) give a value for the ratio of external energy input to the external energy radiated as $E = 1.06 \pm 0.08$. This value is well below the values determined for Jupiter and Saturn indicating a very weak internal heat source. The low energy flux of Uranus has been a puzzle in the past and still remains to be understood.

The temperature pressure profiles (disc integrated and disc resolved) are used to understand the heat balance mechanisms and dynamical processes in the atmosphere. Ingersoll (1984), Wallace (1980) and others have done extensive modeling of a radiative atmosphere under local thermodynamic equilibrium (LTE) and under non-LTE assumptions as well, in order to understand the observed temperature-pressure profiles. Most of the

Figure 1-3 Vertical temperature profiles for the nominal model. The full drawn curve was derived from the radio refractivity data acquired during ingress at planetographic latitudes ranging from 2 to 6 degrees South. The stippled curve was obtained from measurements between 6 and 7 degrees South latitude during egress. Both measurements were conducted near the terminator. The calculations were performed by using a helium to hydrogen abundance ratio of 15/85, and the error bars do not include the uncertainty in the composition. [After Lindal et al. (1987).]

Figure 1-3

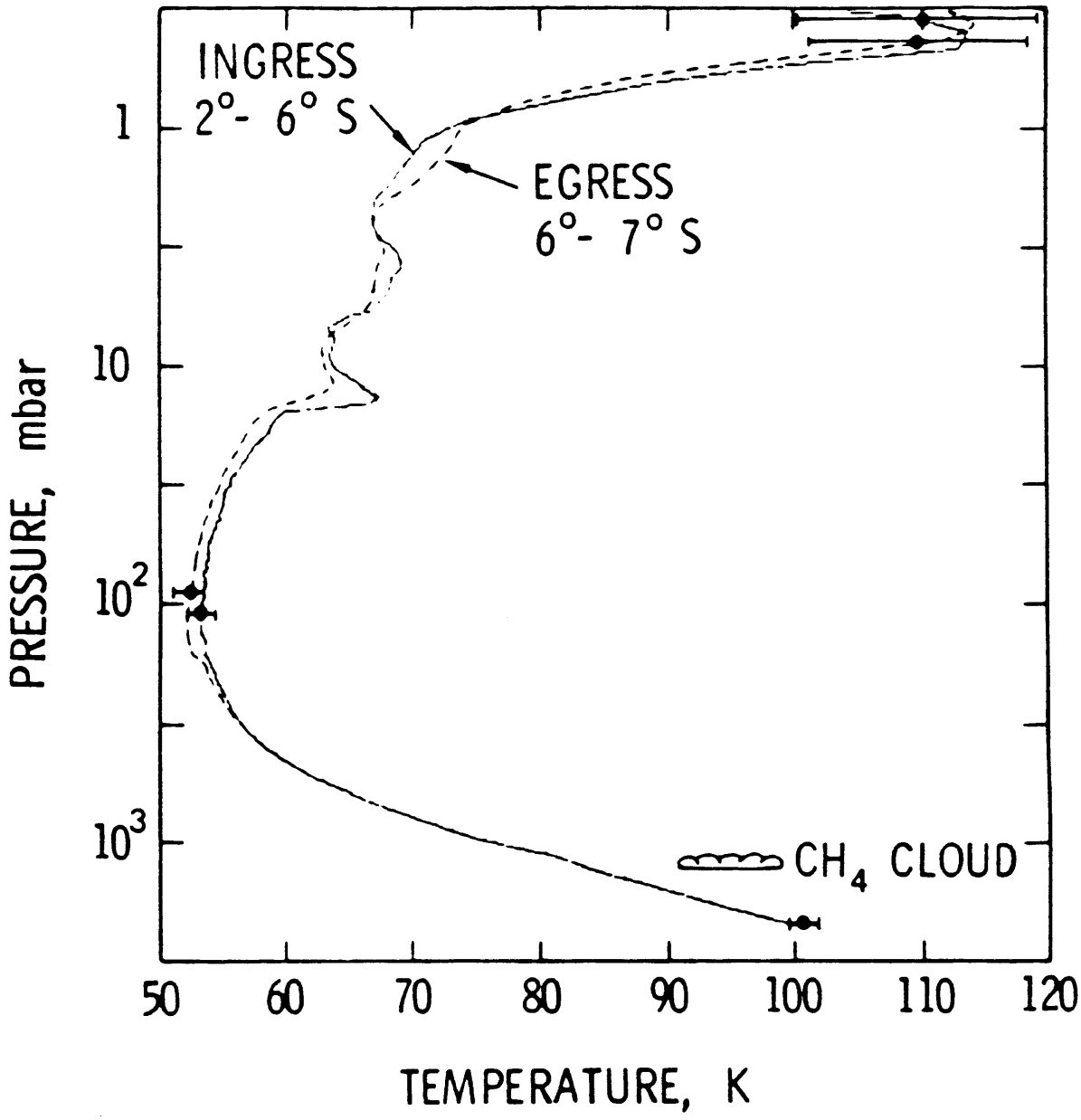
INGRESS
2°- 6° S
EGRESS
6°- 7° S
CH4 CLOUD
PRESSURE, mbar
1
10
10^2
10^3
50
60
70
80
90
100
110
120
TEMPERATURE, K

atmosphere at pressures greater than ≈10-μbar radiates due to $H_2 - H_2$ collision induced transitions. For pressures less than ≈10-μbar cooling appears to be due to C_2H_6 (ethane), C_2H_2 (acetylene), C_4H_4 (diacetylene) or possibly some C_2H_4 (methane) transitions. Figure 1-4 illustrates the radiative-convective equilibrium model atmosphere developed by Appleby (1986). Most of the atmosphere appears to make a good first order match with the model except for the upper stratosphere. Here the higher temperatures in the data (ground-based occultation) do not seem to match the model even when non-LTE modeling is used. This result is one of several indicating an additional source of heating is needed in the stratosphere. French *et al.* (1983) have examined the Earth-based occultation observations in terms of the thermal structure and energy balance possible for the ≈1-30-μbar pressure range

Features in the longer wavelength observations have revealed methane at a pressure of several bars. This is consistent with the inferred methane cloud deck at approximately ≈1.3-bar determined from the radio occultation experiment (Lindal *et al.* 1987). Imaging above the cloud deck (Smith *et al.* 1986) revealed a few thin clouds. These clouds along with the 1-bar equatorial radius determined by the same radio occultation experiment have been used to obtain a differential rotation curve as a function of latitude showing faster rotation at the poles and slower (subrotation) at the equator. Flaser *et al.* (1987) have matched this behavior with an atmospheric Hadley cell circulation model. In this model there is an atmospheric upwelling at latitudes of approximately ±25 degrees latitude spreading towards the pole and equator, producing super-rotation near the poles and subrotation at the equator. These effects are due (to first order) to conservation of angular momentum of the gas as it flows from mid-latitudes to the pole and equator.

A heat balance problem separate from the planet as a whole also appears to exist in the thermosphere, where temperatures of 750 K have been found from the Voyager UVS occultation results. A measured temperature gradient in the thermosphere was used by

Figure 1-4 Temperature profiles and sensitivity tests for Uranus. These models illustrate the effects of changes in several of the basic model parameters. Localized aerosol heating and y = 6% (y is the heating contribution due aerosols in the model) are assumed in (d) (versus a uniform distribution and y = 5% in (b)). Models e and f achieve warmer thermal inversions (relative to (b)) due to changes in the bulk composition and in the solar heating. [After Appleby (1986).]

Figure 1-4

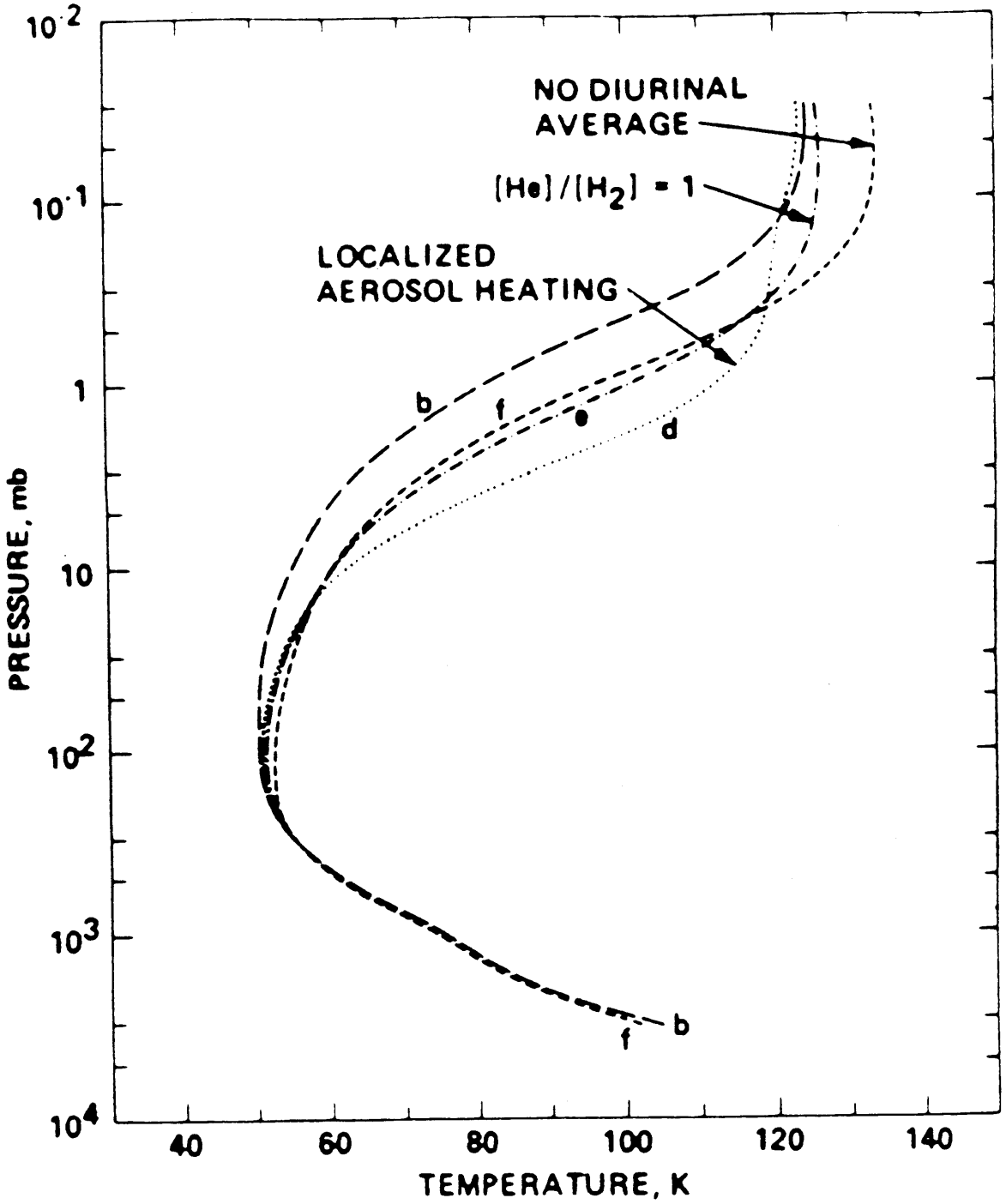
NO DIURINAL AVERAGE
[He]/[H2] = 1
LOCALIZED AEROSOL HEATING
b
f
e
d
b
f
PRESSURE, mb
TEMPERATURE, K
10-2
10-1
1
10
10²
10³
10⁴
40
60
80
100
120
140

Herbert et al. (1987) to determine a heat flux. His value of heat flux could not be accounted for by solar radiation being absorbed in the atmosphere. These temperatures are also very close to regions determined by ground-based occultations to be in the range of 150 K. These facts point to a need to closely examine the energy balance in this region.

1.3 The science goals of this work and beyond

A more precise and thorough understanding of the physics of the Uranian atmosphere is the primary goal. For Uranus, this is a detailed understanding of the inferred upper atmospheric heating mechanism and its implications for other planets. Correlation of the heating rate with Uranian days or seasons would be an intermediate step. A better physical understanding of the atmospheres of the other outer planets in general is also a significant step. The exospheres of both Jupiter and Saturn have been observed with Voyager in the EUV and have high temperatures, comparable to Uranus. Neptune is soon to be explored in a like manner in August 1989. With information from all of these planets, different aspects of possibly the same mechanism may be used to understand the physics taking place.

The pole-on aspect of Uranus will be a prime natural laboratory to study the atmospheric effects of solar insolation as a function of changing latitude on Uranus as the currently totally dark hemisphere warms up. This also presents an opportunity to study the atmospheric dynamics from the perspective of a relatively well known state derived from the combined spacecraft and ground-based observations.

The scientific return from data derived from ground-based occultation lightcurves appears quite substantial in that it can supply atmospheric refractivity and altitude information simultaneously over many atmospheric scale heights. This in turn supplies pressure and temperature information with minimal additional assumptions. The

interpretation of occultation lightcurves in the radio and optical has, on the other hand, been a difficult problem (Hunten and Veverka 1976), but the payoff for atmospheric science is a wealth of data that covers a planet's limb both spatially and temporally.

1.3.1 Stratospheric heating in Uranus' atmosphere - a current problem

Uranian ground-based occultation data has been of high quality only since 1977 when Elliot *et al.* (1977) discovered the now famous rings. In the quest to obtain more precise and higher signal-to-noise data to understand the rings, atmospheric observations were made almost by default. Many of the atmospheric observations that were made have been excellent, and have generally been interpreted as showing a nearly isothermal portion of the stratosphere. With the passage of Voyager 2 through the Uranian system, a hint of a possible inconsistency was the observation of temperatures near 800 K in the thermosphere. Within this context, the analysis of ground-based lightcurves using Voyager 2 data for initial conditions (this work), has shown evidence of a heat source supplying up to 100 times the expected energy input from EUV solar absorption. Auroral heating, thermospheric wind heating, and dissipation of various atmospheric waves (*e.g.*, gravity, sonic, Rossby) are other generally recognized sources of heating. None of these sources have yet been able to fully model the measured heating.

1.4 A synopsis of this work

Chapter 2 of this thesis presents an oblateness determination of Uranus from ground-based data. This determination gave a value with about one tenth the previous error for the half-light occultation level. Primarily it took advantage of the higher accuracy ephemeris information used in understanding ring dynamics. The rings were used as a local

reference frame tied to Uranus to measure the half-light radius for each occultation. In addition, a correction for the bending of a light ray at half-light was made for each observation (rather than as an average) leading to a significant reduction in the formal error. A determination that the scale height and half-light time are strongly negatively correlated was discovered in the data, leading to part of the increase in accuracy.

In Chapter 3 work is presented discussing the large temperatures found in Uranus' stratosphere with Voyager 2. These observations were near the same radius as ground-based occultation half-light radius determinations. The accepted temperature at this radius was of order 150 K. The Voyager data suggested temperatures near 500 K. The work used the Voyager 2 derived model to generate synthetic ground-based lightcurves that were then shown to be consistent with ground-based recorded lightcurves.

In Chapter 4 a method is presented using the Voyager model to impose an atmospheric cap or layer that is used as an initial condition when performing a numerical inversion of a lightcurve. A noise analysis is performed. Noise recorded during the 1 May 1982 stellar occultation by Uranus was used in the analysis.

Chapter 5 uses the method developed in Chapter 4 to invert four high signal-to-noise ground-based lightcurves. The derived temperature-pressure profiles show a steep temperature gradient with altitude near the 1-μbar level. An isothermal region is apparent directly below (higher pressure) the gradient. A simple model of thermospheric heating is given. The heat produced under simplifying assumptions for Uranus is calculated and compared to other estimates.

In Chapter 6 a highly accurate portable quartz clock incorporated into a reference oscillator is described. It has been successfully used in Uranian ring occultations to give closed loop timing to better than a millisecond.

The determination of an excess heat source in the upper part of the Uranian stratosphere is the most important part of this work. It implies that future analyses must be

looked at in terms of what effect this heat will have in determining the behavior of the stratosphere. The heat source will be an essential part of models of the Uranian stratosphere and ionosphere.

Chapter 2 has been published as the following paper:

BARON, R. L., R. G. FRENCH, AND J. L. ELLIOT (1989). The Oblateness of Uranus at the 1-μbar Level. *Icarus* **77**, 113-130.

References

APPLEBY, J. F. (1986). Radiative-convective equilibrium models of Uranus and Neptune. *Icarus* 65, 383-405.

CONRATH, B. J., J. C. PEARL, J. F. APPLEBY, G. F. LINDAL, G. S. ORTON, B. BEZARD. (1989). Thermal structure and energy balance of Uranus. *Uranus* (J. Bergstralh and E. Miner, Ed).Univ. of Arizona Press, Tucson.(manuscript circulated for comment).

DE PATER, I., S. GULKIS (1988). VLA observations of Uranus at 1.3-20 cm.*Icarus* **75**, 306-323.

DE PATER, I., S. T. MASSIE (1985). Models of the millimeter-centimeter spectra of the giant planets. *Icarus* **62**, 143-171.

ELLIOT, JAMES, L.(1979) Stellar Occultation Studies of the Solar System *Ann. Rev. Astron. Astrophys.***17**, 445-475.

ELLIOT, J. L., E. W. DUNHAM, AND D. J. MINK (1977). The rings of Uranus. *Nature* **267**, 328-330.

FLASER, F., M. B. J. CONRATH, P. J. GIERASCH, J. A. PIRRAGLIA (1987). Voyager infrared observations of Uranus' atmosphere: Thermal structure and Dynamics. *J. Geophys. Res.* **92**, 15011-15018.

FRENCH, R. G., J. L. ELLIOT, E. W. DUNHAM, D. A. ALLEN, J. H. ELIAS, J. A. FROGEL, AND W. LILLER (1983). The thermal structure and energy balance of the Uranian upper atmosphere. *Icarus* **53**, 399-414.

HERBERT, F., B. R. SANDEL, R. V. YELLE, J. B. HOLBERG, A. L. BROADFOOT, AND D. E. SHEMANSKY (1987). The Upper Atmosphere of Uranus: EUV Occultations Observed by Voyager 2. *J. Geophys. Res.* **92**, 15093-15109.

HILDEBRAND, R. H., R. L. LOWENSTEIN, A. D. HARPER, G. S. ORTON, J. KEENE, S. E. WHITCOMB. (1985). Far-infrared and submillimeter brightness temperatures of the giant planets.*Icarus*. **64**, 64-87.

HUNTEN, D. M., AND J. VEVERKA (1976). Stellar and spacecraft occultations by Jupiter: a critical review of derived temperature profiles. *Jupiter* (T. Gehrels, Ed). pp. 247-283 Univ. of Arizona Press, Tucson.

INGERSOLL, A. P. (1984). Atmosphere dynamics of Uranus and Neptune: Theoretical considerations. In *Uranus and Neptune*, ed. J. T. Bergstralh (NASA Conference Publication 2330), pp. 263-269.

LINDAL, G. F., J. R. LYONS, D. N. SWEETNAM, V. R. ESHLEMAN, D. P. HINSON, AND G. L. TYLER (1987). The atmosphere of Uranus: Results of radio occultation measurements with Voyager 2. *J. Geophys. Res.* **92**, 14987-15001.

MOSELEY, S. H., D. C. HUMM, J. T. BERGSTRALH, A. L. COCHRAN, W. D. COCHRAN, E. S. BARKER, R. G. TULL. (1984). Absolute spectrophotometry of Titan, Uranus, and Neptune. *Astrophys. J.* **292**, L83-L87.

ORTON, G. S.(1986). The spectrum of Uranus: Implications for large helium abundance. *Science* **231**, 836-840.

ORTON, G. S., M. J. GRIFFIN, P. A. R. ADE, I. G. NOLT, J. V. RADOSTITZ, E. I. ROBINSON AND, W. K. GEAR (1986). Submillimeter and millimeter observations of Uranus and Neptune. *Icarus* **67**, 289-304.

ORTON, G. S., K. H. BAINES, J. T. BERGSTRALH, R. H. BROWN, J. CALDWELL, A. T. TOKUNAGA (1987a). Infrared radiometry of Uranus and Neptune at 21 and 32 μm. *Icarus* **69**, 230-238.

ORTON, G. S., D. K. AITKEN, C. SMITH, P. F. ROCHE, J. CALDWELL, R. SNYDER (1987b). The spectra of Uranus and Neptune at 8-14 and 17-23 μm. *Icarus* **70**, 1-12.

PEARL, J. C., B. J. CONRATH, R. A. HANEL, J. A. PIRRAGLIA, A. COUSTENIS (1987). Energy Balance of Uranus: Preliminary Voyager results. *Bull. Amer. Astron. Soc.* **19**, 852.

RIEKE, G. H, F. J. LOW. (1974). Infrared measurements of Uranus and Neptune. *Astrophys. J.* **193**, L147-L149.

SICARDY, B, M.COMBES, A. BRAHIC, P. BOUCHET, C. PERRIER, R COURTIN (1982). The 15 August 1980 Occultation by the Uranian System: Structure of the Rings and Temperature of the Upper Atmosphere *Icarus* **52**, 454-472.

SMITH, B. A., L. A. SODERBLOM, R. BEEBE, D. BLISS, J. M. BOYCE, A. BRAHIC, G. A. BRIGGS, R. H. BROWN, S. A. COLLINS, A. F. COOK II, S. K. KROFT, J. N. CUZZI, G. E. DANIELSON, M. E. DAVIES, T. E. DOWLING, D. GODFREY, C. J. HANSEN, C. HARRIS, G. E. HUNT, A. P. INGERSOLL, T.V. JOHNSON, R. J. KRAUSS, H. MASURSKY, D. MORRISON, T. OWEN, J. B. PLESCIA, J. B. POLLACK, C. C. PORCO, K. RAGES, C. SAGAN, E. M. SHOEMAKER, L.A. SROMOVSKY, C. STOKER, R. G. STROM, V. E. SUOMI, S. P. SYNNOTT, R.J. TERRILE, P. THOMAS, W. R. THOMPSON, AND J. VEVERKA (1986). Voyager 2 in the Uranian system: Imaging science results. *Science* **233**, 43-64.

TOKUNAGA, A. T., G. S. ORTON, J. CALDWELL. (1983). New observational constraints on the temperature inversions of Uranus and Neptune. *Icarus*. **53**, 141-146.

ULICH, B. L. (1981). Millimeter-wavelength continuum calibration sources. *Astron. J.* **86**, 1619-1626.

WALLACE, L. (1980). The structure of the Uranus atmosphere. *Icarus* 43, 231-259.

WEST, R. A., A. L. LANE, C. W. HORD, L. W. ESPOSITO, K. E. SIMMONS, R. M. NELSON, B. D. WALLIS (1987). Temperature and aerosol structure of the nightside

Uranian stratosphere from Voyager 2 photopolarimeter stellar occultation measurements. *J. Geophys. Res.* **92**, 15030-15036.

Chapter 2

The Oblateness of Uranus at the 1-μbar Level

2.1 Introduction

The equipotential figure of a planet is determined by both the gravitational field associated with the mass distribution of the planet itself, and the centripetal forces associated with its rotation. Departures of the figure from a geoid can reveal information about zonal winds or belts. For instance, spacecraft occultation data for Saturn have been used by Lindal *et al.* (1985) to identify and model deviations from a calculated reference geoid defined by the planet's external gravity field. An additional term representing the differential rotation of an equatorial belt of gas around the planet was needed to model the deviations that formed a bulge in the planet's figure. These deviations, amounting to approximately 2%, are associated with Saturn's strong zonal winds. An accurate determination of the planetary figure, and the implied differential rotation, may also be used to constrain planetary interior models. For example, Hubbard and Stevenson (1984) point out that Saturn's differential rotation may imply that the planet is rotating as individual cylinders, and that the differential rotation changes the values of the gravitational moments by increasing |J2| and |J4| by 0.5% and 2.5%, respectively.

Our knowledge of the figure and rotation properties of Uranus are much less certain. Previous studies of Uranus' oblateness from stellar occultation data (Elliot *et al.* 1980, 1981; French 1984) were limited by small data sets and by significant uncertainties in the occultation geometry. Recent spacecraft occultation data (Lane *et al.* 1986, Holberg *et al.* 1987) and ground-based observations have provided much improved positional accuracy (French *et al.* 1988). In addition, high quality occultation observations from 26

April 1981, 22 April 1982, 1 May 1982, and 25 March 1983 are now available for inclusion in the oblateness solution. We have used the refined event geometry and the full set of earth-based stellar occultation data to determine the figure of Uranus at approximately the 1-μbar level. A summary of the observations is contained in the next section. In Section 2.3, we describe the method used for the oblateness analysis. Section 2.4 presents a discussion of the results, and in Section 2.5 we present our conclusions.

2.2 Observations

Stellar occultations by the Uranian system have been widely observed since the 10 March 1977 discovery of rings about the planet (Elliot *et al.* 1977). From the times of stellar immersion and emersion, the limb of the planet can be measured, and by combining the results from several observations, the shape of the planet can be derived. Although the present pole-on aspect of Uranus restricts to the equatorial region the range of latitudes accessible to occultations, this limitation is partially offset by the presence of the rings, which provide a precise reference frame for determining the relative position of the star and planet throughout the atmospheric occultation. Even an occultation observed from only one station can be useful in defining the limb of Uranus; in contrast, Neptune occultations sample a much larger range of latitudes, but the event geometry must be determined from the atmospheric occultations themselves (French *et al.* 1985, Hubbard *et al.* 1985, Lellouch *et al.* 1986, Hubbard *et al.* 1987).

All Uranus atmospheric occultation observations between 10 March 1977 and 25 March 1983 were examined for use in the oblateness determination. With data in various forms, time resolutions, timing uncertainties, and varying observing conditions, careful consideration must be given to the data used. Observations were selected on the basis of

signal-to-noise, an accurate time base, the quality of observing conditions, and a well-calibrated record. The data considered for use are listed in Table 2-1, along with references where additional information about each observation may be found, with the exception of some observations of the 22 April 1982 occultation of KME14 (Klemola *et al.* 1981) that have not previously been presented in the literature. The circumstances of the observations from the Cerro Tololo Inter-American Observatory (CTIO) have been reported in Elliot *et al.* (1984), and P. Nicholson and K. Matthews obtained observations from the Cerro Las Campanas Observatory (LCO). The two observatories contributed four events apiece: two telescopes at CTIO each recorded both the immersion and emersion events, and a dual channel photometer on the LCO telescope gave independent visual and infrared wavelength data. Several data sets were considered for inclusion in the fit but were omitted from the solution because they did not satisfy our criteria for photometric quality and accurate timing. These are summarized in Table 2-2, along with the reasons for their exclusion.

2.3 Oblateness Analysis

To determine the planetary oblateness from occultation observations, the radius of an isobaric surface in the atmosphere must be found as a function of latitude. We have used the time of half-light of an isothermal model fit to the occultation light curve to define the reference level in the atmosphere for each observation. Although the half-light surface is only approximately isobaric, isothermal fits have the advantage of being easy to perform and much less sensitive to the choice of initial conditions than light curve inversion methods (French and Taylor 1981, Melroy 1984). The model isothermal light curve (Baum and Code 1953) is given by

Table I

URANUS OCCULTATION OBSERVATIONS					
Occultation Date	Occulted Star	Observatory	Recording Medium	Wavelength (μm) (passband)	References
10 Mar. 1977	SAO 158687	KAO	magnetic tape	0.619 (0.0075) 0.728 (0.02) 0.852 (0.021)	Elliot *et al.* (1980) Dunham *et al.* (1980)
		Cape	strip chart	0.8 (0.15)	Elliot *et al.* (1980) Dunham *et al.* (1980)
10 June 1979	KM9	LCO	strip chart	2.2 (0.4)	Nicholson *et al.* (1981) Elliot *et al.* (1981)
15 Aug. 1980	KM12	CTIO	magnetic tape	2.2 (0.4)	Elliot *et al.* (1981) French *et al.* (1982)
		ESO	magnetic tape	2.2 (0.5)	French *et al.* (1982) Sicardy *et al.* (1982)
		LCO	strip chart	2.2 (0.4)	Nicholson *et al.* (1982) French *et al.* (1982)
26 Apr. 1981	KME13	AAT	magnetic tape	2.2 (n/a)	French *et al.* (1983)
		ANU (1m)	magnetic tape	0.44 (0.1) 0.78 (0.18)	French *et al.* (1983)
22 Apr. 1982	KME14	CTIO	magnetic tape	0.88 (0.036)	Elliot *et al.* (1984)
		CTIO (1.5m)	magnetic tape	2.2 (0.4)	Elliot *et al.* (1984)
		ESO	magnetic tape	2.2 (0.5)	Sicardy *et al.* (1985)
		LCO	magnetic tape	0.88 (n/a) 2.2 (n/a)	Unpublished
		TCS	magnetic tape	0.449 (0.009) 0.88 (0.03)	Millis *et al.* (1987)
		OPMT	magnetic tape	2.2 (0.5)	Sicardy *et al.* (1985)
1 May 1982	KME15	Mt. Stromlo	magnetic tape	2.2 (0.4)	French *et al.* (1987)
25 Mar. 1983	KME17b	SAAO	magnetic tape	2.2 (n/a)	Elliot *et al.* (1987)

Note: KM and KME numbers are from Klemola and Marsden (1977) and Klemola *et al.* (1981). The following is a list of codes for the place of observation: KAO- Kuiper Airborne Observatory; Cape- Cape Town South Africa; LCO- Las Campanas Observatory; CTIO- Cerro Tololo Inter-American Observatory; ESO- European Southern Observatory; AAT- Anglo Australian Telescope; ANU- Australian National University; TCS- Teide Observatory at Tenerife; OPMT- Observatoire du Pic du Midi et de Toulouse; SAAO- South African Astronomical Observatory.

Table II

Table 2-2

OCCULTATION OBSERVATIONS NOT USED FOR OBLATENESS DETERMINATION

Occultation Date	Occulted Star	Observatory	Comments	References
15 Aug. 1980	KM12	CTIO	Emersion not used due to variable transmission.	Elliot *et al.* (1981) French *et al.* (1982)
		ESO	Immersion not used due to reported probable guiding error; Emersion not used due to variable transmission.	French *et al.* (1982) Sicardy *et al.* (1982)
		LCO	Emersion not used due to variable transmission.	Nicholson *et al.* (1982) French *et al.* (1982)
22 Apr. 1982	KME14	ESO	Data not available for this analysis	Sicardy *et al.* (1985)
		TCS	Suspected timing uncertainity.	Millis *et al.* (1987)
		OPMT	Only a partial data set available.	Sicardy *et al.* (1985)

$$v_{\perp}(t - t_{1/2}) = H\left[\left(\frac{1}{\phi} - 2\right) + \ln\left(\frac{1}{\phi} - 1\right)\right], \qquad (2\text{-}1)$$

where $v_{\perp}$ is the component of the sky plane stellar velocity perpendicular to the planetary limb, t is time, $t_{1/2}$ is the time at half-light, ϕ is the normalized stellar flux, and the atmospheric scale height H is defined as

$$H = \frac{kT}{\mu m_H g}, \qquad (2\text{-}2)$$

where k is Boltzmann's constant, T is the temperature, μ is the mean molecular weight, m_H is the mass of the hydrogen atom, and g is the local acceleration of gravity, including the effects of centripetal acceleration due to planetary rotation. Figure 2-1 shows a pair of typical light curves, along with the best-fitting isothermal models.

We determined the planetary oblateness and equatorial radius as follows. We first computed the coordinates of the observer projected onto the fundamental plane for the set of half-light times and observatory locations, using the method described by French and Taylor (1981). The coordinates (f, g) of each of the half-light points are measured east and north, respectively, from the predicted location of the center of Uranus, using the JPL DE-125 ephemeris. The offset between the actual and the predicted location of the planet (f_0, g_0) for each occultation was obtained from kinematical orbit fits to the ring occultation data obtained during these same occultations (French *et al.* 1988). The geometric radius of the half-light point is thus

$$r_{geom} = [(f - f_0)^2 + (g - g_0)^2]^{1/2}. \qquad (2\text{-}3)$$

Figure 2-1(a) Immersion occultation light curve from the 22 April 1982 occultation of KME14 observed using the CTIO 4-meter telescope. The smooth line plotted over the data is the best-fitting model occultation curve for an isothermal atmosphere. The zero and full stellar intensity values are derived from the isothermal fit, and noise from a variety of sources may cause signal variations above and below these values.

Figure 2-1(b) Emersion occultation light curve from the 22 April 1982 occultation of KME14 observed using the CTIO 4-meter telescope. The smooth line plotted over the data is the best-fitting model occultation curve for an isothermal atmosphere.

Figure 2-1a

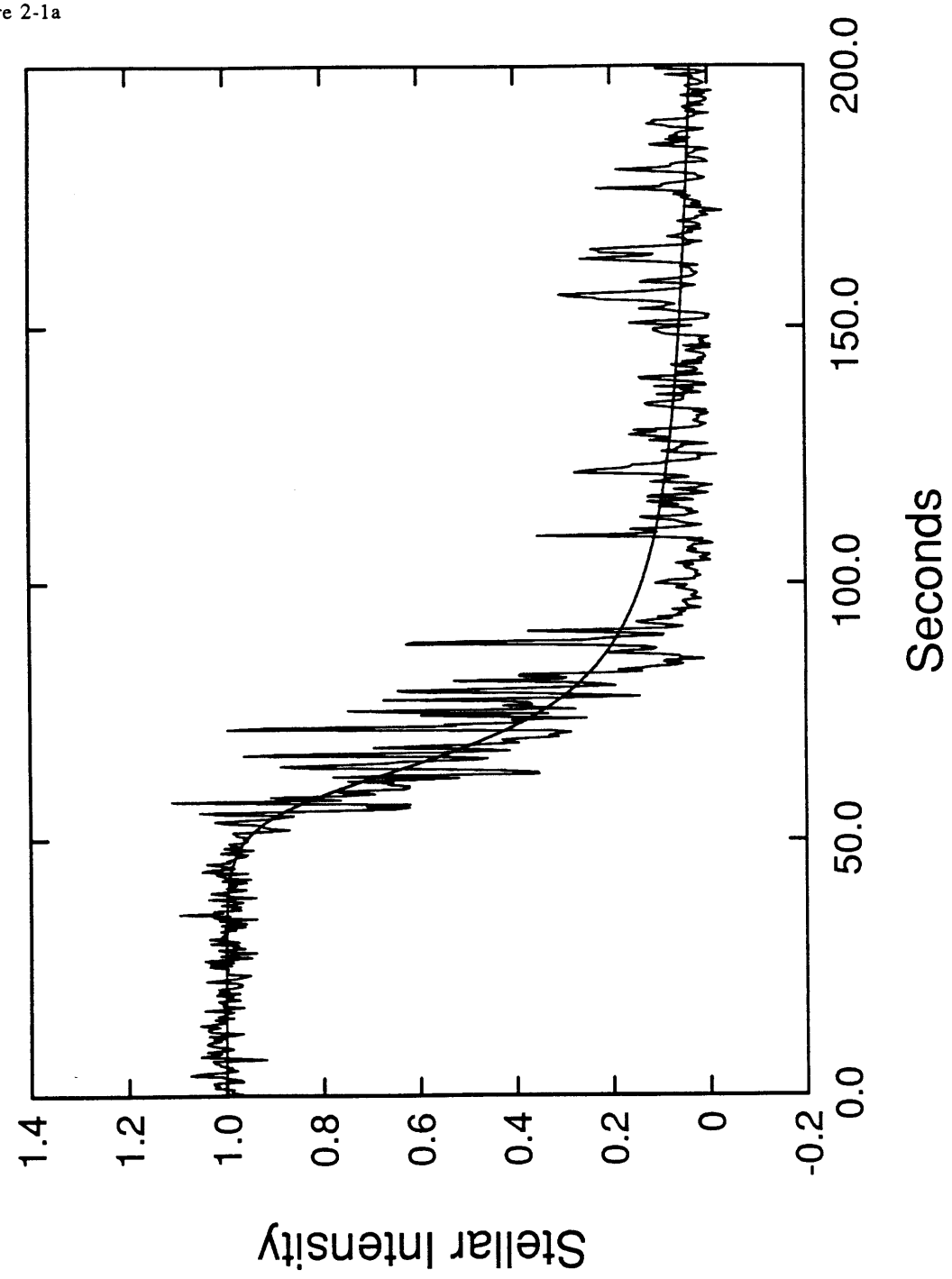
Stellar Intensity
1.4
1.2
1.0
0.8
0.6
0.4
0.2
0
-0.2
0.0
50.0
100.0
150.0
200.0
Seconds

Chapter 2

Figure 2-1b

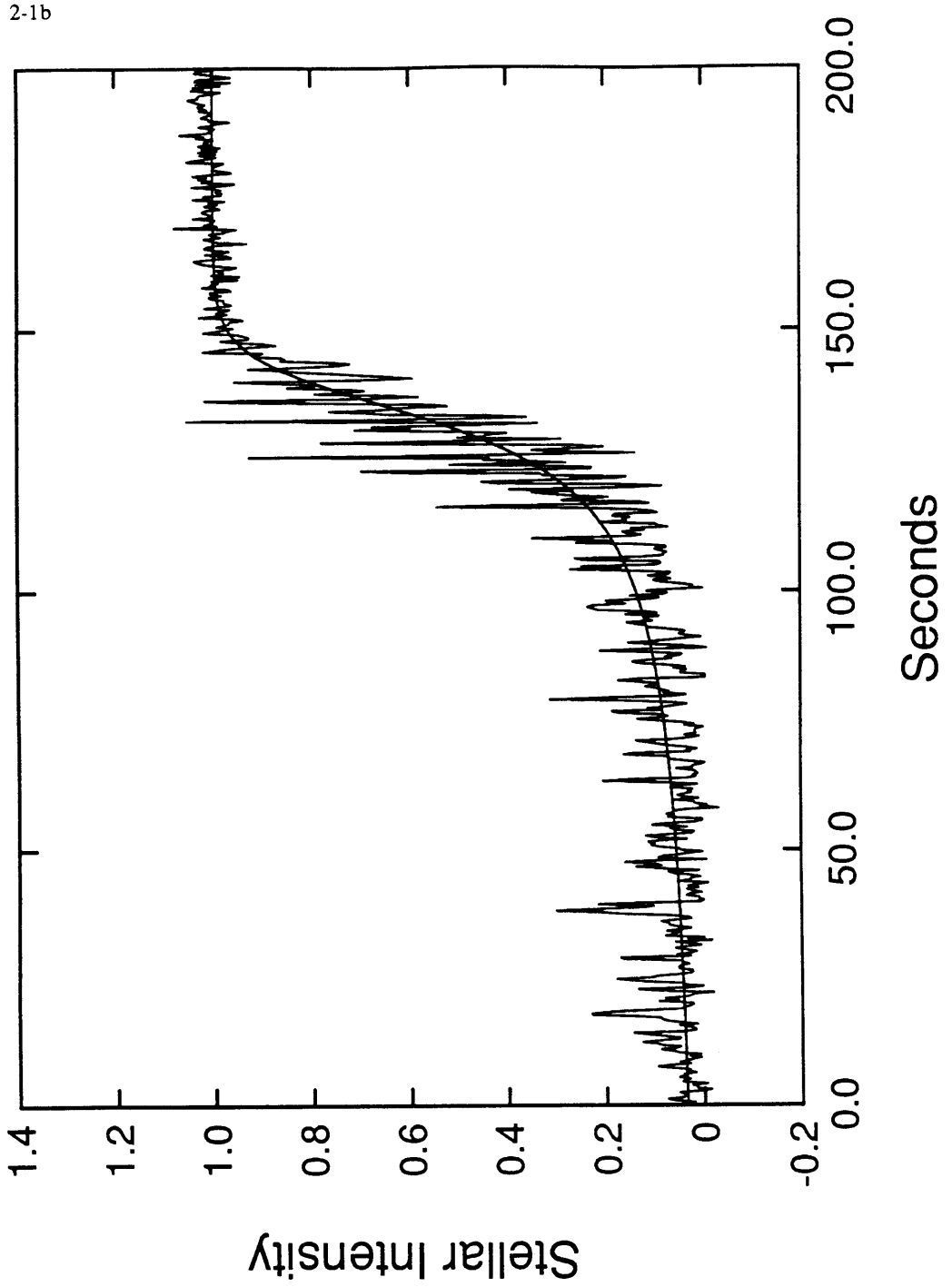

Next, we added a correction for refractive bending of the half-light ray, given by $\Delta r_{rb} = H$, where the scale height H was determined from the isothermal fit to each light curve. An additional radius correction to account for general relativistic bending of the ray is given by

$$\Delta r_{gr} = \frac{4GMD}{rc^2}, \tag{2-4}$$

where G is the gravitational constant, M is the mass of Uranus, D is the distance from Uranus to the Earth, r is the impact parameter of the ray, and c is the speed of light. The correction Δr_{gr} is approximately 27 km for all observations.

For a spherical planet the radius sampled by each half-light ray, corrected for refractive and gravitational bending, is given by

$$r_s = r_{geom} + \Delta r_{rb} + \Delta r_{gr}, \tag{2-5}$$

and the Uranus latitude θ_s of each occultation point is given by

$$\sin \theta_s = \cos B \cos(P - P_0), \tag{2-6}$$

where the French *et al.* (1988) determination of Uranus' pole direction was used to compute the position angle of the pole P and the declination of the earth B, and P_0 is the position angle (measured eastward from north) of the occultation point, determined from

$$\tan P_0 = \left[\frac{f - f_0}{g - g_0}\right]. \tag{2-7}$$

However, when an elliptical planet is touched by a tangent ray from a distant observer, in general the point of contact does not lie in the plane of the sky but will be in front of or behind that plane by a small amount. Thus, for an oblate planet, a tangent ray touches the planet at a radius of

$$r = \left[1 + \gamma^2 \frac{\sin^2 \theta_s}{\cos^2 B} \right] r_s \qquad (2\text{-}8)$$

and at a sub-occultation latitude θ given by

$$\sin\theta = \frac{r_s \sin\theta_s}{r}(1 + \gamma \tan B), \qquad (2\text{-}9)$$

where

$$\gamma = \frac{-\varepsilon \left(1 - \frac{\varepsilon}{2} \right) \sin 2B}{1 - \varepsilon (2 - \varepsilon) \cos^2 B}. \qquad (2\text{-}10)$$

In practice, the effect of these last corrections are quite small as the change in θ acts to cancel the change in r in the derived oblateness.

To second order in ε, an ellipse is an accurate model of a geoid (Zharkov and Trubitsyn 1978). We have minimized the sum of squared radial separations between the data points and model ellipse defined by

$$\frac{r^2 \cos^2 \theta}{R_e^{\,2}} + \frac{r^2 \sin^2 \theta}{R_e^{\,2}(1 - \varepsilon)^2} = 1 \qquad (2\text{-}11)$$

The isothermal fit results and event geometry for the 23 atmosphere events used in the solution are given in Table 2-3, along with the post-fit radius residuals Δr. From our oblateness fit, we find $R_e = 26071 \pm 3$ km and $\varepsilon = 0.0197 \pm 0.0010$, with a corresponding polar radius of $R_p = 25558 \pm 24$ km. The fitted half-light surface, plotted in Figure 2-2, corresponds approximately to the 1-μbar level in the Uranian atmosphere. Table 2-4 summarizes recent Uranus radius and oblateness measurements. The given uncertainties in our oblateness determination are formal errors from the least squares fit. Although not all sources of error are easily quantified, we have identified a number of possible sources of error and we assess their importance as follows:

1) *photon noise* - For an isothermal atmospheric occultation corrupted by photon noise, the error in the half-light time is given by (French *et al.* 1978)

$$\sigma(t_{1/2}) = \frac{3.55}{n_*}\left[\frac{H}{v_\perp}(n_b + \phi n_*)\right]^{1/2}, \qquad (2\text{-}12)$$

where ϕ is the normalized occultation flux, n_* is the rate of photons detected per second from an unocculted star and n_b is the rate from the background. The error in the half-light time from this effect is typically on the order of several tens of milliseconds. At typical event velocities, this corresponds to an error in the derived radius of less than one km, small compared to other external sources of error.

2) *non-isothermal atmosphere* - Although we have fitted the light curves using an isothermal model, the atmosphere is manifestly non-isothermal. The sharp, intense spikes in the light curves (Figure 2-1) are clearly the result of rapid changes in the refractivity gradient in the atmosphere, and numerical inversion of most occultation light curves (whereby a temperature profile for the atmosphere is recovered) show non-isothermal

Figure 2-2 Radius of the half-light level in the Uranian atmosphere as a function of latitude. Each symbol represents the date the occultation took place. The best fit to the observed limb profile is shown as a solid line, corresponding to an oblateness of $\varepsilon = 0.0197$. See the text for a discussion of the uncertainties in the measured radii.

Figure 2-2

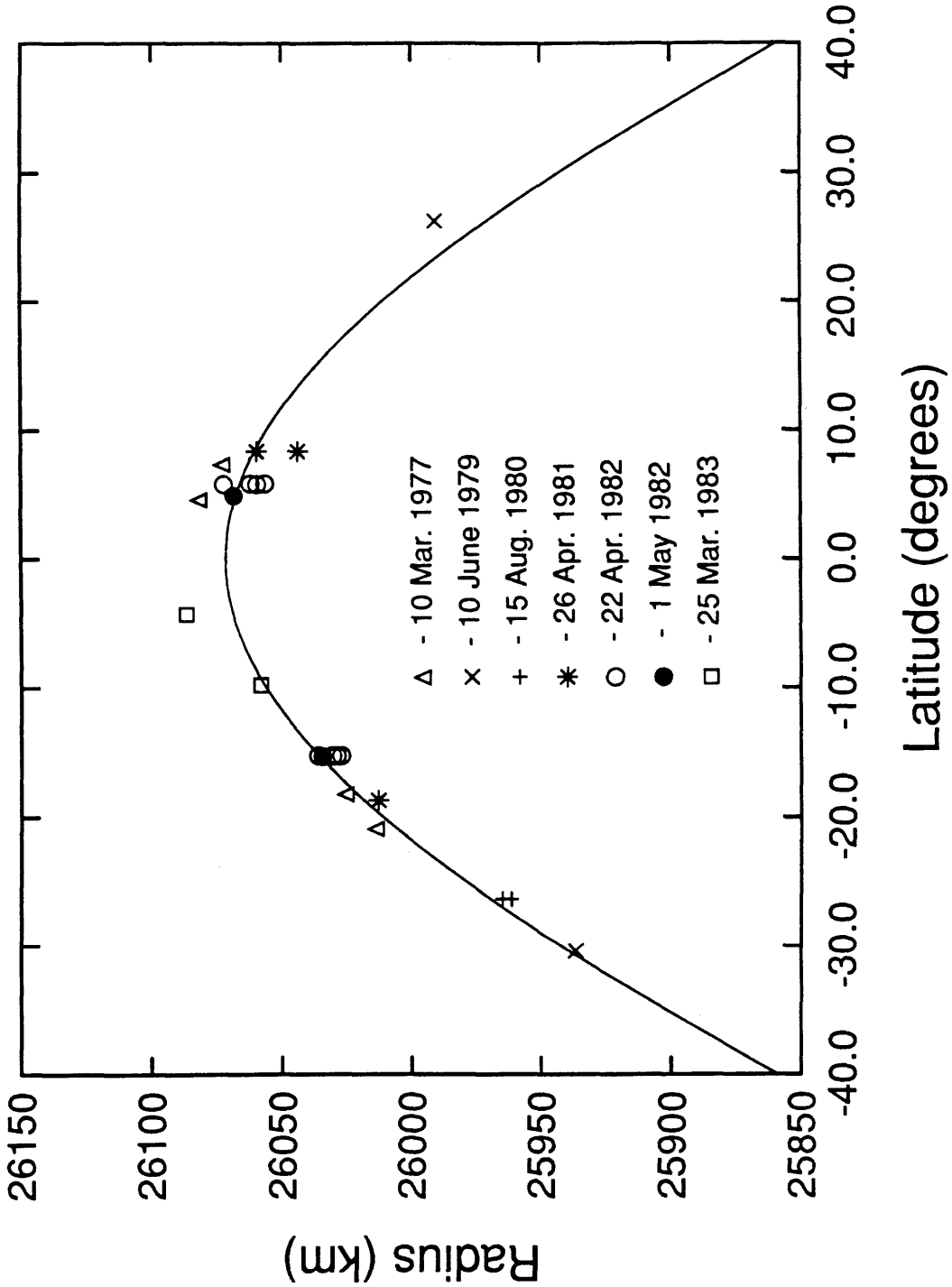
Radius (km)
26150
26100
26050
26000
25950
25900
25850
-40.0
-30.0
-20.0
-10.0
0.0
10.0
20.0
30.0
40.0
Latitude (degrees)
Δ - 10 Mar. 1977
× - 10 June 1979
+ - 15 Aug. 1980
✱ - 26 Apr. 1981
○ - 22 Apr. 1982
● - 1 May 1982
□ - 25 Mar. 1983

Table III

Table 2-3

RESULTS OF ISOTHERMAL FITS AND EVENT GEOMETRY										
Occ. Date	Occulted Star	Observatory	Event I or E	$t_{\frac{1}{2}}$ (UTC)	$v_{\perp}$ (km/sec)	H(km)	T(K)	Latitude (Degrees)	Radius (km)	Δr (km)
10 Mar. 1977	SAO 158687	KAO	I	20:53:27.98	4.00	49.1	114.0	4.5	26081.1	13.0
			E	21:18:08.76	3.83	41.5	101.7	−18.0	26025.2	4.0
		Cape	I	20:57:21.82	4.77	40.7	95.6	7.2	26072.1	9.1
			E	21:28:58.56	4.80	40.7	99.8	−20.6	26014.0	7.8
10 June 1979	KM9	LCO	I	1:52:47.40	18.01	53.1	128.8	25.8	25992.0	20.3
			E	2:37:21.43	17.99	56.2	134.4	−29.9	25938.6	−2.5
15 Aug. 1980	KM12	CTIO	I	22:38:09.07	6.81	70.4	171.0	−25.9	25962.8	−8.1
		LCO	I	22:38:13.34	6.77	63.8	154.9	−25.9	25966.4	−4.7
26 Apr. 1981	KME13	AAT	I	19:33:07.16	15.21	61.9	146.2	8.2	26059.6	−0.9
			E	20:04:44.02	15.17	60.4	148.2	−18.3	26013.5	−5.7
		ANU(1m)	I	19:33:07.80	15.21	55.8	131.9	8.2	26043.8	−16.7
22 Apr. 1982	KME14	CTIO	I	1:58:58.21	14.09	62.8	146.7	5.8	26061.9	−4.1
			E	2:36:30.83	14.12	58.9	143.4	−15.0	26029.3	−6.8
		CTIO(1.5m)	I	1:58:58.68	14.09	64.0	149.6	5.8	26056.5	−9.5
			E	2:36:31.43	14.12	57.7	140.4	−15.0	26036.6	0.4
		LCO	I	1:59:06.99	14.03	71.9	167.8	5.7	26072.1	6.0
			E	2:36:30.38	14.06	56.4	137.3	−15.0	26031.0	−5.2
			I	1:59:07.29	14.03	63.5	148.3	5.7	26059.5	−6.6
			E	2:36:29.96	14.06	58.9	143.4	−15.0	26027.6	−8.6
1 May 1982	KME15	Mt Stromlo	I	16:41:35.47	15.12	61.1	142.2	4.9	26068.4	0.8
			E	17:12:29.05	15.09	59.3	144.3	−15.0	26034.9	−1.1
25 Mar. 1983	KME17b	SAAO	I	2:14:48.71	1.96	76.5	177.4	−4.2	26086.3	17.8
			E	3:04:48.80	1.96	68.8	163.5	−9.6	26058.0	1.4

Table 2-4

Table IV

RADIUS AND OBLATENESS MEASUREMENTS					
Method	Atmospheric Level Probed	Equatorial Radius (km)	Oblateness $(1-R_p/R_e)$		Reference
Stellar occultation (half-light surface)	1 μbar	26,071 ± 3	0.0197	± 0.0010	This work
Stellar occultation (half-light surface)	1 μbar	26,145 ± 30	0.024	± 0.003	Elliot *et al.* (1981)
Stellar occultation ($n = 10^{14}$ cm^{-3})	1 μbar	26,228 ± 30	0.033	± 0.007	Elliot *et al.* (1980)
Re-analysis of Stratoscope images (visible disk)	5 mbar	-	0.022	± 0.001	Franklin *et al.* (1980)
Stratoscope image measurements (visible disk)	5 mbar	25,900 ± 300	0.01	± 0.01	Danielson *et al.* (1972)
Double image micrometer (visible disk)	5 mbar	25,400 ± 280	0.030	± 0.008	Dollfus (1970)
Spacecraft radio ocultation (Voyager 2)	1 bar	25,559 ± 4	0.02293	± 0.00080	Lindal *et al.* (1987)

features with excursions of up to several tens of degrees (*e.g.*, French *et al.* 1983). The error in the radius of the half-light ray from these effects is expected to be a small fraction of a scale height, on the order of several kilometers.

3) *atmospheric dispersion* - The wavelength dependence of the atmospheric refractivity causes the half-light ray at two different wavelengths to correspond to slightly different pressure levels. For an atmosphere of 85% hydrogen and 15% helium, the differential refraction over the range of wavelengths of the observations in this analysis (Table 2-1) amounts to a difference of less than one km in the altitudes sounded by the corresponding half-light rays.

4) *quality of the data* - Each light curve is influenced to some extent by observational effects such as guiding errors, transparency changes, atmospheric scintillation, instrumental time constants, accuracy of the time base used, and short and long term detector and data system noise. In order to estimate the importance of these effects, we performed a series of simulated occultations in which isothermal fits were made to a model isothermal light curve to which we added zero mean (for the segment of noise added) noise. The noise was recorded as part of the observations prior to immersion or after emersion. (No scaling with amplitude of the model lightcurve was attempted. This should provide a conservative estimate of the effects of the noise, since for most infrared observations the amplitude of the noise decreases with the decreasing signal level.)

From these experiments, we learned that there is a very strong negative correlation between the fitted half-light time and atmospheric scale height in the presence of low frequency scintillation noise. We note that the derived half-light radius is related to both the half-light time and the mean scale height, which is used to compute the refractive bending correction. The practical consequence of this anti-correlation is that the errors in the half-light time and the scale height tend to cancel each other. The scintillation-induced error in

the half-light radius is comparable to the individual errors in the half-light time and the fitted scale height, rather than to these errors added in quadrature, as would be the case in the absence of the observed correlation. For typical observations, this amounts to an uncertainty of a few km.

5) *occultation astrometry* - Errors in the predicted relative positions of Uranus and the occultation stars are removed in large part by using the results of ring orbit fits. As reported by French *et al.* (1988), these uncertainties are now at the one km level.

6) *satellite motions* - We have not taken into account the motion of Uranus with respect to the Uranus-satellite barycenter between immersion and emersion. For the occultations considered here, the corresponding radius error is less than one km.

An estimate of the combined effects of the external sources of error is provided by the scatter in the points from simultaneous observations of the same occultation from several nearby telescopes. For the 22 April 1982 event, there is a peak-to-peak deviation of 10 km and 9 km for the visual and infrared, respectively, between the observations at CTIO and LCO.

2.4 Discussion

For a uniformly rotating planet in hydrostatic equilibrium, the oblateness and the lowest order gravitational harmonic coefficients J_2 and J_4 can be used to determine the rotation period (Elliot and Nicholson 1984)

$$T = 2\pi\left\{ \frac{\left(1+\frac{3}{2}\left(\frac{R_r}{R_e}\right)^2 J_2 \right) R_e^3 (1-\varepsilon)}{2GM\left[\varepsilon - \frac{3}{2}\left(\frac{R_r}{R_e}\right)^2 J_2 \left(1+\frac{3}{2}\left(\frac{R_r}{R_e}\right)^2 J_2 \right) - \frac{5}{8}\left(\frac{R_r}{R_e}\right)^4 J_4 \right]} \right\}^{\frac{1}{2}}, \qquad (2\text{-}13)$$

where T is planet's the rotation period, R_e is the equatorial planetary radius, R_r is the reference radius for the harmonic expansion of the gravity potential for J_2 and J_4, and ε is the oblateness. Using $J_2 = (3.34343 \pm 0.00032) \times 10^{-3}$ and $J_4 = (-2.885 \pm 0.045) \times 10^{-5}$ from French *et al.* (1988) and GM = 5,793,939 ± 60 km^3 sec^{-2} for Uranus from Tyler *et al.* (1986), we find T = 17.7 ± 0.6 hr, where the uncertainty is dominated by the formal errors in the oblateness determination.

From Voyager 2 radio observations of the magnetosphere of Uranus, Warwick *et al.* (1986) determined a rotation period of 17.24 ± 0.01 hr. This period is appropriate for the deep interior of the planet, where the magnetic field is presumably generated and coupled to the rotating core. In contrast, our rotation period refers to the upper atmosphere of the planet, averaged over an equatorial region spanning the latitude range ($-30° < \theta < 26°$) sampled by the observations. Smith *et al.* (1986) measured cloud velocities from Voyager 2 images and inferred a strong latitude-dependence to the atmospheric rotation rate. Lindal *et al.* (1987) have combined Smith *et al.*'s (1986) measurements and an analysis of Voyager 2 radio occultation observations to infer a rotation period of 18.0 ± 0.3 hr at $\theta = +5°$ (using the Uranian pole direction given by French *et al.*, 1988).

In Figure 2-3 (adapted from Figure 8 of Smith *et al.* 1986), we have plotted the measured rotation period as a function of latitude. There is a quasi-linear decrease in rotation period with increasing latitude. Furthermore, the atmosphere near the equator rotates *more slowly* than the deep interior of the planet. This equatorial sub-rotation was predicted by Read (1986) and investigated by Flasar *et al.* (1987), and appears to be associated with the large seasonally-averaged polar heating of Uranus due to its large obliquity. The difference between the Voyager 2 Uranus magnetosphere period of 17.24 hr and our derived equatorial period of 17.7 hr corresponds to a retrograde zonal velocity of

Figure 2-3 Uranus rotation period as a function of latitude. The period (17.7 ± 0.6 hr) determined in this work from the occultation data corresponds to the oblateness fit for the latitude range ($-30° < \theta < 26°$) sampled by the observations, and is shown by the large shaded circle, somewhat above the Voyager 2 value (dashed horizontal line) of 17.24 ± 0.01 hr (Warwick *et al.* 1986). Lindal *et al.*'s (1987) determination from Voyager radio occultation observations is shown by the triangle. The open circles are from Voyager 2 cloud motion studies (Smith *et al.* 1986). A clear trend is evident of increasing period with decreasing latitude, suggestive of Uranian equatorial sub-rotation.

Figure 2-3

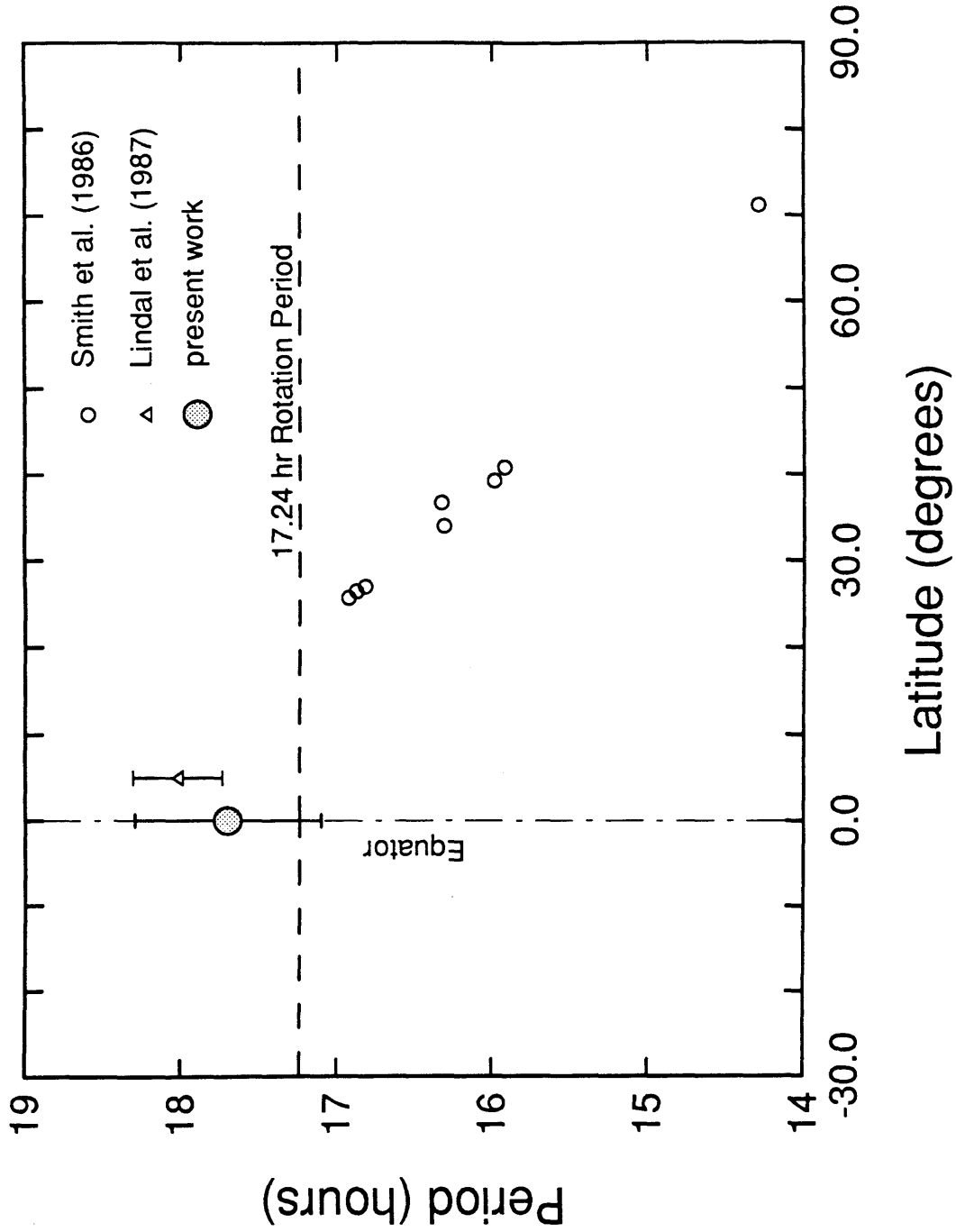
Smith et al. (1986)
Lindal et al. (1987)
present work
17.24 hr Rotation Period
Equator
Period (hours)
19
18
17
16
15
14
-30.0
0.0
30.0
60.0
90.0
Latitude (degrees)

about 76 m sec^{-1}. In contrast, Venus, Jupiter, and Saturn exhibit equatorial *super*-rotation with zonal velocities on the order of hundreds of m sec^{-1} (Smith *et al.* 1979a, 1979b, 1982).

Differential heating of the Uranian atmosphere is ultimately responsible for the pressure gradients associated with the observed zonal winds, but the radiative time constants deep in the atmosphere, where solar radiation is absorbed, are much longer than in the upper atmospheric regions sampled by the occultations (French *et al.* 1983). Consequently, the upper atmospheric dynamics and thermal structure may well be quite different from those in the troposphere. For example, the very small zonally averaged latitude temperature gradient near the cloud deck found by Hanel *et al.* (1986) reflects the very long radiative time constant at these pressure levels. At stratospheric levels, the response time of the atmosphere to radiative heating is much shorter, and diurnal variations are likely to be more substantial.

The oblateness at 1-bar (0.02293 ± 0.00080 Lindal *et al.* 1987) may be compared with the value obtained here by assuming solid body rotation and hydrostatic equilibrium. Under these conditions, a change in oblateness between two heights in the atmosphere is given by (Hubbard *et al.* 1987, Zharkov and Trubitsyn 1978):

$$\frac{d \ln \varepsilon}{d \ln R} = 3 - \frac{15}{2}\frac{J_2}{\varepsilon}. \qquad (2\text{-}14)$$

Using the two radii 25559 km and 26071 km for 1-bar and 1-μbar respectively, and the ellipticity at 1-μbar, the predicted value of oblateness at the 1-bar level is

$$\text{predicted:} \qquad \varepsilon(1\text{-bar}) = 0.9661\ \varepsilon(1\text{-}\mu\text{bar}). \qquad (2\text{-}15)$$

In contrast, the observations show that the oblateness at 1-bar is greater than at 1-μbar.

$$\text{observed:} \qquad \varepsilon(\text{1-bar}) = 1.1640 \pm 0.0406\ \varepsilon(\text{1-}\mu\text{bar}) \qquad (2\text{-}16)$$

The same effect is seen in measurements of Neptune's oblateness (Hubbard *et al.* 1987).

In Figure 2-4(a), we have plotted the temperature as a function of latitude for the occultations analyzed in this work. The data points show no apparent trend with latitude. An analysis by Sicardy *et al.* (1985) shows a uniform variation of scale height with latitude for a *single* occultation observed at several latitudes simultaneously. For a single occultation, the average diurnal insolation maps simply into latitude, but when observations over several years are combined, the situation is more complex. Furthermore, because of the small solar phase angles during the observations, the occultation observations inevitably sample regions near the terminator, where the strong insolation variations are likely to influence both the temperature profiles and the dynamics of the regions.

When the mean temperatures obtained by the isothermal fits are plotted as a function of date of observation (Figure 2-4(b)), rather than latitude, a more definite pattern appears. A least squares fit to the points suggests an increase in mean temperature of about 8 K yr^{-1}. This temperature increase has been noted previously (French *et al.* 1983; Sicardy *et al.* 1985). The details of Figure 2-4(b) should probably not be taken too literally, since the scale heights are determined from isothermal fits to light curves, and in some cases have given a systematically higher (approximately 20 K) temperature than that calculated from an inversion of the light curve. Also, the light curves contain non-isothermal features, such as spikes and lower frequency phenomena, that are not accounted for in each fit and may contribute a random component to the derived scale heights. If the temperature contrast of

Figure 2-4(a) Mean Uranian atmospheric temperature near the 1-μbar pressure level as a function of latitude. In spite of the greater insolation experienced in high northern latitudes, there is no systematic trend in temperature with latitude.

Figure 2-4(b) Mean Uranian atmospheric temperature near the 1-μbar pressure level, plotted against the observation date. In spite of the range of latitudes covered by the observations, there persists a systematic increase in temperature with date. The straight line, intended merely to be suggestive, corresponds to an upper atmospheric heating rate of about 8 K yr^{-1}.

Figure 2-4a

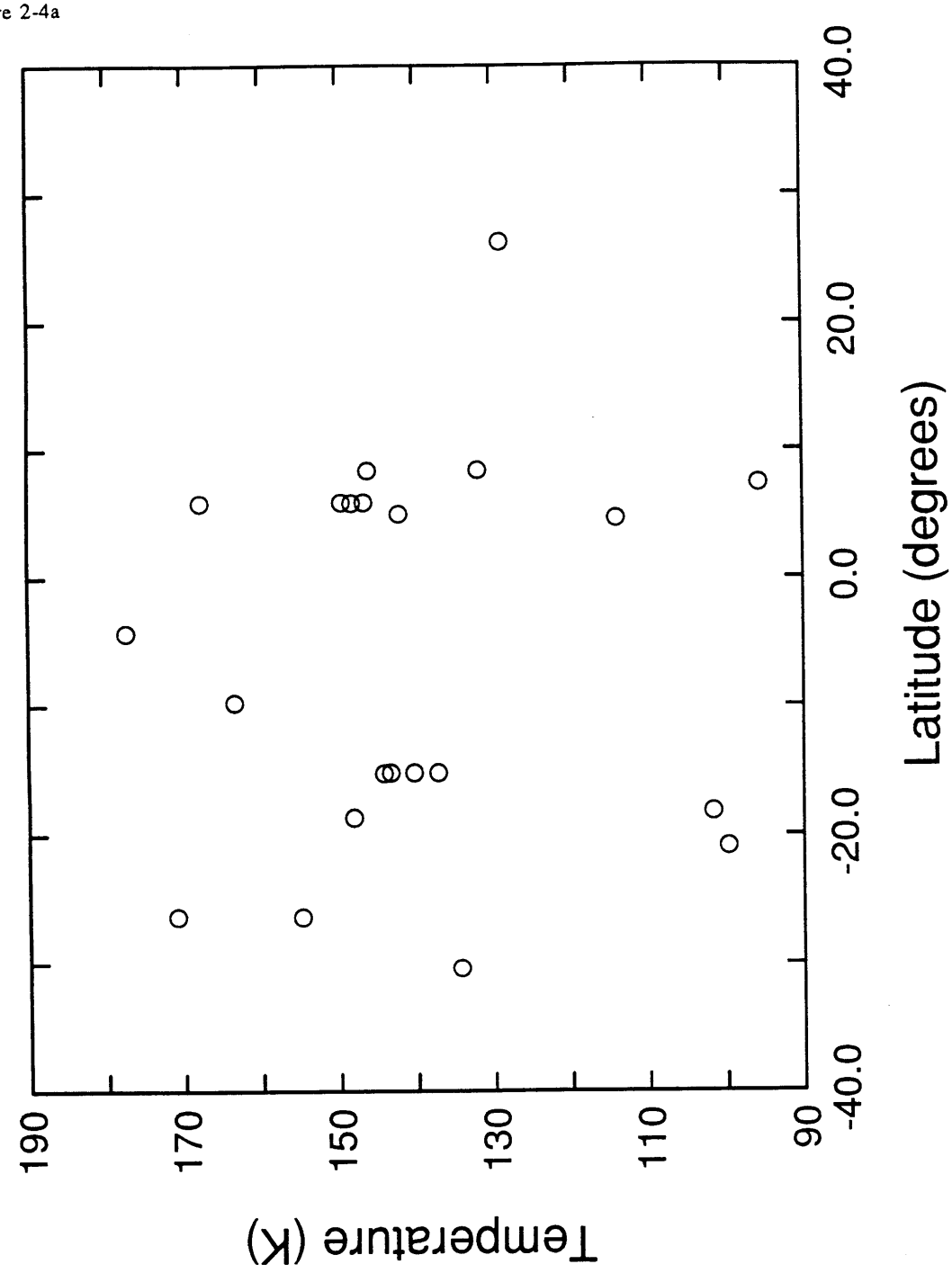
Temperature (K)
190
170
150
130
110
90
Latitude (degrees)
40.0
20.0
0.0
-20.0
-40.0

Figure 2-4b

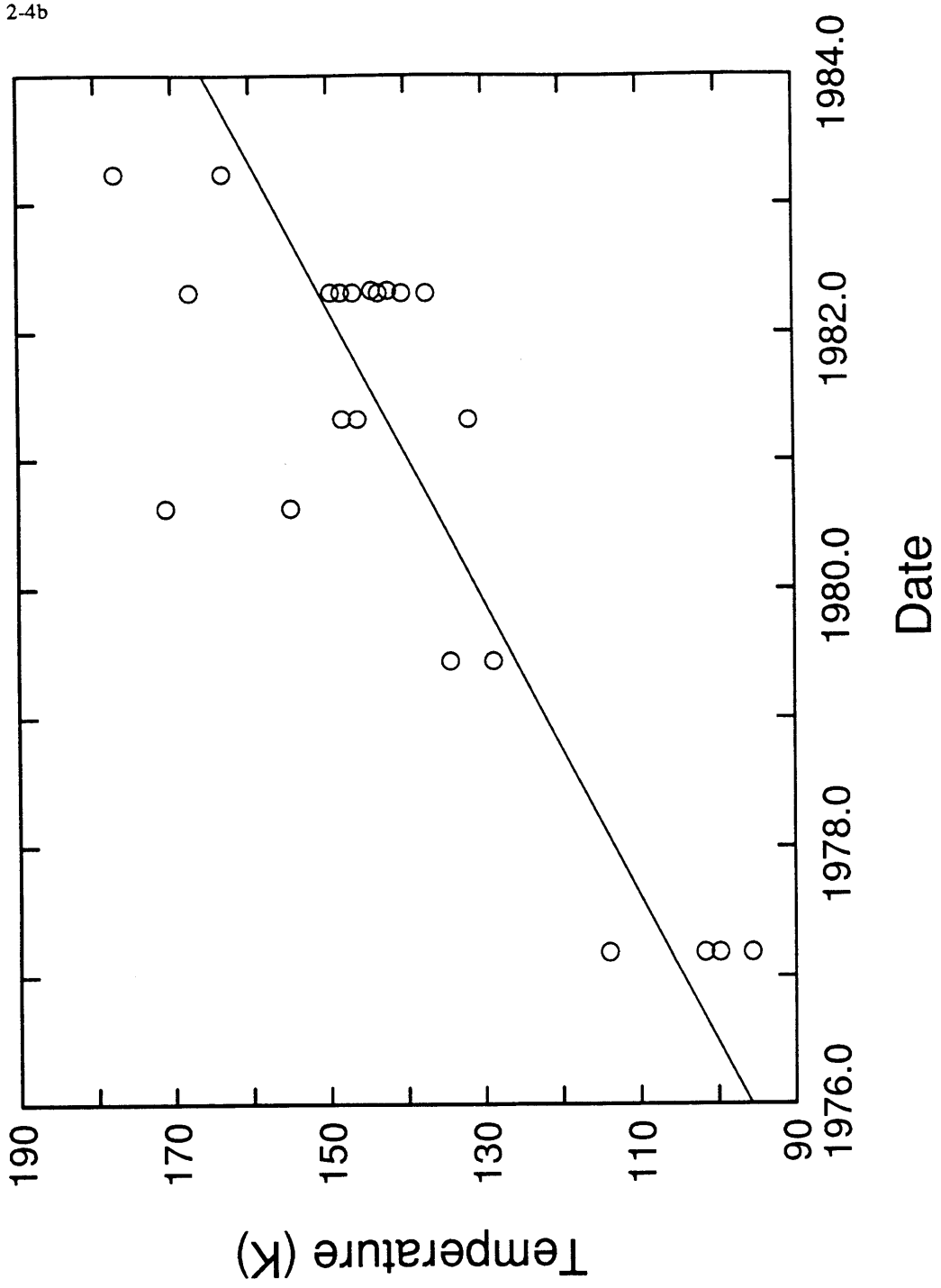
Temperature (K)
190
170
150
130
110
90
1976.0
1978.0
1980.0
1982.0
1984.0
Date

approximately 50 K indicated in Figure 2-4(b) extends deep into the atmosphere below the 1-μbar level, an increase in R_e with time would be expected. However Figure 2-2 shows no annual trend in radius suggesting either the temperature trend is more moderate or warming is localized in the atmosphere. Further work may show the true nature of this warming.

2.5 Conclusions

A substantially improved value for the oblateness at the 1-μbar level in the Uranian atmosphere has been obtained from an extensive set of stellar occultation observations. The equatorial rotation period of 17.7 ± 0.6 hr implied by the 1-μbar oblateness is consistent with an equatorial subrotation of the planet, a possibility supported by Voyager 2 observations of Smith *et al.* (1986) and Lindal *et al.* (1987).

References

BAUM, W. A., AND A. D. CODE (1953). A photometric observation of the occultation of σ Arietis by Jupiter. *Astron. J.* **58**, 108-112.

DANIELSON, R. E., M. G. TOMASKO, AND B. D. SAVAGE (1972). High-resolution imagery of Uranus obtained by Stratoscope, II. *Astrophys. J.* **178**, 887-900.

DOLLFUS, A. (1970). New optical measurements of the diameters of Jupiter, Saturn, and Neptune. *Icarus* **12**, 101-117.

DUNHAM, E., J. L. ELLIOT, AND P. J. GIERASCH (1980). The upper atmosphere of Uranus: Mean temperature and temperature variations. *Astron. J.* **235**, 274-284.

ELLIOT, J. L., I. S. GLASS, R. G. FRENCH, AND J. A. KANGAS (1987). The occultation of KME 17 by Uranus and its rings. *Icarus* **71**, 91-102.

ELLIOT, J. L., R. G. FRENCH, JAY A. FROGEL, J. H. ELIAS, D. J. MINK, AND W. LILLER (1981). Orbits of nine Uranian rings. *Astron. J.* **86**, 444-455.

ELLIOT, J. L., R. G. FRENCH, K. J. MEECH, AND J. H. ELIAS (1984). Structure of the Uranian rings I: Square-well model and particle size constraints. *Astron. J.* **89**, 1587-1603.

ELLIOT, J. L., E. W. DUNHAM, AND D. J. MINK (1977). The rings of Uranus. *Nature* **267**, 328-330.

ELLIOT, JAMES L., EDWARD DUNHAM, AND DOUGLAS MINK (1980). The radius and ellipticity of Uranus from its occultation of SAO 158687. *Astron. J.* **236**, 1026-1030.

ELLIOT, J. L., AND P. D. NICHOLSON (1984). The rings of Uranus. In *Planetary Rings* (Richard Greenberg and Andre Brahic, ed.), pp. 25-72. Univ. of Arizona Press, Tucson.

FLASAR, F. M., B. J. CONRATH, P. J. GIERASCH, AND J. A. PIRRAGLIA (1987). Voyager infrared observations of Uranus' atmosphere: Thermal structure and dynamics. *J. Geophys. Res.* **92**, 15011-15018.

FRANKLIN, F. A., C. C. AVIS, G. COLOMBO, AND I. I. SHAPIRO (1980). The geometric oblateness of Uranus. *Astrophys. J.* **236**, 1031-1034.

FRENCH, RICHARD G. (1984). Oblatenesses of Uranus and Neptune. Proceedings of the Uranus and Neptune workshop, Pasadena, CA, February 6-8, 1984, pp. 347-356. NASA Conference Publication 2330.

FRENCH, R. G., J. L. ELLIOT, E. W. DUNHAM, D. A. ALLEN, J. H. ELIAS, J. A. FROGEL, AND W. LILLER (1983). The thermal structure and energy balance of the Uranian upper atmosphere. *Icarus* **53**, 399-414.

FRENCH, RICHARD G., J. L. ELLIOT, LINDA M. FRENCH, JULIE A. KANGAS, KAREN J. MEECH, MICHAEL E. RESSLER, MARC W. BUIE, JAY A. FROGEL, J. B. HOLBERG, JESUS J. FUENSALIDA, AND MARSHALL JOY (1988). Uranian ring orbits from Earth-based and Voyager occultation observations. *Icarus* **73**, 349-378.

FRENCH, R. G., J. L. ELLIOT, AND P. J. GIERASCH (1978). Analysis of stellar occultation data: Effects of photon noise and initial conditions. *Icarus* **33**, 186-202.

FRENCH, R. G., J. L. ELLIOT, B. SICARDY, P. NICHOLSON AND K. MATTHEWS (1982). The upper atmosphere of Uranus: A critical test of isotropic turbulence models. *Icarus* **51**, 491-508.

FRENCH, R. G., T. J. JONES, AND A. R. HYLAND (1987). The 1 May 1982 stellar occultation by Uranus and the rings: Observations from Mount Stromlo Observatory. *Icarus* **69**, 499-505.

FRENCH, RICHARD G., PAMELA A. MELROY, RICHARD L. BARON, EDWARD W. DUNHAM, KAREN J. MEECH, DOUGLAS J. MINK, J. L. ELLIOT, DAVID A. ALLEN, MICHAEL C. B. ASHLEY, KENNETH C. FREEMAN, EDWIN F. ERICKSON, JAY GOGUEN, AND H. B. HAMMEL (1985). The 1983 June 15 occultation by Neptune. II. The oblateness of Neptune. *Astron. J.* **90**, 2624-2638.

FRENCH, RICHARD G., AND GORDON E. TAYLOR (1981). Occultation of ε Geminorum by Mars. IV. Oblateness of the Martian upper atmosphere. *Icarus* **45**, 577-585.

HANEL, R., B. CONRATH, R. M. FLASAR, V. KUNDE, W. MAGUIRE, J. PEARL, J. PIRRAGLIA, R. SAMUELSON, D. CRUIKSHANK, D. GAUTIER, P. GIERASCH, L. HORN, AND P. SCHULTE (1986). Infrared observations of the Uranian system. *Science* **233**, 70-74.

HOLBERG, J. B., P. D. NICHOLSON, R. G. FRENCH, AND J. L. ELLIOT (1987). Stellar occultation probes of the Uranian rings at 0.1 and 2.2 microns: A comparison of Voyager ultraviolet spectrometer and Earth-based results. *Astron. J.* **94**, 178-188.

HUBBARD, W. B., H. P. AVEY, B. CARTER, J. E. FRECKER, H. H. FU, J. A. GEHRELS, T. GEHRELS, D. M. HUNTEN, H. D. KENNEDY, L. A. LEBOFSKY, K. MOTTRAM, T. MURPHY, A. NIELSEN, A. A. PAGE, H. J. REITSEMA, B. A. SMITH, D. J. THOLEN, B. VARNES, F. VILAS, M. D. WATERWORTH, H. H. WU, AND B. ZELLNER, (1985). Results from observations of the 15 June 1983 occultation by the Neptune system. *Astron. J.* **90**, 655-667.

HUBBARD, W. B., PHILIP D. NICHOLSON, EMMANUEL LELLOUCH, BRUNO SICARDY, ANDRE BRAHIC, FAITH VILAS, PATRICE BOUCHET, ROBERT A. MCLAREN, ROBERT L. MILLIS, LAWRENCE H. WASSERMAN, J. H. ELIAS, K. MATTHEWS, AND C.

PERRIER (1987). Oblateness, radius, and mean stratospheric temperature of Neptune from the 1985 August 20 occultation. *Icarus* **72**, 635-646.

HUBBARD, W. B., AND D. J. STEVENSON (1984). Interior structure of Saturn. In *Saturn.* (T. Gehrels and M. Matthews, eds.), pp. 47-87. Univ. of Arizona Press, Tucson.

KLEMOLA, A. R., AND B. G. MARSDEN (1977). Predicted observations by the rings of Uranus, 1977-1980. *Astron. J.* **85**, 1663-1669.

KLEMOLA, A. R., D. J. MINK, AND J. L. ELLIOT (1981). Predicted occultations by Uranus: 1981-1984. *Astron. J.* **86**, 138-140.

LANE, A. L., C. W. HORD, R. A. WEST, L. W. ESPOSITO, K. E. SIMMONS, R. M. NELSON, B. D. WALLIS, B. J. BURATTI, L. J. HORN, A. L. GRAPS, AND W. R. PRYOR (1986). Photometry from Voyager 2: Initial results from the Uranian atmosphere, satellites, and rings. *Science* **233**, 65-70.

LELLOUCH. E., W. B. HUBBARD, B. SICARDY, F. VILAS, AND P. BOUCHET (1986). Occultation determination of Neptune's oblateness and stratospheric methane mixing ratio. *Nature* **324**, 227-231.

LINDAL, G. F., J. R. LYONS, D. N. SWEETNAM, V. R. ESHLEMAN, D. P. HINSON, AND G. L. TYLER (1987). The atmosphere of Uranus: Results of radio occultation measurements with Voyager 2. *J. Geophys. Res.* **92**, 14987-15001.

LINDAL, G. F., D. N. SWEETNAM, AND V. R. ESHLEMAN (1985). The atmosphere of Saturn: An analysis of the Voyager radio occultation measurements. *Astron. J.* **90**, 1136-1146.

MELROY, P. A. (1984). Master's thesis, Department of Earth, Atmospheric and Planetary Sciences, Massachusetts Institute of Technology.

MILLIS, ROBERT. L., LAWRENCE H. WASSERMAN, AND RICHARD G. FRENCH (1987). Observations of the April 1982 stellar occultation by Uranus and the rings. *Icarus* **69**, 176-184.

NICHOLSON, P. D., K. MATTHEWS, AND P. GOLDREICH (1981). The Uranus occultation of 10 June 1979. I. The rings. *Astron. J.* **86**, 596-606.

NICHOLSON, P. D., K. MATTHEWS, AND P. GOLDREICH (1982). Radial widths, optical depths, and eccentricities of the Uranian rings. *Astron. J.* **87**, 433-447.

READ, P. L. (1986). Super-rotation and diffusion of axial angular momentum: II. A review of quasi-axisymmetric models of planetary atmospheres. *Quart. J. Roy. Met. Soc.* **112**, 253-272.

SICARDY, B., M. COMBES, A. BRAHIC, P. BOUCHET, C. PERRIER, AND R. COURTIN (1982). The 15 August 1980 occultation by the Uranian system: Structure of the rings and temperature of the upper atmosphere. *Icarus* **52**, 459-472.

SICARDY, B., M. COMBES, J. LECACHEUX, P. BOUCHET, A. BRAHIC, P. LAQUES, C. PERRIER, L. VAPILLON, AND Y. ZEAU (1985). Variations of the stratospheric temperature along the limb of Uranus: Results of the 22 April 1982 stellar occultation. *Icarus* **64**, 88-106.

SMITH, B. A., L. A. SODERBLOM, R. BATSON, P. BRIDGES, J. INGE, H. MASURSKY, E. M. SHOEMAKER, R. BEEBE, J. M. BOYCE, G. A. BRIGGS, G. BUNKER, S. A. COLLINS, C. HANSEN, T.V. JOHNSON, J. L. MITCHELL, R. TERRILE, A. F. COOK, J. CUZZI, J. B. POLLACK, G. E. DANIELSON, A. P. INGERSOLL, M. E. DAVIES, G. E. HUNT, D. MORRISON, T. OWEN, C. SAGAN, J. VEVERKA, R. STROM, AND V. E. SUOMI (1982). A new look at the Saturn system: The Voyager 2 images. *Science* **215**, 504-537.

SMITH, B. A., L. A. SODERBLOM, R. BEEBE, D. BLISS, J. M. BOYCE, A. BRAHIC, G. A. BRIGGS, R. H. BROWN, S. A. COLLINS, A. F. COOK II, S. K. KROFT, J. N.

CUZZI, G. E. DANIELSON, M. E. DAVIES, T. E. DOWLING, D. GODFREY, C. J. HANSEN, C. HARRIS, G. E. HUNT, A. P. INGERSOLL, T.V. JOHNSON, R. J. KRAUSS, H. MASURSKY, D. MORRISON, T. OWEN, J. B. PLESCIA, J. B. POLLACK, C. C. PORCO, K. RAGES, C. SAGAN, E. M. SHOEMAKER, L.A. SROMOVSKY, C. STOKER, R. G. STROM, V. E. SUOMI, S. P. SYNNOTT, R.J. TERRILE, P. THOMAS, W. R. THOMPSON, AND J. VEVERKA (1986). Voyager 2 in the Uranian system: Imaging science results. *Science* **233**, 43-64.

SMITH, B. A., L. A. SODERBLOM, R. BEEBE, J. M. BOYCE, G. A. BRIGGS, M. CARR, S. A. COLLINS, A. F. COOK II, G. E. DANIELSON, M. E. DAVIES, G. E. HUNT, A. P. INGERSOLL, T. V. JOHNSON, H. MASURSKY, J. MCCAULEY, D. MORRISON, T. OWEN, C. SAGAN, E. M. SHOEMAKER, R. G. STROM, V. E. SUOMI, AND J. VEVERKA (1979b). Voyager 2 encounter with the Jovian system. *Science* **206**, 925-950.

SMITH, B. A., L. A. SODERBLOM, T.V. JOHNSON, A. P. INGERSOLL, S. A. COLLINS, E. M. SHOEMAKER, G. E. HUNT, H. MASURSKY, M. H. CARR, M. E. DAVIES, A. F. COOK II, J. BOYCE, G. E. DANIELSON, T. OWEN, C. SAGAN, R. F. BEEBE, J. VEVERKA, R. G. STROM, J. F. MCCAULEY, D. MORRISON, G. A. BRIGGS, AND V. E. SUOMI (1979a). The Jupiter system through the eyes of Voyager 1. *Science* **204**, 952-972.

TYLER, G. L. , D. N. SWEETNAM, J. D. ANDERSON, J. K. CAMPBELL, V. R. ESHLEMAN, D. P. HINSON, G. S. LEVY, G. F. LINDAL, E. A. MAROUF, AND D. P. HINSON (1986). Voyager 2 radio observations of the Uranian system: Atmosphere, rings, and satellites. *Science* **233**, 79-84.

WARWICK, J. W., D. R. EVANS, J. H. ROMIG, C. B. SAWYER, M. D. DESCH, M. L. KAISER, J. K. ALEXANDER, T. D. CARR, D. H. STAELIN, S. GULKIS, R. L. POYNTER, M. AUBIER, A. BOISCHOT, Y. LEBLANC, A. LECACHEUX, B. M. PEDERSON, AND P. ZARKA (1986). Voyager 2 radio observations of Uranus. *Science* **233**, 102-106.

ZHARKOV, V. N., AND V. P. TRUBITSYN edited by W. B. Hubbard, (1978). *Physics of Planetary Interiors*. Tucson: Pachart Publishing House.

Chapter 3

Temperature of the Uranian Upper Stratosphere at the 1-μbar Level: Comparison of Voyager 2 UVS Data to Occultation Results

3.1 Introduction

Before the Voyager 2 encounter with Uranus, our understanding of the region near the 1-μbar level in Uranus' upper atmosphere was based primarily on ground-based stellar occultations. Several approaches were used to derive atmospheric information from these observations. The first was to fit an isothermal model to the data, resulting in a single effective scale height or temperature for the occultation (Dunham *et al.* 1980). This simple model's use was justified because there was insufficient information for the use of a more complex one. The second approach numerically inverted the recorded lightcurve to derive the atmospheric temperature and number density profiles as a function of height (Dunham *et al.* 1980). Wasserman and Veverka (1973) review these two approaches and conclude that the inversion method is "the preferable form of analysis and that it yields good results even in the presence of spikes." Sicardy *et al.* (1982) review the inversion method and the use of initial or boundary conditions for the high altitude starting point. French *et al.* (1978) also discuss the problems of initial conditions in the application of an atmosphere inversion. They recommended that the part of a lightcurve produced by the upper atmosphere (the atmosphere above an arbitrary altitude defined by signal-to-noise considerations in the lightcurve) be handled separately. To do this, they fitted an isothermal model to the upper atmosphere to determine a single scale height. They then assumed that the upper atmosphere is isothermal (with the fitted scale height) and inverted the

atmosphere from infinity to the minimum radius allowed by the noise of the occultation. A third approach was a study of the turbulence in the planetary atmosphere. Generally, the spike patterns from two or more simultaneous observations offset along the limb of the planet are cross-correlated in order to give a measure of the lateral extent of a feature. The vertical extent of a feature comes directly from the lightcurve. Narayan and Hubbard (1988) and Hubbard *et al.* (1988) review much of the work in this area and present a theory of refractive scintillation in a planetary atmosphere. The theory was applied to an occultation of Neptune that was observed at multiple sites. A general review of occultation astronomy is given by Elliot (1979) in which he covers methods of analysis including isothermal model fitting, inversions and the study of spike patterns.

The arrival of the Voyager 2 spacecraft at Uranus has since given additional ultraviolet and radio atmospheric occultation data, most of it higher (ultraviolet) or lower (radio) in the Uranian atmosphere, thus complementing that obtainable from ground-based observations.

Analysis of the Voyager 2 UVS occultation experiment by Herbert *et al.* (1987) determined temperature profiles for the Uranian upper atmosphere at planetocentric latitudes of −63.7 and +69.7 degrees for the γ Pegasi occultation and −3.6 degrees for a solar occultation (latitude with respect to the IAU pole-naming convention). In order to use the profiles of Herbert *et al.*, the calculations were duplicated here. Figures 3-1 and 3-2 are calculated temperature versus height and temperature versus pressure profiles using the formulas and parameters as presented by Herbert. Figure 3-1 is a computed temperature profile which reproduces in detail the profile as shown in Figure 16 of Herbert *et al.* (1987) and labeled as "T"; an isothermal tail above 30,000 km (10^{-6}-μbar) has not been included. The profiles computed in this work cover 4,500 km (zero reference altitude is

Figure 3-1 Temperature versus altitude profile for the Uranian atmosphere based on Table 3-1 "Best Compromise" parameters from Voyager 2 analysis by Herbert *et al.* (1987). This figure corresponds to the curve labeled "T" in Figure 16 of Herbert *et al.* (1987). The tail above 30,000 km has been omitted.

Figure 3-2 Temperature versus pressure profile for the Uranian atmosphere based on Voyager 2 analysis by Herbert *et al.* (1987). This corresponds to the curve labeled "b" (right) in Figure 7 of Herbert *et al.* (1987). The dashed curve represents a typical temperature-pressure inversion profile as previously reported for Uranian occultations.

Figure 3-1

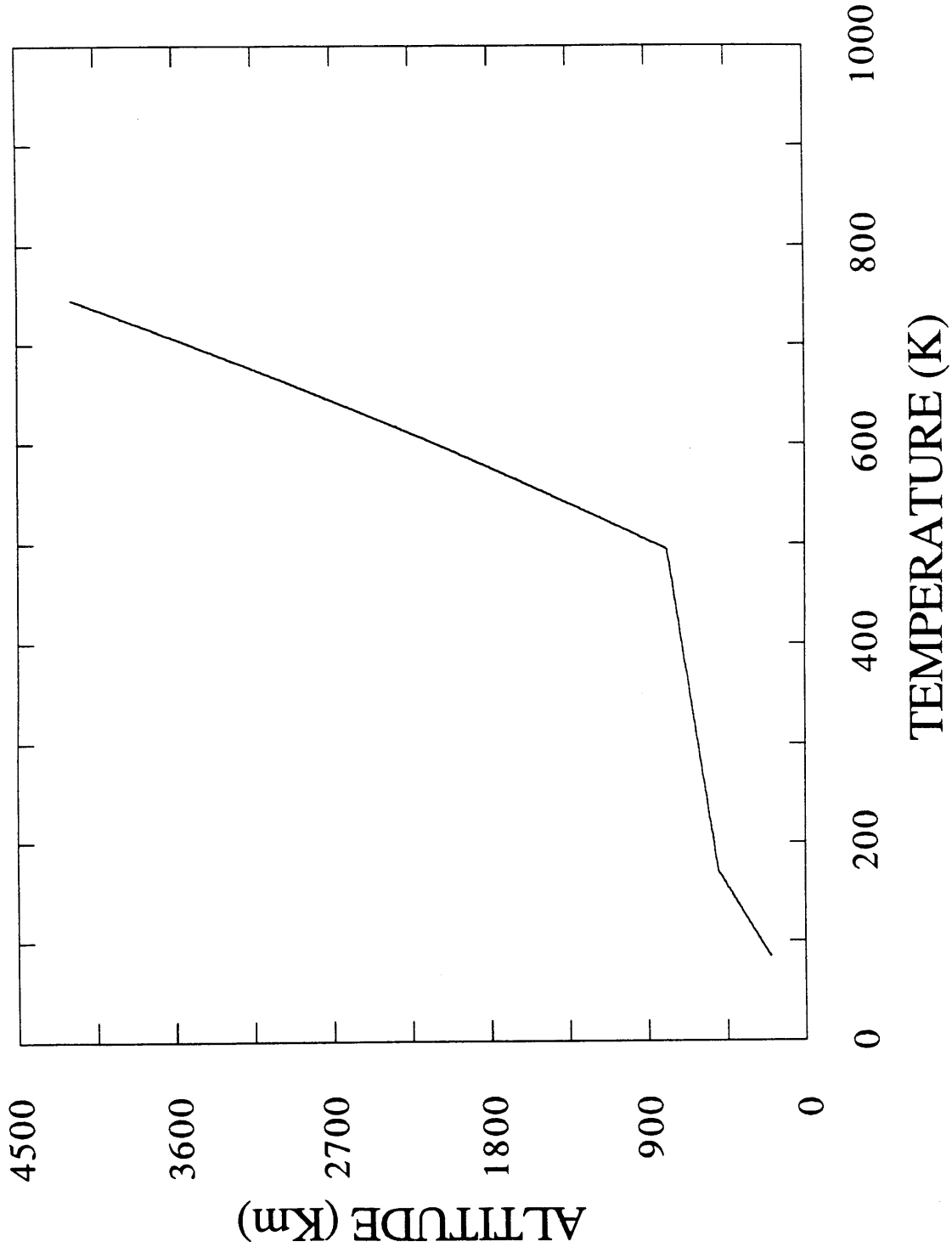
ALTITUDE (Km)
4500
3600
2700
1800
900
0
TEMPERATURE (K)
0
200
400
600
800
1000

Figure 3-2

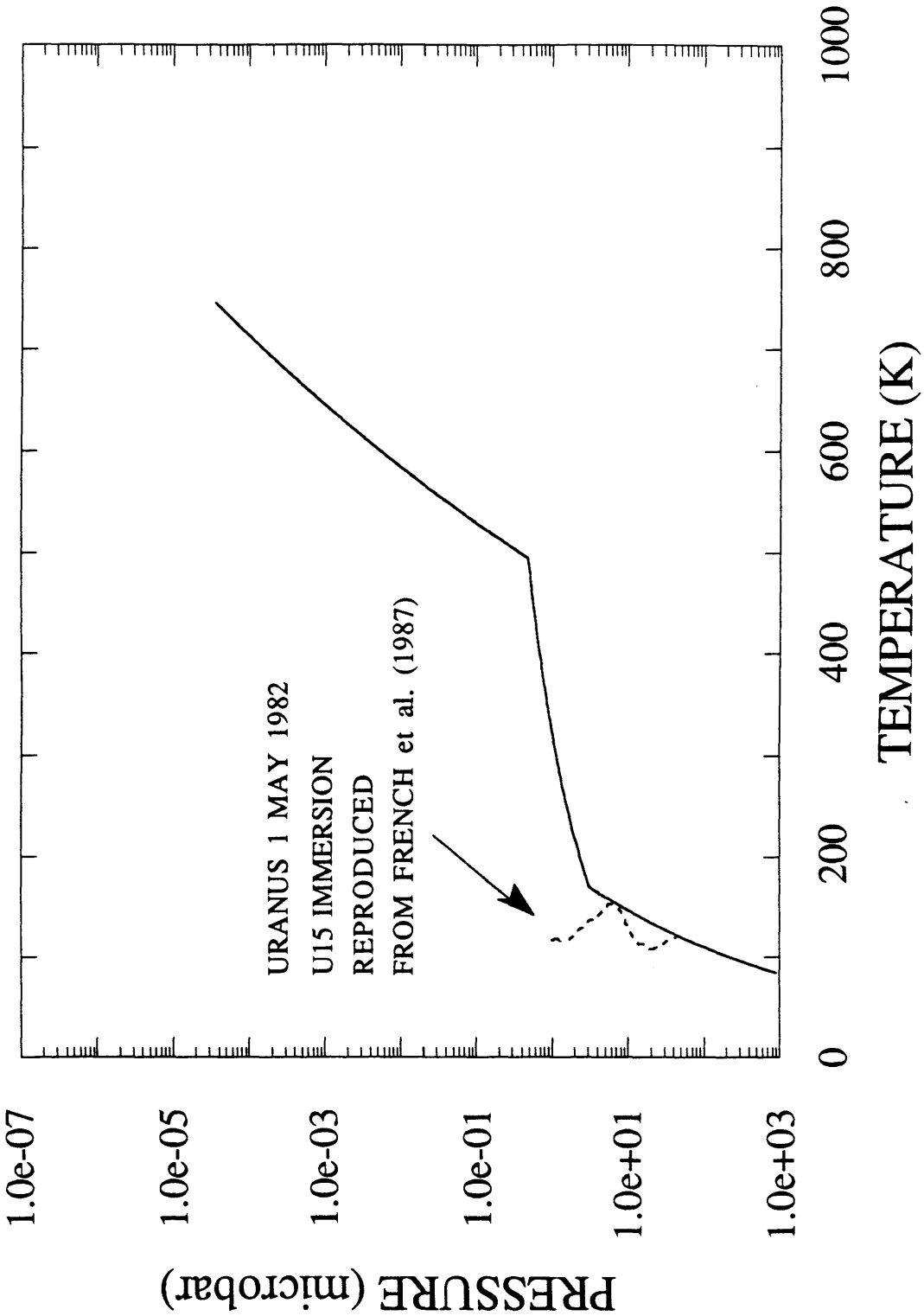
URANUS 1 MAY 1982
U15 IMMERSION
REPRODUCED
FROM FRENCH et al. (1987)
PRESSURE (microbar)
1.0e-07
1.0e-05
1.0e-03
1.0e-01
1.0e+01
1.0e+03
0
200
400
600
800
1000
TEMPERATURE (K)

Table 3-1

UVS Model Parameters

γ Peg Measurements			Best Compromise			Solar Occultation		
P, μbar	T, K	α	P, μbar	T, K	α	P, μbar	T, K	α
10^4	63	-0.122	10^4	63	-0.122	10^4	63	-0.122
51	120	-0.130	51	120	-0.127	51	120	-0.137
1	200	-0.569	3.3	170	-0.572	10	150	-0.501
0.2	500	-0.059	0.5	500	-0.043	1	475	-0.045
$2x10^{-4}$	750		10^{-5}	800		10^{-5}	800	

At 320 km, P_{H_2} = 51 μbar. At 200 km (model standard reference point), P_{H_2} = 0.81 mbar. All altitudes are measured from an equatorial radius of 25,550 km. The atmosphere is assumed to be diffusively separated above z = 500 km; below that point it is assumed to be well mixed with a mean molecular mass of 2.3 amu.

25,550 km at the equator) and have been scaled as closely as possible to the work of Herbert *et al.* Figure 3-2 is the temperature versus pressure profile and corresponds to the curve labeled "b" (right) in Figure 7 of Herbert *et al.*(1987). The temperature gradient shown in both Figures 3-1 and 3-2 corresponds to a change in temperature of 330 K over a pressure range from 3.3-μbar to 0.5-μbar; this corresponds to an altitude interval of 270 km. Figure 3-2 also displays a reproduction (dashed curve) of the temperature versus pressure profile from the inversion of the 1 May 1982 Uranian occultation recorded at Mount Stromlo Observatory in Australia. This inversion is displayed to give some indication of the 'typical' inversion profiles previously reported for Uranus. It appears clear that this does not reveal any portion of the temperature gradient.

The steep temperature gradient, evident in both Figures 3-1, and 3-2, was not suspected from the analysis of ground-based occultations. Is it consistent with these occultation lightcurves? The work here has been undertaken to determine whether the Voyager 2 observations are compatible with the previous ground-based atmospheric observations. The approach taken is to generate synthetic stellar occultation lightcurves (based on the three Voyager 2 atmospheric models) as they would be observed from the Earth. The synthetic curves once generated are appropriately scaled and compared to historical ground-based atmospheric occultations and the best fitting isothermal model lightcurve for each occultation. The occultations were chosen to represent the range of scale heights and thus temperatures reported in various analyses (for a synopsis see Table III in Baron *et al.* 1989).

3.2 Model Atmosphere

In the model, the two equations governing the atmosphere are the equation of hydrostatic equilibrium and the equation of state (the perfect gas law). We will assume a model calculation on the equator of a rotating spherical planet. The first equation may be written as

$$dP = -\rho\, g(r)\, dr\,, \tag{3-1}$$

where P is the pressure, ρ the mass density, and g(r) the local acceleration of gravity. The local acceleration of gravity g(r) may be written as

$$g(r) = \frac{dU}{dr}, \tag{3-2}$$

where, the potential function U is assumed to have the form

$$U = -\frac{GM}{r} - \frac{1}{2}\Omega^2 r^2\,. \tag{3-3}$$

Here M is the mass of the planet, G is the universal gravitational constant, r is the distance from the center of the planet (assumed spherical), and Ω is the angular velocity of the planet (solid body rotation assumed). The mass distribution of the planet is assumed spherical. Substituting for ρ in terms of μ the mean molecular weight, m_{amu} the atomic mass unit, and N the number density gives

$$dP = -\mu\, m_{amu}\, N\, dU\,. \tag{3-4}$$

The equation of state is given by

$$P = NkT\,, \tag{3-5}$$

where k is Boltzmann's constant and T is the temperature. Dividing the two equations gives

$$\frac{dP}{P} = -\frac{\mu m_{amu}}{kT}\,dU. \tag{3-6}$$

To facilitate an analytic solution, define the quantity q as

$$q = -\frac{kT}{\mu m_{amu}} \tag{3-7}$$

and assume that q is a linear function of the potential, thus

$$q = q_o + \alpha\,(U - U_o)\,. \tag{3-8}$$

Here q_o and U_o are values at an arbitrary zero reference and α is a constant. We note that the total derivative of q is

$$dq = \alpha\,dU. \tag{3-9}$$

The model used is a piecewise continuous set of segments linear in the change of q as a function of potential. Substitute q and dq into Equation (3-6) to get

$$\frac{dP}{P} = \frac{1}{\alpha}\frac{dq}{q}. \tag{3-10}$$

Upon integration this gives

$$\frac{P}{P_o} = \left(\frac{q}{q_o}\right)^{\frac{1}{\alpha}}, \tag{3-11}$$

where P_o is the value of P at the arbitrary reference point. Assuming that μ is constant throughout a segment, we substitute for q and q_o to get

$$\frac{P}{P_o} = \left(\frac{T}{T_o}\right)^{\frac{1}{\alpha}}, \tag{3-12}$$

where T_o is the value of T at the arbitrary reference point. Using Equations (3-5), (3-11) and (3-12) and substituting for q, and q_o we may solve for N to get

$$N = N_o\left\{1 - \frac{\alpha\mu\, m_{amu}}{kT_o}\left[U - U_o\right]\right\}^{\left(\frac{1-\alpha}{\alpha}\right)}. \tag{3-13}$$

Substitute for U to get

$$N = N_o\left\{1 + \frac{\alpha\mu\, m_{amu}}{kT_o}\left[GM\left(\frac{1}{r} - \frac{1}{r_o}\right) + \frac{\Omega^2}{2}\left(r^2 - r_o^2\right)\right]\right\}^{\left(\frac{1-\alpha}{\alpha}\right)}, \tag{3-14}$$

where N_o, T_o, and r_o are now the values of the number density, the temperature and the radius, respectively, at the starting radius of each atmospheric segment. Equation (3-14) is the form used to produce the unlabeled temperature versus altitude and temperature versus pressure profiles in Figures 3-1 and 3-2.

3.3 Simulated Lightcurve

A synthetic ground-based lightcurve was generated using a numerical calculation starting with Equation (3-14) above. In order to use the results of Herbert *et al.* (1987) the atmosphere was calculated in a series of vertical segments using the parameters given in Table 1 of Herbert *et al.* (1987), part of which is reproduced as Table 3-1 here. Each segment was specified with an initial temperature T_o and an initial pressure (used with the perfect gas law to obtain an initial number density).

The synthetic lightcurve was generated in a series of steps. A number density profile was first generated for the atmosphere starting at a reference level of 25,550 km and a reference pressure of 0.81 mbars for H_2. For each segment of the atmosphere for which a different α or μ was specified, a starting temperature and number density were first calculated and then used throughout the segment. These were calculated in such a manner as to insure no discontinuities in the number density profile with height. To simulate a homopause in the planetary atmosphere, a change in μ from 2.3 to 2.0 occurs at 500 km from the model standard reference point (see notes at bottom of Table 3-1). Next, the refractivity was determined using

$$\nu(r) = \frac{\nu_{STP}}{L} N(r) \ , \qquad (3\text{-}15)$$

where L is Loschmidt's number, and ν_{STP} is the refractivity at standard temperature and pressure at a specified wavelength. For starlight passing through the planetary atmosphere as shown in Figure 3-3, bending angles $\theta(r)$ are found from the following equation

$$\theta(r) = \int_{-\infty}^{\infty} \frac{d\nu}{dr}\, dx\ , \qquad (3\text{-}16)$$

where ν is the refractivity, and dr and dx are along the r and x directions. The bending angle is in turn used to determine a distance perpendicular (i.e., the y-axis or path of observer) to a ray from the occulted star through the center of the planet (Figure 3-3). The final step is to determine the normalized flux ϕ along this perpendicular, where

$$\phi = \frac{1}{1 - D\,\frac{d\theta}{dr}}\ . \qquad (3\text{-}17)$$

The lightcurve simulation program was checked by:

1) Producing a synthetic isothermal lightcurve with the simulation program. This curve was checked by making an isothermal fit to it to see if the input parameters could be recovered. The input parameters were recovered consistent with the number of altitude steps used to generate the synthetic lightcurve and the granularity of the binning in the flux calculation. This checked the special case of an isothermal lightcurve produced with constant gravity and constant molecular weight as inputs (e. g., g= 818 cm sec^{-2}, μ = 2.0, H = 70 km, T ≈150 K).

Figure 3-3 Overall geometry of a synthetic occultation. See section on Model Atmosphere for details on the calculation of the synthetic lightcurve.

Chapter 3

Figure 3-3

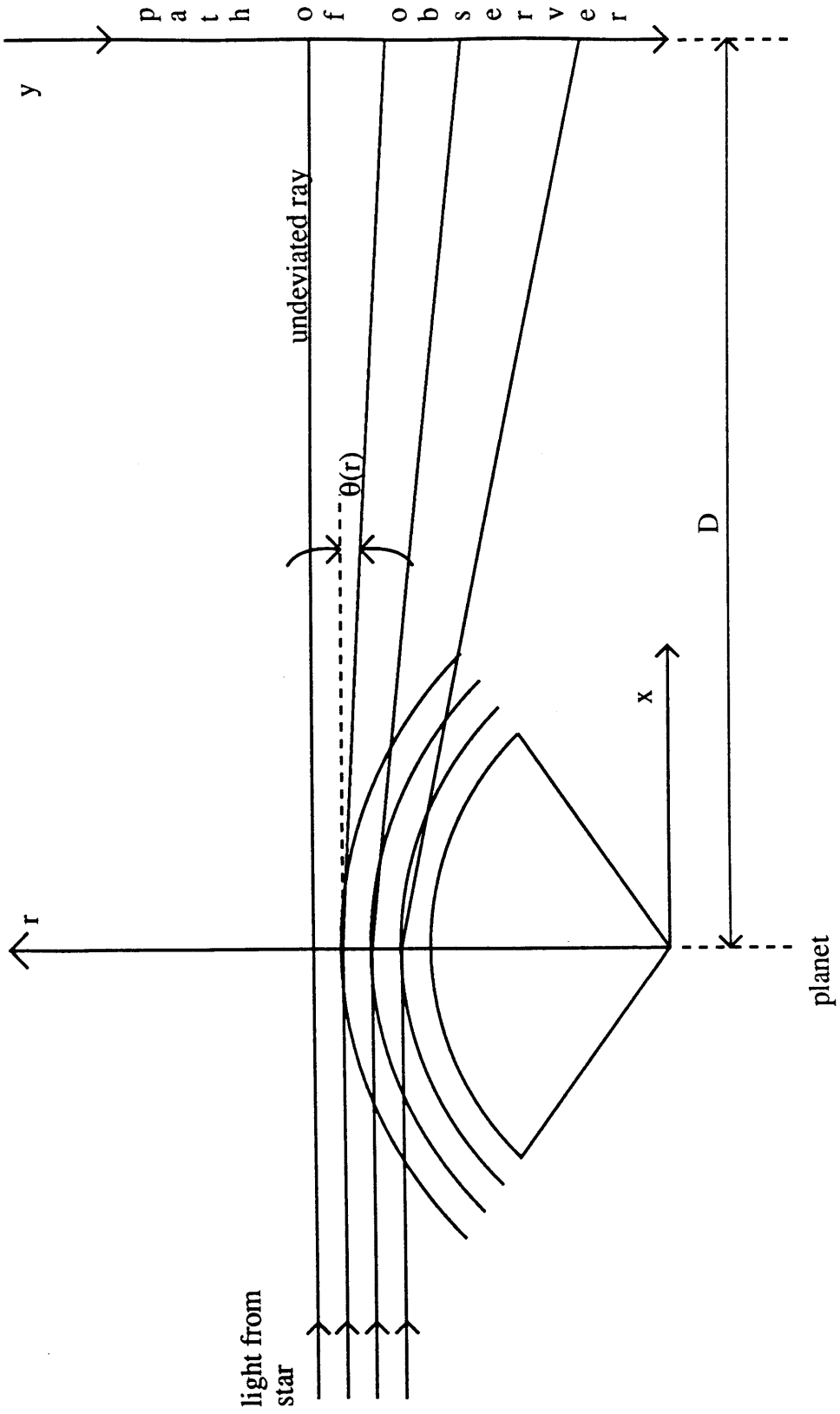

2) Using the synthetic lightcurve produced with parameters which Herbert *et al.* (1987) label as "Best Compromise" (Table 3-1), referred to here as the UVSbc lightcurve, as the input to an atmospheric inversion program. The inversion program produces a temperature-pressure profile. When appropriate conditions (constant gravity and constant molecular weight with height in the atmosphere) are imposed on a parallel calculation to produce a temperature-pressure curve within the simulation program, the two temperature-pressure curves agree to within 2% in temperature and 4% in pressure from a radius of approximately 230 km below half-light to 1360 km above half-light in the planetary atmosphere.

Figure 3-4 is the synthetic UVSbc lightcurve. In this curve and the two other models, one or more spikes show in the graph. The spikes arise from the discontinuous first derivative of q as a function of radius. No attempt was made to remove these spikes in the model (see the results of a test removal of the spike in the following Observations section). For purposes of comparison, an isothermal model lightcurve (70 km scale height, dashed line) is shown overlaid on the UVSbc lightcurve.

The isothermal curve represents a temperature of approximately 150 K; however, the slope in the region of half-light is clearly less steep than the similar region on the UVSbc lightcurve (which corresponds to an atmospheric region with a large temperature gradient). Now, with reference to Equation 11 of Baum and Code (1953) describing the occultation of a star by an isothermal atmosphere, we have,

$$\left(\frac{1}{\phi} - 2\right) + \ln\left(\frac{1}{\phi} - 1\right) = \frac{1}{H} v t . \qquad (3\text{-}18)$$

Figure 3-4 The UVSbc model lightcurve (solid) and an isothermal model simulated lightcurve (dashed). The solid curve uses UVS "Best Compromise" parameters from Voyager 2 as analyzed by Herbert *et al.* (1987) and is overlaid with a 70 km scale height (approximately 150 K) isothermal model curve. Note the horizontal offset (and spike) in the UVSbc lightcurve (solid) near half-light.

Figure 3-4

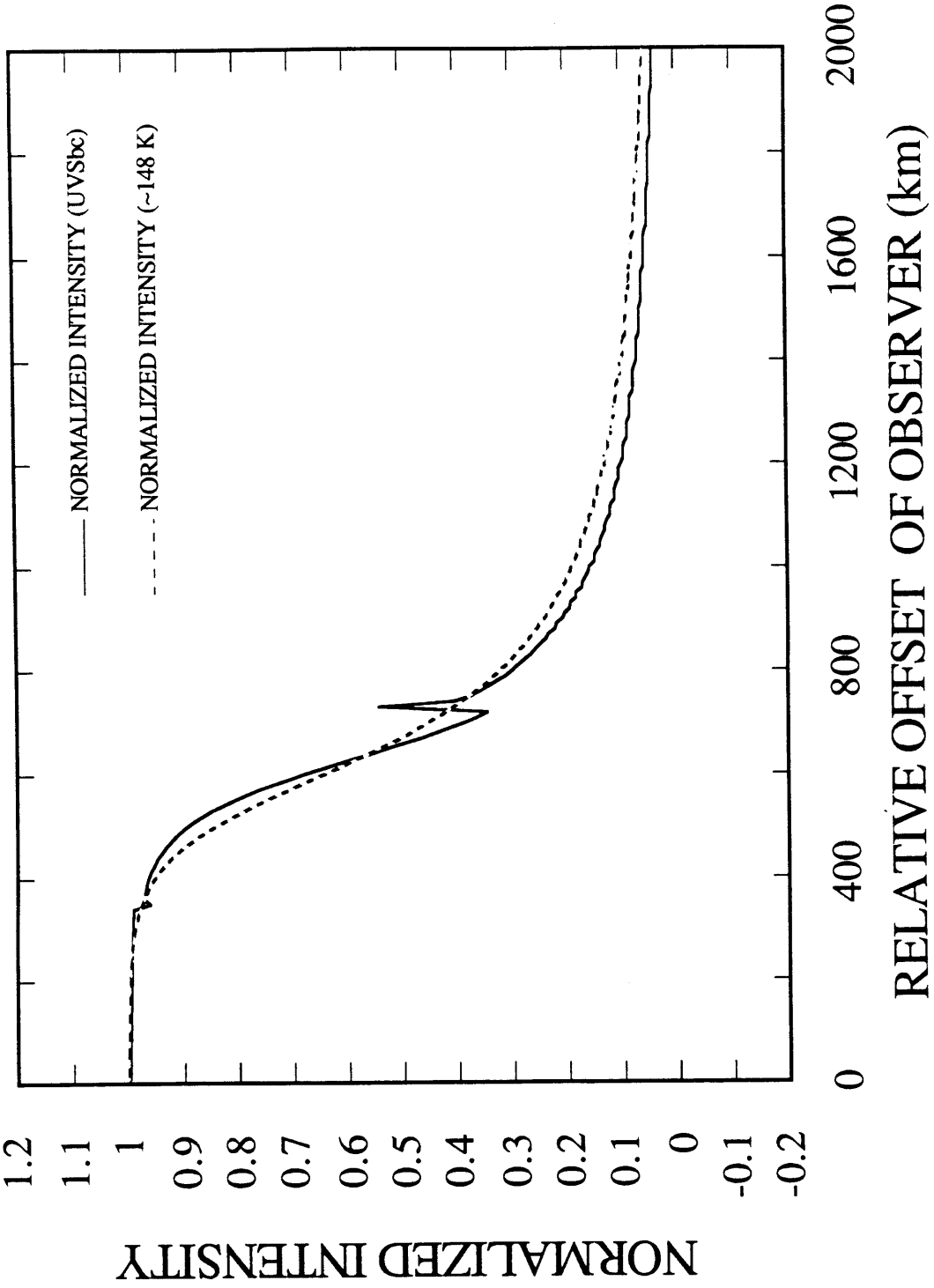
NORMALIZED INTENSITY (UVSbc)
NORMALIZED INTENSITY (~148 K)
NORMALIZED INTENSITY
1.2
1.1
1
0.9
0.8
0.7
0.6
0.5
0.4
0.3
0.2
0.1
0
-0.1
-0.2
0
400
800
1200
1600
2000
RELATIVE OFFSET OF OBSERVER (km)

Here the equation has been written in terms of the normalized stellar flux ϕ, the scale height H, which is $\frac{1}{a}$ in their notation, v the velocity along the "path of observer" (Figure 3-3) (v is assumed constant during the event), and t is the time with respect to $t_{1/2}$. The event geometry is assumed the same as in the model calculation above. The change in stellar flux near half-light as a function of distance, is given by Equation A21 of Elliot *et al.* (1989). In terms of our notation this is,

$$\frac{d\phi}{dy} = \frac{1}{8H} . \qquad (3\text{-}19)$$

Terms of order $\delta = \frac{H}{R_U}$, where R_U is the radius of Uranus, have been dropped from the equation of Elliot *et al.*, since for Uranus, $\delta \ll 1$. Therefore, a larger H (hence T) implies that the lightcurve will have a gentler slope than for a smaller H. But, from the perspective of an isothermal atmosphere, the temperature of the UVSbc model atmosphere should be cooler (not hotter), than the curve representing an atmosphere at 150 K. This enigma may be resolved by realizing that a temperature gradient in an atmosphere will modify the derived temperature. Goldsmith (1963) has shown that the scale height derived from an isothermal model fit to a lightcurve will need a first order correction of the form

$$H_o = H_i \left(1 + \frac{3}{2}\beta\right), \qquad (3\text{-}20)$$

where H_i, the fit isothermal scale height must be multiplied by a factor dependent on the sign and value of β (the gradient of the scale height with height) to obtain H_o, the scale height at the half-light radius. For example, if β is 0.1, the scale height H_o in the atmosphere is 1.15 times larger than the results of a fit to an isothermal model.

3.4 Comparison with Ground-based Atmospheric Occultations

Figures 3-5a and 3-5b show the lightcurves derived from the three models presented by Herbert *et al.* (1987). The lightcurves designated UVSbc, UVSgPeg, and UVSsol correspond to curves generated from the parameters in Table 3-1 in the columns "γ Peg Measurements," "Best Compromise," and "Solar Occultation" respectively. The curves are normalized to unit intensity and are shown vertically offset by 0.2 units of intensity in Figure 3-5a in order to readily compare the structure of the individual curves. In Figure 3-5b, the curves are shown overlaid one on top of the other. The curves are coincident at half-light as determined by individual isothermal model fits to the three model curves. In the following we compare the three curves to three historical ground-based data sets both by overlaying the curves onto scaled data and by finding the variance as a function of the position of the models with respect to the data along the path of the observer (Figure 3-3). Figures 3-6a, 3-7a and 3-8a are scaled lightcurves from previously reported historical events, compared to the best fit isothermal curve for each event and to the UVSbc lightcurve. The lightcurves are shown with an event velocity of 10 km sec^{-1} and are averaged to approximately 10 km per point. Each recorded lightcurve has been scaled to unit stellar flux. Excursions above unity and below zero are possible because of focusing of starlight and various types of noise. The horizontal axes are coincident at half-light as determined by an isothermal model fit to each lightcurve. The KME star designations are from Klemola and Marsden (1977) and Klemola *et al.* (1981).

Figure 3-5a Simulated lightcurves UVSbc, UVSgPeg, and UVSsol. UVSbc, UVSgPeg, and UVSsol lightcurves are generated from the parameters in Table 3-1 in the columns "γ Peg Measurements," "Best Compromise," and "Solar Occultation" respectively. The curves are all normalized to unit intensity. UVSgPeg and UVSsol are offset vertically by +0.2 and –0.2 units of intensity, respectively.

Figure 3-5b The three model lightcurves are the same as shown in Figure 5a but here they are overlaid one on the other in order to show emphasize the differences between curves. The curves are coincident at half light as determined by an isothermal fit to each curve.

Figure 3-6a The immersion lightcurve from the 10 March 1977 occultation of SAO 158687 (U0) (Elliot *et al.* 1980 and Dunham *et al.* 1980) scaled and shown as an overlay to the synthetic UVSbc model lightcurve (bold) and the best fit isothermal model curve (circles). The horizontal axes are coincident at half-light as determined by an isothermal model fit to each lightcurve. All curves are scaled to a 10 km sec^{-1} event velocity and averaged to 10 km per point.

Figure 3-6b The variance minima for three simulated model lightcurves and the best fit isothermal model compared to the recorded data of 10 March 1977 (U0). The x-axis represents the distance along the path of observer (Figure 3-3).The y-axis is the variance as a function of the relative offset of the lightcurves along the path of observer. The best fit isothermal model is shown as a solid line and the curves for the "UVS" models are indicated as various dashed lines. The UVSbc

model gives a lower minimum variance than the best fit isothermal model for this data set.

Figure 3-7a The emersion lightcurve from the 1 May 1982 occultation of KME 15 (U15) (French *et al.* 1987) scaled and shown as an overlay to the synthetic UVSbc model lightcurve (bold) and the best fit isothermal model curve (circles). The lightcurves are coincident at half-light as determined by an isothermal model fit to each lightcurve. All curves are scaled to a 10 km sec^{-1} event velocity and averaged to 10 km per point.

Figure 3-7b The variance minima for three simulated model lightcurves and the best fit isothermal model compared to the recorded data of 1 May 1982 (U15). The x-axis represents the distance along the path of observer (Figure 3-3).The y-axis is the variance as a function of the relative offset of the lightcurves along the path of observer. The best fit isothermal model is shown as a solid line and the curves for the "UVS" models are shown as various dashed lines. The UVSbc and the UVSgPeg models are nearly indistinguishable from the best fit isothermal model for this data set.

Figure 3-8a The emersion lightcurve from the 25 March 1983 occultation of KME 17b (Elliot *et al.* 1987) scaled and shown as an overlay to the synthetic UVSbc model lightcurve (bold) and the best fit isothermal model curve (circles). The horizontal axes are coincident at half-light as determined by an isothermal model fit to each lightcurve. All curves are scaled to a 10 km sec^{-1} event velocity and averaged to 10 km per point.

Figure 3-8b The variance minima for three simulated model lightcurves and the best fit isothermal model compared to the recorded data of 25 March 1983 (U17). The y-axis is the variance as a function of the relative offset of the lightcurves along the "path of observer." The best fit isothermal model is shown as a solid line and the curves for the "UVS" models are shown as various dashed lines. The UVSbc model does not reach as low a minimum as the best fit isothermal model for this data set. However, a sharper minimum is produced by the UVSbc model lightcurve than the best fit isothermal model lightcurve.

Figure 3-5a

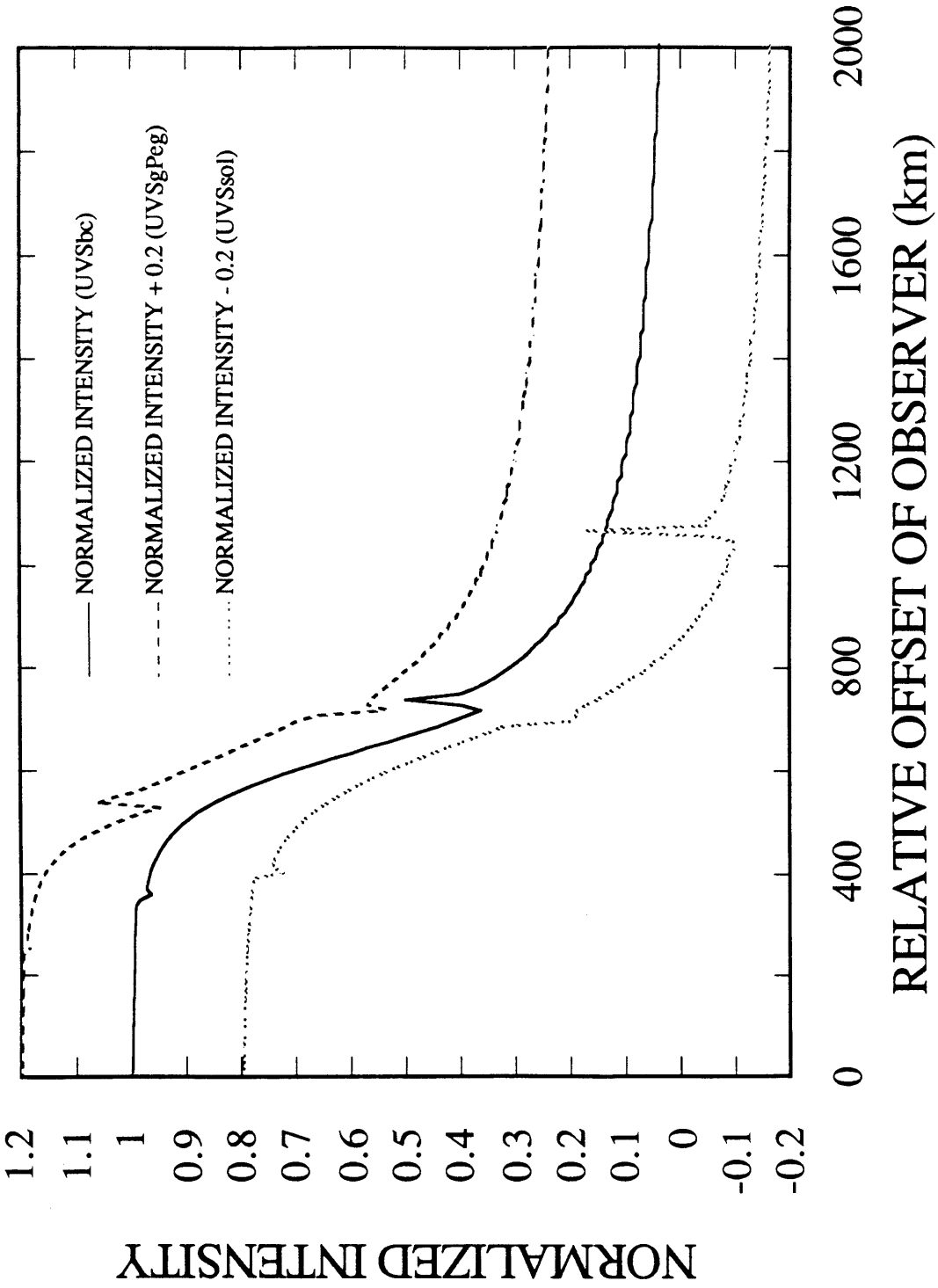
NORMALIZED INTENSITY (UVSbc)
NORMALIZED INTENSITY + 0.2 (UVSgPeg)
NORMALIZED INTENSITY - 0.2 (UVSsol)
NORMALIZED INTENSITY
1.2
1.1
1
0.9
0.8
0.7
0.6
0.5
0.4
0.3
0.2
0.1
0
-0.1
-0.2
0
400
800
1200
1600
2000
RELATIVE OFFSET OF OBSERVER (km)

Figure 3-5b

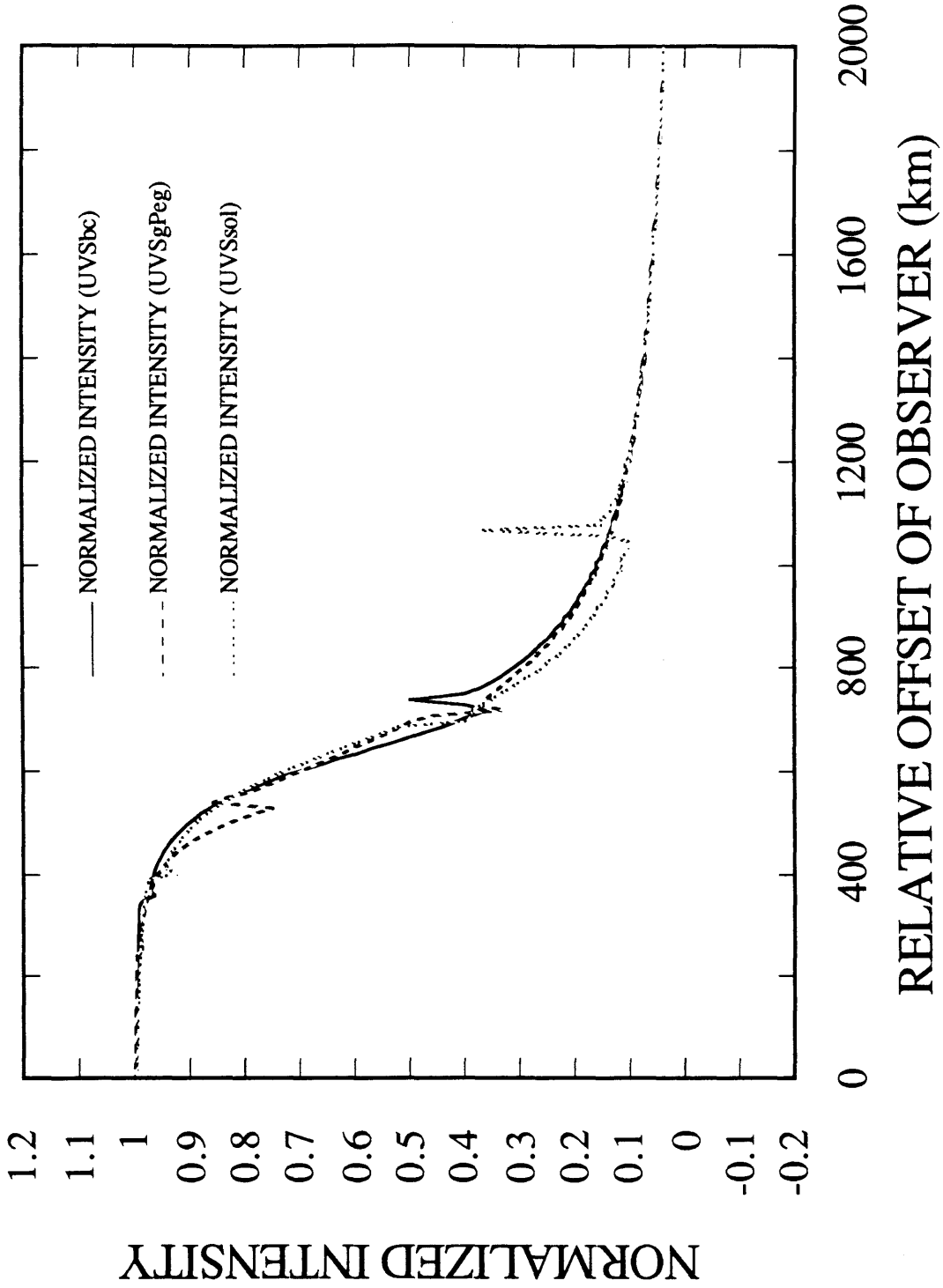
NORMALIZED INTENSITY (UVSbc)
NORMALIZED INTENSITY (UVSgPeg)
NORMALIZED INTENSITY (UVSsol)
NORMALIZED INTENSITY
RELATIVE OFFSET OF OBSERVER (km)
1.2
1.1
1
0.9
0.8
0.7
0.6
0.5
0.4
0.3
0.2
0.1
0
-0.1
-0.2
0
400
800
1200
1600
2000

Chapter 3

Figure 3-6a

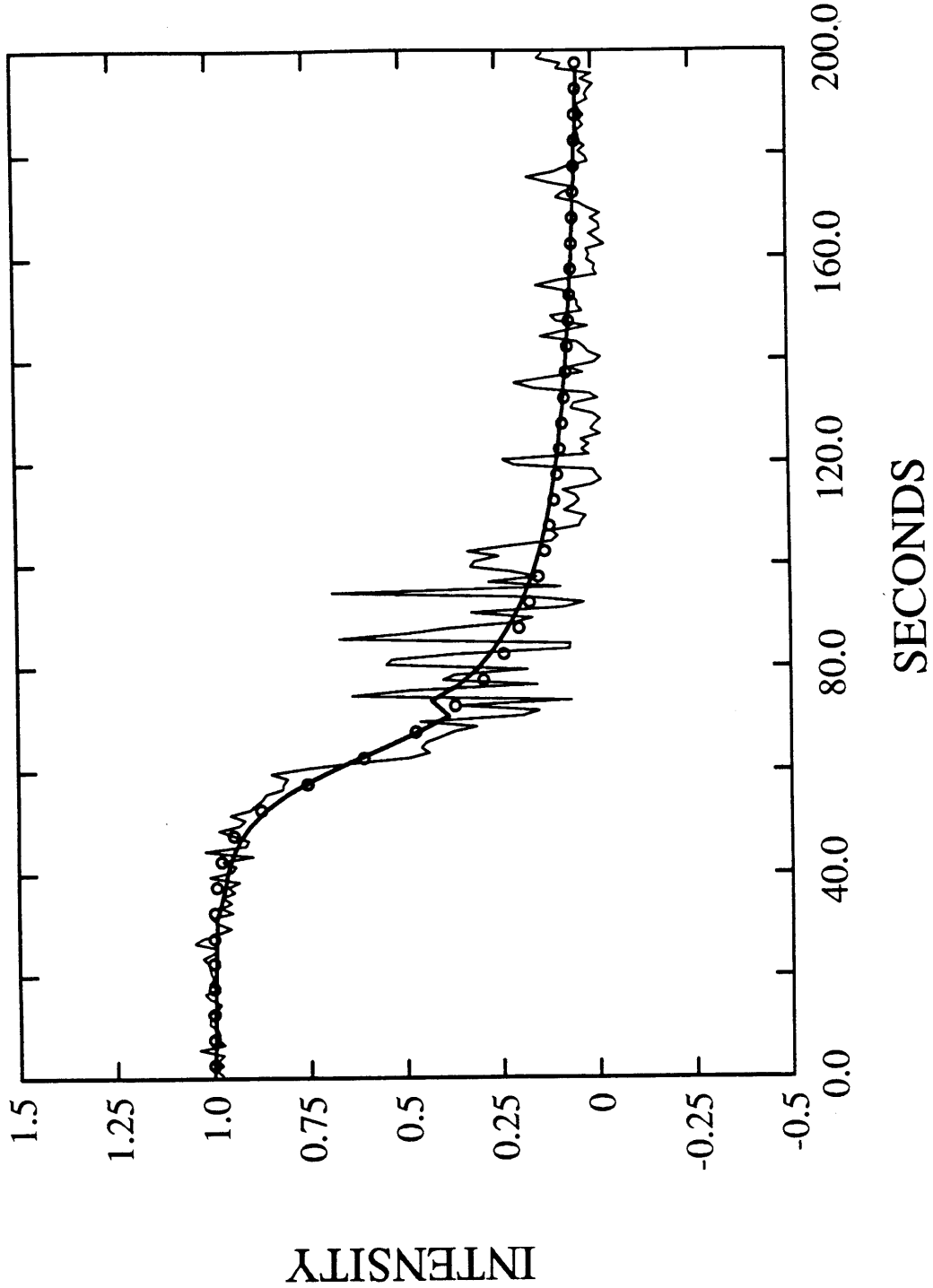

Figure 3-6b

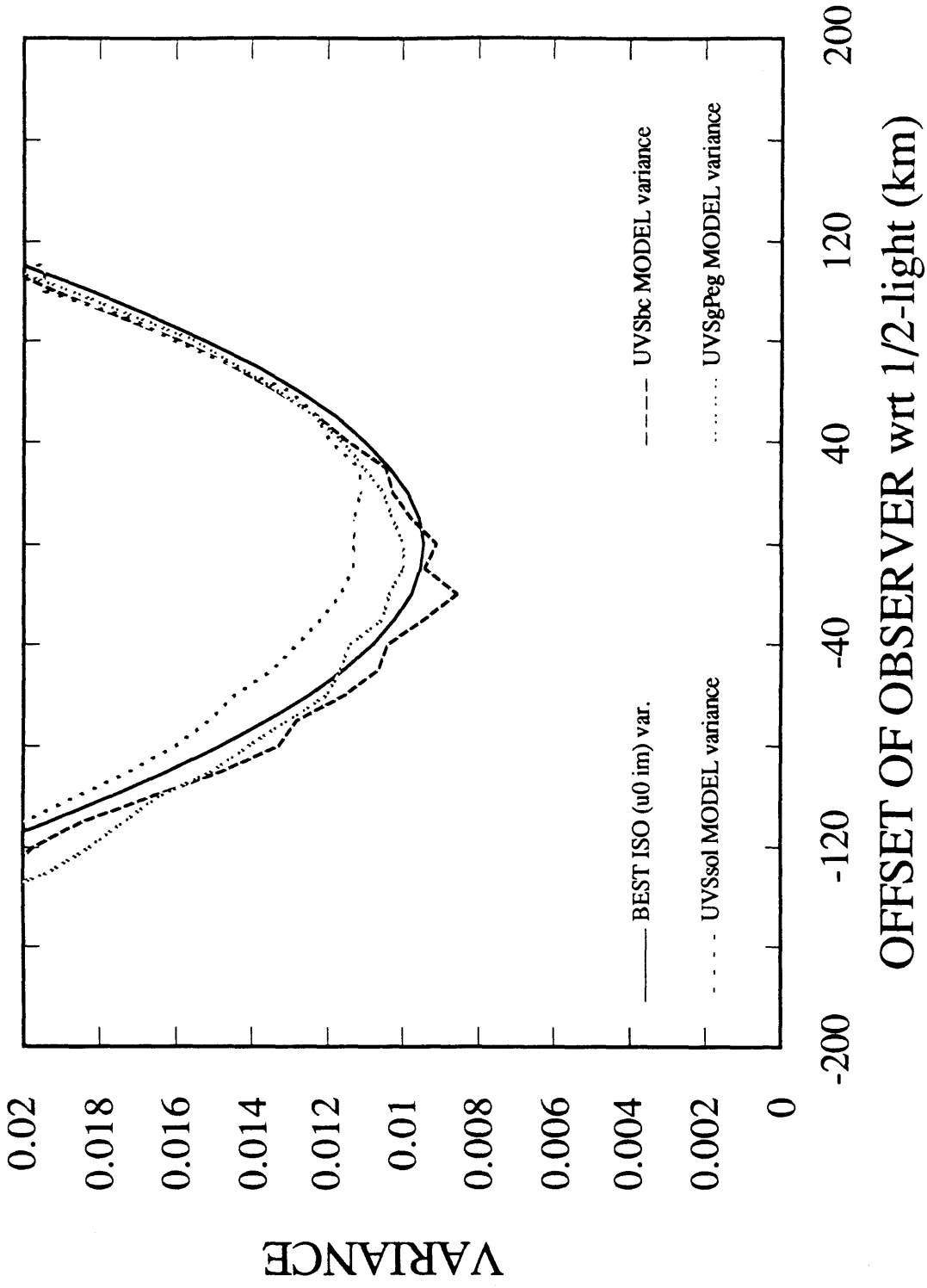
VARIANCE
0.02
0.018
0.016
0.014
0.012
0.01
0.008
0.006
0.004
0.002
0
-200
-120
-40
40
120
200
OFFSET OF OBSERVER wrt 1/2-light (km)
BEST ISO (u0 im) var.
UVSsol MODEL variance
UVSbc MODEL variance
UVSgPeg MODEL variance

Figure 3-7a

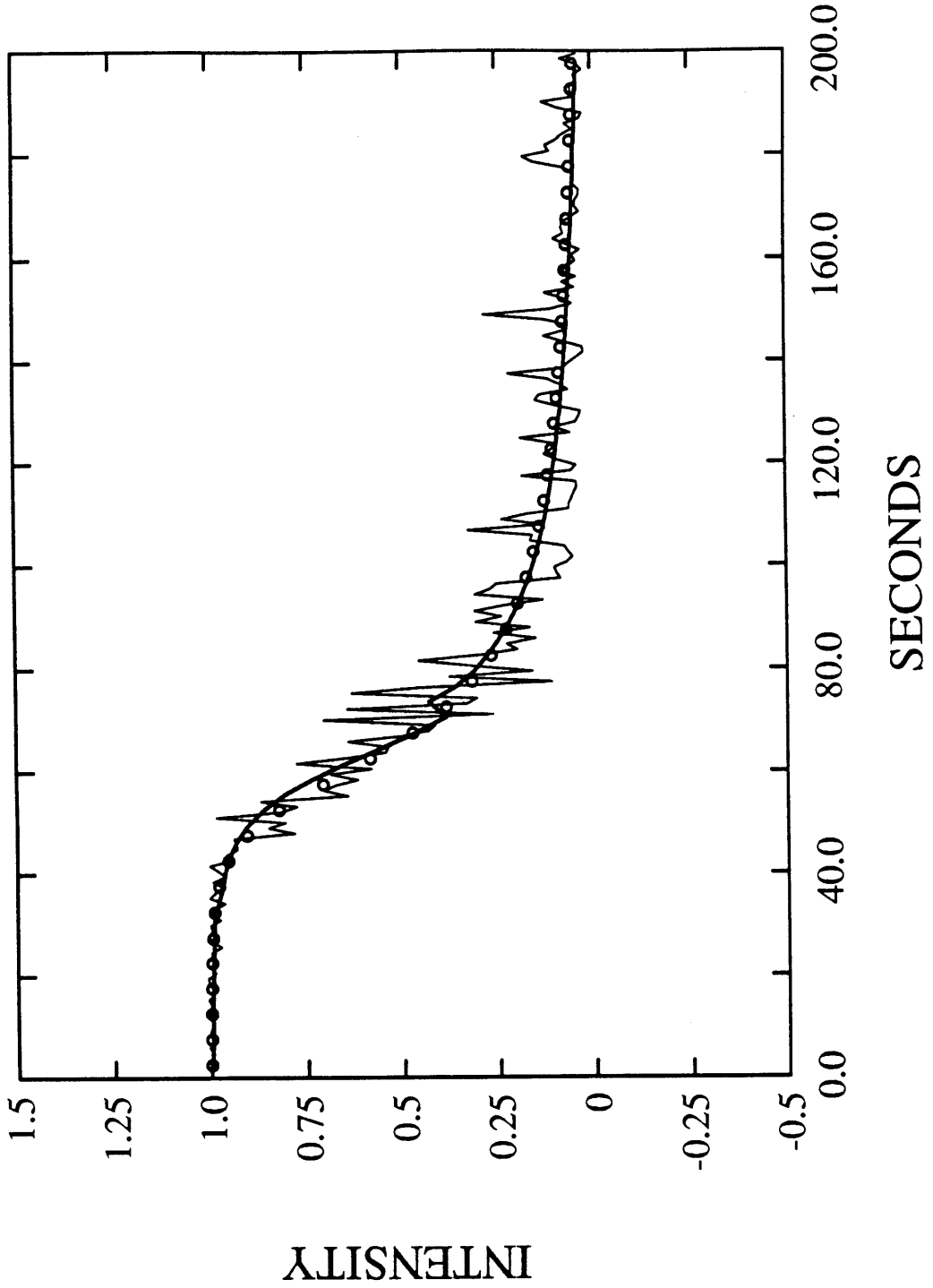
INTENSITY
1.5
1.25
1.0
0.75
0.5
0.25
0
-0.25
-0.5
0.0
40.0
80.0
120.0
160.0
200.0
SECONDS

Chapter 3

Figure 3-7b

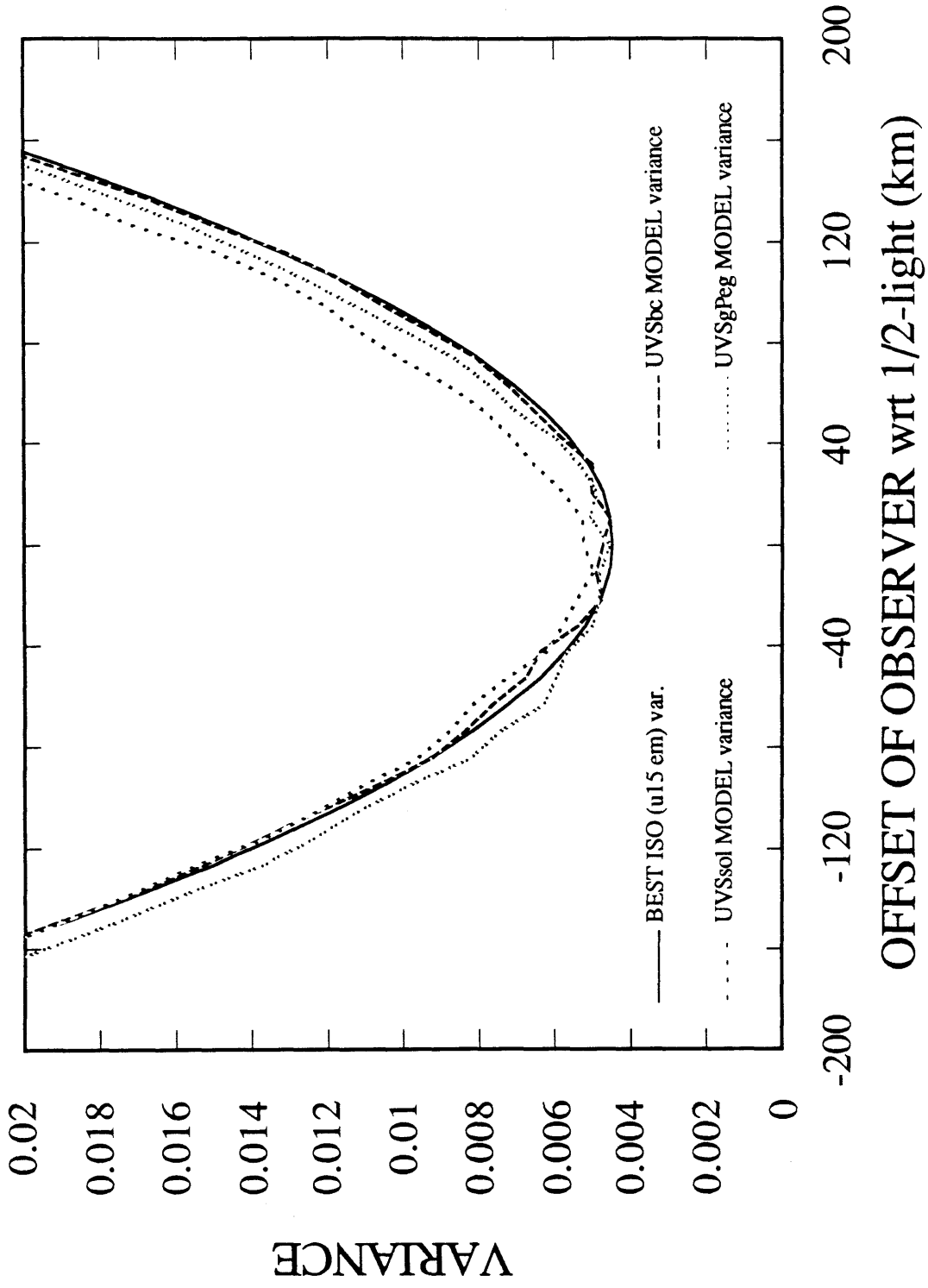

Figure 3-8a

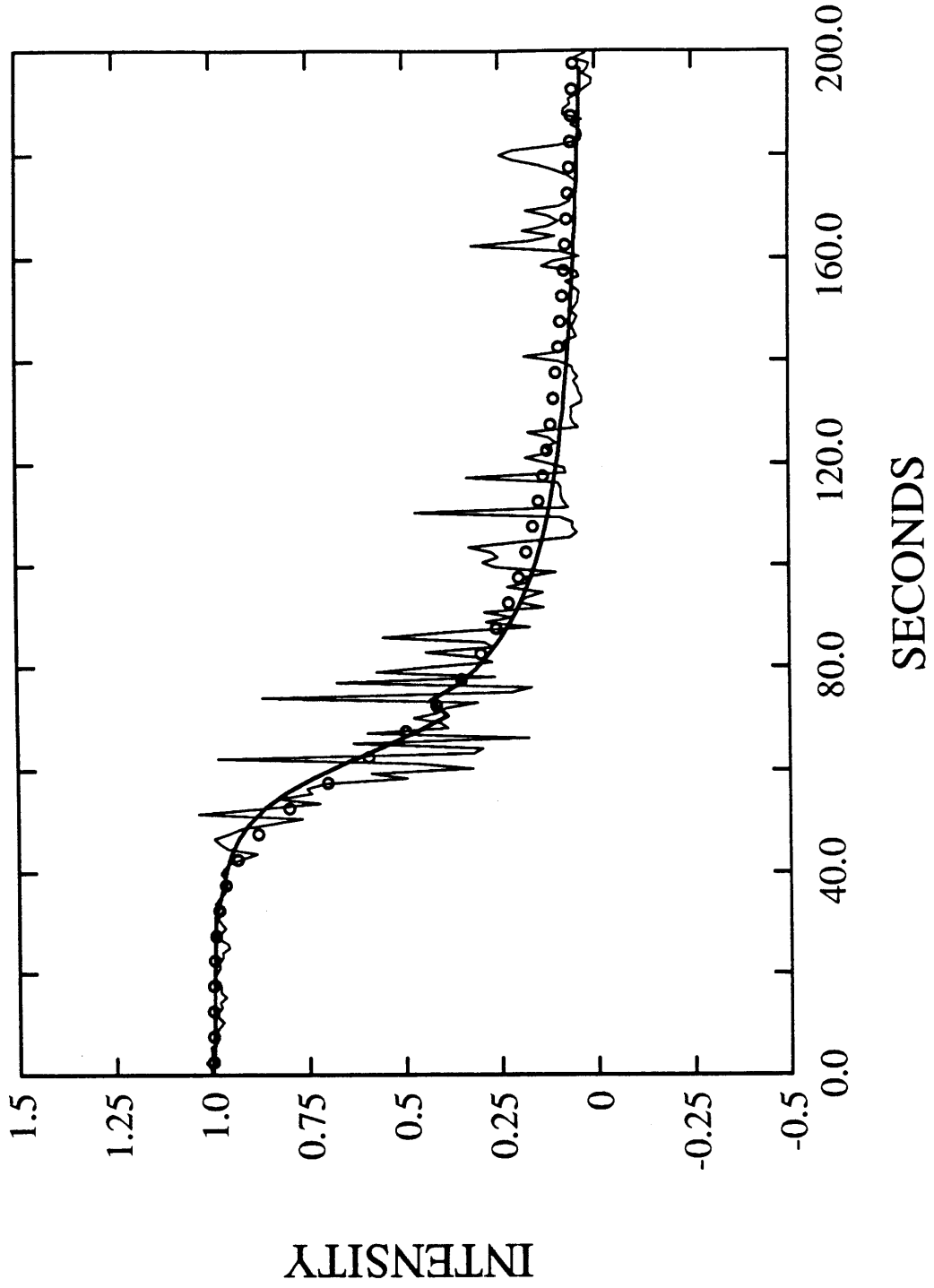
INTENSITY
1.5
1.25
1.0
0.75
0.5
0.25
0
-0.25
-0.5
0.0
40.0
80.0
120.0
160.0
200.0
SECONDS

Figure 3-8b

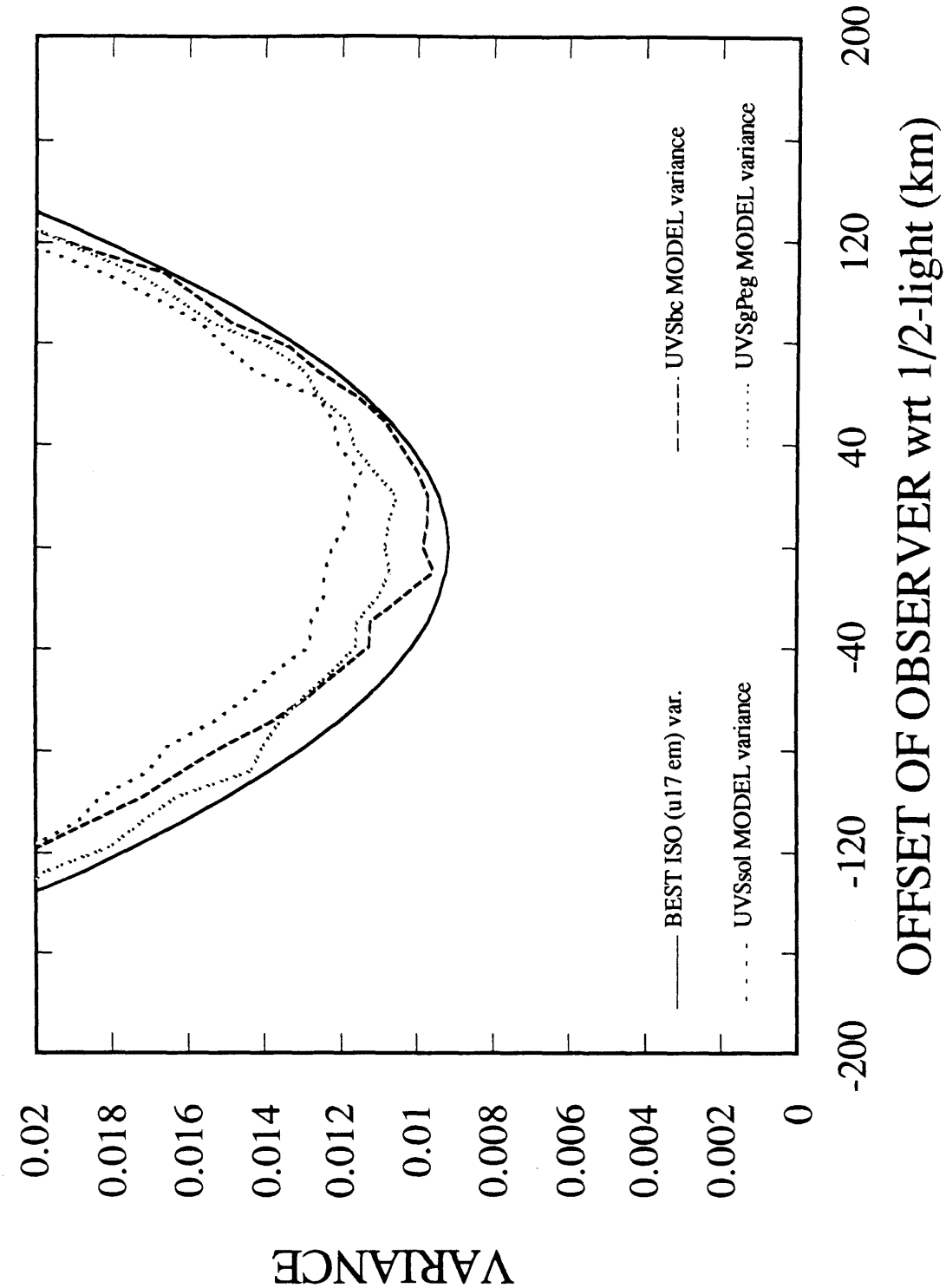
VARIANCE
0.02
0.018
0.016
0.014
0.012
0.01
0.008
0.006
0.004
0.002
0
-200
-120
-40
40
120
200
OFFSET OF OBSERVER wrt 1/2-light (km)
BEST ISO (u17 em) var.
UVSbc MODEL variance
UVSsol MODEL variance
UVSgPeg MODEL variance

The 10 March 1977 planetary immersion occultation data shown in Figure 3-6a were taken aboard the Kuiper Airborne Observatory and have been rebinned to obtain a constant planetary radial velocity (Dunham *et al.* 1980). The 1 May 1982 (French *et al.* 1987) and the 25 March 1983 (Elliot *et al.* 1987) events (Figures 3-7a and 3-8a, respectively) are Uranian atmosphere emersion events and are time reversed for ease of comparison.

A quantitative comparison of the three model lightcurves and the best fit isothermal model curves with respect to each recorded lightcurve has also been made. Each model was generated to have the same number of kilometers per bin and the same averaging as the recorded data for each event; and they were scaled to unit stellar intensity. The isothermal model and the three UVS models; each extending for approximately 2,000 km along the path of the observer, (Figure 3-3), including the half-light point, were used to determine the variance as a function of offset along the path of the observer, with respect to the data. A ±200 km offset range with respect to half-light, determined from isothermal fits to all three "UVS" model lightcurves and to each data set, was used in the calculation. Plots of the variance are shown in Figures 3-6b, 3-7b, and 3-8b. The UVSbc lightcurve, a best fit isothermal model lightcurve and the corresponding data are shown in Figures 3-6a, 3-7a, and 3-8a respectively. The isothermal models have been fit to each individual recorded lightcurve (data); however, the same three "UVS" models are used for all three data sets.

A check to see if the presence of the spike (between 1000 and 1100 km) on the UVSsol lightcurve (Figure 3-5a) might substantially increase the variance for this case was made. This check consisted of using the intensity value directly after the spike to replace the values in the two bins that the spike occupied. This altered lightcurve was then used to compute a variance curve. The altered and original lightcurves produced variance curves that are extremely similar to each other; thus, the spike is not a factor in the comparison.

The results of this comparison of models to data are different for each data set. The UVSbc curve has a lower minimum variance for the 10 March 1977 (U0) event (Figure 3-6a) than the best fit isothermal model or the other two "UVS" models (Figure 3-6b). For the 1 May 1982 (U17) data set (Figure 3-7a), the UVSgPeg, UVSsol, and the best fit isothermal models are nearly indistinguishable (Figure 3-7b). For the 25 March 1983 (U17) event (Figure 3-8a), the UVSbc model minimum is slightly higher than the isothermal fit model, but the UVSbc model exhibits a narrower parabola like curve (Figure 3-8b). The UVSgPeg model and the UVSsol model definitely show a larger minimum variance across all three data sets. Also, for these three cases, the UVSbc synthetic lightcurve appears to represent the data at least as well as the individually best fit isothermal model for each data set.

3.5 Conclusions

1) Synthetic lightcurves produced with parameters derived from the Voyager 2 spacecraft observations as reported by Herbert *et al.* (1987) are compatible with ground-based stellar occultations.

2) Synthetic lightcurves are consistent with the overall structure of ground-based recorded lightcurves, and in comparison to an isothermal model lightcurve, the UVSbc synthetic curve in particular conforms more closely to the observed lightcurves in the vicinity of half-light and the lower baseline. The similar general appearance of the "UVS" model lightcurves to the data, and the variance tests of the three "UVS" models and the isothermal model to three historical occultations,

support the existence of a temperature gradient in the Uranian atmosphere as reported by Herbert *et al.* (1987).

References

BARON, R. L., R. G. FRENCH, AND J. L. ELLIOT (1989). The oblateness of Uranus at the 1-μbar level. *Icarus* **77**, 113-130.

BAUM, W. A., AND A. D. CODE (1953). A photometric observation of the occultation of σ Arietis by Jupiter. *Astron. J.* **58**, 108-112.

DUNHAM, E., J. L. ELLIOT, AND P. J. GIERASCH (1980). The upper atmosphere of Uranus: Mean temperature and temperature variations. *Astron. J.* **235**, 274-284.

ELLIOT, JAMES, L. (1979) Stellar occultation studies of the Solar system *Ann. Rev. Astron. Astrophys.***17**, 445-475.

ELLIOT, J. L., E. W. DUNHAM, A. S. BOSH, S. M. SLIVAN, L.A. YOUNG, L.H. WASSERMAN, AND R. L. MILLIS (1989). Pluto's atmosphere. *Icarus* **77**, 148-170.

ELLIOT, JAMES L., EDWARD DUNHAM, AND DOUGLAS MINK (1980). The radius and ellipticity of Uranus from its occultation of SAO 158687. *Astron. J.* **236**, 1026-1030.

ELLIOT, J. L., I. S. GLASS, R. G. FRENCH, AND J. A. KANGAS (1987). The occultation of KME 17 by Uranus and its rings. *Icarus* **71**, 91-102.

FRENCH, R. G., J. L. ELLIOT, AND P. J. GIERASCH (1978). Analysis of stellar occultation data: Effects of photon noise and initial conditions. *Icarus* **33**, 186-202.

FRENCH, R. G., T. J. JONES, AND A. R. HYLAND (1987). The 1 May 1982 stellar occultation by Uranus and the rings: Observations from Mount Stromlo Observatory. *Icarus* **69**, 499-505.

GOLDSMITH, D. W. (1963). Differential refraction in planetary atmospheres with linear scale height gradients *Icarus* **2**, 341-349.

HERBERT, F., B. R. SANDEL, R. V. YELLE, J. B. HOLBERG, A. L. BROADFOOT, AND D. E. SHEMANSKY (1987). The upper atmosphere of Uranus: EUV occultations observed by Voyager 2. *J. Geophys. Res.* **92**, 15093-15109

HUBBARD, W. B., E. LELLOUCH, B. SICARDY, A. BRAHIC, F. VILAS, P. BOUCHERT, R. A. MCLAREN, C. PERRIER (1988). Structure of scintillations in Neptune's occultation shadow. *Astrophys. J.* **325**, 490-502.

KLEMOLA, A. R., AND B. G. MARSDEN (1977). Predicted observations by the rings of Uranus, 1977-1980. *Astron. J.* **85**, 1663-1669.

KLEMOLA, A. R., D. J. MINK, AND J. L. ELLIOT (1981). Predicted occultations by Uranus: 1981-1984. *Astron. J.* **86**, 138-140.

NARAYAN, R, AND W. B. HUBBARD (1988). Theory of anisotropic refractive scintillation-application to stellar occultations by Neptune *Astrophys. J.* **325**, 503-518.

SICARDY, B, M.COMBES, A. BRAHIC, P. BOUCHET, C. PERRIER, R. COURTIN (1982). The 15 August 1980 occultation by the Uranian system: Structure of the rings and temperature of the upper atmosphere *Icarus* **52**, 454-472.

VEVERKA,J., L. H. WASSERMAN, J. ELLIOT, AND CARL SAGAN, W. LILLER (1974). The occultation of β Scorpii by Jupiter I. The structure of the Jovian upper atmosphere. *Astron. J.* **79**, 73-84.

WASSERMAN L., J. VEVERKA (1973). On the reduction of occultation light curves. *Icarus* **20**, 322-345.

Chapter 4

A Method of Inverting Uranian Ground-based Stellar Occultation Lightcurves Using the Results of the Voyager 2 UVS Experiment

4.1 Introduction

We wish to be able to make a numerical inversion of a ground-based data set in such a manner that the uncertainty in the temperature as a function of pressure and altitude for Uranus' atmosphere can be minimized by using the information obtained from Voyager 2.

This chapter describes the method that was developed to invert ground-based occultation data. The method uses information based on the Voyager 2 UVS observations of Uranus' upper atmosphere as reduced by Herbert *et al.* (1987). The UVS work allows the introduction of a model initial layer or atmospheric cap into the numerical inversions of a lightcurve. Logical steps of the method as well as necessary data manipulation are discussed.

4.2 The Method

The analysis of a single immersion or emersion lightcurve will in general deal with two pieces of information:

1) The recorded ground-based lightcurve.

2) A synthetic ground-based model lightcurve.

The method may be divided into three parts:

1) Generate a UVS model synthetic ground-based lightcurve. This model is generated from geometric parameters corresponding to the event to be analyzed, and Uranian atmospheric

parameters obtained by Herbert *et al.* (1987) from Voyager 2 UVS observations. A portion of the model lightcurve will substitute for the upper atmosphere part of the ground-based recorded lightcurve.

2) Generate a series of composite lightcurves that consist of an upper Uranian atmosphere part taken from the UVS model lightcurve and a lower Uranian atmosphere part taken from a recorded ground-based lightcurve. The series of lightcurves represents a variation in how the model lightcurve is joined to the ground-based recorded lightcurve.

3) Numerically invert the composite lightcurves to obtain temperature-pressure and temperature-altitude profiles. Inverting the multiple composite lightcurves produces a band of temperature profiles for the atmosphere.

When implementing this method we are making assumptions about the physics of the Uranian atmosphere, and the conditions imposed on the recorded ground-based lightcurve. The atmosphere that we assume may be differentiated vertically with the upper part composed of the UVS model joined to a lower part that is the true Uranian atmosphere, as represented by a recorded ground-based data lightcurve (Figure 4-1). The starlight (immersion case) recorded during a ground-based occultation is initially at full intensity. As more and more planetary atmosphere intercepts the starlight, it becomes dimmer and dimmer owing to differential refraction. When the portion of the atmosphere represented by the UVS model starts to refract the starlight, the total refraction is so small that the dimming is much less than the noise (e.g., scintillation, instrumental, shot) present in the ground-based data lightcurve. As the drop in intensity of starlight becomes greater it will reach a point where it is approximately the same as the level of the noise. Near this level of stellar intensity is where we want the UVS model to end. At this same point, and farther along the lightcurve as well, we need the Uranian atmosphere to be characterized by the recorded data in order to retrieve the atmospheric temperatures.

Figure 4-1 Schematic representation of occultation geometry showing two parts to the Uranian atmosphere. The stippled region is modeled and used to produce a synthetic ground-based lightcurve. Starlight propagating through the atmosphere directly below the stippled region (clear) produces the high signal-to-noise portion of the ground-based recorded (data) lightcurve. Each of the two regions of the atmosphere can be mapped into a portion of the composite lightcurve as shown on the right-hand side of the figure (no ray crossing is assumed). The "path of observer" is an idealized path perpendicular to Uranus' limb at the Uranus-Earth distance.

Chapter 4

Figure 4-1

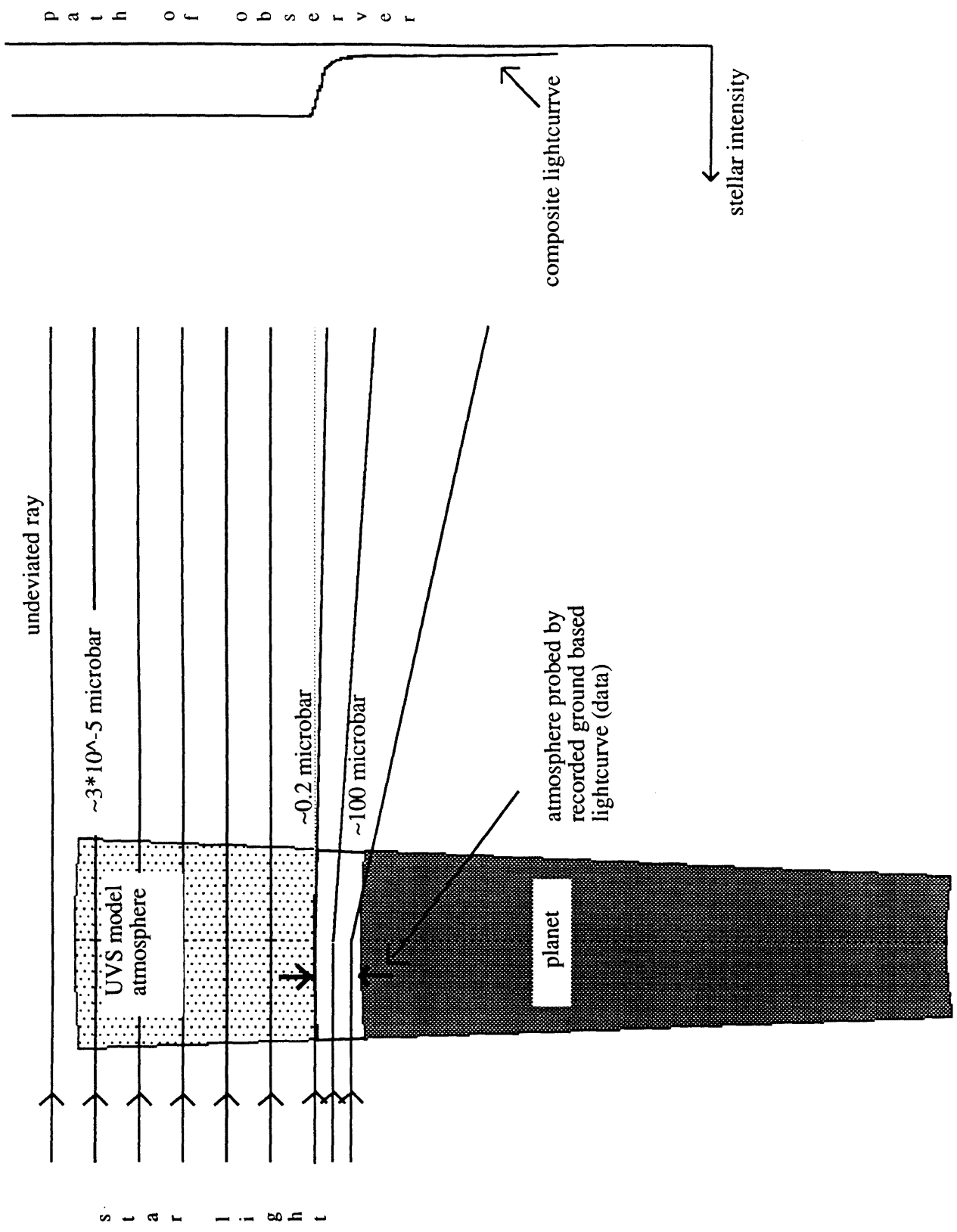

4.3 The UVS Model Synthetic Lightcurve

The results of the previous chapter have shown that of the three UVS models, the UVSbc (UVS best compromise) model most accurately matches the lightcurves examined there. All three models investigated in the last chapter have the same high altitude temperature profile (to within a few percent) above the approximately 0.2 μ-bar level (radii greater than approximately 26,500 km on Uranus). In terms of synthetic ground-based lightcurves, each of the three models produces a lightcurve whose upper atmosphere portions are nearly the same. This upper atmosphere portion is what will be used in making the composite lightcurve mentioned in the part 2 of the method (above). Of the three models, we have adopted the UVSbc model to use in the following and will refer to it as the model.

For any one event, either an atmospheric immersion or emersion, we generate a synthetic model lightcurve with the geometric parameters of the recorded ground-based lightcurve (data) to be analyzed. About 4,000 km of altitude on Uranus is used to produce a synthetic lightcurve. Rays passing through this range of altitude propagate to the path of the observer, producing a lightcurve at that distance from Uranus. We have for convenience used a 4 km altitude layer or bin in our calculations for which we note $\Delta h << H$ (where H is the scale height). The path of observer is an idealized path perpendicular to Uranus' limb at the point of stellar occultation, at the Uranus-Earth distance (Figure 4-1 and Figure 3-3). The Uranus to path of the observer distance of the model is set equal to the Uranus-Earth distance at the time the ground-based lightcurve was recorded. Generally, only the upper atmosphere portion of the model lightcurve becomes part of an inversion when inverting a composite lightcurve. The remainder of the curve, including the half-light point (defined below), is used for reference and comparison to ground-based data. For convenience we select a segment of the model lightcurve that is about 10,000 km long with half-light near the 5,000 km point. This allows, on inversion, recovery and stabilization of the model

Uranian temperature profile before the recorded data portion of the composite lightcurve begins.

The synthetic lightcurve is normalized to unit stellar flux, it has zero background and is referenced to the path of the observer. Lightcurve binning along this distance axis is converted to a time axis corresponding to a particular recorded event by multiplying by the factor $1/v_{\perp}$, where $v_{\perp}$ is the component of the sky plane stellar velocity perpendicular to the planetary limb. For convenience in processing, we have occasionally averaged the raw data in order to keep the total number of bins within the range of several thousand.

For an emersion event, a model lightcurve with the distance axis reversed is made.

4.4 The Composite Lightcurve: Model and Data

Simply stated, we join the upper atmosphere portion of the model lightcurve to the lower atmosphere portion of the recorded ground-based lightcurve. The various parts of a lightcurve as used in this chapter may be identified in Figure 4-2. This figure shows a model lightcurve with the piece to the far left identified as an upper baseline, the next item to the right as a JAR (joint averaging region), and the half-light point and lower baseline identified in order proceeding to the right. For emersion, the lightcurve would be reversed about the half-light point.

To produce an accurately determined composite lightcurve, the following steps in the analysis are taken:

1) A simple isothermal model is fit to the stellar flux and background. This fitting procedure determines:

a) The stellar flux.

b) The background flux. The stellar flux and background flux determination allow background subtraction and a preliminary flux normalization as a first step to a more precise scaling of the data lightcurve to the model lightcurve.

Figure 4-2 Lightcurve shown for reference. The JAR is a joint averaging region of the lightcurve (see text for use of the region). The half-light point on the lightcurve is designated by vertical dashed line. Upper and lower baselines are approximations to a constant flux and depend on the distance from half-light.

Chapter 4

Figure 4-2

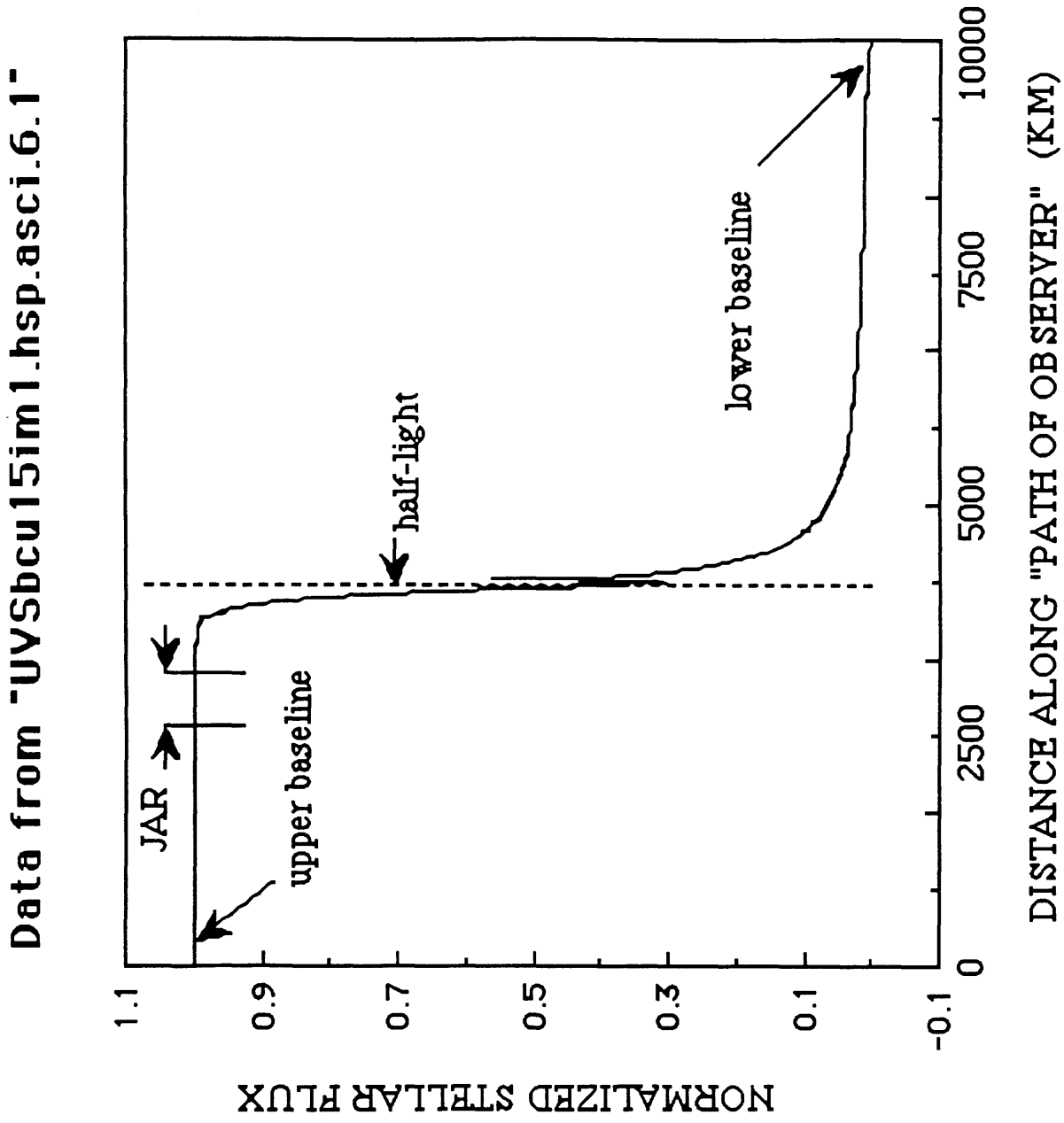

c) The half-light time. This datum is used in the calculation of the half-light radius.

d) A quantity composed of the scale height divided by $v_\perp$. This quantity is the time along the path of observer it takes an observer, moving at a speed $v_\perp$, to traverse the rays received from one scale height of the planet's atmosphere. The scale height along with the half-light time is used in determining the half-light radius. Errors in the half-light radius are discussed below.

2) A local measure of the upper baseline average is made in one or more regions of the lightcurve. These averages are used to discriminate against low frequency noise in the upper baseline when a composite lightcurve is produced. The averaging regions are usually several hundred kilometers in length (referred to the path of observer), and are called JARs (joint averaging regions, see Figure 4-1). Each JAR may be specified in terms of its length and center distance. The distance is measured from the half-light point along the path of observer. Positive values are at greater Uranian radii when referenced to the planet. The length of the JAR is also specified in kilometers along the path of observer. The JAR has been specified in terms of a length (rather than time) to allow the JAR characteristics of any ground-based data lightcurve to ultimately be related to the same amount and radial location of atmosphere probed by any other ground-based lightcurve.

3) A JP (joint point) is specified. This point is calculated in kilometers along the lightcurve using the half-light point as zero reference. Many JPs may be specified; each is used to make another composite lightcurve. To accurately join the two lightcurves, the JP on both curves must in general be on the same pressure surface in the planet's atmosphere. For a homogeneous spherically symmetric planet this would also correspond to the same radius.

To join the data to the synthetic lightcurve, assume the data lightcurve may be represented by

$$n_{LC-dat}(t) = n_{b-dat} + n_{*dat}\,\phi_{dat}(t) + n_{noise}(t)\ , \qquad (4\text{-}1)$$

where $n_{LC-dat}(t)$ is the rate of photons detected per second for the ground-based data lightcurve, n_{b-dat} and n_{*dat} are the rates of photons detected from the unocculted star and the steady state background, $n_{noise}(t)$ is the time varying equivalent rate of detected photons per second from all noise sources, and $\phi_{dat}(t)$ is the noise free occultation flux of the data. Assume the background and star flux as determined by the previously mentioned isothermal fit approximate n_{b-dat} and n_{*dat} well enough that they may be directly substituted. We now subtract the background count and normalize by the star count to obtain the following intermediate value,

$$\beta = \phi_{dat}(t) + \frac{n_{noise}(t)}{n_{*dat}} . \qquad (4\text{-}2)$$

To minimize the effect of low frequency amplitude noise components inherently added to the upper baseline (the last term Equation 2) of the data lightcurve on the retrieved temperature profile, we determine a scale factor from a pair of JARs. One JAR along the ground-based data lightcurve and the other along the model ground-based lightcurve at the same relative points. The length of these regions is several hundred kilometers along the path of observer and they are generally located approximately two to six hundred kilometers above half-light. The ratio of the average intensities computed in respective JARs is now used to scale the right-hand side of Equation 2. This has the effect of discriminating against noise with a wavelength longer than the JAR. We now have for the processed data,

$$n_{proc-dat}(t) = \frac{\langle JAR_{mdl}(t_s - t_e)\rangle}{\langle JAR_{dat}(t_s - t_e)\rangle}\left[\phi_{dat}(t) + \frac{n_{noise}(t)}{n_{*dat}}\right], \qquad (4\text{-}3)$$

where the angle brackets indicate an average over the region defined by the JAR. The quantities t_s and t_e are the start and end times respectively of a JAR. The quantity

$JAR_{mdl}(t_s - t_e)$ refers to a JAR on the synthetic ground-based model lightcurve, where the times t_s and t_e are also referenced to this curve.

Conceptually, the now processed ground-based data lightcurve is placed on the same distance axis as the model lightcurve and the data are shifted along this axis such that the curves are coincident at half-light. The error bars for the ground-based data lightcurves referenced to the Uranian equator (Baron *et al.* 1989) and those for the UVSbc model ground-based lightcurve (Herbert *et al.* 1987) overlap; therefore, we do not compensate for any offsets. In order to obtain consistent half-light values for the data as well as the model, both lightcurves were previously fit with an isothermal model to determine their respective half-light points.

We now have the data and model lightcurves scaled in intensity with the background subtracted from the data. The curves are also on the same distance axis with the same binning, and the half-light bins are coincident. We now use some JP (joint point) specified in terms of a distance (along the path of the observer) from half-light, and join the first part of the model lightcurve to the rest of the data lightcurve at that point to form a composite lightcurve.

4.5 Inversion of the Composite Lightcurve

The composite lightcurves produced with various joining criteria are now ready to be numerically inverted. The details of the lightcurve inversion method we use have been presented in work by Wasserman and Veverka (1973) and French *et al.* (1978). We have reviewed the theory in Appendix I. A brief sketch of the method will be given here. Wasserman and Veverka (1973) have shown that

$$\nu(r) = \frac{1}{\pi\ (2\ R_p)^{1/2}} \int_{\infty}^{r} \frac{\theta(r')}{(r' - r)^{1/2}}\, dr' \ , \qquad (4\text{-}4)$$

providing $H/R_{planet} << 1$, where H is the scale height and R_{planet} is the planetary radius. The number density may be written as

$$n(r) = L \frac{\nu(r)}{\nu_{STP}} \ , \qquad (4\text{-}5)$$

where L is Loschmidt's number, ν_{STP} is the refractivity of the gas at standard temperature and pressure at the wavelength observed. From the hydrostatic equation we have

$$dp(r) = - m_{avgm}(r)\ g(r)\ N(r)\ dr \ , \qquad (4\text{-}6)$$

where $m_{avgm}(r)$ is the average mass (grams) per molecule of the atmosphere as function of radius, and g(r) is the local gravity as a function of radius. We may obtain the pressure by integrating as

$$p(r) = \frac{L}{\nu_{STP}} \int_{r_1}^{\infty} m_{avgm}(r)\ g(r)\ N(r)\ \ dr \ . \qquad (4\text{-}7)$$

With the use of the perfect gas law we may obtain the temperature as

$$T(r) = \frac{p(r)}{N(r)\ k} \ , \qquad (4\text{-}8)$$

where k is Boltzman's constant.

For a real planet we cannot integrate to infinity, nor do we have data out to infinity. We must instead use some initial conditions as a starting point for our inversion. The effect of starting conditions on a numerical inversion is discussed by Hunten and Veverka (1976). They have commented on and reviewed the "large, unavoidable uncertainties in the upper parts of a derived temperature profile in both optical and radio cases" of planetary atmospheric occultations. Here we seek to avoid this general problem by starting from "known" temperature and pressure conditions in a layer above the region probed by the lightcurve. To the extent the conditions in this "known" region are temporally stable, uniform about the planet, and are accurately quantified, the uncertainty in our result will be limited by the quality of the recorded ground-based lightcurve and the availability of corollary information such as exact composition with altitude.

In order to retrieve the model temperature profile, we use as initial condition values (for the composite lightcurve inversion) the temperature and pressure from the upper most layer of the model. Once the model profile is reproduced in the inversion, the data part of the composite lightcurve begins.

Owing to a lack of data on the exact composition with altitude for this part of the atmosphere (including the homopause), we will use a constant value for the mean molecular mass for convenience. It is assumed that the homopause is within the region probed by the ground-based data lightcurves, but experimental evidence is lacking as to its exact level. The composition in this region is helium and hydrogen (molecular), but the ratios are not firmly established. At lower altitudes (below the 10-mbar level), the Voyager 2 experiments (Hanel *et al.* 1986) have indicated a helium mole fraction of 0.15 ± 0.05. The temperature will scale directly as the ratio of the mean molecular weights.

4.6 The Effect of Noise on the Method

In recorded data, noise is ever present. We must therefore understand what effects noise in the data will have on the resultant profiles. The case of Poisson noise in an isothermal lightcurve was treated in detail by French *et al.* (1978). Their approach, though valid, has not been generally applicable to observed lightcurves. Except for data taken aboard the Kuiper Airborne Observatory for the 1977 Uranian occultation (Elliot *et al.* 1977, Dunham *et al.* 1980) noise obeying Poisson statistics has not been the dominant source of noise for Uranus occultations. In many observations the dominant noise sources appear to be atmospheric scintillation, detector noise, guiding errors, and baseline drift, to name a few. Few assumptions can be made about these noise sources due to their variable and erratic nature. Instead, to investigate the effect of noise, we add recorded noise from an observed event to a model lightcurve and treat the modified model lightcurve as synthetic data.

The first part of the method entails generation of a ground-based model lightcurve. We have used the Uranus-Earth distance and the event perpendicular velocity from the U15 Mount Stromlo occultation (French *et al.* 1987) in the model calculation. For this occultation 600 seconds of lightcurve covers the range of Uranian atmosphere desired. Figure 4-3 shows the ground-based model lightcurve with appropriate scaling of the time axis.

The second part of the method is to generate a series of composite lightcurves, consisting of an upper atmosphere part taken from a model lightcurve and the remainder from a ground-based recorded lightcurve. Here we must substitute our synthetic data for the ground-based recorded lightcurve. We have generated synthetic ground-based data lightcurves as follows:

Figure 4-3 A simulated lightcurve produced with the "Best Compromise" model atmospheric parameters from Voyager 2 UVS observations as analyzed by Herbert *et al.* (1987) and geometric, and velocity parameters corresponding to the U15 Mount Stromlo event. Seconds along the horizontal axis are arbitrarily set to zero at the start of the lightcurve.

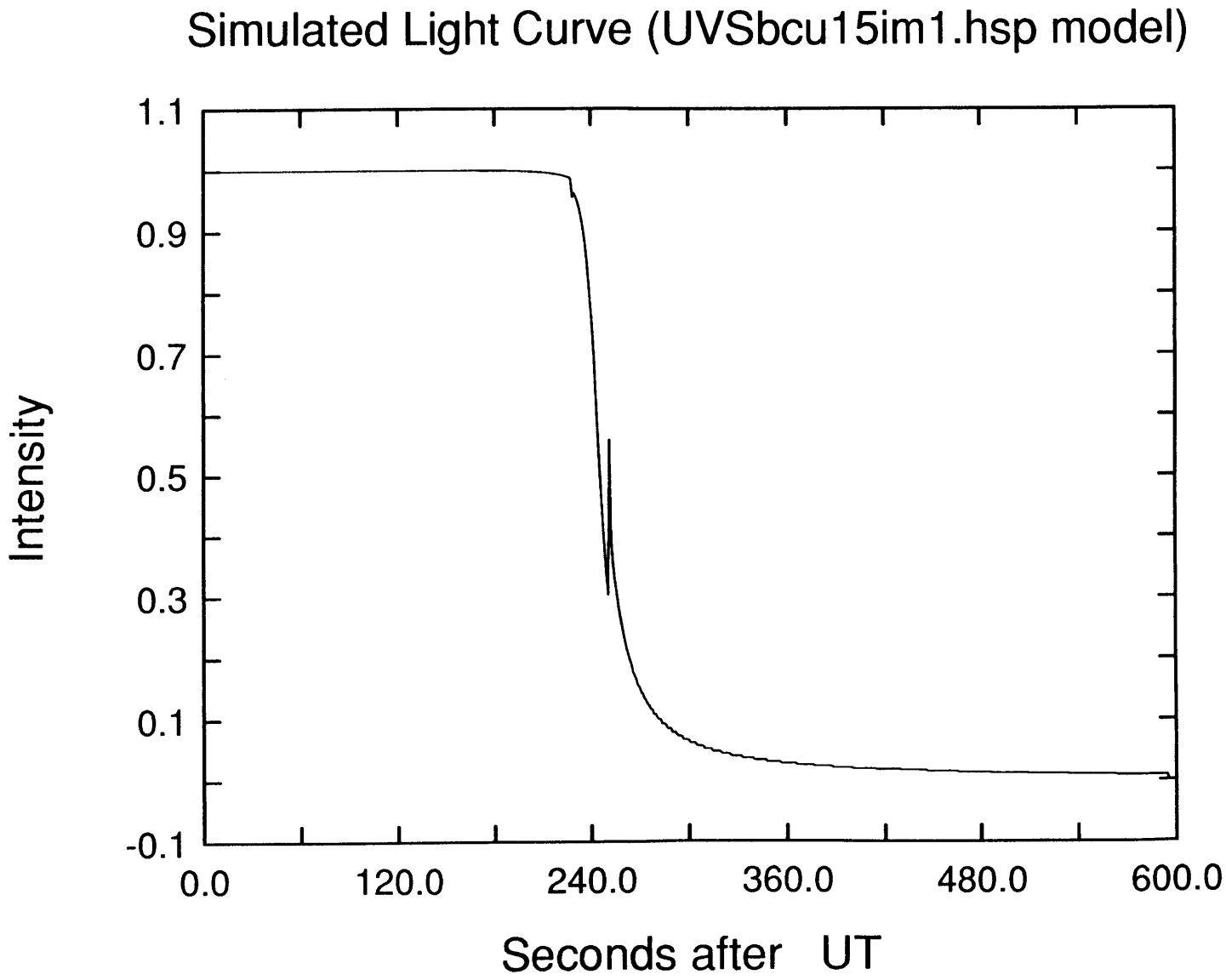

Chapter 4 Figure 4-3

The ground-based model lightcurve, generated above, is now used as the basic lightcurve to which noise is added. Figure 4-4 shows 1200 seconds of upper baseline recorded prior to immersion for the U15 Mount Stromlo event. This section of noise is comparable (to within 20 percent) to that at the time of each event, and was chosen since it is continuous without ring events or zero checks. Five synthetic data lightcurves have been produced from part of this noise. By multiplying the noise by some factor, and again proceeding with compositing and inverting, we have found a linear dependence between the input noise amplitude and the fractional error in temperature (compared to the model value) on output. We have, therefore, chosen to multiply the input noise by a factor of 2 in order to more readily show the deviations of the noise after inversion. The first synthetic ground-based data lightcurve is produced by adding the first 600 seconds of upper baseline to a copy of the ground-based model lightcurve. A mean of this 600 seconds of baseline has been calculated and subtracted from the noise prior to adding to the ground-based model lightcurve. Four additional synthetic ground-based data lightcurves are produced by selecting 600 seconds of noise starting at 60 sec., 120 sec., 180 sec., and 240 sec. from the start of the upper baseline file. Figures 4-6 through 4-10 show the five synthetic ground-based data lightcurves.

We have directly added noise to the model lightcurve to obtain synthetic data. No attempt was made to simulate the decrease in noise with signal level (e.g., shot noise, scintillation) found in most infrared observations. The procedure should therefore give a conservative measure of the influence of the noise on the resultant temperature profile.

Each of these five synthetic ground-based data lightcurves was used to make a series of composite lightcurves. Following the procedure for recorded data, the next step is to make simple isothermal model lightcurve fits to each synthetic ground-based data lightcurve to determine a half-light point. For the noise used here the half-light values do

Figure 4-4 Upper baseline noise from the U15 Mount Stromlo event. This figure has been scaled such that full stellar flux would cover 5/6 of the its vertical range (same as Figure 4-3). The zero of the time axis is 15:57:20 UT the date of the observation. This noise was added to synthetic lightcurves to study the influence on the derived temperatures after numerical inversions of the lightcurves.

Figure 4-5 The same piece of upper baseline as in Figure 4-4 is displayed here but with 100 sec averaging and the vertical scale has been expanded by a factor of 100.

Figure 4-6 The UVS "best Compromise" model with the first 600 sec of U15 noise added. The noise was multiplied by a factor of 2 to more readily demonstrate its effect. The average value of the 600 sec of noise was subtracted to give a zero mean before addition to the model.

Figure 4-7 The UVS "best Compromise" model with 600 sec of U15 noise added starting 60 sec into the noise file. The noise was multiplied by a factor of 2 to more readily demonstrate its effect. The noise was also added with a zero mean for the 600 sec.

Figure 4-8 The UVS "best Compromise" model with 600 sec of U15 noise added starting 120 sec into the noise file. The noise was multiplied by a factor of 2 to more readily demonstrate its effect. The noise was also added with a zero mean for the 600 sec.

Figure 4-9 The UVS "best Compromise" model with 600 sec of U15 noise added starting 180 sec into the noise file. The noise was multiplied by a factor of 2 to more readily demonstrate its effect. The noise was also added with a zero mean for the 600 sec.

Figure 4-10 The UVS "best Compromise" model with 600 sec of U15 noise added starting 240 sec into the noise file. The noise was multiplied by a factor of 2 to more readily demonstrate its effect. The noise was also added with a zero mean for the 600 sec.

Figure 4-4

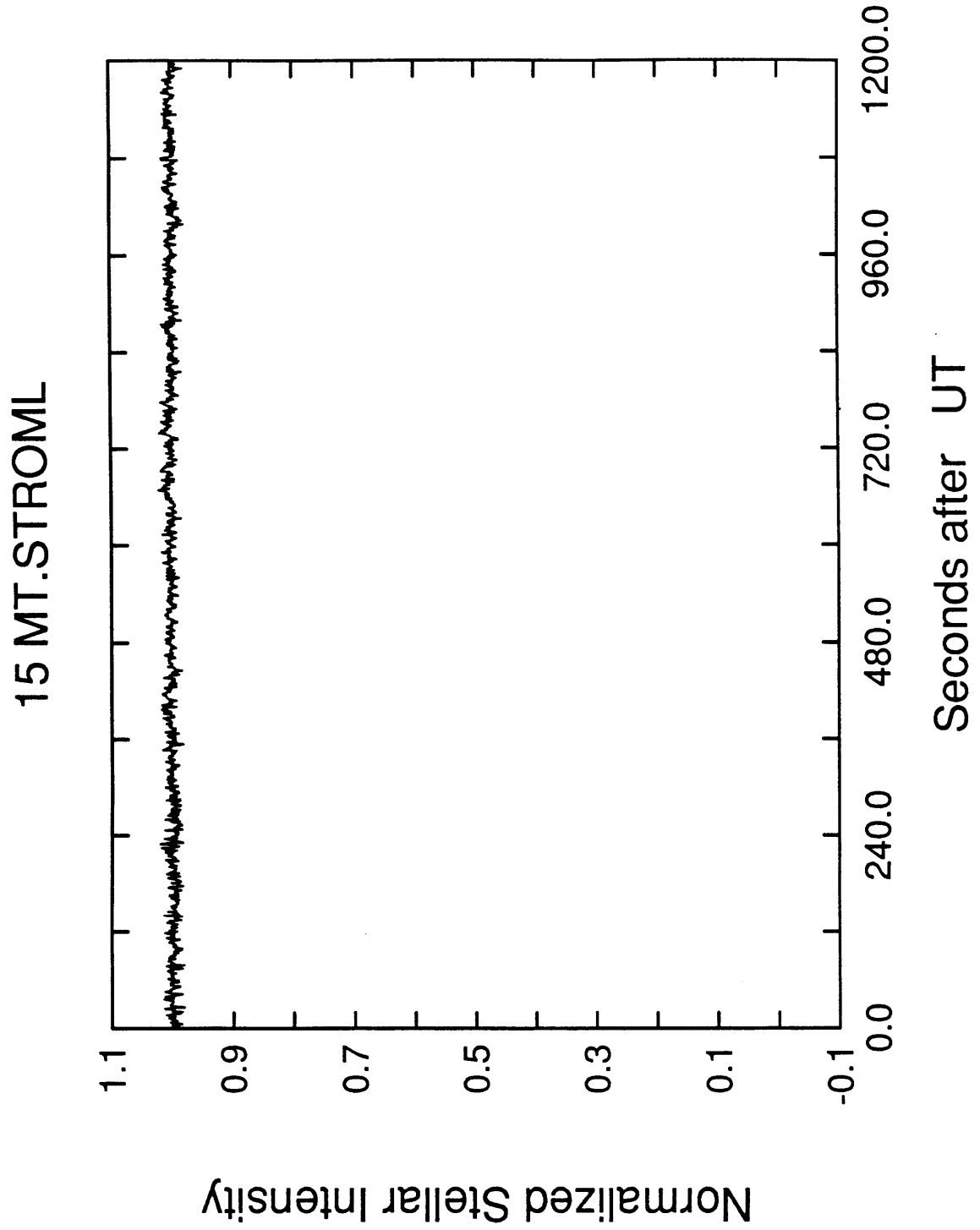
15 MT.STROML
Normalized Stellar Intensity
1.1
0.9
0.7
0.5
0.3
0.1
-0.1
0.0
240.0
480.0
720.0
960.0
1200.0
Seconds after UT

Chapter 4

Figure 4-5

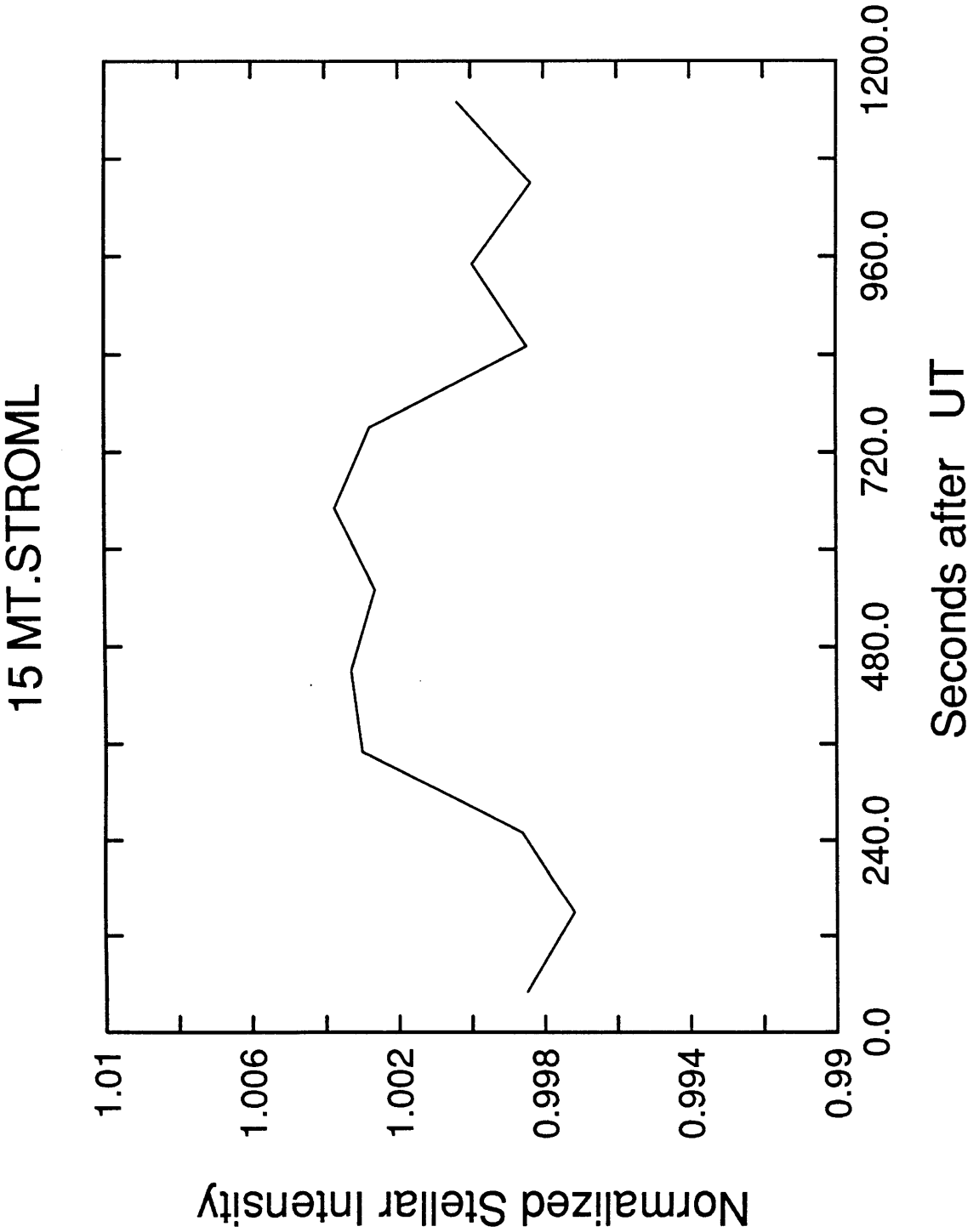

Figure 4-6

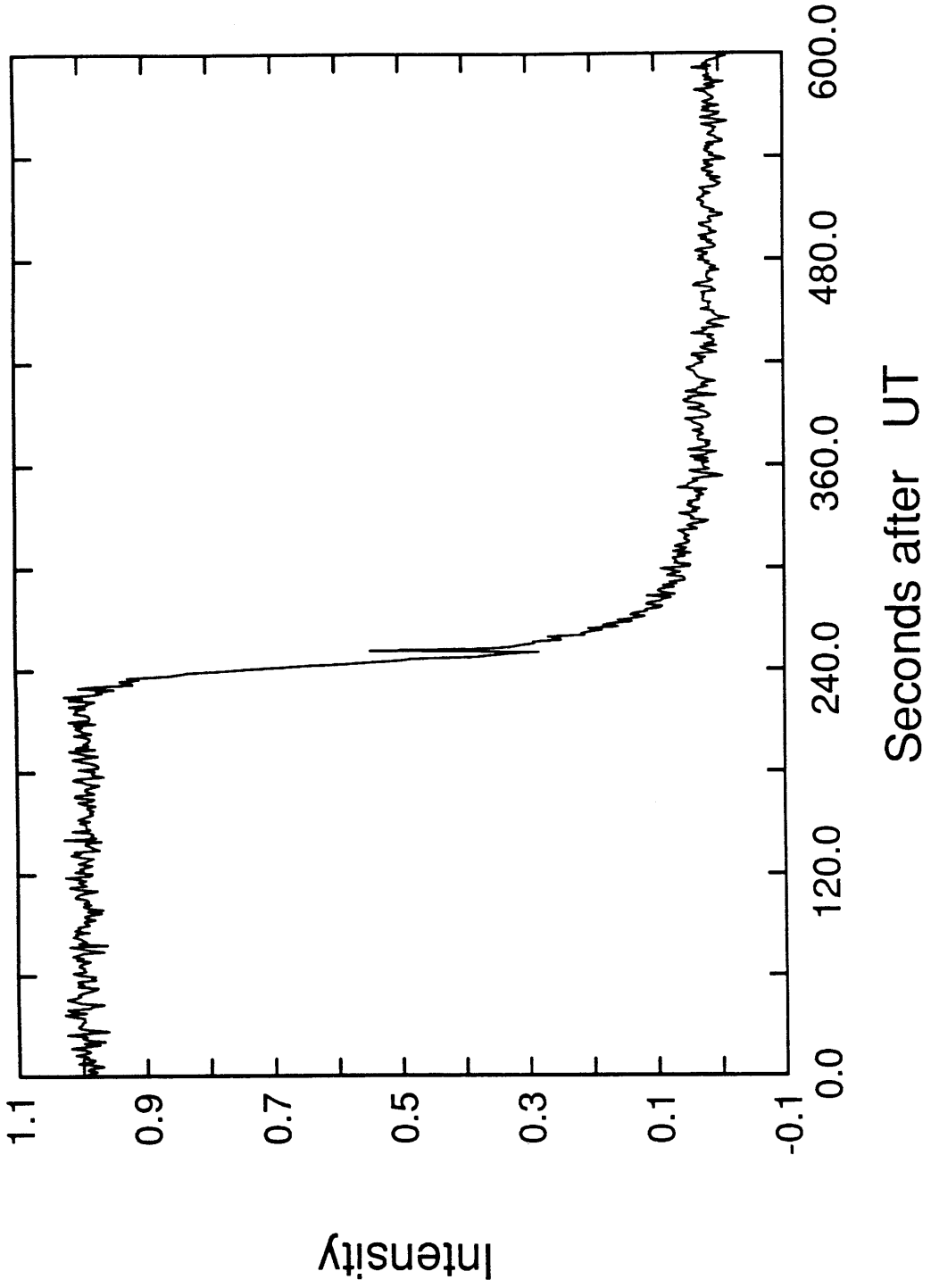
Intensity
1.1
0.9
0.7
0.5
0.3
0.1
-0.1
0.0
120.0
240.0
360.0
480.0
600.0
Seconds after UT

Chapter 4

Figure 4-7

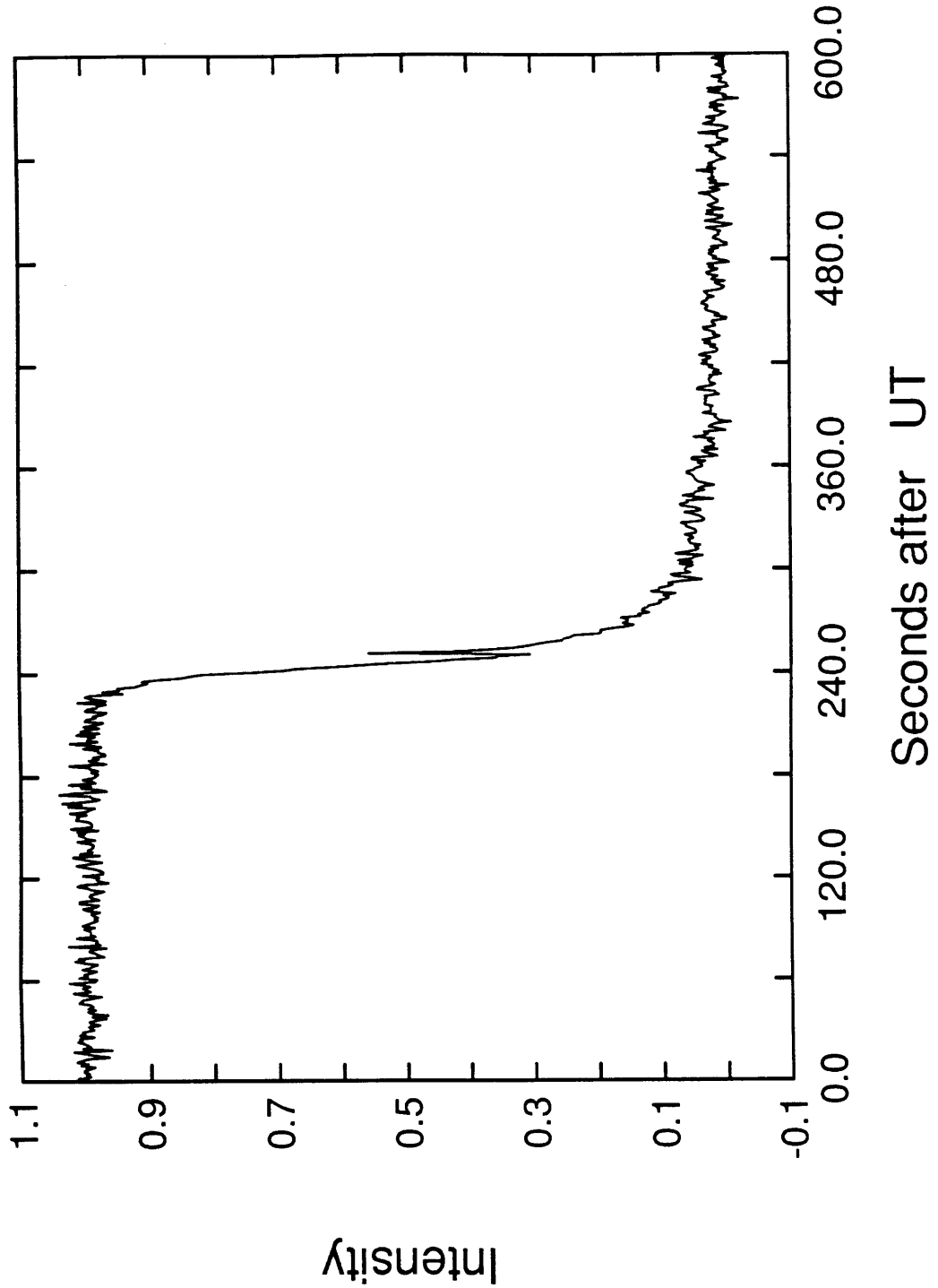

Figure 4-8

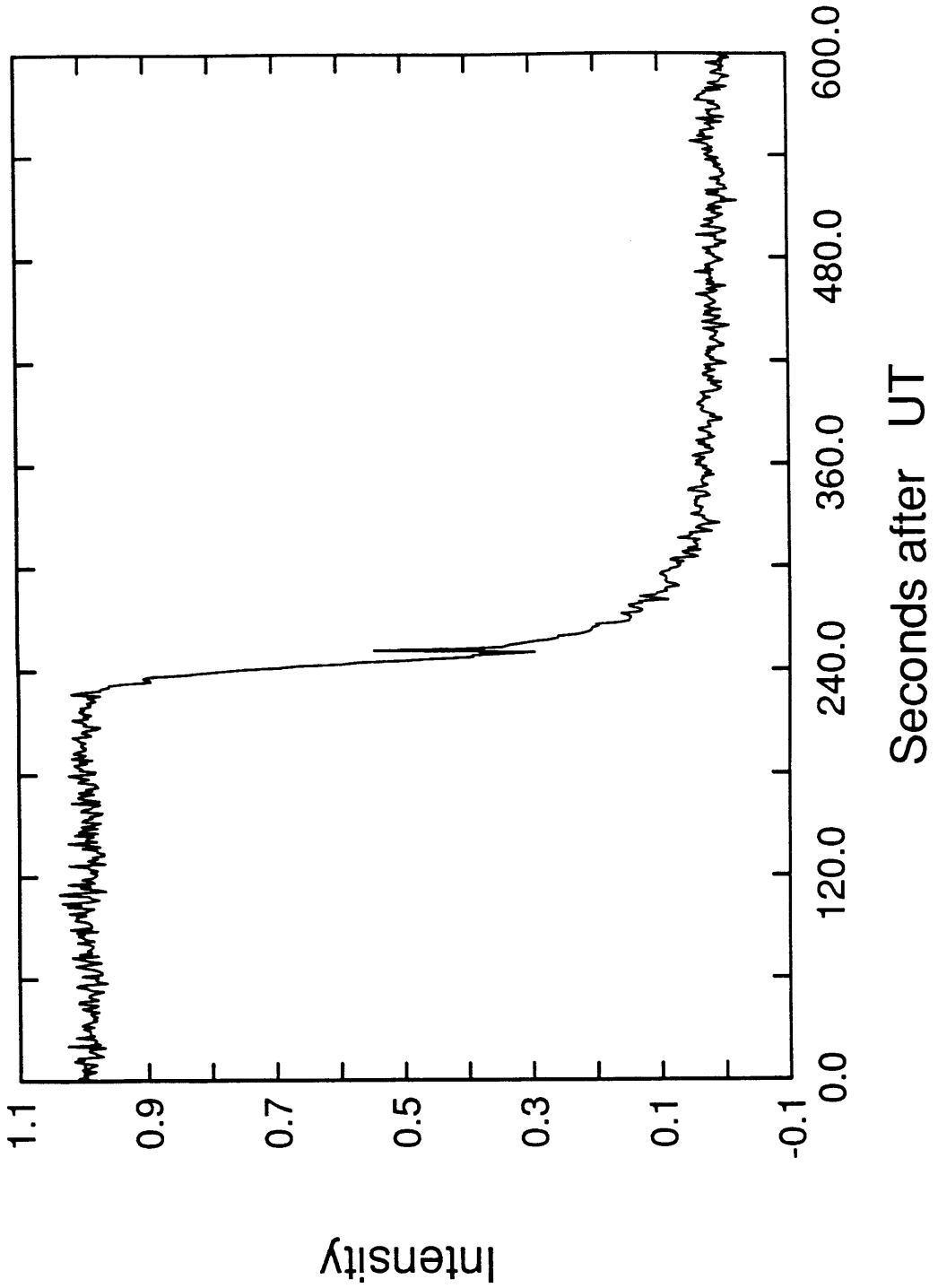
Intensity
1.1
0.9
0.7
0.5
0.3
0.1
-0.1
0.0
120.0
240.0
360.0
480.0
600.0
Seconds after UT

Chapter 4

Figure 4-9

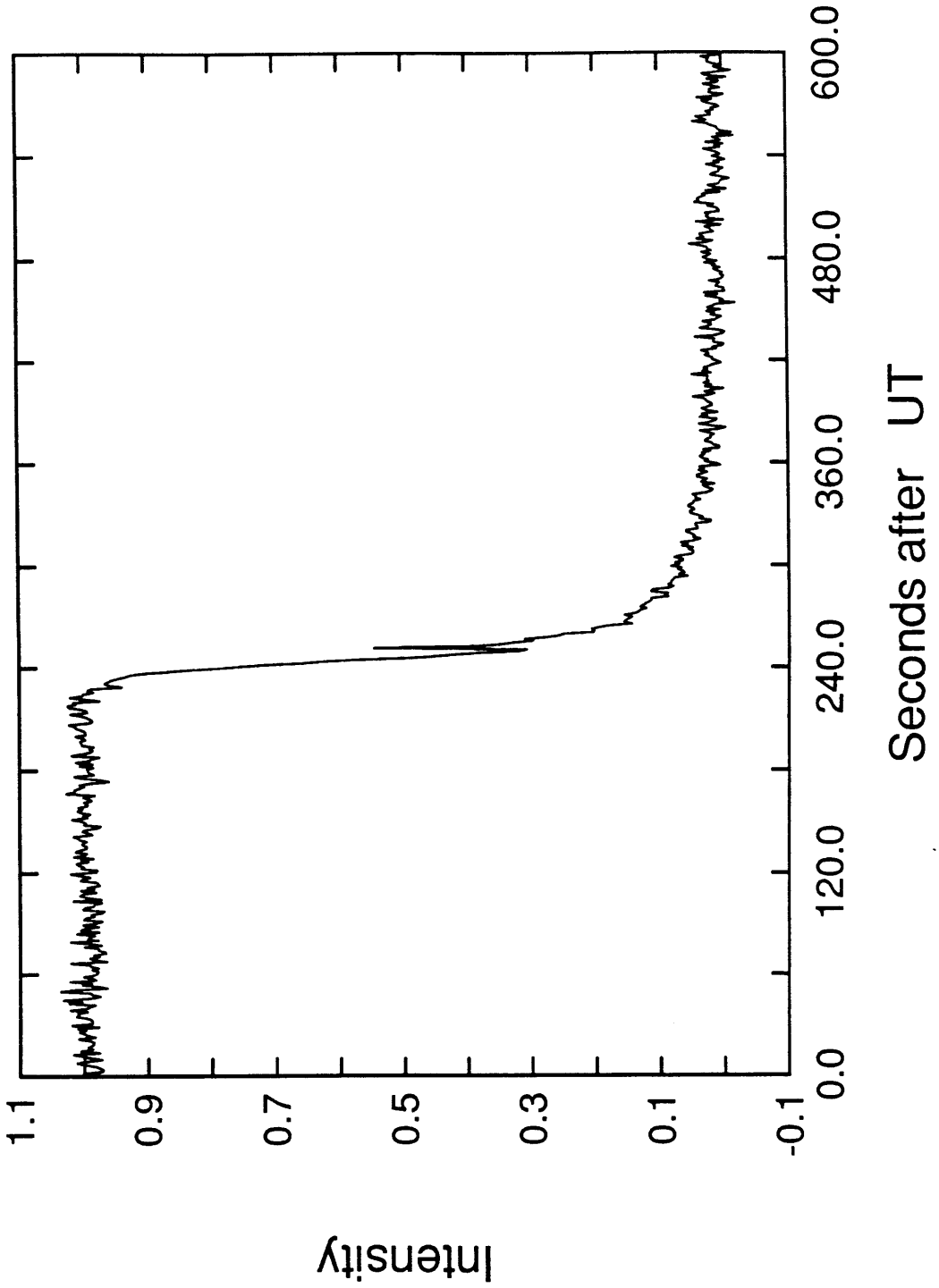

Figure 4-10

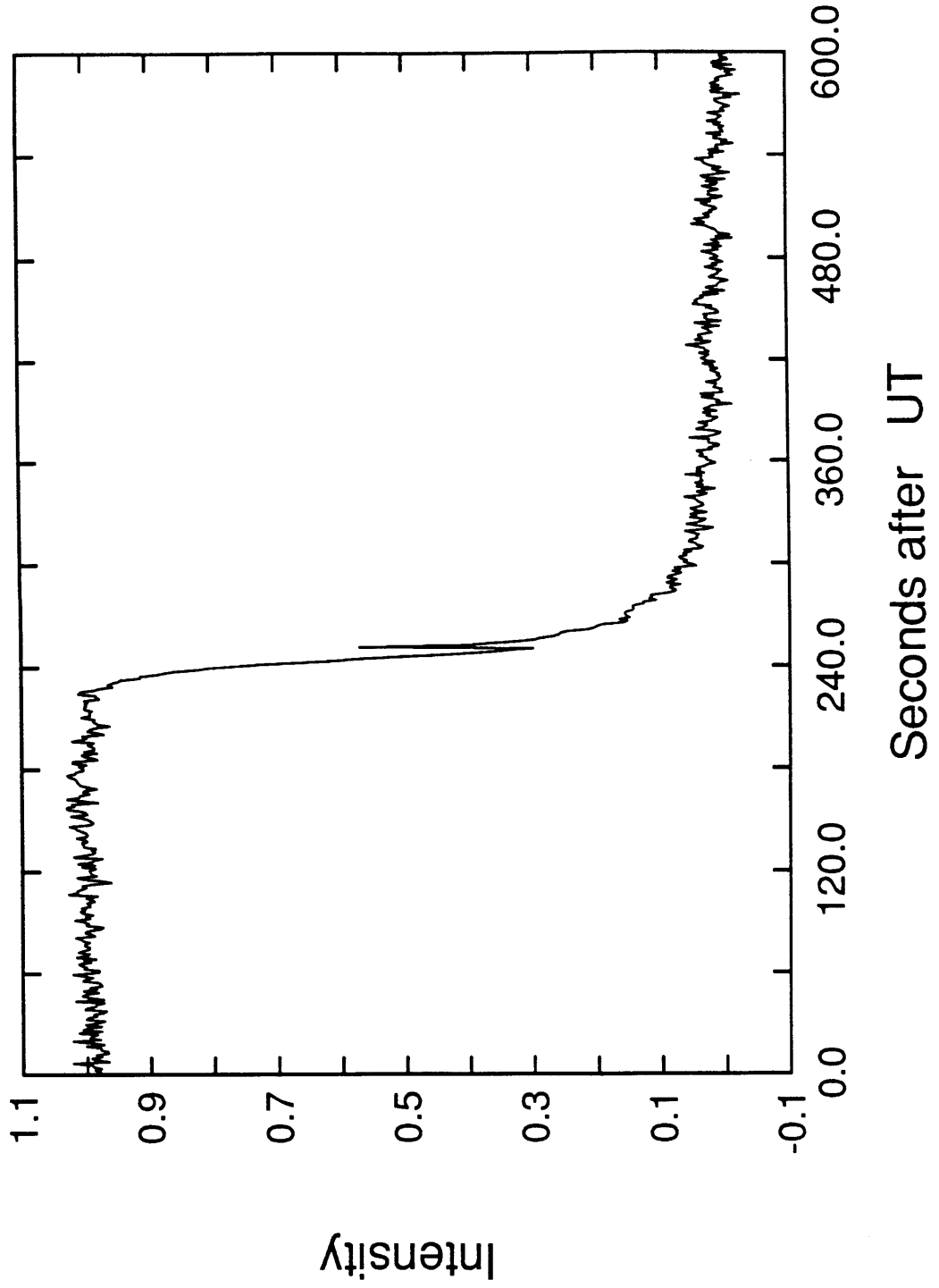
Intensity
1.1
0.9
0.7
0.5
0.3
0.1
-0.1
0.0
120.0
240.0
360.0
480.0
600.0
Seconds after UT

not differ significantly from those of the model lightcurve alone. An internal consistency of ± 10 km has been shown for the ground-based data lightcurve's half-light radius determinations (Baron *et al.* 1989). The UVS model reference points are quoted by Herbert *et al.* (1987) to be ± 10 km for the UVS solar occultation, ± 20 km and ± 40 km for the γ Peg immersion and emersion, respectively. Next, two JARs were specified with centers at 300 and 600 km from the half-light point. The length of each JAR is 250 km. Five JPs were also specified for each JAR value. The JPs were located at 0 km, 150 km, 300 km, 450 km, and 600 km from the half-light point along the path of observer. These are shown in Figures 4-11 through 4-15, respectively. Ten composite lightcurves were made for each synthetic ground-based data lightcurve. A total of 50 composite lightcurves were made for inversions.

For the final step in the method, we need to invert the composite lightcurves. The pressure and temperature in the top layer of the calculated model (used to generate the ground-based model lightcurves) are used as initial values for the inversion. For the work in this noise section (only), we have used a value of 2.3 for the mean molecular mass in the inversion procedure. The model half-light radius (determined from an isothermal fit to a ground-based model lightcurve) is used to set the zero point for the calculation of local gravity by the inversion program. Figures 4-16 through 4-20 show the resultant temperature-pressure profiles. Each figure corresponds to all the composite lightcurves that used a particular value of JP; the figures progress through the values 0 km to 600 km, respectively.

We can examine these curves in terms of the error in temperature from the noiseless model profile (bold and dashed). In Figures 4-16 and 4-17, the maximum error is at the highest pressure (smallest radius) and does not exceed approximately 20 K. In Figure 4-18 (JP = 300 km), the deviation at the low pressure end of the large temperature gradient (the JP) is nearly the same as that at the high pressure end of the complete temperature profile.

Figure 4-11 A composite ground-based lightcurve. The first part of the curve is the UVSbc model. It joins scaled data at the half-light point (0 km). The spike near the half-light point is due to a discontinuous second derivative of the model atmosphere temperature gradient.

Figure 4-12 A composite ground-based lightcurve. The first part of the curve is the UVSbc model. It joins scaled data at 150 km before the half-light point (measured along the path of the observer). The spike near the half-light point is due to a discontinuous second derivative of the model atmosphere temperature gradient.

Figure 4-13 A composite ground-based lightcurve. The first part of the curve is the UVSbc model. It joins scaled data at 300 km before the half-light point (measured along the path of the observer). The spike near the half-light point is due to a discontinuous second derivative of the model atmosphere temperature gradient.

Figure 4-14 A composite ground-based lightcurve. The first part of the curve is the UVSbc model. It joins scaled data at 450 km before the half-light point (measured along the path of the observer). The spike near the half-light point is due to a discontinuous second derivative of the model atmosphere temperature gradient.

Figure 4-15 A composite ground-based lightcurve. The first part of the curve is the UVSbc model. It joins scaled data at 600 km before the half-light point (measured along the path of the observer). The spike near the half-light point is due to a discontinuous second derivative of the model atmosphere temperature gradient.

Figure 4-16 The derived temperature profiles from the inversion of five noise samples added to the UVSbc synthetic lightcurve using two JARs for a total of ten lightcurves. All of these composite lightcurves were joined at half-light. The heavy dotted profile is the model profile without added noise.

Figure 4-17 The derived temperature profiles from the inversion of five noise samples added to the UVSbc synthetic lightcurve using two JARs for a total of ten

lightcurves. All of these composite lightcurves were joined at 150 km from half-light. The heavy dotted profile is the model profile without added noise.

Figure 4-18 The derived temperature profiles from the inversion of five noise samples added to the UVSbc synthetic lightcurve using two JARs for a total of ten lightcurves. All of these composite lightcurves were joined at 300 km from half-light. The heavy dotted profile is the model profile without added noise.

Figure 4-19 The derived temperature profiles from the inversion of five noise samples added to the UVSbc synthetic lightcurve using two JARs for a total of ten lightcurves. All of these composite lightcurves were joined at 450 km from half-light.

Figure 4-20 The derived temperature profiles from the inversion of five noise samples added to the UVSbc synthetic lightcurve using two JARs for a total of ten lightcurves. All of these composite lightcurves were joined at 600 km from half-light. Near 0.1-μbars the deviations from the model profile are quite large. This can be traced to the poor signal-to-noise for the parts of the composite lightcurves that were used to derive the temperatures.

Figure 4-11

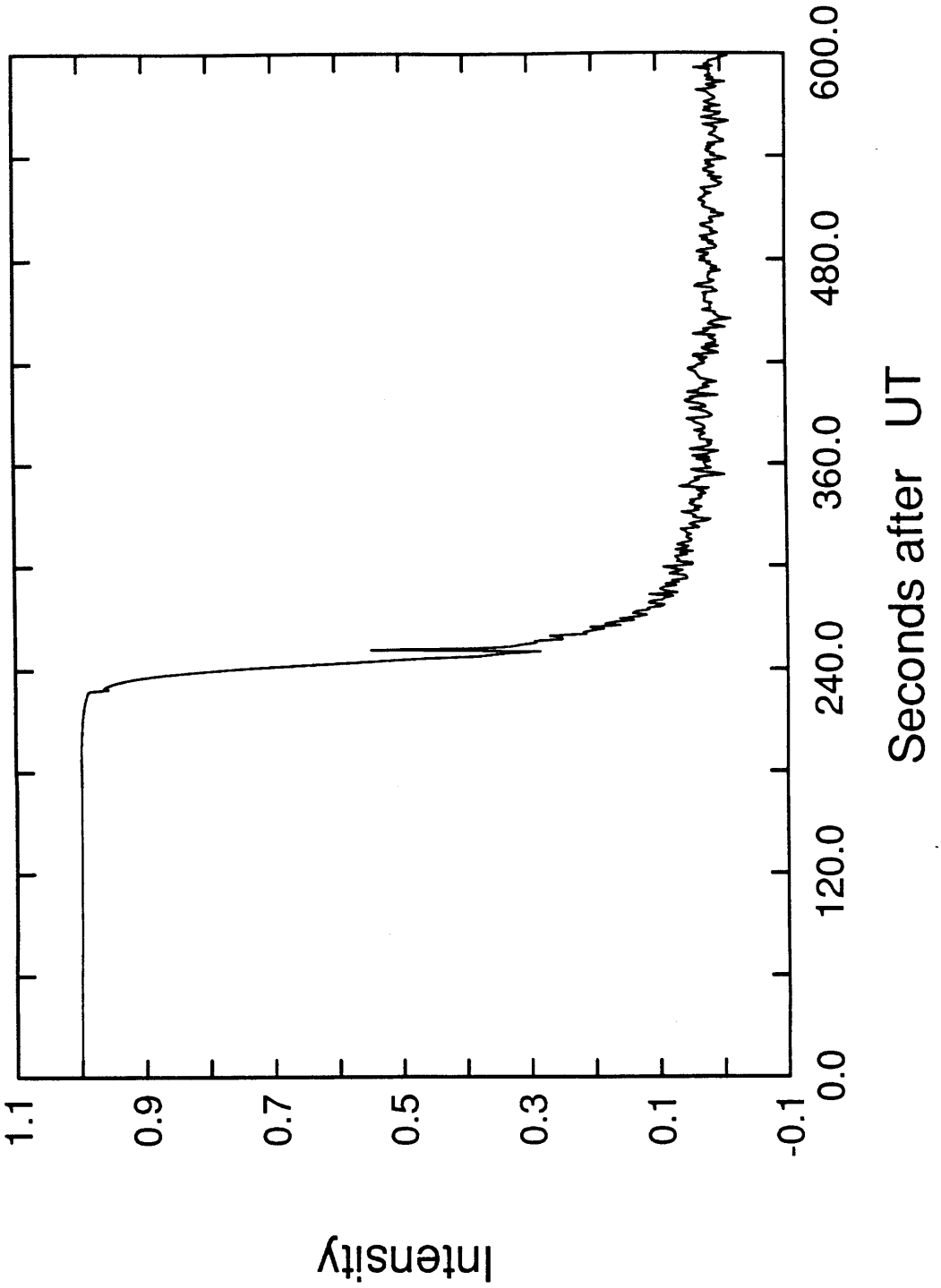
Intensity
1.1
0.9
0.7
0.5
0.3
0.1
-0.1
0.0
120.0
240.0
360.0
480.0
600.0
Seconds after UT

Chapter 4

Figure 4-12

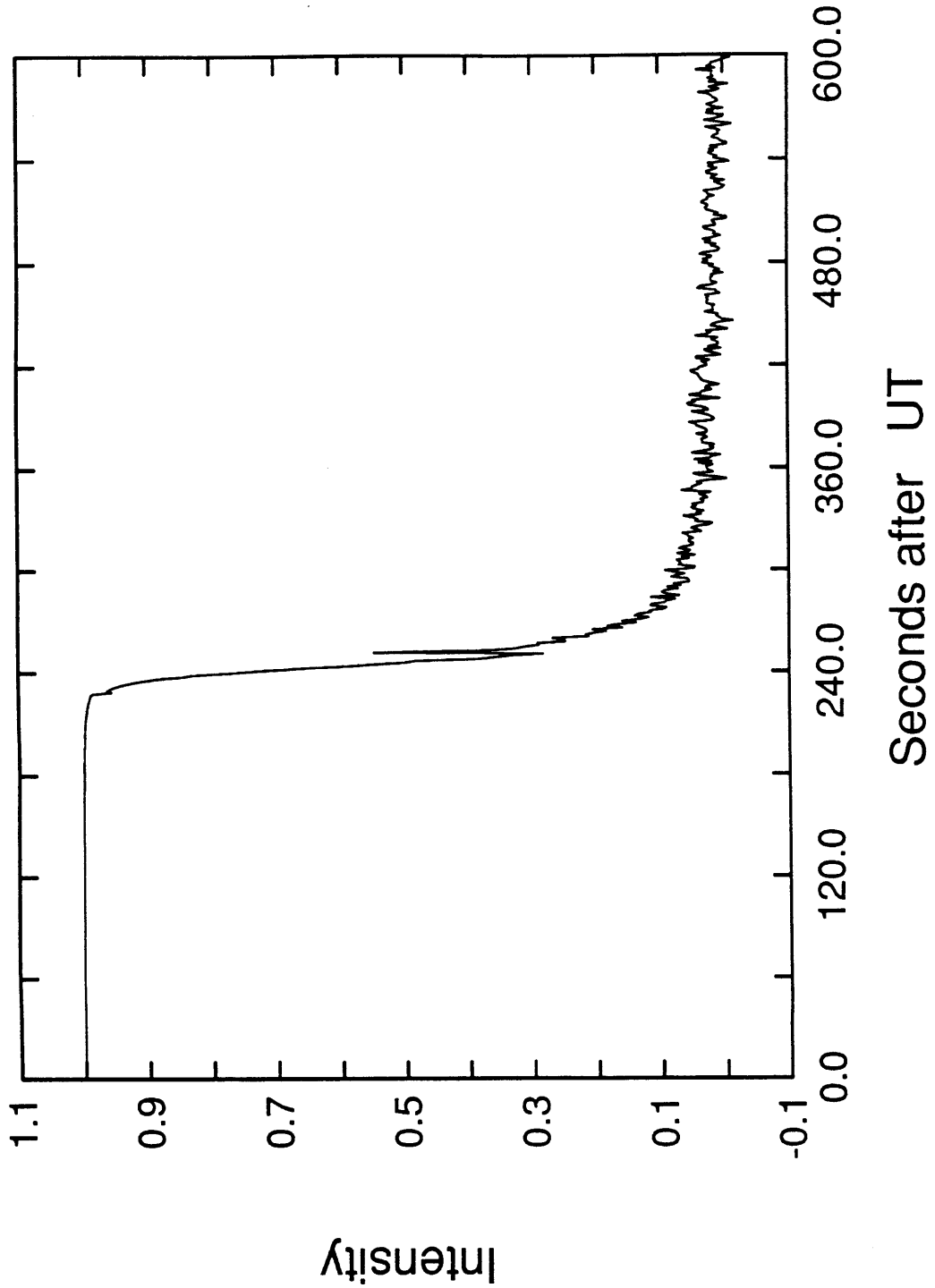

Figure 4-13

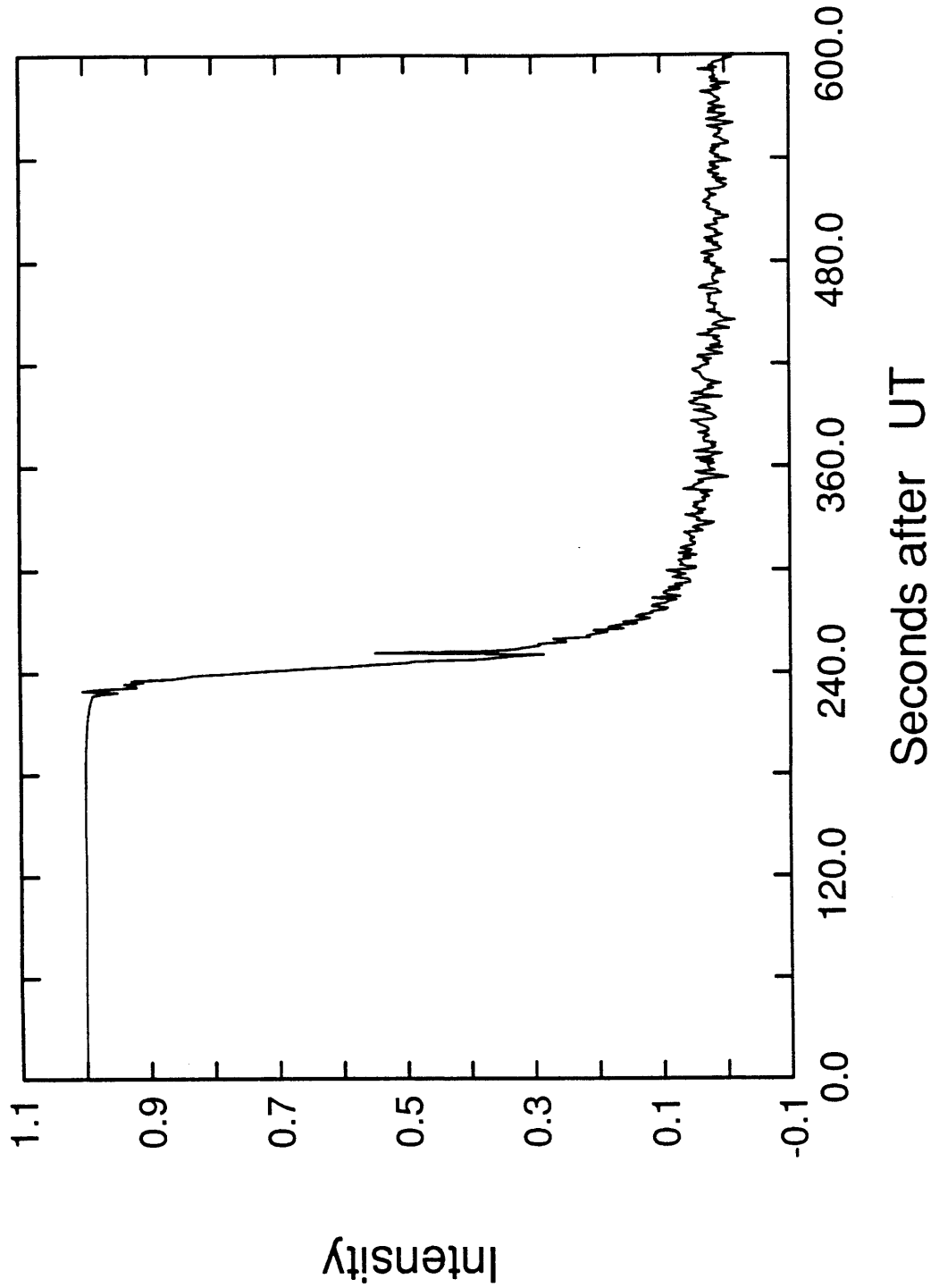
Intensity
1.1
0.9
0.7
0.5
0.3
0.1
-0.1
0.0
120.0
240.0
360.0
480.0
600.0
Seconds after UT

Figure 4-14

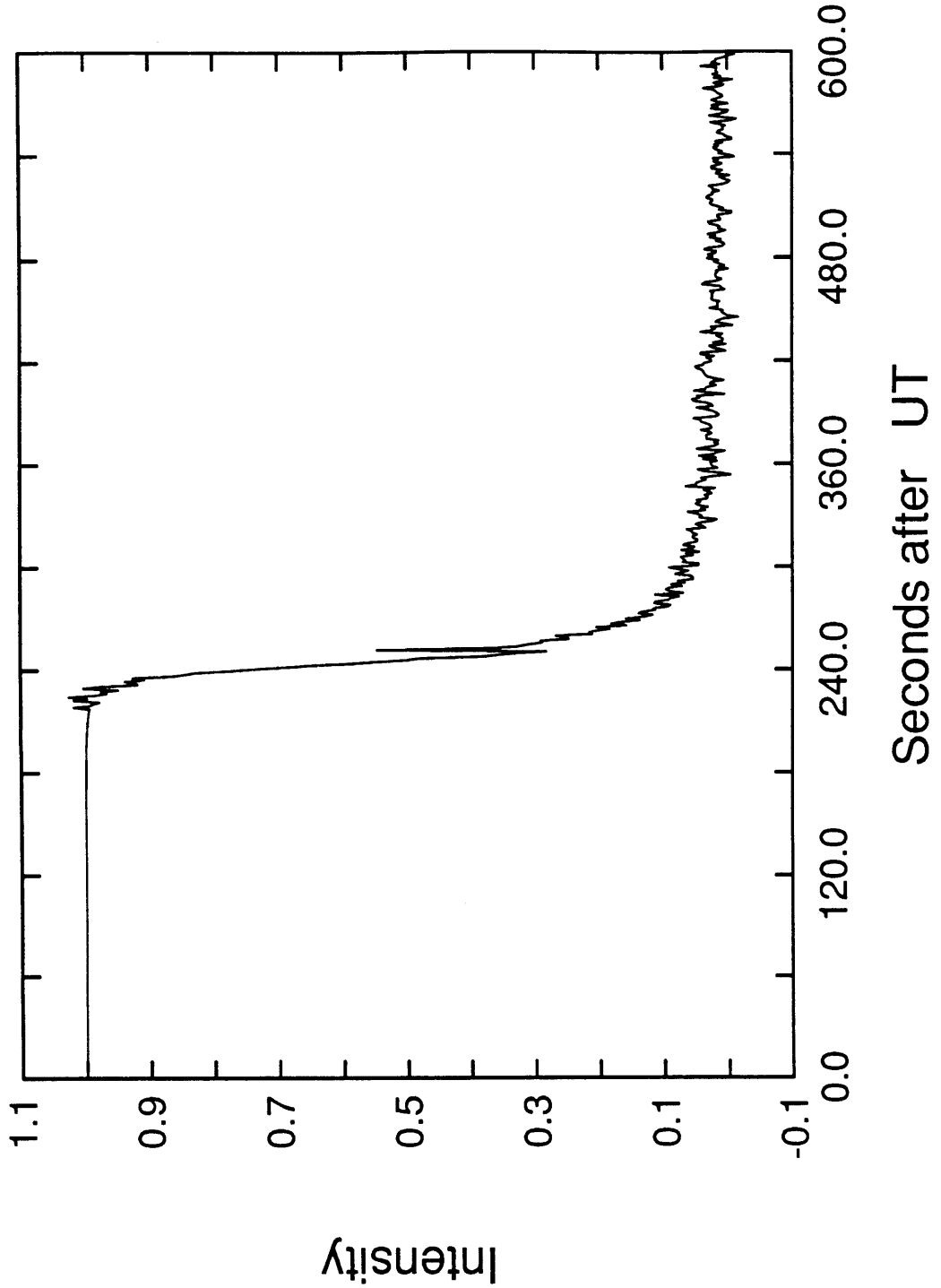
Intensity
1.1
0.9
0.7
0.5
0.3
0.1
-0.1
0.0
120.0
240.0
360.0
480.0
600.0
Seconds after UT

Figure 4-15

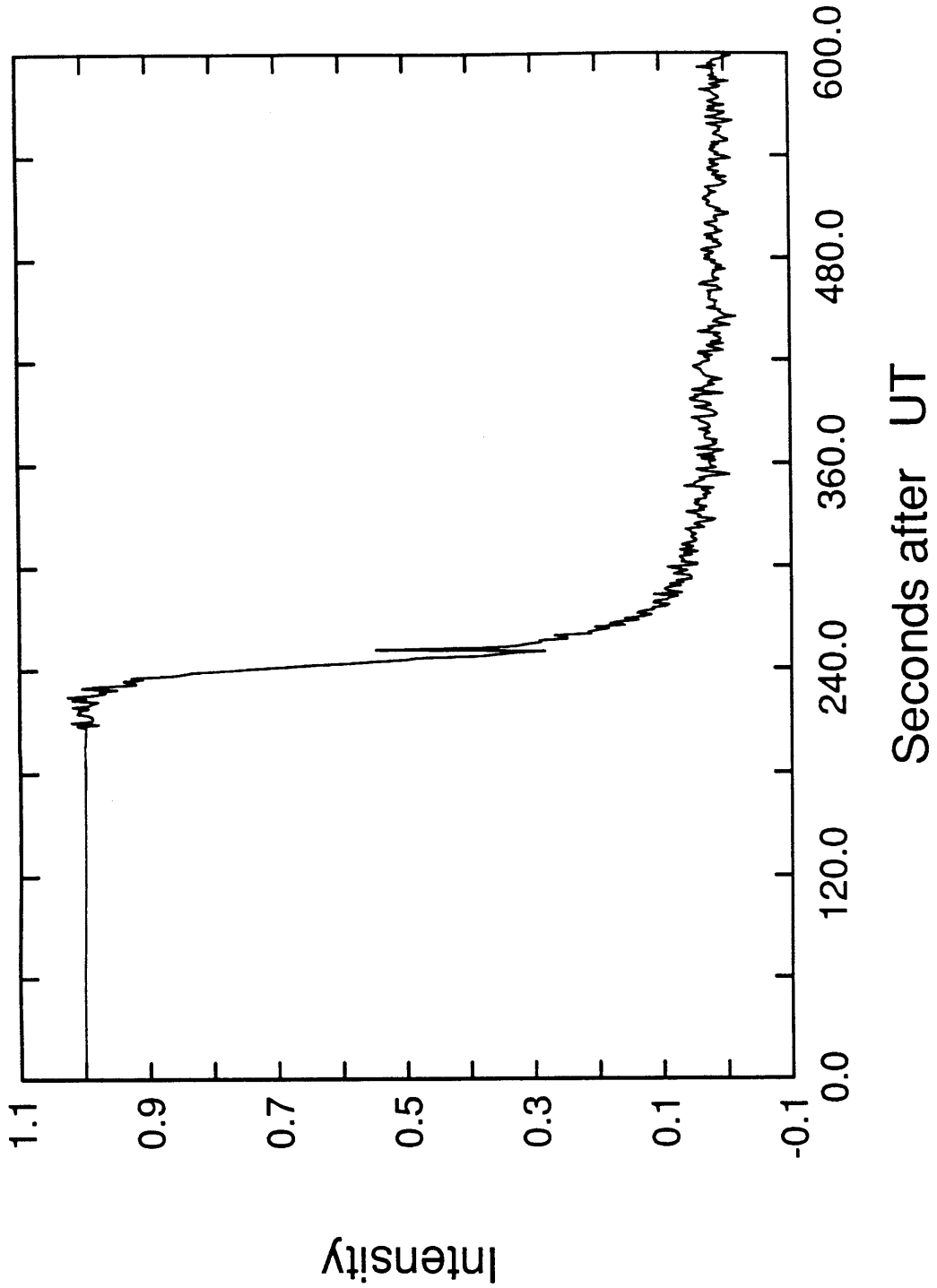
Intensity
1.1
0.9
0.7
0.5
0.3
0.1
-0.1
0.0
120.0
240.0
360.0
480.0
600.0
Seconds after UT

Figure 4-16

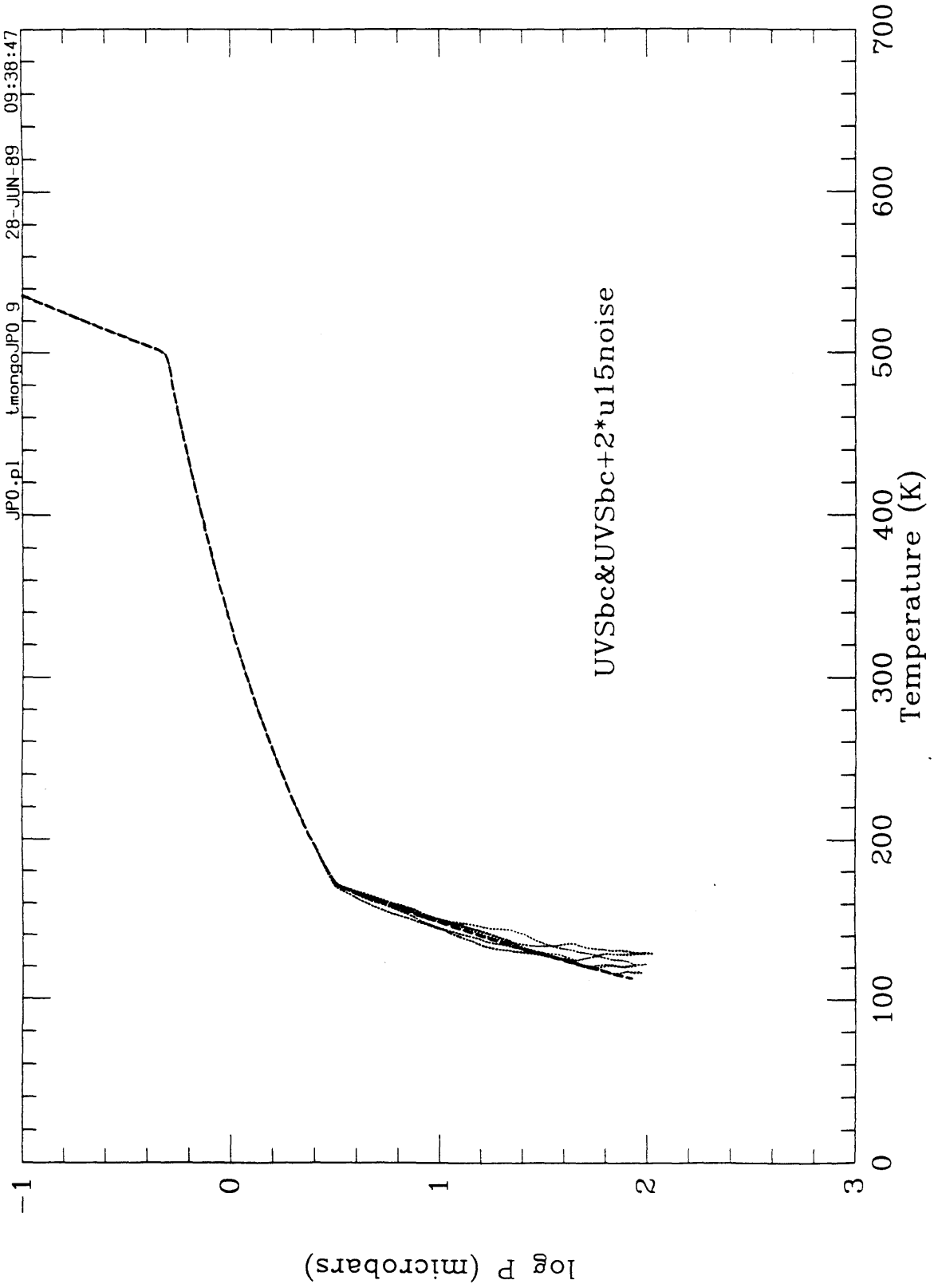
JP0.pl tmongoJP0 9
28-JUN-89 09:38:47
UVSbc&UVSbc+2*u15noise
Temperature (K)
log P (microbars)
0
100
200
300
400
500
600
700
-1
0
1
2
3

Figure 4-17

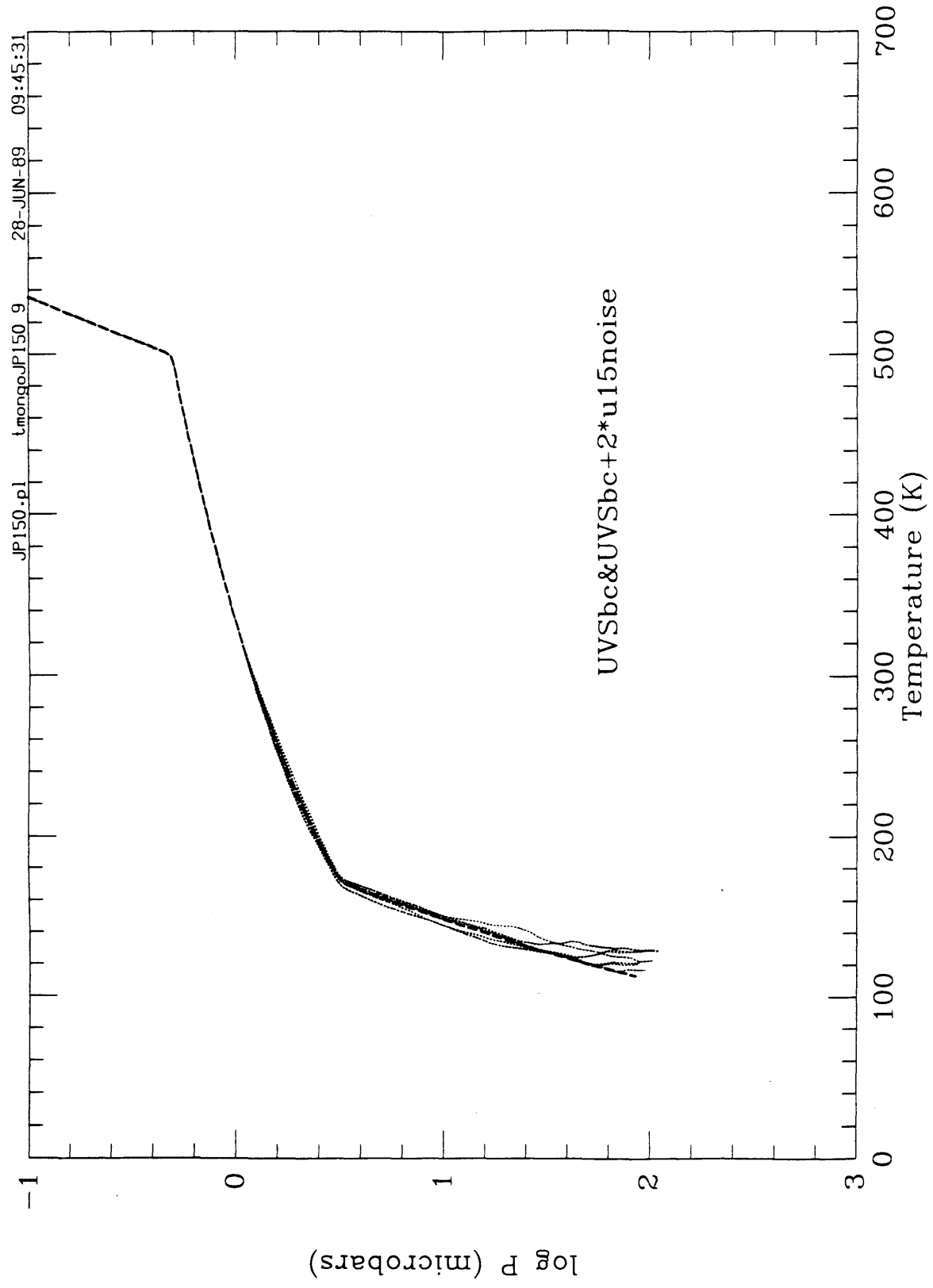
JP150.p1 tmongoJP150 9 28-JUN-89 09:45:31
UVSbc&UVSbc+2*u15noise
log P (microbars)
Temperature (K)
-1
0
1
2
3
0
100
200
300
400
500
600
700

Chapter 4

Figure 4-18

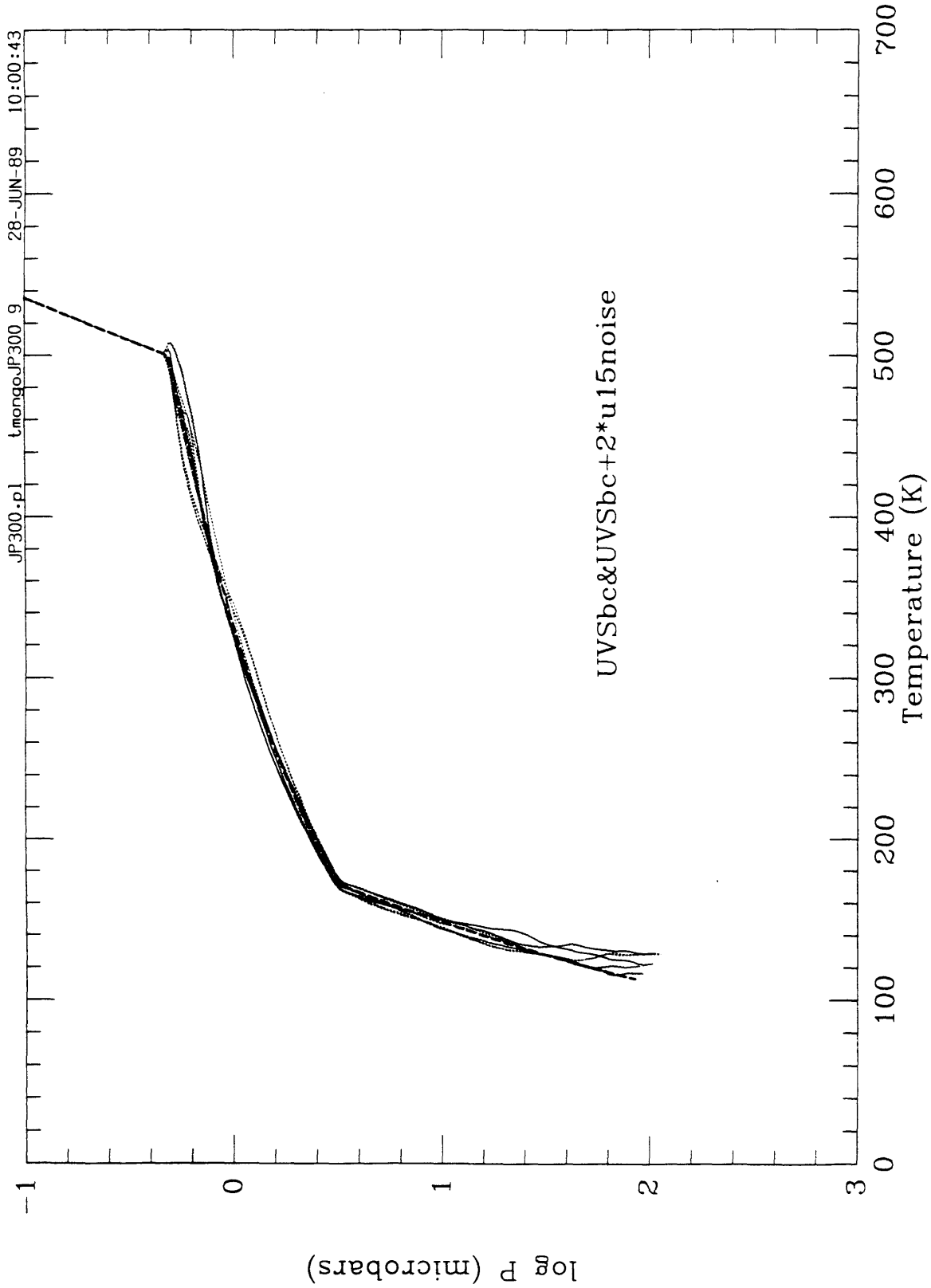

Figure 4-19

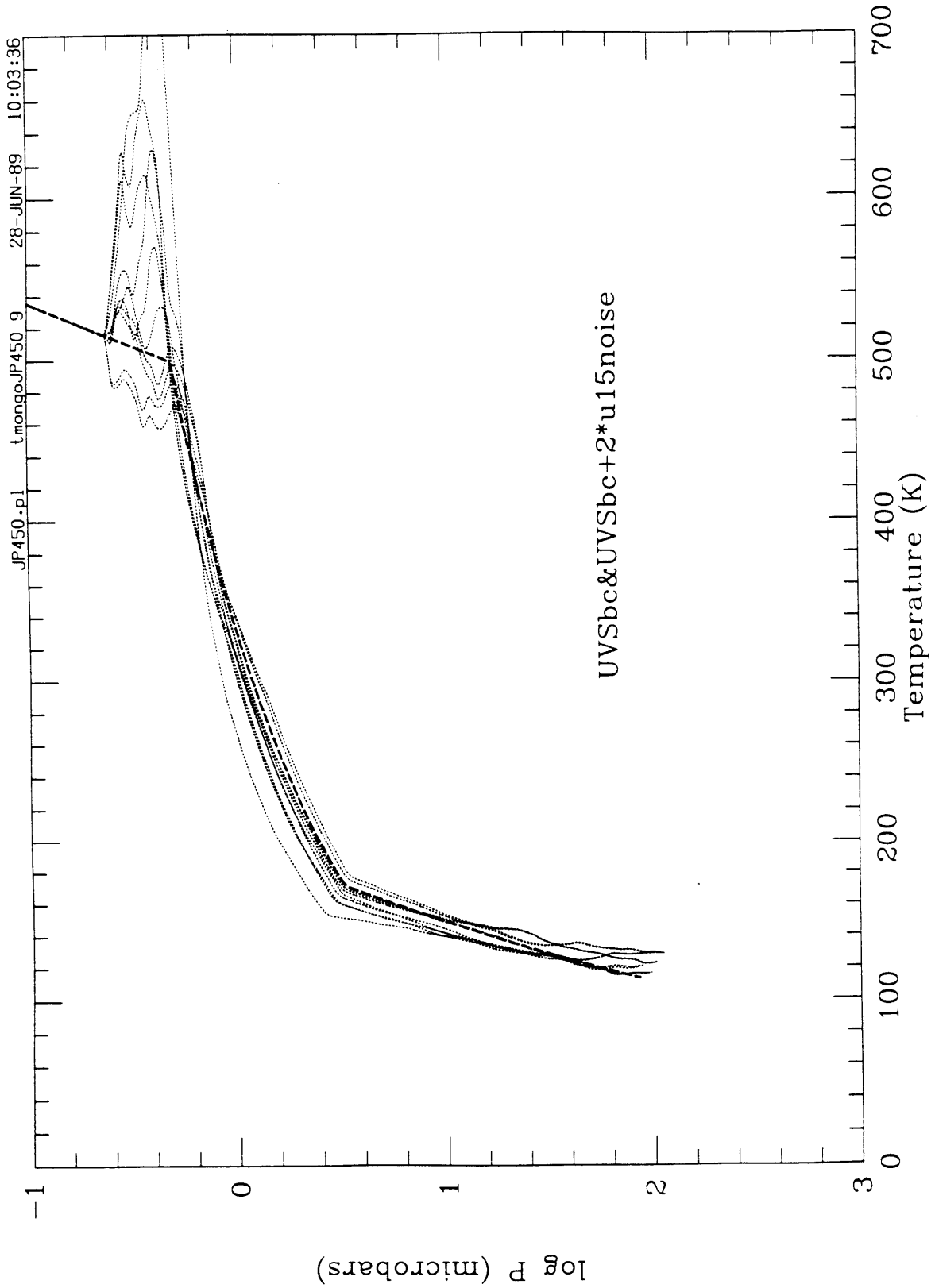
JP450.pl tmongoJP450 9 28-JUN-89 10:03:36
UVSbc&UVSbc+2*u15noise
log P (microbars)
Temperature (K)
-1
0
1
2
3
0
100
200
300
400
500
600
700

Figure 4-20

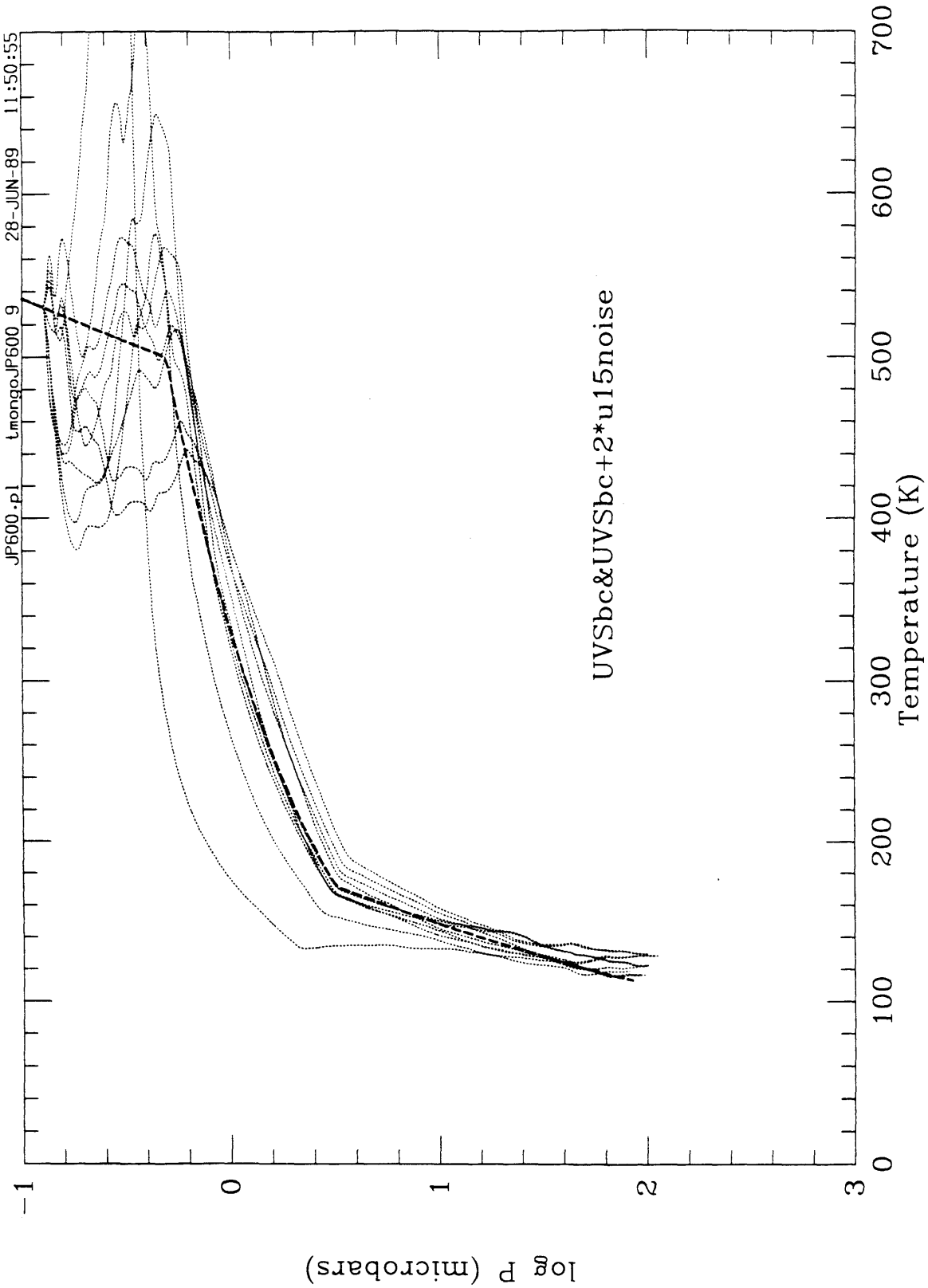
JP600.pl tmongoJP600 9 28-JUN-89 11:50:55
UVSbc&UVSbc+2*u15noise
Temperature (K)
log P (microbars)
0
100
200
300
400
500
600
700
-1
0
1
2
3

A low frequency component of the added noise will produce this type of temperature error at the high pressure end of the complete profile. This low frequency component may be seen in Figure 4-5, where we have displayed the noise averaged to 100 seconds per point, and the vertical scale has been expanded by a factor of 100 compared to Figure 4-4. Recall that for each synthetic data lightcurve, only a 600 second segment of the 1200 seconds of noise was used. The noise near the 300 km JP on the temperature-pressure profile, on the other hand, is caused by noise localized near that JP on the composite lightcurve. This effect may be seen more dramatically in the remaining two figures. Figure 4-19 (JP = 450) shows temperature errors of over 200 K near the JP; in Figure 4-20 these errors are even larger and propagate down the profile to higher pressures. Each synthetic data lightcurve at this JP that is inverted creates a new rather wildly deviating temperature error for these low pressure (high altitude) JPs. However, even in this case (JP = 600 km), with the exception of two outliers, the inverted profiles are within a narrow band about the model temperature profile once the large temperature gradient in the atmosphere begins. Referenced to the input synthetic data lightcurve, these deviations are caused by poor signal-to-noise on the upper baseline. To understand the signal and noise in more detail, we have used *s* (the sample standard deviation) as a noise measure (though approximate) in the two JARs and we will compare this with the signal available along the upper baseline of the synthetic ground-based model lightcurve. We note that the sample standard deviation is only exactly valid for Gaussian noise, but, we use it here for convenience with this limitation in mind, to obtain at least some approximation for the noise.

Recalling that the two JARs used in the noise analysis are at 300 km and 600 km from the half-light point along the path of observer and that they have a length of 250 km, the sample standard deviations for the first synthetic data lightcurve (Figure 4-4) produced are $s_{300} = 0.025$ and $s_{600} = 0.012$ respectively. The values of $(n_* - n_*\phi(t))/n_*$ averaged over the respective JARs for the model are $AVG_{300} = 0.025$ and $AVG_{600} = 0.0030$. Thus the signal-to-noise in the first case is $S/N_{300} = 0.98$ and in the second case it is $S/N_{600} =$

0.025. With such a low signal-to-noise at 600 km from half-light, the erratic behavior of the retrieved profiles is quite understandable. At 300 km and less from half-light, the signal-to-noise very rapidly improves to over 1.0 and results in the small temperature errors shown on the corresponding figures. The 450 km case is somewhere in between these values.

In the case of ground-based recorded lightcurves we will make a series of composite lightcurves with joints to the model ground-based lightcurve in the region where the upper baseline begins to rapidly fall off towards half-light. Here we have examined the effect of noise for JPs above and below this region. We estimate the fractional error in noise to be 1.5 to 2.0 percent, and a fractional error in the retrieved temperature is estimated at 5 to 7 percent (Figure 4-21). This gives a conservative amplification factor of the noise of 5 for that part of the lightcurve less than 300 km from half-light. The fractional eror in the retrieved pressure is shown in Figure 4-22. The overall character of the fractional error in pressure with altitude appears much different than for temperature; here, the values from the deepest part of the atmosphere are most affected by the noise. When analyzing a recorded ground-based lightcurve, we trade off the height in the atmosphere at which a joint can be made against the error in the retrieved profile.

4.7 Summary

We have developed a new method to retrieve temperature-pressure and temperature-altitude profiles from the region of Uranus' atmosphere where ground-based occultation measurements are most sensitive, but have been limited in their accuracy by the difficulty in choosing initial conditions indicative of the overlying atmosphere. This method of inversion capitalizes on the Voyager 2 UVS derived parameters to supply those initial conditions. A model synthetic ground-based lightcurve, based on UVS parameters, is substituted for the high altitude portion of a data lightcurve to form a composite lightcurve.

When the composite lightcurve is numerically inverted, the model atmosphere is retrieved first, forming an initial atmospheric layer or cap for the inversion.

A noise analysis that applies noise from the U15 Mount Stromlo occultation (French *et al.* 1987) to a model synthetic ground-based lightcurve has been performed. The noise in the retrieved temperature-pressure profile is related to the noise of the input lightcurve in a complex manner. This relationship has been documented in the form of a number of test cases that show the varying effect of the noise with distance from half-light.

Figure 4-21 The fractional temperature errors for five noise samples added to a UVSbc model synthetic lightcurve at 0, 150, and 300 km from half-light using two JARs and inverted to obtain retrieved temperatures. The fractional error is computed by subtracting the model temperature from the retrieved noise temperatures and dividing by the model temperature. The error curves are from a total of 30 inversions. The horizontal scale is depth in the atmosphere of Uranus from the half-light radius.

Figure 4-22 The fractional pressure errors for five noise samples added to a UVSbc model synthetic lightcurve at 0, 150, and 300 km from half-light using two JARs and subsequently inverted to obtain retrieved pressures. The fractional error is computed by subtracting the model pressure from the retrieved noise pressures and dividing by the model pressure. The error curves are from a total of 30 inversions. The horizontal scale is depth in the atmosphere of Uranus from the half-light radius.

Figure 4-21

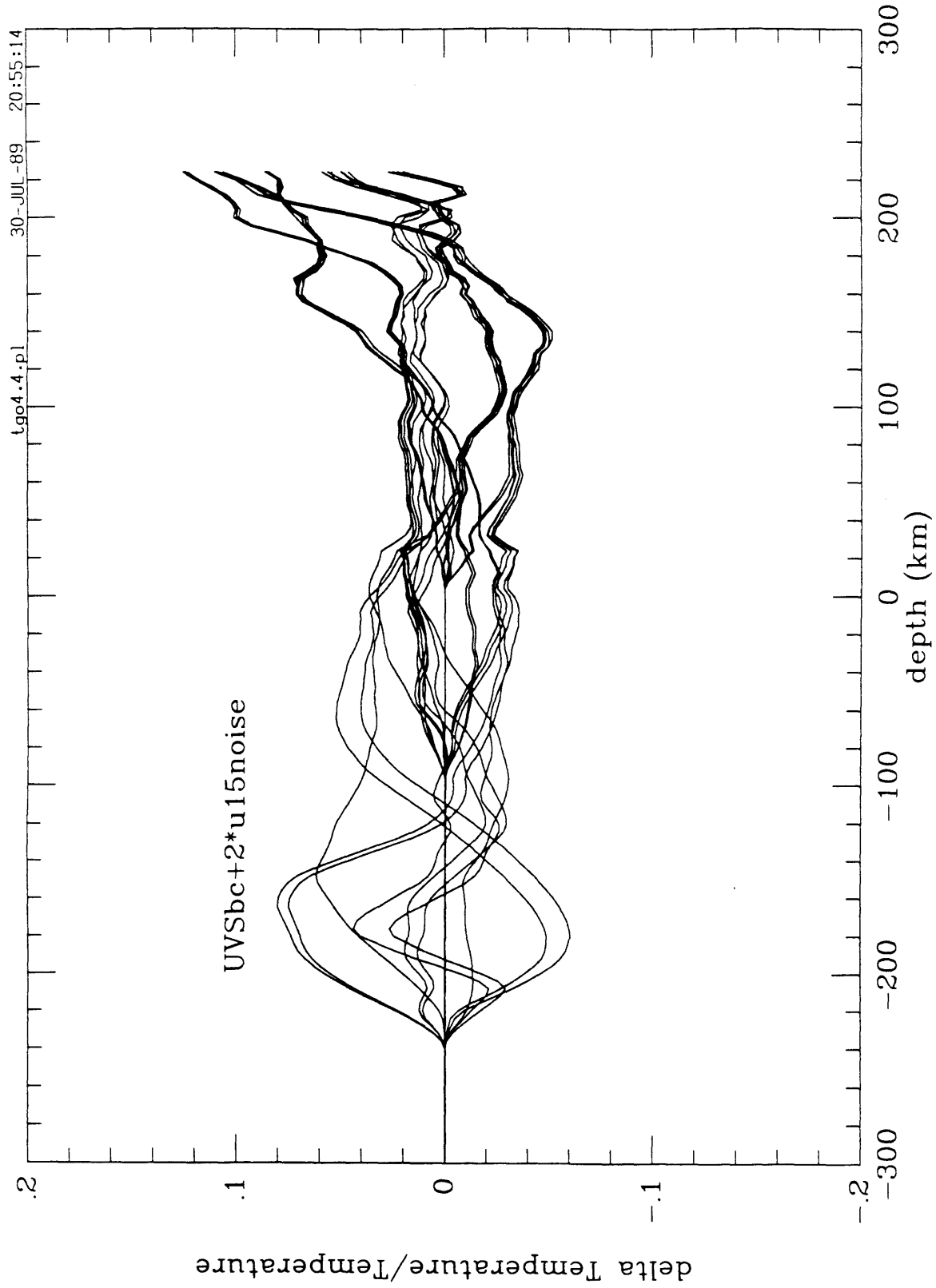
tgo4.4.pl
30-JUL-89 20:55:14
UVSbc+2*u15noise
delta Temperature/Temperature
depth (km)
.2
.1
0
-.1
-.2
300
200
100
0
-100
-200
-300

Figure 4-22

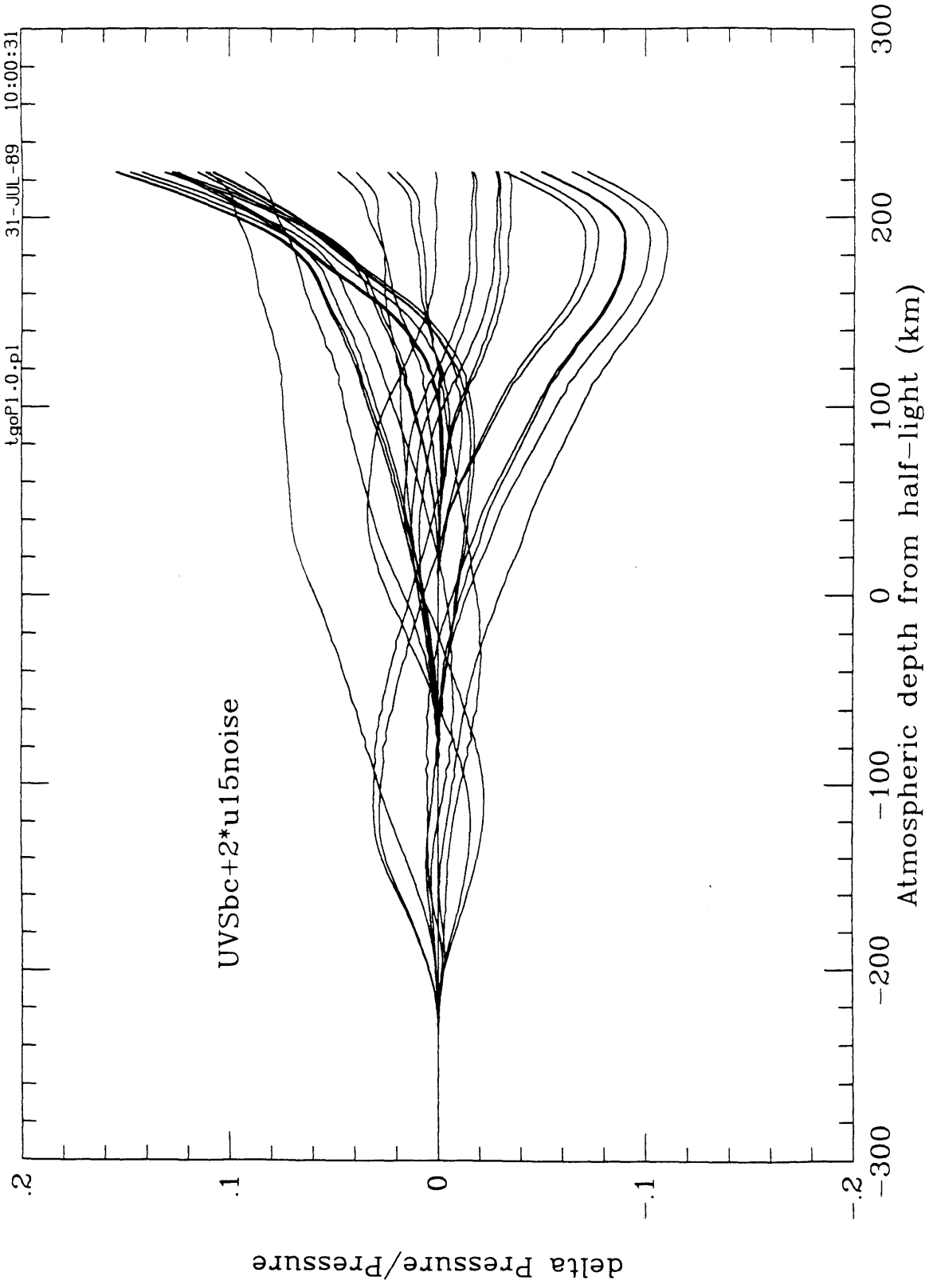
tgoP1.0.p1
31-JUL-89 10:00:31
UVSbc+2*u15noise
delta Pressure/Pressure
.2
.1
0
-.1
-.2
-300
-200
-100
0
100
200
300
Atmospheric depth from half-light (km)

References

BARON, R. L., R. G. FRENCH, AND J. L. ELLIOT (1989). The oblateness of Uranus at the 1-μbar level. *Icarus* **77**, in press.

BAUM, W. A., AND A. D. CODE (1953). A photometric observation of the occultation of σ Arietis by Jupiter. *Astron. J.* **58**, 108-112.

DUNHAM, E., J. L. ELLIOT, AND P. J. GIERASCH (1980). The upper atmosphere of Uranus: Mean temperature and temperature variations. *Astron. J.* **235**, 274-284.

ELLIOT, J. L., E. W. DUNHAM, AND D. J. MINK (1977). The rings of Uranus. *Nature* **267**, 328-330.

ELLIOT, JAMES L., EDWARD DUNHAM, AND DOUGLAS MINK (1980). The radius and ellipticity of Uranus from its occultation of SAO 158687. *Astron. J.* **236**, 1026-1030.

FRENCH, R. G., J. L. ELLIOT, AND P. J. GIERASCH (1978). Analysis of stellar occultation data: Effects of photon noise and initial conditions. *Icarus* **33**, 186-202.

FRENCH, R. G., T. J. JONES, AND A. R. HYLAND (1987). The 1 May 1982 stellar occultation by Uranus and the rings: Observations from Mount Stromlo Observatory. *Icarus* **69**, 499-505.

HERBERT, F., B. R. SANDEL, R. V. YELLE, J. B. HOLBERG, A. L. BROADFOOT, AND D. E. SHEMANSKY (1987). The upper atmosphere of Uranus: EUV occultations observed by Voyager 2. *J. Geophys. Res.* **92**, 15093-15109

HANEL, R., B. CONRATH, R. M. FLASAR, V. KUNDE, W. MAGUIRE, J. PEARL, J. PIRRAGLIA, R. SAMUELSON, D. CRUIKSHANK, D. GAUTIER, P. GIERASCH, L. HORN, AND P. SCHULTE (1986). Infrared observations of the Uranian system. *Science* **233**, 70-74.

HUNTEN, D. M., AND J. VEVERKA (1976). Stellar and spacecraft occultations by Jupiter: A critical review of derived temperature profiles. *Jupiter* (T. Gehrels, Ed). pp. 247-283 Univ. of .Arizona Press, Tucson.

SICARDY, B, M.COMBES, A. BRAHIC, P. BOUCHET, C. PERRIER, R. COURTIN (1982). The 15 August 1980 occultation by the Uranian system: Structure of the rings and temperature of the upper atmosphere *Icarus* **52**, 454-472.

WASSERMAN L., AND J. VEVERKA (1973). On the reduction of occultation light curves. *Icarus* **20**, 322-345.

Chapter 5

New Uranian Atmospheric Temperatures: KME 15 and KME 17 Atmospheric Profiles with Voyager 2 EUV Initial Conditions

5.1 Introduction

Temperature profiles of the Uranian upper atmosphere are one of the primary inputs necessary to acquire an understanding of the physics taking place there. For Uranus, a major unsolved problem is the nature of the heating and cooling of the upper atmosphere implied by these temperature profiles. We endeavor to present a more accurate picture of the temperature structure based on ground-based data from stellar occultations.

The new analysis method presented in the last chapter has been applied in the reanalysis of data lightcurves from the Uranian stellar occultations of 1 May 1982 (KME 15) and 25 March 1983 (KME 17). The four atmospheric lightcurves in these occultations are among those with the highest signal-to-noise of all Uranian events analyzed and reported.

The 1 May 1982 observation (French *et al.* 1987) took place at the Mt. Stromlo observatory in Australia. The occultation was observed in the infrared at a wavelength of 2.2 μm with a bandwidth of 0.4 μm and was recorded on magnetic tape. The 25 March 1983 occultation (Elliot *et al.* 1987) observation took place at the SAAO (South African Astronomical Observatory) and also was observed at a 2.2 μm wavelength (standard K filter) and recorded on magnetic tape.

5.2 Analysis of Data

Before applying our method of analysis, we subtracted a background slope of 0.5452 counts per second from the KME17 data, including both the immersion and emersion lightcurve. No slope was removed from the KME15 data. From a length of data somewhat greater than that used in previous reported isothermal fit analysis, each lightcurve was analyzed with an isothermal model fit to determine the half-light times, scale height, stellar flux and background flux. Table 5-1 lists the values determined under the heading "from isothermal fit." The quantities found here differ only slightly from those reported in the respective published papers. For the purpose of uniformity in future analysis, we report the lengths of data used, computed along the path of observer. The length equals approximately 10,000 km; less data were used if noise or data availability dictated. Half-light is located in this data segment.

The analysis method presented in the last chapter is used to numerically invert the lightcurves. We used an UVS best compromise model synthetic lightcurve to simulate an initial known atmospheric layer. A ground-based recorded lightcurve rapidly deteriorates in signal-to-noise with altitude above the approximate pressure level of 1.0 to 0.2-μbar, where the signal corresponds to the change in intensity of the unacculted source. The portion of the ground-based recorded lightcurve above this level has been replaced by the corresponding portion of the model synthetic lightcurve.

Background and stellar flux levels found from isothermal fits to the data lightcurves were used to scale the flux intensities of the data to the model lightcurve. The half-light time also found from the isothermal fit was used to match the altitude scales between the data and model (see previous chapter). The scaling was incrementally changed by using the ratio of local averages determined in respective JARs (joint averaging regions, Figure 4-2 previous chapter) for the model and data. Each JAR is a 200 to 600 km region located close

Table 5-1

Analysis Parameters

PARAMETER	KME15im	KME15em	KME17im	KME17em
recorded data				
slope rmvd (cts /sec)	0	0	0.5452	0.5452
from isothermal fit				
data Δtime (sec/bin)	1.0	1.0	1.0	1.0
data start UT	16:37:28.0	17:06:47.00	2:09:18.00	2:42:38.00
data end UT	16:47:28.0	17:16:47.00	2:35:58.00	3:15:58.00
half-light UT	16:41:40.55	17:12:39.85	2:14:42.30	3:04:51.32
half-light wrt. file start (sec)	252.55	352.85	324.30	1333.33
half-light radius (if at equator) km	26071	26071	26071	26071
scale height /$v_\perp$ (sec)	4.00	3.94	35.69	31.90
bkg flux (cts/sec)	1398902.0	1427558.5	58951.88	58654.14
star flux (cts/sec)	3833343.8	3810420.5	10721.66	10851.99
from astrometry (Earth-Uranus) Dist. (km)	$2.68 \times 10^{+9}$	$2.68 \times 10^{+9}$	$2.76 \times 10^{+9}$	$2.76 \times 10^{+9}$
$v_\perp$ (km/sec)	15.12	15.09	1.96	1.96
model atmos	UVSbc	UVSbc	UVSbc	UVSbc
Δradius (km.)	4.0	4.0	4.0	4.0
n_radial_incr	1000	1000	1000	1000
†lgth lightcurve (km)	9072	9054	9800	9800
n_lc_incr	600	600	5000	5000
Δtime (sec)	1.0	1.0	1.0	1.0
half-light (iso-fit mdl file strt) (sec)	247.05	352.47	1905.72	3094.26

Table 1 cont.

$\nu_{STP2.2}$ (H_2)	1.3595×10^{-4}	1.3595×10^{-4}	1.3595×10^{-4}	1.3595×10^{-4}
Composite lightcurve				
JAR1--				
*l_s, l_e (km)	325, 925	325, 925	200, 400	200, 400
Avg_{mdl}	0.9965	0.9962	0.9689	0.9683
Avg_{data}	5217636.8	5222526.1	69240.2	69294.8
JAR2--				
*l_s, l_e (km)	925, 1525	925, 1525	400, 600	400, 600
Avg_{mdl}	0.99967	0.99963	0.9949	0.9949
Avg_{data}	5229498.8	5235761.4	69575.0	60400.2
*JP1 (km)	620	620	0	0
*JP2 (km)	1225	1225	300	300
*JP3 (km)	–	–	600	600
Inversion				
mean mass per molecule (amu)	2.0	2.0	2.0	2.0
$\nu_{STP2.2}$ (H_2)	1.3595×10^{-4}	1.3595×10^{-4}	1.3595×10^{-4}	1.3595×10^{-4}

* Distance from half-light point along the path of observer, positive distances are towards greater Uranian radii.
† Distance along path of observer.
Path of observer is defined as the perpendicular to the limb of the planet at the point that the star occults, and at the distance of the observer from the planet.

to, and may include, the point where the model and data lightcurves join. This procedure substantially discriminates against any low frequency noise that exists in the data lightcurve before immersion or after emersion. Low frequency noise that does occur during immersion (or emersion) will have much less effect on the retrieved temperature profiles (see last chapter).

From the data lightcurves and the UVS best compromise synthetic ground-based lightcurve, composite lightcurves were made. The criteria used to join the curves were varied to determine the effects of noise on the analysis. Figures 5-1 to 5-4 show the composite lightcurves for a typical joint criterion for KME15 immersion, KME15 emersion, KME17 immersion, and KME17 emersion, respectively; these curves also give an indication of the relative noise present in these observations.

The composite lightcurves were numerically inverted with the geometric and atmospheric parameters shown in Table 5-1. A mean mass per molecule of 2.0 (amu) is used for the upper atmosphere part of the model and for the inversion. This allows recovery of the model atmosphere before the recorded data part of the composite lightcurve is inverted (see previous chapter for further discussion). For each atmospheric event, retrieved temperature profiles are shown in Figures 5-5 through 5-8. The panel on the right-hand side of each figure shows the stellar flux intensity as a function of pressure in the atmosphere of Uranus and facilitates comparison between lightcurve features and the results of numerical inversion.

5.3 Treatment of Noise

For the case of KME 15, the noise has been formally treated in the previous chapter by taking a representative segment of upper baseline noise and adding it to a model

Figure 5-1 Composite Lightcurve - UVSbc model and KME 15 immersion. The joint has zero added offset, and is at 625 km from half-light along the path of the observer. The JAR (joint averaging region) is located at 600 km and is 600 km in length.

Figure 5-2 Composite Lightcurve - UVSbc model and KME 15 emersion. The joint has zero added offset, and is at 625 km from half-light along the path of the observer. The JAR is located at 600 km and is 600 km in length.

Figure 5-3 Composite Lightcurve - UVSbc model and KME 17 immersion. The joint has zero added offset, and is at 600 km from half-light along the path of the observer. The JAR (joint averaging region) is located at 500 km and is 200 km in length.

Figure 5-4 Composite Lightcurve - UVSbc model and KME 17 emersion. The joint has zero added offset, and is at 600 km from half-light along the path of the observer. The JAR is located at 500 km and is 200 km in length.

Chapter 5

Figure 5-1

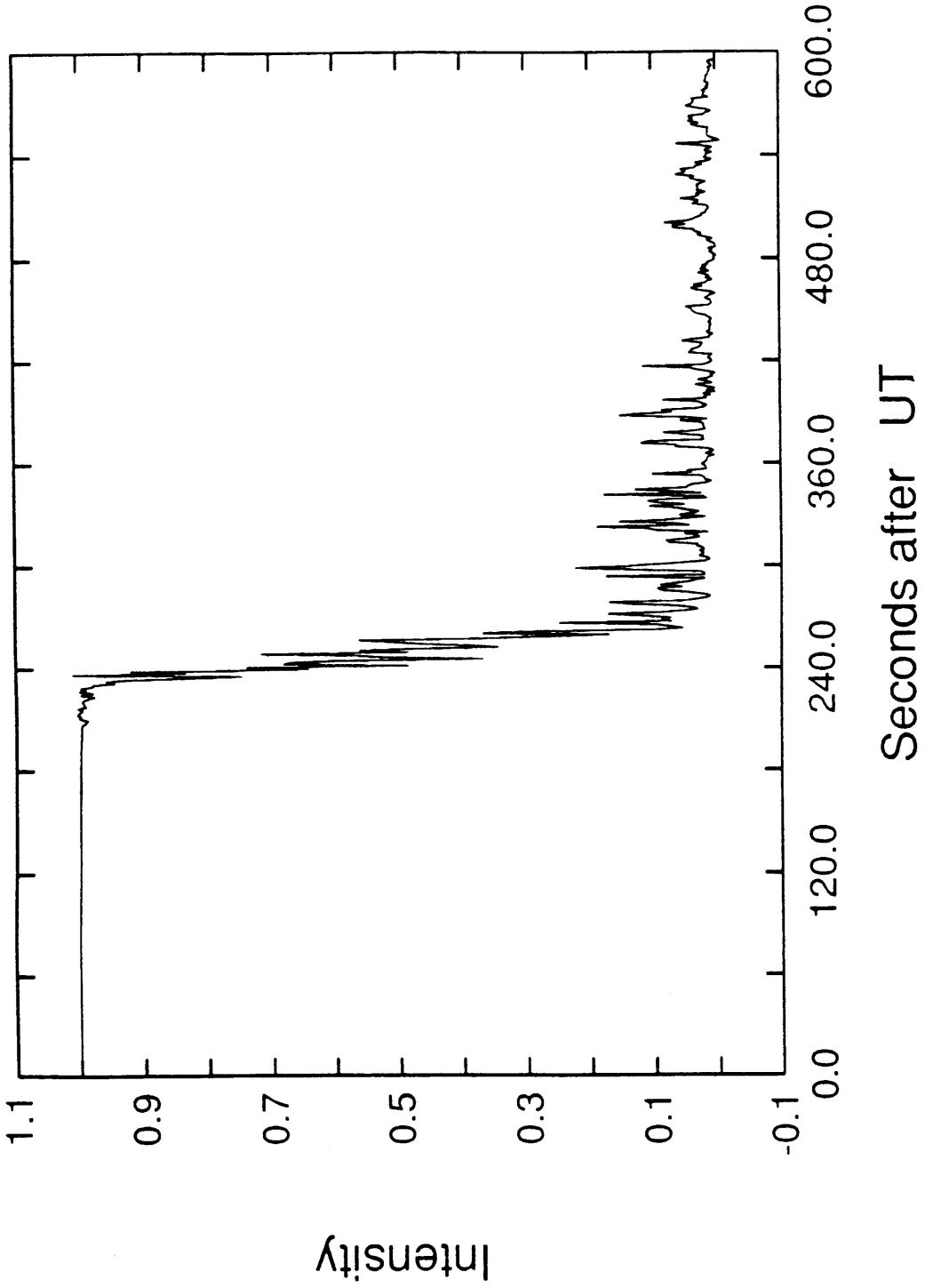

Chapter 5

Figure 5-2

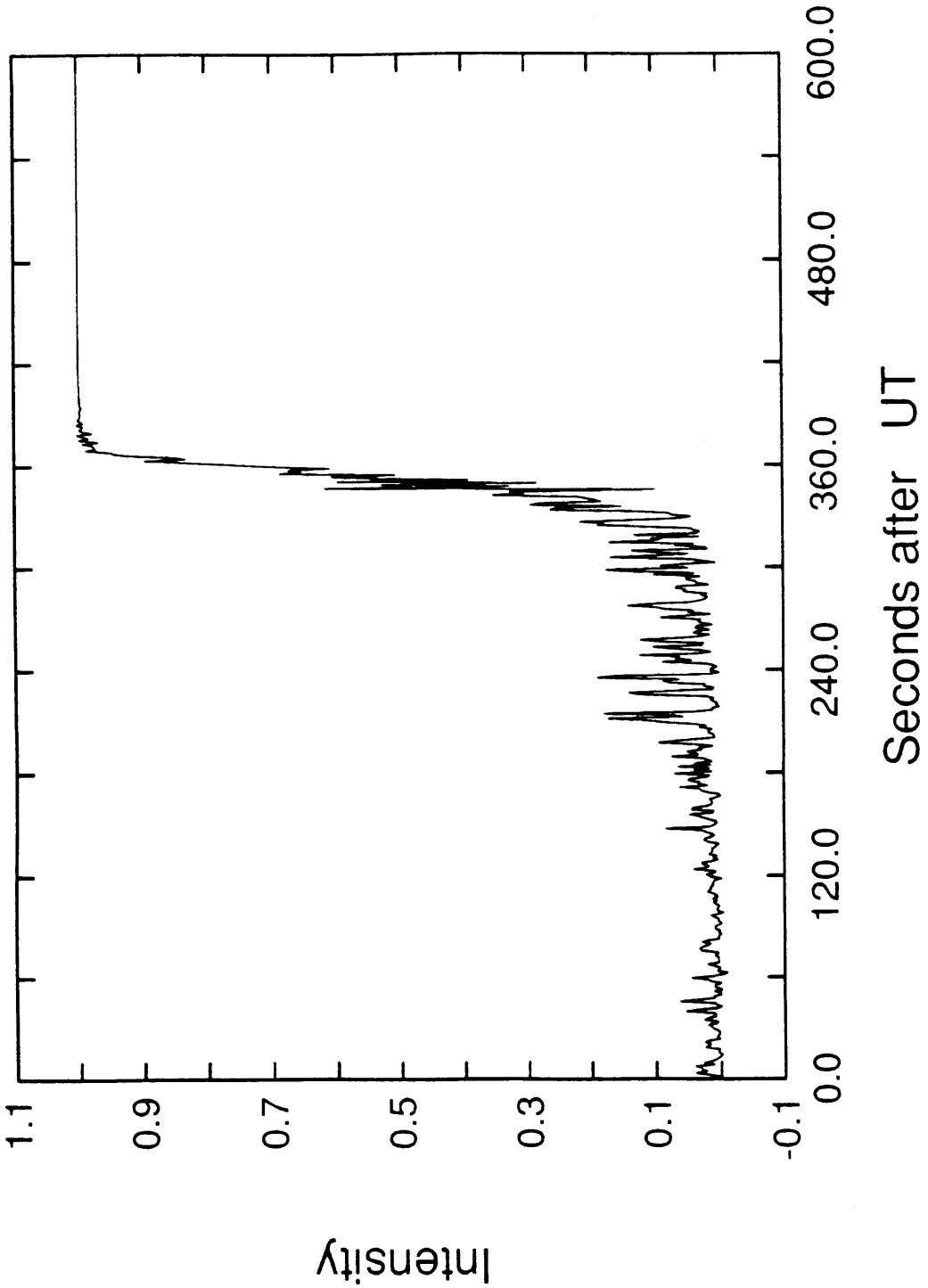

Chapter 5

Figure 5-3

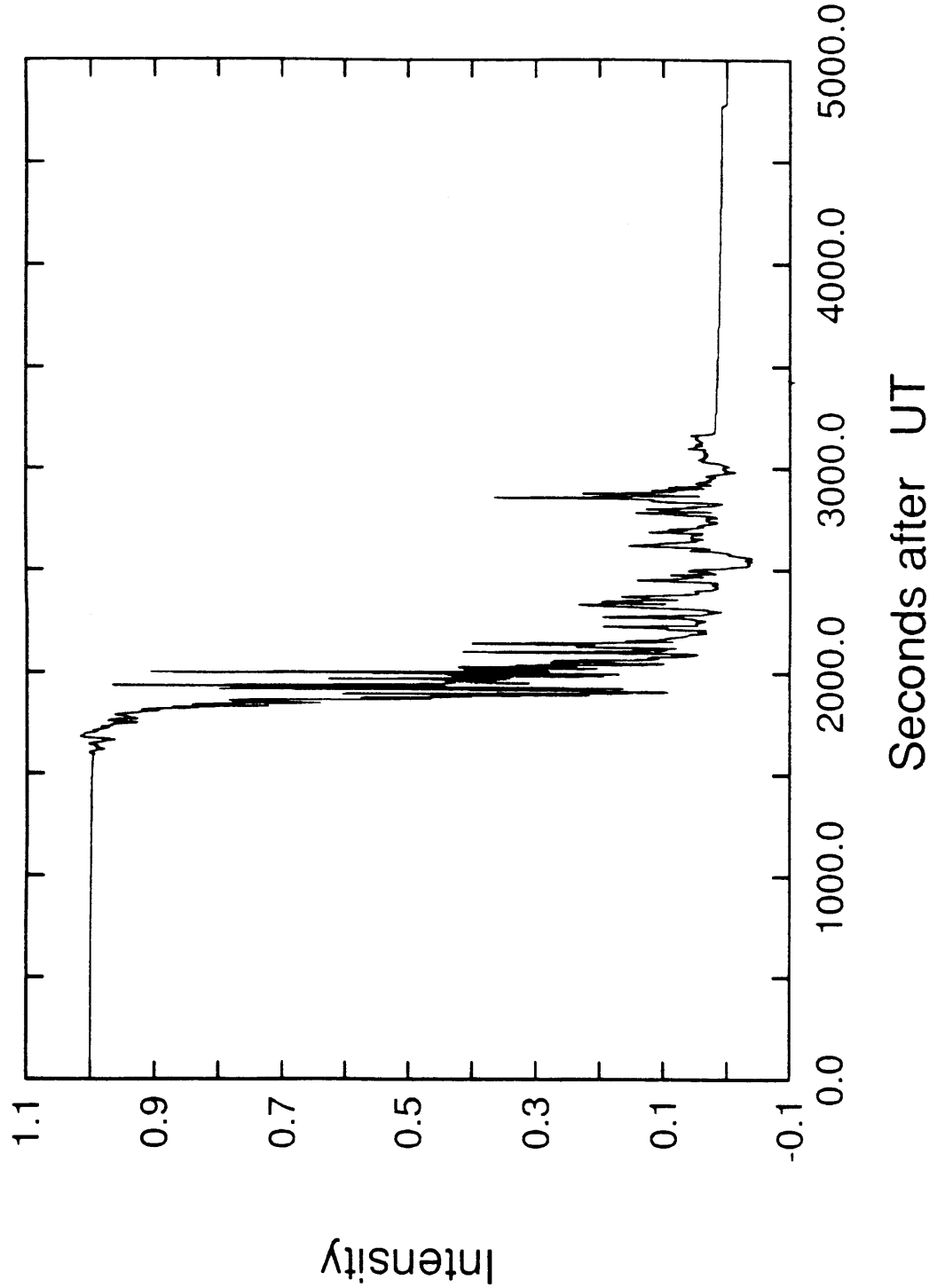

Chapter 5

Figure 5-4

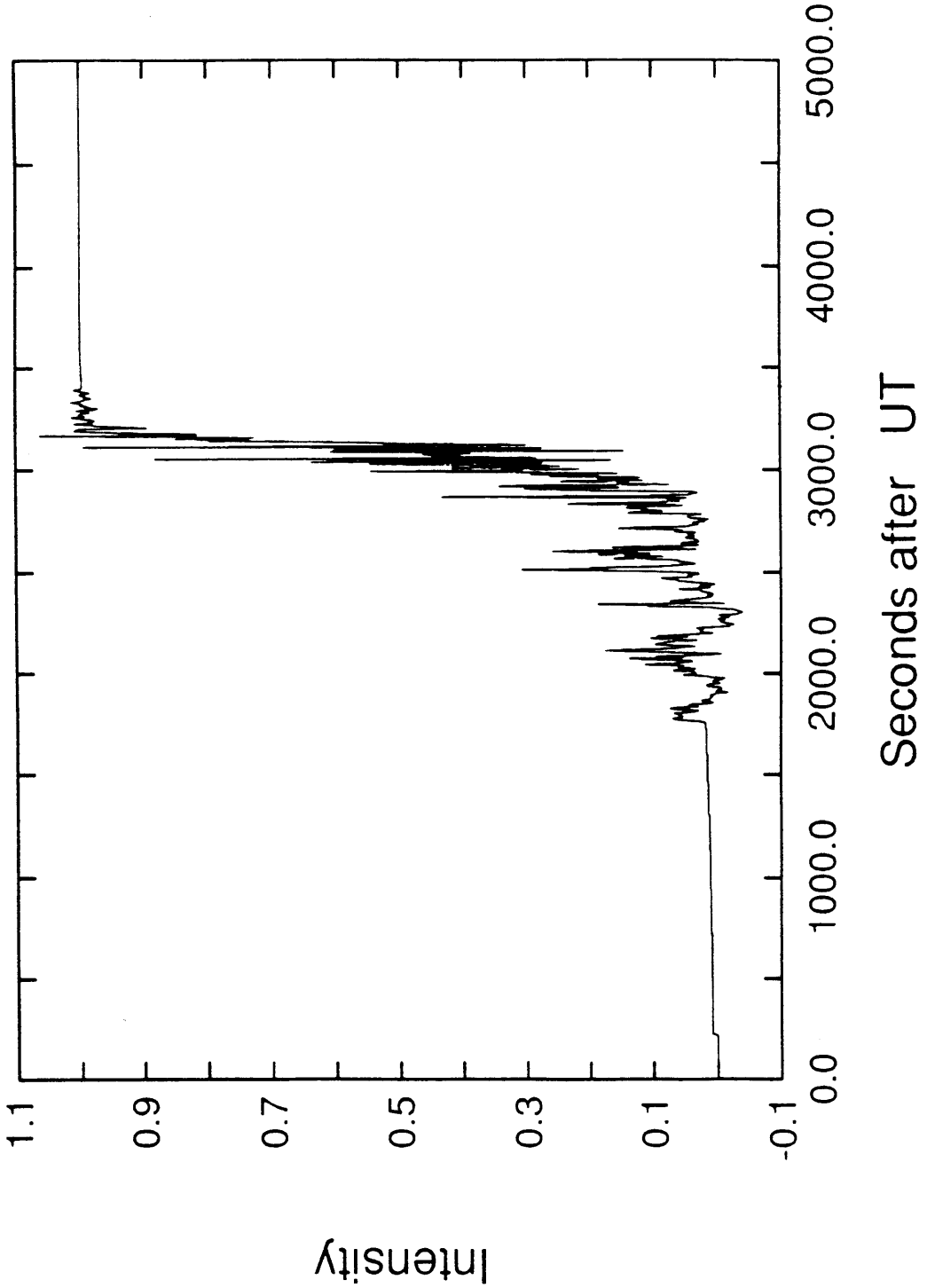

lightcurve to determine the error introduced in the derived temperature-pressure and temperature-radius profiles. Figure 4-21 of the previous chapter shows the result of this procedure in terms of the fractional error in the derived temperatures as a function of the distance in the atmosphere calculated from the half-light radius. For the four lightcurves analyzed here, we have in addition made the approximation that the noise is Gaussian and used the sample standard deviation s as a measure. The scaling factor determined from the JARs (above) was multiplied by $(1 \pm s)$ to obtain two slightly different factors, each of these new scaling factors was used to generate a set of composite lightcurves. Also, with the upper baseline joint to the synthetic model lightcurve fixed, the scaling factor was multiplied by $(1 \pm s)$ to effectively offset the lower baseline by $\pm s$. This gave an indication of the effect the noise could have on the temperature in the lower atmosphere part of the retrieved temperature profile.

5.4 Results from the Inversions

The temperature-pressure profiles have the following features that will be discused in more detail as they apply to each inversion:

Starting in the region from 0.1 to approximately 0.5-μbar, each profile (e.g., Figure 5-5) recovers the input determined by the UVS best compromise model (model temperatures show as a straight line from lower pressures and terminate at joint point). For pressures less than approximately 0.2-μbar, the temperature slowly increases from near 500 K, as determined by the UVSbc model. In the next region, from approximately 0.5 to 2.5-μbar, the recorded ground-based data now determine the profile, and a temperature gradient from approximately 500 K to around 150 K is present. From approximately 2.5 to 10-μbar, an isothermal region with a temperature near 150 K appears in three of the four inversions

Figure 5-5 Temperature-pressure profile of KME 15 immersion. On the left panel, the band of dashed profiles represents the inversion, and the width a formal error (see text). The right panel is the composite lightcurve plotted as a function of pressure.The bold profile is the previously reported inversion of this event (French *et al.* 1987).

Chapter 5

Figure 5-5

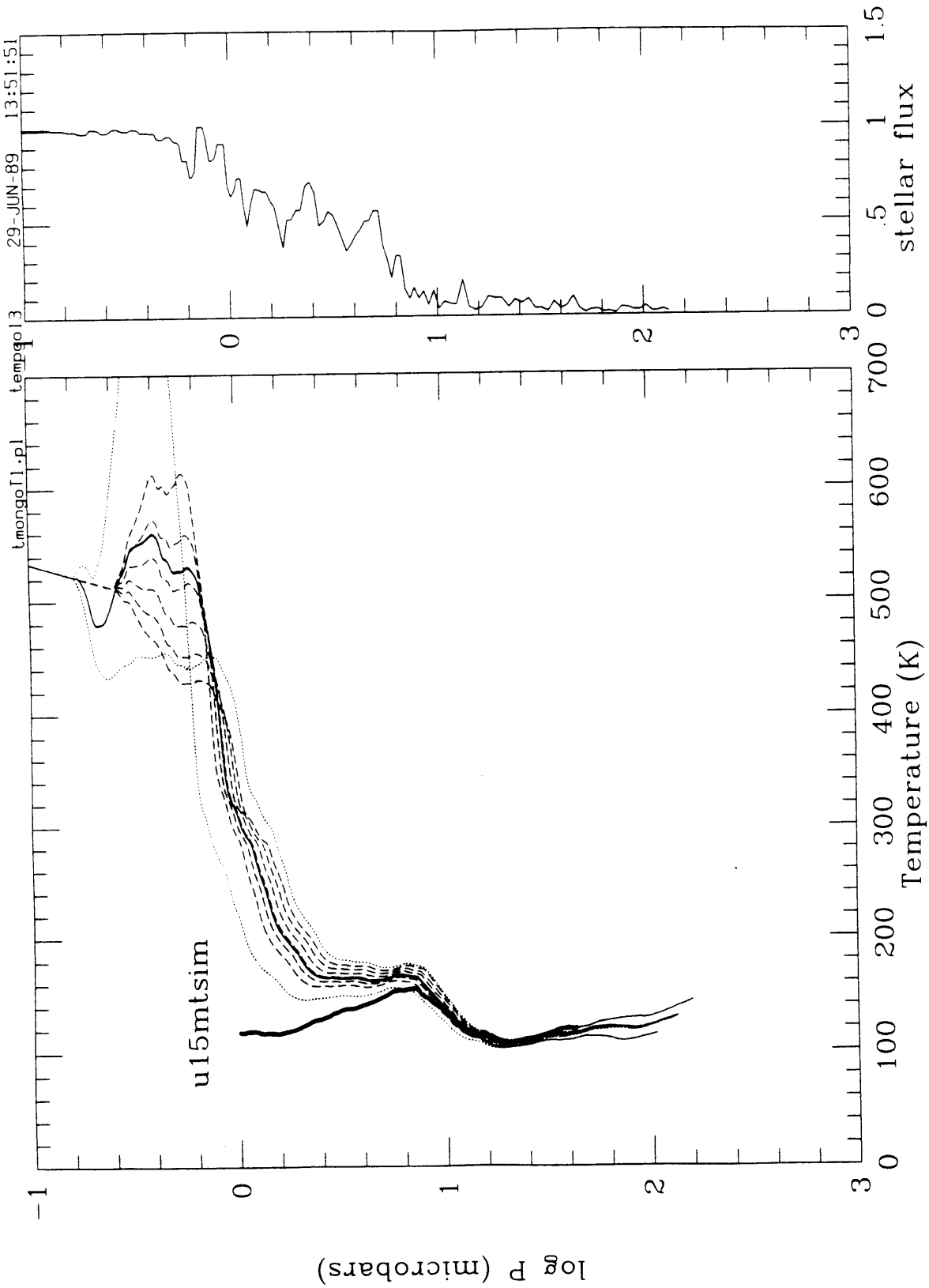

examined. Below 10-μbar, the inversions assume a profile closely duplicating previously reported analysis (French *et al.* 1987, Elliot *et al.* 1987). At the bottom of the band of temperature profiles, two solid profiles may be seen defining the temperature limits of the band. These outliers (solid line) were produced as part of the noise treatment, when the lower baseline was offset by ± *s* (Treatment of Noise above).

Figure 5-5 shows the atmospheric temperature profile for the numerical inversion of the KME15 immersion. The first obvious feature, compared to the previously reported profile (bold profile), is the steep gradient in the 0.5 to 2.5-μbar region. Since the upper atmosphere temperature is constrained by the model to over 500 K, a gradient connecting these two regions must exist in some form. The nature of the gradient is, however, determined by the recorded data. This gradient measures approximately 1.8 K km^{-1} near a temperature of 250 K. At lower pressures, it is even steeper, nearly 2.8 K km^{-1} at a temperature of 350 K. The altitude intervals at Uranus over which the gradients were measured are 56 and 36 km respectively. At the high pressure end of the gradient, near 2.0-μbar, the profile abruptly changes to a highly isothermal region (a small constant temperature gradient is not ruled out) extending to approximately 8.0-μbar. Half-light occurs in this region at the approximate temperature and pressure of 2.2-μbar and 175 K.

In the KME15 emersion profile (Figure 5-6), the same general behavior of temperature versus pressure is observed. A major exception is the behavior just below half-light located near 2.2-μbar. Instead of abruptly changing from a steep temperature gradient to an isothermal layer, this profile slowly arcs over with increasing pressure into a region with an apparently constant temperature gradient with pressure. For the same Uranian altitudes used for the immersion calculations (above), the corresponding temperature gradients and mean temperatures are 1.6 K km^{-1} at 256 K and 2.3 K km^{-1} at 342 K. There

Figure 5-6 Temperature-pressure profile of KME 15 emersion. On the left panel, the band of dashed profiles represents the inversion, and the width a formal error (see text). The right panel is the composite lightcurve plotted as a function of pressure. The bold profile is the previously reported inversion of this event (French *et al.* 1987).

Chapter 5

Figure 5-6

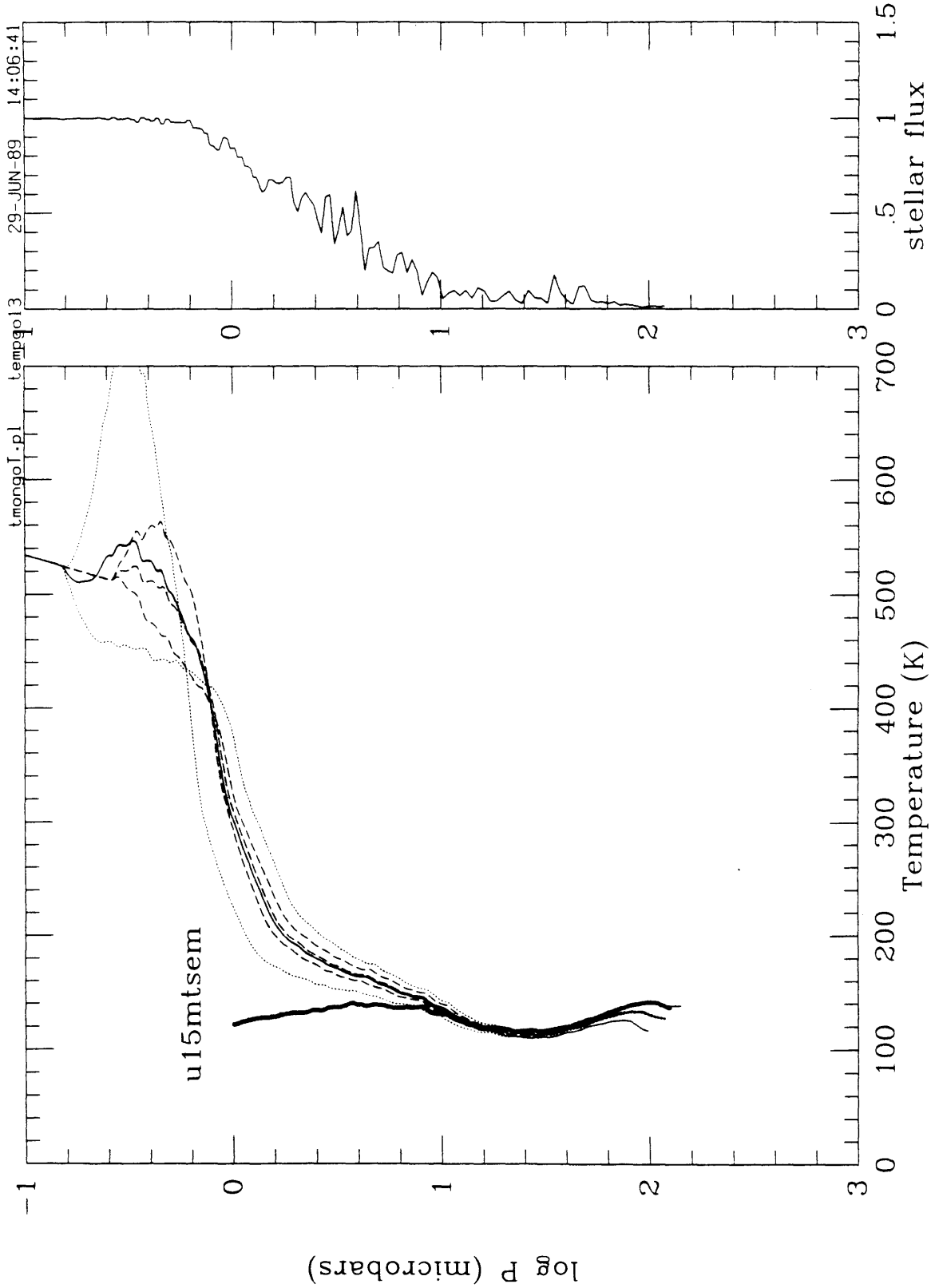

is no obvious indication of a warm layer at the 8.0-μbar level. The profile effectively duplicates the previously reported profile (bold profile) of French *et al.* (1987) for pressures greater than 10-μbar.

For KME17 immersion (Figure 5-7), the general profile looks similar to KME15 immersion. The signal-to-noise is lower than for KME15 as can be seen from the greater range of temperatures covered by the outlying temperature profiles (dotted profiles). In the corresponding lightcurve (Figure 5-8, right panel) this noise signal shows as variations along the upper baseline. The temperature profile shows a similar abrupt change in slope at the high pressure end of the steep gradient as for the KME15 immersion. The curve traversing the steep gradient, denoted with a solid line, corresponds to the UVSbc model. It shows up here because one of the joint points used for the composite curves was at half-light. Like the KME15 immersion, an apparently highly isothermal region starts at a pressure slightly greater than half-light. This isothermal region extends from approximately 2.5 to 10-μbar; the bottom of the 10-μbar interval could be consistent with the 8.0-μbar feature noted by Sicardy *et al.* (1985).

Figure 5-8 shows the emersion profile for KME17. This profile differs from KME17 immersion primarily in the transition from the steep gradient region near half-light to an isothermal layer. Compared to the immersion profile it has a more gradual transition to the isothermal region.

The isothermal region from just below half-light (approximately 2.0-μbar see Table 5-3) to approximately 10-μbar appears unique in its near total lack of fluctuations in temperature. In fact, the fluctuations apparent on the profiles are consistent with the noise seen prior to immersion and after emersion on the upper baseline of the lightcurves. The assumed composition in this region is 85 percent molecular hydrogen and 15 percent helium by weight. The parahydrogen content is likely that of the colder region below, approximately 60 percent para, 40 percent ortho (Gierasch 1989). We note for future

Figure 5-7 Temperature-pressure profile of KME 17 immersion. On the left panel, the band of dashed profiles represents the inversion, and the width a formal error (see text). The right panel is the composite lightcurve plotted as a function of pressure.The bold profile is the previously reported inversion of this event (Elliot *et al.* 1987).

Figure 5-8 Temperature-pressure profile of KME 17 emersion. On the left panel, the band of dashed profiles represents the inversion, and the width a formal error (see text). The right panel is the composite lightcurve plotted as a function of pressure.The bold profile is the previously reported inversion of this event (Elliot *et al.* 1987).

Chapter 5

Figure 5-7

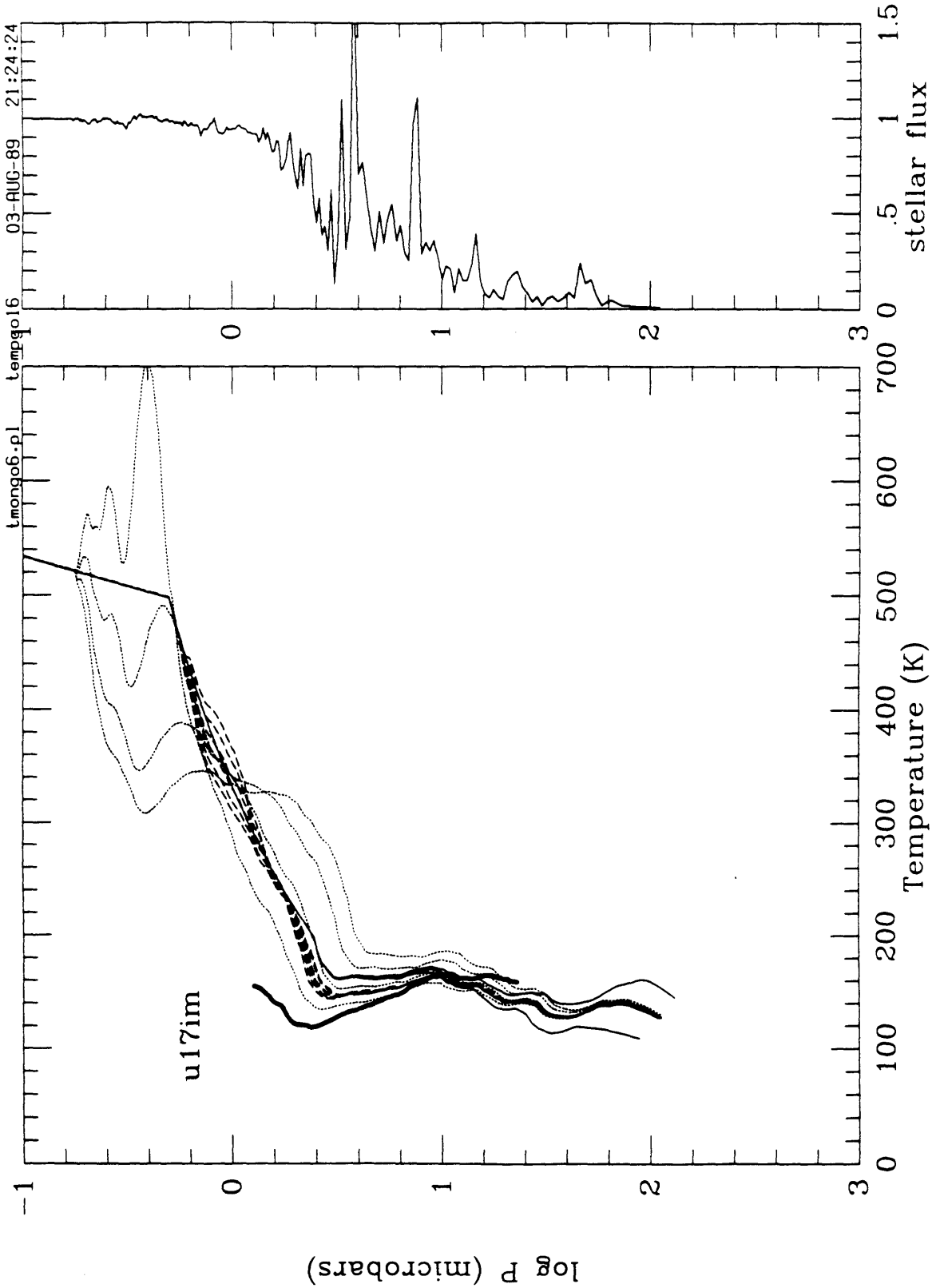

Chapter 5

Figure 5-8

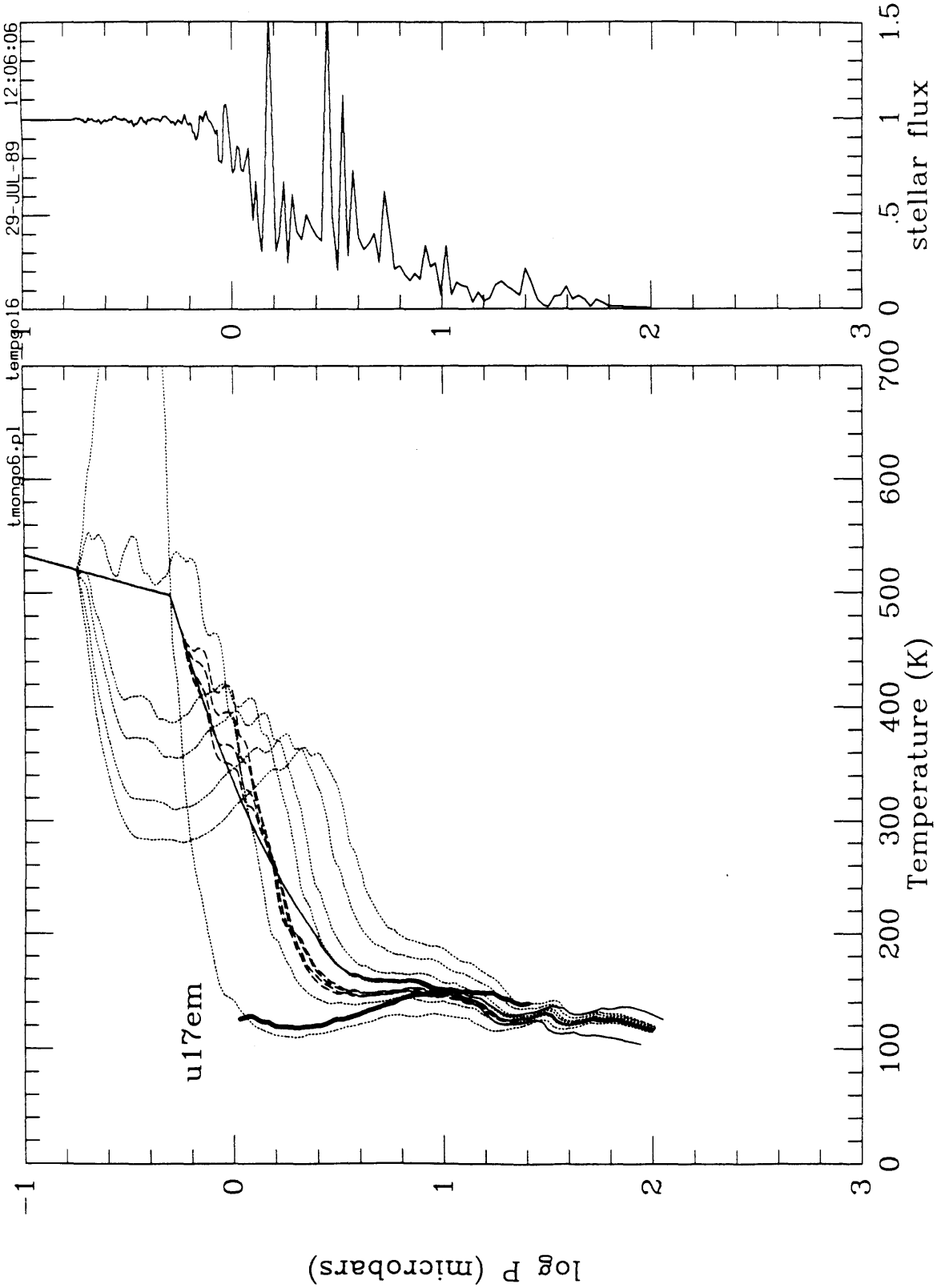

consideration that the thermal conductivity of parahydrogen undergoes an abrupt change in slope near 150 K (McCarty 1981).

Earth based observations of Uranian stellar occultations provide very high signal-to-noise observations of Uranus' upper atmosphere. Voyager 2 UVS observations as modeled by Herbert *et al.* (1987), also provide possible temperature pressure profiles for this atmospheric region. Figure 5-9 displays the three UVS temperature-pressure profiles and their respective synthetic lightcurves, plotted to the same scale as the observations reduced here. Of the three models, the UVSbc (best compromise) comes closest to matching the general character of the ground-based observations. It is clear that much detailed atmospheric structure is available in the ground-based data.

5.5 Conductive Heat Flux Determinations

Use of the UVS model as an initial atmospheric layer for the inversion, results in relatively steep temperature gradients with altitude. These gradients are determined by the vertical conductive heat flux through the atmosphere. It is assumed heating takes place directly above the region of steep gradient and that conduction is the primary mechanism of heat loss. This vertical heat flux may be computed from the heat conduction equation (molecular diffusion equation of French *et al.* 1983),

$$F_m = -2\,\mu\, m_H\, c_v \frac{(dT/dz)(kT/\pi\,\mu\, m_H)^{1/2}}{3\sigma}, \qquad (5\text{-}1)$$

Figure 5-9 Temperature-pressure profiles of UVSbc, UVSγPeg and UVSsol models. The panel on the right shows the synthetic ground-based lightcurve produced from each of the models. When compared to numerically inverted data, the UVSbc profile is the best match for all events that have been investigated.

Chapter 5

Figure 5-9

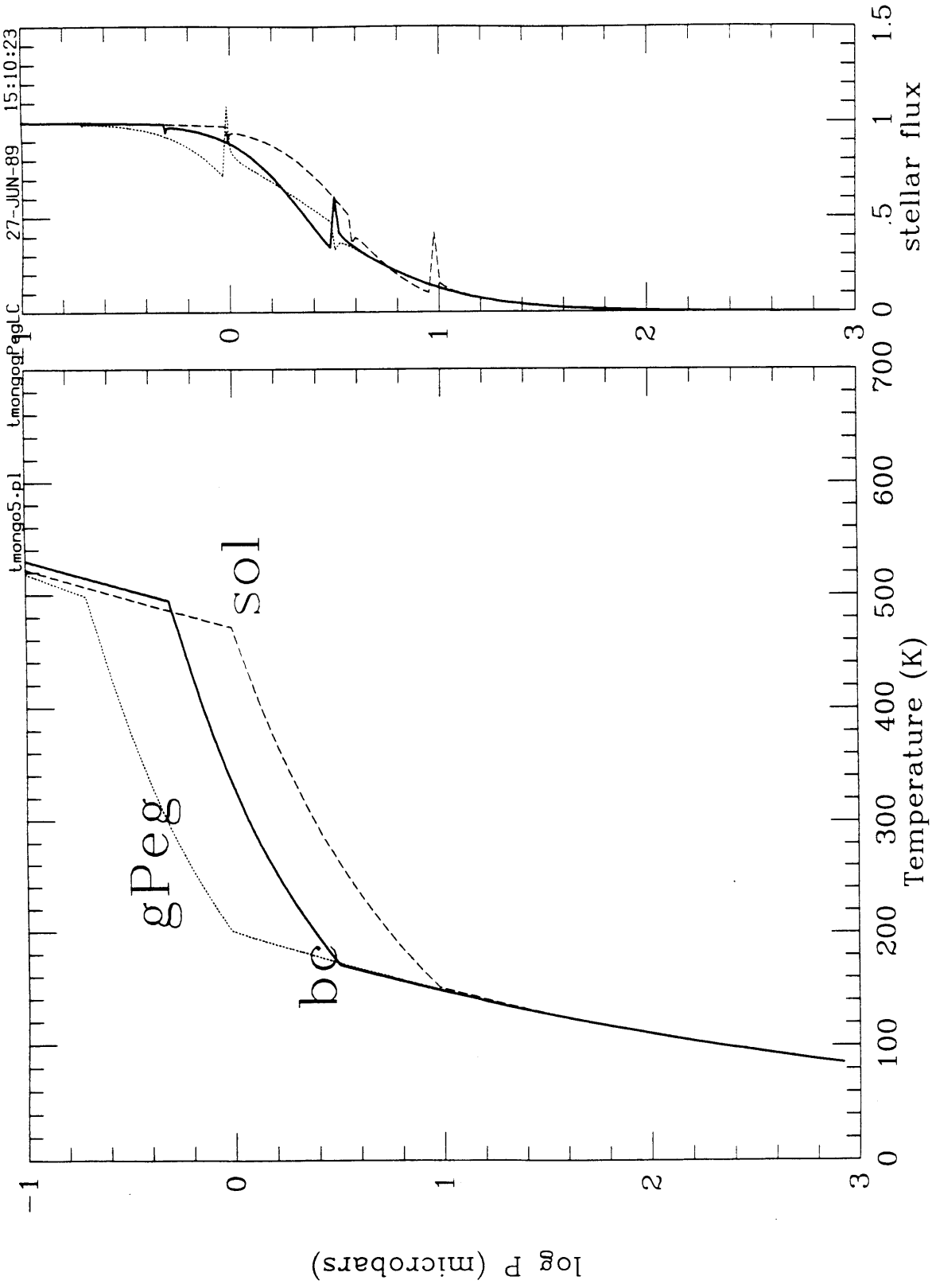

where c_v is the specific heat at constant volume, μ is the mean molecular weight, m_H is the mass of hydrogen, k is Boltzmann's constant, T is the mean atmospheric temperature, σ is the collision cross section of the dominant atmospheric constituent, and dT/dz is the mean vertical temperature gradient.

Table 5-2 shows the conductive heat flux determinations and related gradients. Two intervals of altitude were chosen along the steep temperature gradient for the temperature profile of KME15 immersion. The same altitude intervals (shown in Table 5-2) were also used for the other three derived temperature profiles. We determined a mean temperature, temperature gradient (as a function of altitude), and conductive heat flux for all four derived temperature profiles, two immersions and two emersions. The eight heat flux determinations (Table 5-2) have been averaged to obtain a mean flux of 0.47 ± 0.19 erg cm^{-2} sec^{-1}. This value of flux is two orders of magnitude larger than the 0.004 erg cm^{-2} sec^{-1} determined for the direct ionization by EUV solar radiation (Broadfoot *et al.* 1986) and cannot be accounted for by currently accepted theories. Yelle *et al.* (1987) review the energy input to this region and report a column heating rate of 0.08 erg cm^{-2} sec^{-1}, inferred from the observed temperature (Voyager 2 measurements). This is 20 times higher than the EUV input. The energy in this region has been linked to the far ultraviolet electroglow emissions, identified on Saturn and Jupiter as well as on Uranus. The electroglow phenomenon shows daytime EUV emissions with a spectrum that implies excitation by low energy electrons (3 eV Maxwellian distribution, Broadfoot *et al.* 1986).

Chandler and Waite (1986) modeled the case of a 1.0 erg cm^{-2} sec^{-1} flux of 100 eV electrons and a 0.6 erg cm^{-2} sec^{-1} flux of 10 KeV electrons incident at the top of the atmosphere. Their results give an electron density for the atmosphere that is high by two orders of magnitude compared to the measurements reported by Lindal *et al.* (1987) from Voyager 2 observations. Peak observed electron densities are however comparable to the model.

Table 5-2

Thermal Flux Determinations

PARAMETER	KME15im	KME15em	KME17im	KME17em
radius interval 1				
26103-26159 (km)	56	56	56	56
mean temperature (K)	257	256	284	287
dT/dz (K km^{-1})	1.77	1.58	1.35	1.49
radius interval 2				
26159-26195 (km)	36	36	36	36
mean temperature (K)	356	342	340	348
dT/dz (K km^{-1})	2.77	2.32	0.96	1.08
†Flux1(mol.diff)				
(erg cm^{-2} sec^{-1})	0.46	0.41	0.37	0.41
†Flux2(mol.diff)				
(erg cm^{-2} sec^{-1})	0.84	0.69	0.29	0.33
Avg Flux (both intv)				
(erg cm^{-2} sec^{-1})	0.65	0.55	0.33	0.37

Average thermal flux (all events) = 0.47 ± 0.19 erg cm^{-2} sec^{-1}

† $c_v = 2.00 * 10^{+8}$ erg gr^{-1} (molecular hydrogen at 300 K)

Table 5-3

Derived Half-light Temperature and Pressure

PARAMETER	KME15im	KME15em	KME17im	KME17em
half-light †Temperature (K)	175 ± 8	188 ± 6	186 ± 3	182 ± 2
half-light †Pressure (μbar)	2.2 ± 0.2	2.2 ± 0.1	2.2 ± 0.1	2.1 ± 0.1
half-light Number density (*10^{+13})	9.1 ± 0.4	8.5 ± 0.5	8.8 ± 0.5	8.5 ± 0.2

† Formal errors are shown, these do not include systematic errors. The systematic errors are estimated to be ± 15 K for the temperature and for the pressure ± 0.5-μbar.

Another model is that of Clarke *et al.* (1986), who use the solar EUV radiation to initiate a process of *in situ* acceleration of low energy electrons by a type of dynamo associated with the magnetic field of Uranus. This tends to amplify the effect of the daytime incident solar EUV energy, providing the convenient features of diurnal variability and additional energy.

5.6 Joule Heating

Uranus, Saturn, and Jupiter all have thermospheres that are much hotter than can be accounted for by absorbed solar EUV radiation or internal heat from the planet. Jupiter has a thermosphere that is close to 1000 K rather than the predicted temperature of around 200 K (Festou *et al.* 1981). Saturn also has a high measured temperature of about 400 K (Festou and Atreya 1982). Uranus is no exception with its 800 K reported temperature (Herbert *et al.* 1987).

The mechanism of Joule or resistive heating could, however, supply sufficient energy (Atreya 1986). The equations governing this mechanism follow those of simple electrical circuits. The power or energy dissipated in a circuit is computed as the current times the potential drop across the circuit. In terms of the ionosphere this is,

$$Q_J = j * E, \qquad (5\text{-}2)$$

where Q_J is the energy, j is the current and E is the electric potential. Ohms law for our analogous circuit gives the current in terms of a resistance and a conductance (inverse resistance). For the atmosphere we can write this as,

$$j = (\sigma)\, E, \qquad (5\text{-}3)$$

where (σ) is the conductivity tensor. The tensor notation is used to accommodate the directional component of conductivity. The tensor may be broken down into three convenient cases: Conductivity perpendicular to the magnetic field, σ_P (Pederson conductivity). Conductivity perpendicular to both the electric and magnetic field, σ_H (Hall conductivity). Conductivity parallel to the magnetic field, σ_L (Longitudinal conductivity). These three conductivities may be written as,

$$\sigma_P \approx \frac{N_i\, e\, \nu_{in}\, f_i}{B\, (\nu^2_{in} + f^2_i)}, \tag{5-4}$$

$$\sigma_H = \frac{N_i\, e^2\, f_i}{m_i\, (\nu^2_{in} + f^2_i)}, \tag{5-5}$$

and

$$\sigma_L \approx \frac{N_i\, e^2}{m_e\, \nu_{en}}, \tag{5-6}$$

where N_i is the ion (or electron) number density, m_e is the electron mass, m_i is the ion mass, ν_{en} and in are the respective electron-neutral and ion-neutral collision frequencies, and f_i is the ion cyclotron frequency (e B/f_i).

With this formalism, we are not able to determine the Joule heating since the requisite electric field strength and thermospheric wind velocity is not known. We will, therefore, estimate with an approximate model the thermospheric wind speed necessary for a particular flux.

The energy dissipated per ion-neutral collision for a neutral thermospheric wind passing through ions that are bound to the planet's magnetic field is

$$E_{in} = \frac{1}{2} \mu_{in} V^2_{in}, \qquad (5\text{-}7)$$

where E_{in} is the energy per collision, V_{in} is the wind speed, and μ_{in} is the reduced mass of the ion and neutral ($m_i m_n/(m_i + m_n)$). We assume the electrons will have a negligible effect on the neutrals and that the energy of the ion-neutral interaction is totally converted into heat. We model the wind with a constant density, constant temperature cross section allowing a single mfp (mean free path) to be specified for the wind. The energy dissipated for a column of volume V_{col} is

$$Q_J = V_{col} \; N_i \frac{V}{mfp} E_{in} , \qquad (5\text{-}8)$$

where the first two terms are the number of interacting particles in the column, and the fractional term is the frequency of interaction per particle. Substituting for E_{in} gives

$$Q_J = V_{col} \; N_i \frac{V^3}{2 \; mfp} \mu_{in}, \qquad (5\text{-}9)$$

where an explicit dependence on the cube of the wind velocity is apparent. For Uranus, we assume that the ions are protons, the dominant neutral species in the thermosphere is H_2, the column height is $5*10^{+8}$ cm (Figure 7. of Lindal *et al.* 1987), the column cross section is 1 cm^{-2}, the mfp is on the average 100 cm, the average ion density is $1*10^3$ cm^{-3} (Lindal *et al.* 1987), and that the wind speed is 200 m sec^{-1}. We obtain an energy production rate of 0.02 erg cm^{-2} sec^{-1}. An estimate of the Joule heating by Herbert *et al.* (1987) for an atmospheric model with $N_i = 1*10^5$ cm^{-3} was 2.5 erg cm^{-2} sec^{-1}, a number in close agreement with this simple approximate model noting the linear dependence on N_i.

5.7 Conclusions

A new method of analysis has been applied to the stellar occultations of KME15 and KME17 by Uranus. For KME15 immersion this has revealed a steep temperature gradient with values over 2.0 K km^{-1} directly above the half-light pressure of approximately 2.2–μbar. The other lightcurves show a similar gradient but somewhat less steep. The retrieved temperatures at 1-μbar are approximately 300 K, and the half-light temperatures have been increased from previously determined values to about 180 K. Slightly higher temperatures from half-light to approximately the 10-μbar level have also been found. We have identified a highly isothermal region directly below half-light in three of the four lightcurves examined. The exact nature of this feature remains to be determined; however, an 8-μbar feature reported by Sicardy *et al.* (1985) appears to coincide with the low altitude end of the region.

We have used known atmospheric parameters to specify the atmospheric layer or cap above the region probed by the ground-based recorded occultation. This modified inversion method effectively replaces the temperature-pressure uncertainty associated with the ad hoc assumptions, or poorly determined initial conditions (lightcurve noise limited) used in past numerical inversions with a model atmosphere directly above the region probed by the ground-based lightcurve.

The application of this method of analysis for ground-based observations of planetary occultations of stellar sources is directly applicable to Saturn. Voyager 2 UVS observations were made during its flyby and may be used to construct an atmospheric cap for inversions of lightcurves from this planet. Reaching out beyond Uranus to Neptune, the scheduled flyby in August 89 should enable a similar analysis of Neptune data, some of which is already in hand.

We have examined Joule heating with a first order approximation and found it to be a possible source of the large observed heat flux at the bottom of the thermosphere. Under the approximations made here, a wind velocity of order 400 m sec^{-1} could supply sufficient energy to satisfy the conductive heat flux. Whether or not the thermospheric winds are of this velocity remains to be determined.

References

ATREYA, S. K. (1986). *Atmospheres and Ionospheres of the Outer Planets*. Springer Verlag Berlin Heidelberg, Germany.

BARON, R. L., R. G. FRENCH, AND J. L. ELLIOT (1989). The oblateness of Uranus at the 1-μbar level. *Icarus* **77**, 113-130.

BROADFOOT, A. L., F HERBERT, J. B. HOLBERG, D. M. HUNTEN, S. KUMAR, B. R. SANDEL, D. E. SHEMANSKY, G. R. SMITH, R. V. YELLE, D. F. STROBEL, H. W. MOOS, T. M. DONAHUE, S. K. ATREYA, J. L. BERTAUX, J. E. BLAMONT, J. C. MCCONNELL,A. J. DRESSLER, S. LINIK, R. SPRINGER (1986). Ultraviolet spectrometer observations of Uranus. *Science* **233**, 74.

CHANDLER, M.O., J. H. WAITE, JR (1986). The ionosphere of Uranus: A Myriad of Possibilities. *Geophys. Res.Letters* **13**, 6-9.

CLARKE, J. T., M. K. HUDSON, AND Y. K. YUNG (1987). The excitation of the far ultraviolet electroglow emissions on Uranus, Saturn and Jupiter.*J. Geophys. Res.* **92**, 15139-15147.

FESTOU, M. C., AND S. K. ATREYA (1982). Voyager Ultraviolet Stellar occultation measurements of the composition and thermal profiles of the Saturnian upper atmosphere. *Geophys. Res Lett.* **9**, 1147-1150.

FESTOU, M. C., S. K. ATREYA, T. M. DONAHUE, D. E. SHEMANSKY, B. R. SANDEL, AND A. L. BROADFOOT (1981). Composition and thermal profiles of the Jovian upper atmosphere determined by the Voyager ultraviolet stellar occultation experiment. *Geophys. Res Lett.* **86**, 5715-5725.

GIERASCH, P. (1989) Personal communication.

HERBERT, F., B. R. SANDEL, R. V. YELLE, J. B. HOLBERG, A. L. BROADFOOT, AND D. E. SHEMANSKY (1987). The Upper Atmosphere of Uranus: EUV Occultations Observed by Voyager 2. *J. Geophys. Res.* **92**, 15093-15109.

LINDAL, G. F., J. R. LYONS, D. N. SWEETNAM, V. R. ESHLEMAN, D. P. HINSON, AND G. L. TYLER (1987). The atmosphere of Uranus: Results of radio occultation measurements with Voyager 2. *J. Geophys. Res.* **92**, 14987-15001.

LINDAL, G. F., D. N. SWEETNAM, AND V. R. ESHLEMAN (1985). The atmosphere of Saturn: An analysis of the Voyager radio occultation measurements. *Astron. J.* **90**, 1136-1146.

MCCARTY, R. D., J. HORD, H. M. RODER (1981). *Selected properties of hydrogen (Engineering Design Study).* U. S. Government Printing Office, Washington.

YELLE, R. V., J. C. MCCONNELL, B. R. SANDEL, A. L. BROADFOOT (1987). The Dependence of Electroglow on the Solar Flux *J. Geophys. Res.* **92**, 15110-15124.

Chapter 6

Precision Time Keeping- A Portable Time Standard

6.1 Introduction

The time base used previously for most ground-based stellar occultations has been limited to whatever was available at the observatory used for the observation. In many cases, the time was derived from a radio time signal. The radio signal could have traveled by various paths, with delays of up to nearly 100 milliseconds, assuming it propagated around the earth and could not be received by the most direct route. Reception from the time station could also be extremely poor or nonexistent until after the observation.

Recent analysis of occultation data (*e.g.*, French *et al.* 1988, Baron *et al.* 1989) have shown a need for millisecond to sub-millisecond relative accuracy between simultaneous observations at different worldwide sites. As a result, we developed a set of portable time standards for occultation observations.The primary constraints on these systems were portability, modest cost and a short design and construction time. There were various commercial systems available at the time this project was undertaken but all were much more costly and did not have the required portability. For instance, Hewlett-Packard's portable rubidium standard was very expensive, heavy and it also required a separate seat when taken aboard a commercial air flight.

6.2 Overall Description

The approach taken was to buy commercial crystal frequency standards and to design and build low power clock circuits that became an integral part of the standards. The circuit requirements were to:

1. Display the precise time.
2. Generate an accurate one second timing edge for incorporation into a data train or synchronization of a data system.
3. Determine and display the time offset between itself and some other time standard to sub-microsecond accuracy.

The oscillators used for this project were three temperature regulated oven stabilized quartz crystal oscillators from Vectron Laboratories Incorporated and one with similar specifications from the Hewlett-Packard Company.

6.3 Circuit Description - General

The clock circuit is nominally designed to be integrated into a frequency standard source of 1.0, 5.0, or 10.0 Mhz of 4.5 to 7 Volt peak to peak amplitude. It uses complementary metal oxide semiconductor (CMOS) integrated circuits (ICs) in order to minimize the amount of power needed to run the circuit and as an additional benefit gives significant design flexibility. Low power commercial circuit applications such as timers, clocks and display drivers are numerous and the technology is relatively mature with a proliferation of integrated circuits including most of the transistor transistor logic (TTL) designs.

The circuit can be divided into three major sections: the time keeping function, the time setting function, and the time checking function. These functions are implemented by a

variety of circuits, where any one circuit may participate in one, two or all three functions as described below. Figure 6-1 depicts the layout of the circuit board and Figure 6-3 is a schematic diagram of the circuit. Table 6-2 is a parts list for the circuit with a brief description of each part. The circuit specifications are given in Table 6-1 and assume installation in a frequency standard.

6.3.1 Time Keeping Circuit

The time keeping circuitry consists of a counter chain of 74HC390's, two Intersil 7224's for counting and displaying the hours, minutes and seconds and a 24 hour reset circuit. The input to the counter chain is capacitively coupled through a 0.0039 microfarad capacitor into a 74C04 inverter used as a discriminator and buffer. Two 1N4148 high speed low power diodes clip voltages that either exceed the power supply voltage (+V) plus the voltage drop of the diode or negative voltages that exceed the voltage drop of the diode.

Four 74HC390 dual decade counter ICs are used to divide the input frequency down to 1 hz. The input to this chain is selected by soldered jumper to accommodate a 1, 5, or 10 Mhz frequency source. Intermediate frequencies generated in the chain are used to increment the hours, minutes and seconds display when they are set and as a source along with the input frequency for the time offset measurement circuit (described below).

The minutes and second and hour display may be set using the following procedure here described for the minutes and seconds case. Select "fast" or "slow" on the "set speed" switch (SW3) and actuate the "set mmss" switch (SW5) until the desired time is displayed (Figures 1, 2 and 3).

Table 6-1

CLOCK SPECIFICATIONS	
Input:	
Hardware:	Externally mounted BNC connector.
Signal required:	Signal compatible with TTL voltage levels (a high impedance source exceeding these voltage levels will be clipped by a limiting diode). The first rising edge is used for timing. Impedance: CMOS input.
Output:	
Hardware:	Externally mounted BNC connector.
Signals:	
1 Hz:	Unbuffered CMOS 74C04, recommend loading with 100 KΩ or greater (eg. oscilloscope probe is generally 10 MΩ).
5 MHz:	Unmodified, determined by frequency standard.
Timebase requency :	The clock circuit is nominally designed to operate from a frequency source of 1, 5 or 10 MHz.
Environmental:	Compatible with specifications of the frequency standard that the circuit is used in.
Power:	Determined by frequency standard used. Clock circuit power is negligible compared to that needed for operation of the temperature controlled oven. In the case of a shunt regulating Zener diode working from a 15 Volt power source internal to a Vectron Frequency Standard, the quiescent power suppy current (LED and output not drawing current) is 2.6 mA
Circuit dimensions:	
width:	8.9 cm.
length:	25.3 cm.
Height:	1.6 cm.

Table 6-2

Parts List

Reference designation	Part number	Description
U1	74HC390	CMOS dual 4-bit decade counter
U2	74C04	CMOS Hex inverter
U3	74C221	CMOS dual monostable multivibrator
U4	74HC390	CMOS dual 4-bit decade counter
U5	74HC74	CMOS dual D flip-flop
U6	74HC74	CMOS dual D flip-flop
U7	74HC00	CMOS quad 2-input NAND gate
U8	74HC390	CMOS dual 4-bit decade counter
U9	74HC221	CMOS dual monostable multivibrator
U10	74HC08	CMOS quad 2-input AND gate
U11	CD4040	CMOS 12-stage ripple-carry binary counter/divider
U12	74HC04	CMOS Hex inverter
U13	74HC390	CMOS dual 4-bit decade counter
U14	74HC221	CMOS dual monostable multivibrator
U15	ICM7224IPL	CMOS 4 1/2-digit LCD/LED display counter, 15 Mhz
U16	ICM7224IPL	CMOS 4 1/2-digit LCD/LED display counter, 15 Mhz
R1	100 kΩ 1/8 watt	resistor, carbon composition
R2	4.7 kΩ 1/8 watt	resistor, carbon composition
R3	100 kΩ 1/8 watt	resistor, carbon composition
R4	100 kΩ 1/8 watt	resistor, carbon composition
R5	100 kΩ 1/8 watt	resistor, carbon composition
R6	7.5 MΩ 1/8 watt	resistor, carbon composition
R7	7.5 MΩ 1/8 watt	resistor, carbon composition
R8	7.5 MΩ 1/8 watt	resistor, carbon composition
R9	100 kΩ 1/8 watt	resistor, carbon composition
R10	7.5 MΩ 1/8 watt	resistor, carbon composition
R11	7.5 MΩ 1/8 watt	resistor, carbon composition
R12	1.6 MΩ 1/8 watt	resistor, carbon composition
R13	2.7 kΩ 1/8 watt	resistor, carbon composition
C 0	30 µf 35 V	capacitor, electrolytic
C 1	0.0039 µf	capacitor, glass
C 2	0.01 µf 30 V	capacitor, glass
C 3	18 pf 30 V	capacitor, glass

Table 6-2 (cont.)

C 4	0.01 µf 30 V	capacitor, glass
C 5	18 pf 30 V	capacitor, glass
C 6	0.01 µf 30 V	capacitor, glass
C 7	18 pf 30 V	capacitor, glass
C 8	18 pf 30 V	capacitor, glass
C 9	0.1 µf 30 V	capacitor, ultraminiature ceramic
C 10	0.1 µf 30 V	capacitor, ultraminiature ceramic
D 0	5.1B3	Zener diode $V_Z = 5.1V$
D 1	1N4148	PIV = 75 V, $T_{rr} = 4.0ns$
D 2	1N4148	PIV = 75 V, $T_{rr} = 4.0ns$
D 3	1N4731	Zener diode $V_Z = 4.3$ V
D 4	1N4148	PIV = 75 V, $T_{rr} = 4.0ns$
D 5	1N4148	PIV = 75 V, $T_{rr} = 4.0ns$
SW1	mil surplus	miniature, dpdt switch
SW2	mil surplus	miniature, dpdt switch
SW3	mil surplus	miniature, spdt switch
SW4	mil surplus	miniature, spdt switch
SW5	mil surplus	miniature, spdt switch
SW6	mil surplus	miniature, spdt switch
LCD 1	4 1/2 digit	LCD display part of Intersil ICM7224EV/KIT
LCD 2	4 1/2 digit	LCD display part of Intersil ICM7224EV/KIT
LED 1	Radio Shack LED	light emitting diode
header 1	3M 3446	3M 10 pin ribbon cable header with latch

Figure 6-1 Clock circuit board layout. See parts list for detailed parts identification. Those items shown with a dashed outline are mounted on the reverse side of the circuit board.

Figure 6-2 Clock circuit control panel. A description of the function of the switches and indicator is given in the text. The center and bottom boxes represent 4 -1/2 digit LCD displays. The center box shows only the hour function active. All of the digits in this display are used when the time offset measurement function is active.

Figure 6-3 Schematic diagram of the precision clock circuit. Component designators R, C, D, and U corresponding to resistors, capacitors, diodes and integrated circuits respectively as listed in Table 6-2. See text for circuit description and references for detailed integrated circuit and diode specifications.

Figure 6-1

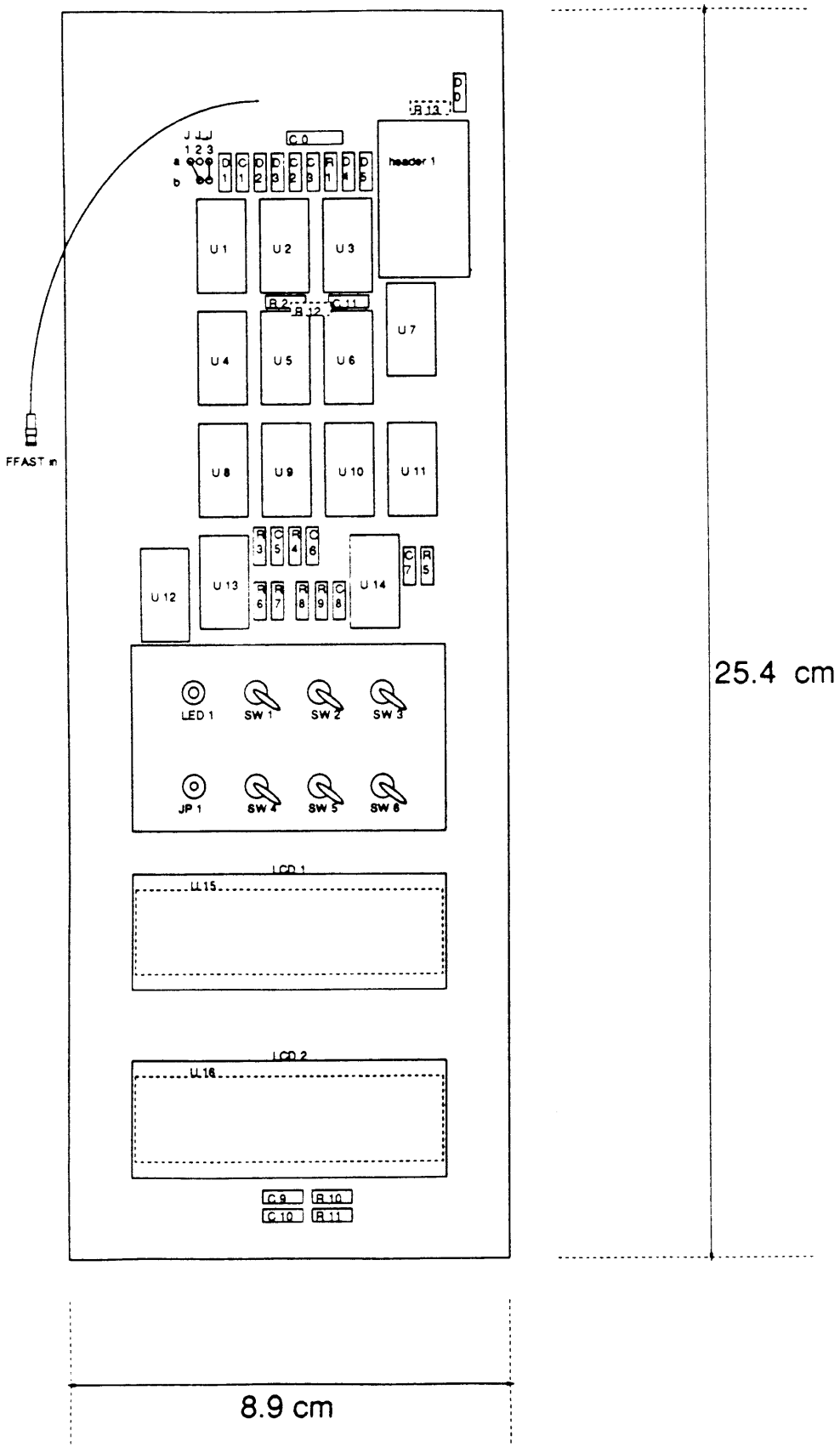
FFAST in
header 1
U1
U2
U3
U4
U5
U6
U7
U8
U9
U10
U11
U12
U13
U14
LED 1
SW 1
SW 2
SW 3
JP 1
SW 4
SW 5
SW 6
LCD 1
LCD 2
25.4 cm
8.9 cm

Figure 6-2

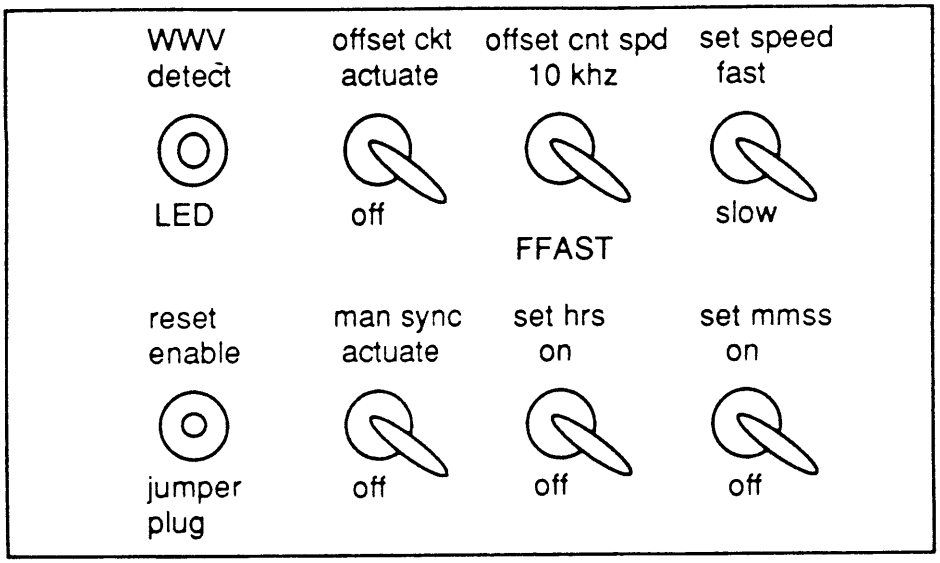

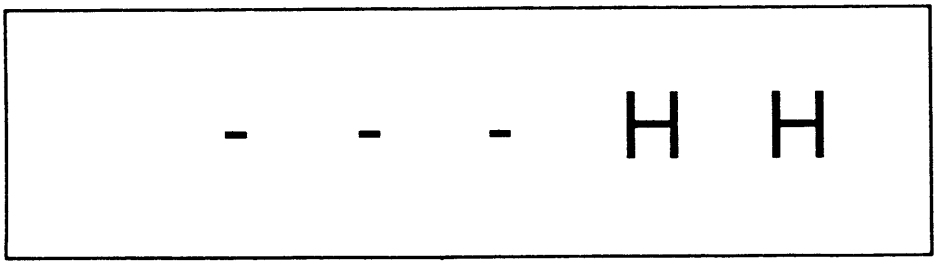

HOURS OR OFFSET UNITS

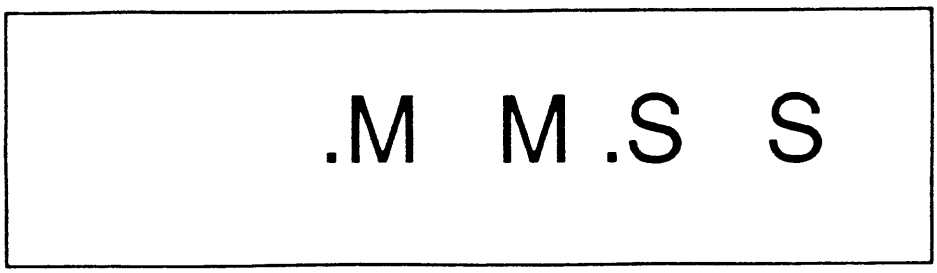

Figure 3

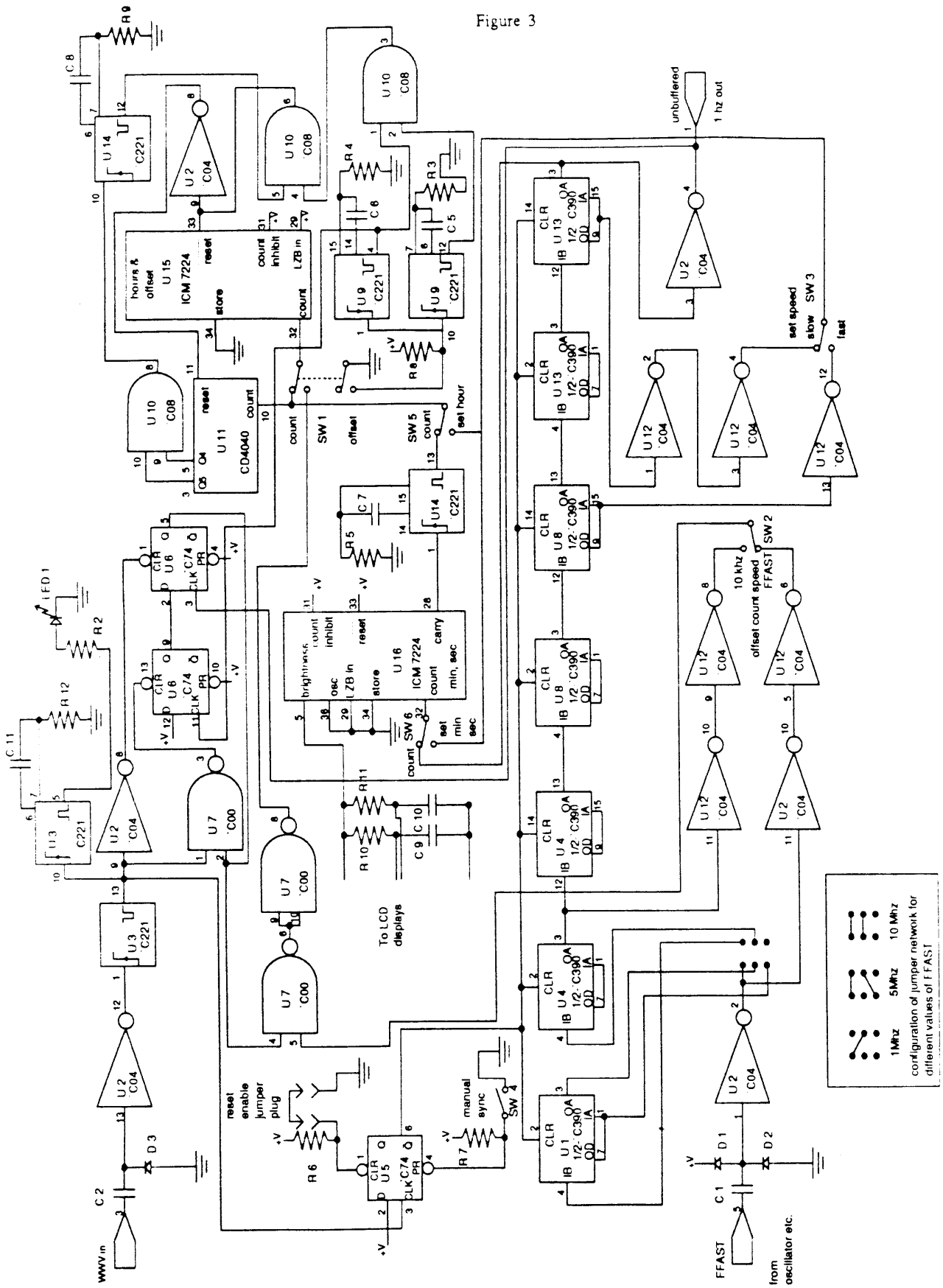
unbuffered
1 hz out
set speed
slow SW 3
fast
offset count speed
FFAST SW 2
10 khz
SW 1
offset
SW 5
count
set hour
SW 6
set
min
sec
To LCD displays
reset enable jumper plug
manual sync SW 4
WWV in
FFAST
from oscillator etc.
1Mhz 5Mhz 10 Mhz
configuration of jumper network for different values of f FAST

6.3.2 Synchronization Circuit

Input to the synchronization circuit is through the externally mounted BNC connector labeled "WWV". The signal is capacitively coupled through a 0.01 microfarad capacitor into a 74C04 inverter IC used as a discriminator and buffer. A 1N4731 Zener diode (1 watt dissipation) is used to clip voltages that either exceed the Zener voltage of the diode or negative voltages that exceed the forward voltage drop of the diode.

Synchronization is produced by actuating a flip flop circuit (U5) which in turn allows a previously reset counter chain to begin counting the local high frequency signal (from the frequency standard). Additional pulses on the input have no effect until the counter chain is again reset allowing a repeat of the synchronization cycle. In the event the circuit need be synchronized manually (*e. g.*, during testing), a "man synch" switch (SW4) is provided. Reset is produced by momentarily plugging in a miniature audio plug that shorts the preset terminal of the one shot to ground. The plug is used to protect against inadvertently destroying the time by actuating a wrong switch.

The 1 Hz output is counted by U16, a 5959 type counter driving a liquid crystal display (LCD). The carry output goes to U15 where it is counted and displayed as hours on the other LCD. Twenty four hour rollover on U15 is done by using U11. When U11 reaches a count of 24, this is detected and used to reset U15 and U11 to zero. This causes the hours LCD to become blank.

In order to ascertain if an external timing signal (edge) is available to produce synchronization of the clock, a one shot circuit (U3) is triggered by the sync signal causing a light emitting diode (LED) to flash on for a few milliseconds. The flash gives the operator a visual indication of the presence of a synchronization signal and at approximately what interval it occurs. This capability may be used to set the level of the input signal without the use of an oscilloscope or when synchronization must be taken from a possibly fading

broadcast time signal. This indicator may also be used as a convenient check to determine whether the clock itself is working by observing it when the 1 second output pulse is fed back to the sync input.

6.3.3 Time Offset Measurement Circuit

The offset circuit makes it possible to determine the time difference between the leading edge of a pulse from an external source and the leading edge of the internally generated one second pulse. The leading (positive rising) edge from an external pulse enables counting of a high frequency from the time standard until the 1 second internal pulse leading edge shuts off the counting and allows display of the time offset. The external input for this circuit is through the "WWV" BNC connector. Each time the "offset ckt" switch (SW1) is actuated one offset measurement is automatically performed.

The offset in time between the two edges can be displayed in two different modes selected by switch S2. The "10 kHz" mode counts and displays the offset in terms of the number of periods of a 10 khz source. The "FFAST" mode counts and displays the number of periods of a 1, 5, or 10 Mhz source (determined by the frequency standard used). The number of periods is counted modulo 20,000 by the Intersil 7224 counter IC.

Circuit operation begins when switch S1 is placed in the offset mode, two one shot circuits on U9 are triggered resetting U11 and U15 and clocking half of U6. In this state the internal 1 Hz signal will within 1 second clock the other half of U6 allowing the signal selected ("10 kHz" or "FFAST") to propagate to U15 where it is counted. Counting will continue until a positive rising edge is input to the "WWV" connector, this will clear one of the 74C74 flip flops on U6 and stop the signal to the counter (U15). The count is automatically displayed by U15.

It is possible to measure an arbitrary time offset to within one count of the highest available frequency (1, 5 or 10 MHz). This can be done by the following procedure. First, the time offset can be obtained to the nearest second by simply comparing the the clock display with the reference clock. Second, the fractional second part of the time offset can be determined to the nearest 100 μsec by using the "10 kHz" offset option. Finally, the offset can be measured modulo 20,000 with the highest resolution available by using the "FFAST" mode. There is no ambiguity in the measurement due to the overlap between the two modes. For a detailed recipe to calculate the offset see Appendix 2. The circuit may be used to determine drift over seconds to years with an accuracy of one period of the high frequency internal source.

In order to minimize the complexity of the design, the use of the offset circuit corrupts the hour count of the clock since it uses the same 7224 IC. This may be reset if desired without corrupting the minute or second count by selecting "fast" or "slow" on the "set speed" switch (SW3) and actuating the "set hr" switch (SW5) until the desired time is displayed (Figures 1, 2 and 3).

6.3.4 1 Hz Output and Circuit Power

An unbuffered output signal of 1 Hz is available from the BNC connector labeled "1 Hz". This output will supply 1.75 ma. with a low impedance power supply. However, the power supply is designed to be a high impedance source, so **loading the output (low resistive, capacitive or inductive impedance to ground)will pull down the power supply voltage for the entire clock circuit.** Only a high impedance load (100 kΩ or greater) should be used to monitor or use this signal.

The implementation of the power circuit in the Vectron case is with a 5.1 V Zener diode fed from a 15 V source available from the Vectron frequency standard and a 18.7 V source from the Hewlett-Packard standard. Any number of different methods may be employed to obtain the required 5 V supply.

6.4 Control Panel

The control panel is made integral to the clock circuit board. Additional grounding is provided in order that static charge from an operator does not interfere with circuit operation. Six switches, one reset plug, one LED and two LCD four digit displays make up the user interface. Figure 6-2 shows the panel layout with the name of each function.

Liquid crystal displays were chosen for their extremely low power drain and ability to be driven by CMOS circuits. The LCD nearest the control switches (Figure 6-2) displays hours modulo 24 or the time offset when the time offset circuit is actuated while the other displays minutes and seconds.

6.5 Construction

The primary concern in the circuit construction was the reliability of the clocks once they were put into service. The approach to this problem was to use the internal oscillator power supply and to install the clock circuit directly into the oscillator enclosure. In order to do this, some of the existing countdown circuitry (used to produce and output submultiples of the master frequency) in the oscillators was removed and physically replaced with the clock circuit. This enhanced the reliability due to the absence of external cables and connectors that would have been required from the oscillator to the clock circuit if they

were in separate enclosures, avoiding the possibility of snagging a vital cable or external connector and losing the time.

Each frequency standard was modified by remounting critical externally mounted controls fuses and switches inside the enclosure so a conscious effort is needed to change them.

In order to secure a final circuit with a high degree of reliability, the circuit board is specified to be made with grade G10 epoxy fiberglass. Circuit board metalization patterns were produced from layouts made in our lab. The layout was in turn made into a positive transparency which was used by a local vendor to make the final circuit board.The sockets used for the components were specified with a gold layer on the mating surfaces in order to inhibit corrosion failure mechanisms. The use of very low power CMOS circuits should contribute to high reliability since they will operate with a low internal temperature rise thereby inhibiting solid state high temperature failure mechanisms (*e. g.*, solid state migration).

One consequence of the exceedingly low power of CMOS circuits is their susceptibility to static electricity disrupting circuit operation or even destroying the circuit. The destruction of CMOS circuits was a major problem with initial production of CMOS ICs but has been greatly reduced in later designs through the use of protection diodes and redesign of the input and output stages of the IC. The clock circuit design is susceptible to static charge interfering with its operation if it is left unprotected. Protection has been added in the form of input protection diodes and use of a partial Faraday cage design around the finished circuit. A second Faraday cage produced by the enclosure of the commercial frequency standard gives final protection.

There have been reported cases of static electricity causing the clock display to jump when the cover was removed. Further investigation of this issue should be pursued.

6.6 Performance

The oscillators with the installed clock circuits perform well if operated within their published specifications. For world travel, the battery life between recharge cycles was found to be too short (the Vectron standards are specified at approximately 24 hours). When on a plane bus or car, power generally does not exist even when requested ahead of time and many times power is only available after significant effort at a terminal or other waiting area. A possible solution is to procure a second battery that may be plugged in to the standard to increase the time without commercial power to approximately 48 hours.

The frequency standards were found to be sensitive to their orientation with respect to the local gravity (possibly due to crystal stresses). A drift of order 1 nanosecond per second is produced when a Vectron oscillator is turned 90 degrees.

The Hewlett-Packard standard performed flawlessly in a closed loop test during an observing run at Mauna Kea Hawaii. The first leg of the loop consisted of a flight to Kauai Hawaii to synchronize the Hewlett-Packard standard against the National Bureau of Standards time standard. From there the clock was flown as hand luggage to the island of Hawaii, Hawaii. On Hawaii the clock was taken by automobile to the living quarters at 9,000 feet on Mauna Kea and immediately plugged in to recharge the battery. After the observing run on Mauna Kea the clock was flown to Oahu and plugged in at a hotel until a flight could be arranged to Kauai to determine the accumulated time offset between the Hewlett-Packard standard and the National Bureau of Standards time standard (nb., the clock was always kept in a horizontal position). Over a period of 14 days, the accumulated drift was 4.6 microseconds fast (a calculated stability of 3.8×10^{-12}). This number must be considered in light of a measurement versus a second standard (a portable rubidium clock on loan from the National Bureau of Standards) which indicated a drift of 14.2 microseconds fast for the Hewlett-Packard oscillator at 7 days into the 14 day period. Since

the change in pressure at the top of Mauna Kea is expected to change the drift of both oscillators, some caution must be used in interpreting these numbers. For comparison, the portable rubidium standard drifted 1.4 microseconds slow during the same 14 day period. The rubidium clock was also transported to the top of Mauna Kea and used as a second reference. A further comparison can be made with respect to the specifications given in the Hewlett-Packard manual. The manual quotes a stability of approximately $5x10^{-11}$ for various operating conditions after removal of crystal ageing which is quoted as less than $|\ 0.5x10^{-10}\ |$ per 10 days.

Table 6-3 gives a synopsis of the performance of the clocks for three occultation expeditions.

Table 6-3

OCCULTATION OBSERVATIONS TIMED WITH PRECISION CLOCKS

Occultation date	Star occulted	Observatory	Clock used	Intermediate check elapsed days	Intermediate check std used	Intermediate check stability	closed loop check elapsed days	closed loop check std used	closed loop check stability
4 May 1985	U23	CTIO	210	10	clk 208	$\sim 3 \times 10^{-10}$	------	none	------
		Teide	209	------	------	------	------	note 2	------
		McDonald	208	4	Mc O. Ces	6.4×10^{-11}	15	Haystack Obs	3.8×10^{-10}
24 May 1985	U25	CTIO	210	------	------	------	8	Haystack Obs	1.8×10^{-10}
		McDonald	209	------	------	------	8	Haystack Obs	9.0×10^{-9}
		IRTF	208	------	------	------	8	Haystack Obs	3.0×10^{-7}
1 April 1987	U36	CTIO	210	------	------	------	10	Haystack Obs	1.1×10^{-9}
		AAT	209	------	------	------	------	note 3	------
		MTS	208	------	------	------	------	note 3	------
		IRTF	HP	7	portable rubidium	2.4×10^{-11}	14	Barking Sands	3.8×10^{-12}

Note 1. The stability is a measured number that makes no compensation for observed drift rates and ageing.
The stars identified as U23, U25 and U36 are from Mink and Klemola (1985). The following is a list of codes for the place of observation: AAT Anglo Australian Telescope; CTIO, Cerro Telolo Inter-American Observatory; MTS Mount Stromlo Observatory; IRTF NASA Infrared Telescope Facility.
Note 2. Clock 209 was severely jarred after the observation and lost 410 ms; calculated error at time of observation assuming observed drift rate is 49 μs slow.
Note 3. Synchronization was lost, the exact cause is unknown

References

BARON, R. L., R. G. FRENCH, AND J. L. ELLIOT (1989). The oblateness of Uranus at the 1-μbar level. *Icarus* **77**, 113-130.

MINK, DOUGLAS J., AND ARNOLD KLEMOLA (1985). Predicted occultations by Uranus, Neptune and Pluto: 1985–1990. *Astron J.* **90**, 1894–1899.

NATIONAL SEMICONDUCTOR CORPORATION (1975). CMOS Integrated Circuits. 2900 Semiconductor Drive Santa Clara California 95051 Telephone: 408-732-5000.

D.A.T.A. INC A CORDURA COMPANY(1976). DIODE .D.A.T.A.. 32 Lincoln Avenue Orange New Jersey 07050 Telephone: 201-673-8030

FRENCH, RICHARD G., J. L. ELLIOT, LINDA M. FRENCH, JULIE A. KANGAS, KAREN J. MEECH, MICHAEL E. RESSLER, MARC W. BUIE, JAY A. FROGEL, J. B. HOLBERG, JESUS J. FUENSALIDA, AND MARSHALL JOY (1988). Uranian ring orbits from Earth-based and Voyager occultation observations. *Icarus* **73**, 349-378.

VECTRON LABORATORIES INC. Frequency Standard Model FS-321 Instruction Manual. 166 Glover Avenue, Norwalk Connecticut 06850 Telephone: 203-853-4433.

INTERSIL INC (1987). Intersil Component Catalog 1987. 106000 Ridgeview Court, Cupertino Ca. 95014 Telephone: 408-996-5000.

HEWLETT PACKARD COMPANY (1968). Quartz Oscillators 105A/B. 1501 Page Mill Road Palo Alto California.

Chapter 7

Summary / Future Work

7.1 Summary

Two fundamental aspects of the Uranian upper atmosphere have been investigated with ground-based observations of stellar occultations. The two areas investigated are the figure (diameter and oblateness) at half-light radius, and the vertical thermal atmospheric structure and energy balance. In the latter case, a synthesis of Voyager 2 data with ground-based data for Uranus has been achieved. The Voyager data is used to provide an initial condition for the numerical inversion of ground-based data by defining the atmosphere above that probed by the ground-based data.

In Chapter 2, a substantially improved value for the Uranian oblateness (0.0197 ± 0.0010) and radius ($R_e = 26071 \pm 3$) at the 1-μbar level in the Uranian atmosphere has been obtained from ground-based Uranian stellar occultation observations. The data used spans the period from 1977 to 1983. The major contributing factors to the improved value are: a much better available pole position for Uranus (from Uranian ring occultation analysis), a larger data set, and a modified analysis procedure to include refractive corrections on the basis of each lightcurve analyzed rather than as an overall correction.

The compatibility of temperature pressure profiles as determined by Voyager 2 data and that of Uranian ground-based recorded stellar occultations was addressed in Chapter 3. It was found that the highly non-isothermal profiles as reported by Voyager 2 were in fact compatible with ground-based observations. Chapter 4 then addressed the problem of starting (initial) conditions in the numerical inversion of ground-based lightcurves for the case of Uranus and how noise influenced the rest of the inversion of a lightcurve. A

procedure to analyze the effect of recorded noise (as part of an occultation observation) was presented using the noise recorded as part of the KME 15 event of 1 May 1982. A model of the atmosphere (based on Voyager 2 data reduction by Herbert *et al.* 1987) above that probed by the ground-based lightcurve is used to supply the initial conditions for the inversion. The procedure uses the upper atmospheric part of a synthetic ground-based lightcurve (based on the model) to replace the corresponding part of the observed lightcurve. The composite lightcurve, so produced, is then numerically inverted to recover the model parameters for the upper atmosphere part and the observed quantities in the remainder of the composite lightcurve.

The work described in Chapter 5 uses the new initial conditions or atmospheric cap to invert four of the highest signal-to-noise recorded ground-based lightcurves. A relatively large heat flux ($\approx$0.5 erg cm^{-2} sec^{-1}) in the upper stratosphere of Uranus has been found from these inversions. The source of heat to supply this flux must be investigated in terms of the heating and cooling mechanisms possible in this region of the atmosphere. Absorbed solar ultraviolet radiation is too small by approximately two orders of magnitude to supply the heat. A simple model of possible Joule heating in the thermosphere was used to estimate the thermospheric wind speed necessary to supply the needed heat. A wind speed of 400 m sec^{-1} would supply the heat. For comparison, a maximum wind speed of 200 m sec^{-1} is estimated from studies of differential rotation with latitude (Smith *et al.* 1986).

Also in Chapter 5, a newly identified nearly isothermal region ($\approx$2.5 to 10-μbar) in the retrieved (vertical) temperature-pressure atmospheric profile appears in three of the four profiles examined. The temperature of this region is approximately 160 K. The lower altitude end of this region appears to coincide with a previously reported warm layer at $\approx$8-μbar (Sicardy *et al.* 1985). The atmospheric mechanism to produce and maintain this

temperature profile remains to be identified. A thermostatic mechanism (conductive, radiative or dynamic) seems to be the most likely explanation.

In Chapter 6, a clock circuit that may in general be adapted to run from nearly any high stability (1 to 10 Mhz or greater with TTL output) oscillator has been documented in terms of operation, construction, and performance as experienced in the field. The performance of the circuit is limited by the battery (power supply) capability, stability of the oscillator, and how much physical and electrical abuse (static discharges) the housing can withstand. It is noted that, as the price of global positioning satellite (GPS) systems is reduced in the future, the need for this type of time keeping will diminish, with the added benefit of a position determination along with the accurate time.

7.1 Future Work

Several directions are possible for future work. Broadly, they may be categorized in terms of analysis of data sets already acquired, additional observations, and further theoretical modeling in terms of the physics and chemistry of the atmosphere to account for the results of the observations. Additional work in analysis or observations should be motivated from a framework of the physical processes that determine the conditions of the Uranian atmosphere.

Uranian data sets available for inversion with the upper atmosphere initial condition (layer) inversion technique are those listed in Table 2-3. The data sets recorded on a chart as the primary recording medium should probably be excluded from analysis. A first look at this data indicates it to be of slightly lower quality than the KME 15 and KME17b events already inverted. Additional care will probably have to be used in the selection of joint points and joint averaging regions (and additional joint points and averaging region trials

should be used) when making composite lightcurves to be numerically inverted. For the U36 four day event beginning March 30, 1987 (not listed in Table 2-3), the data from the CTIO observation for the atmosphere should be useable. The U36 CTIO data does not have an extended upper baseline, but it does appear to have a stable lower baseline and very low instrumental and scintillation noise (from the Earth's atmosphere). The event velocity for U36 CTIO is very slow (approximately 1 km sec^{-1}) and varies nonlinearly during the atmosphere event, this will need to be quantified and evaluated as to its effect on the profile. The U36 SAAO atmosphere data appears to have significant variation in its background during the atmosphere event. A preliminary look at this data indicates some rapid and relatively large offsets in the background (possible transparency changes) that will make accurate subtraction of the baseline difficult. The sky checks appear to be too few for the type of variations encountered. This SAAO data should probably only be used if good modeling or removal of the noted effects can be obtained.

The question of where the heat comes from in the upper stratosphere is a prime extension of this work. Three possible sources of heating were identified in Chapter 5: solar UV absorption; auroral and electron precipitation; and thermospheric winds. An analysis of possible heating mechanisms in terms of their effect on the detailed temperature-pressure profile should be attempted. The general wisdom is that radiative heating and cooling by trace hydrocarbons (and or particulates) in the atmosphere control the temperature profiles. Modeling presented by Appleby (1986) and others has not been able to duplicate the warm temperatures in the upper stratosphere with this technique. Strobel *et al.* (1985) present several temperature-altitude profiles for inertia gravity waves breaking in the mesosphere of the earth. Are the profiles presented applicable to Uranus, and if not, what are the expected changes for Uranian conditions? Rossby waves are due to the latitudinal variation of the Coriolis force, which causes a wave to propagate relative to the

mean zonal flow. Rossby waves also propagate at a few meters per second, is there some way to sample the same portion of the atmosphere during a short period of time (say 10 minutes to an hour) to look for changes on this time scale?

Future observations should be planned to further the understanding of the physics taking place. For instance, the atmospheric response to solar radiation might be better understood by sampling throughout the diurnal cycle at nearly the same latitude. Some effort to identify possible candidate stars to complete the coverage would be in order. Since a solar phase angle of 3 degrees is accessible from the earth, this may be quite possible.

The following discussion concerns suggested scientific questions to be addressed in further analysis of the Uranian ground-based data. What is the role of insolation in the character of the lightcurves. Examination of ionospheric profiles (Lindal *et al.* 1987) show a large variation in the altitude (a change of nearly 1000 km) of the peak electron density between ingress (at sunrise) and egress (at sunset). Can this variation be correlated with one or more features of the ground-based lightcurves. Are there equivalent sunrise-sunset pairs of lightcurves? The ion profiles reach down to an altitude of approximately 800 km above the 1-bar level; whereas, the inverted stellar lightcurve profiles are sensitive to around 650 km above the 1-bar level.

Latitudinal changes in the Uranian atmosphere as determined from the lightcurves should become apparent as more data is reduced, covering a greater latitude range. Preliminary display of the lightcurves (scaled to the same velocity along the path of the observer) has shown a possible change in shape of the lightcurves as a function of latitude. What this change means in terms of a temperature-pressure profile will be part of the result of properly inverting the lightcurves.

The nearly isothermal region from ≈2.5-μbar to ≈10-μbar reported in the Chapter 5 reduction of ground-based occultation lightcurves may be a key piece in understanding the

energy balance and or dynamics of this region. One avenue to investigate is the marked change in thermal conductivity of parahydrogen near 160 K. McCarty *et al.* (1981) tabulates the change in conductivity for parahydrogen near 160 k but the temperature steps are relatively large. Gierasch (1989) recommends that a simple quantum mechanical calculation be made to accurately determine the thermal conductivity of para and ortho hydrogen (he has used this calculation in his own work) in this temperature region. The change in conductivity may be able to thermostatically control the temperature of this region, but needs to be modeled. A calculation to determine the amount of hydrocarbon (likely ethane) necessary in the nearly isothermal region to regulate its temperature is another avenue of investigation.

One of the questions that can validly be asked is whether the Voyager 2 observations represent the normal time independent state of the thermosphere or are there large fluctuations over the period of a year or ten years? A second question is: whether this technique is applicable to the one planet (Pluto) not encountered by the Voyager spacecraft? Both questions may be answered by determining if a stellar occultation can be observed in the EUV by an earth satellite. If so, and the signal-to-noise is sufficient, an analysis of the temperature and absorbing molecules should be obtainable. A model of the atmosphere produced with the UV information may then act as an initial condition for ground-based data recorded at longer wavelengths.

The following are recommendations for reduction of the Saturn ground-based observation of a stellar occultation as currently understood. This is probably the next best planet for application of the technique used in Chapter 5. Voyager data has been reduced to give a general temperature profile; but, a strict modeling of the atmosphere as Herbert *et al.* (1987) did with Uranus is not available. Some discrepancy in the reduction of the Voyager 2 UVS data appears to exist in the literature. Smith *et al.* (1983) report an upper

atmosphere temperature of 420 ± 30 K above 1600 km from the 1-bar level. Festou and Atreya (1982), however, report an upper atmosphere (exospheric) temperature of 850 (+150, −120) K above 1540 km. In practice this will make the overall inversion less constrained, resulting in additional uncertainty in the upper atmosphere temperature-pressure profile. How this uncertainty will propagate into the lower atmosphere part of a ground-based observation of a stellar occultation must be determined as part of the reduction. A Bates model of the atmosphere is used by Smith *et al.* (1983) with parameters given in terms of the model. This model may have to be reconstructed in order to properly reduce the ground-based lightcurve. A second (expeditious) approach is to use approximate parameters relevant to Saturn in the model developed for Uranus.

Jupiter is also a good candidate for the modified inversion technique. The Voyager UVS analysis of the upper atmosphere has been completed (Atreya *et al.* 1981 and Festou *et al.* 1981). A temperature of 1100 ± 200 K was determined for pressures less than about 1 x 10^{-3}-μbars. The only ground-based lightcurves recorded for Jupiter are those for β Sco reported by Veverka et al. (1974). Since this is very poor sampling in this region of the atmosphere, an investigation of the IR brightness of Jupiter near 4 μm should be carried out and compared to possible occultation candidates. If the brightness of Saturn (known to be quite low) in this wavelength region is comparable, then an occultation candidate search should be undertaken.

The application of the inversion method as used in Chapter 5 to Neptune ground-based observations should be delayed until reduction of the Voyager 2 UVS data is available. Once available, a straight forward substitution into the Uranian model should be possible.

References

APPLEBY, J. F. (1986). Radiative-convective equilibrium models of Uranus and Neptune. *Icarus* **65**, 383-405.

ATREYA, S. K., T. M. DONAHUE, M. C. FESTOU. (1981). Jupiter: structure and composition of the upper atmosphere. *Astrophys. J.* **247**, L43-L47.

FESTOU, M. C., S. K. ATREYA, T. M. DONAHUE, D. E. SHEMANSKY, B. R. SANDEL, AND A. L. BROADFOOT (1981). Composition and thermal profiles of the Jovian upper atmosphere determined by the Voyager ultraviolet stellar occultation experiment. *Geophys. Res Lett.* **86**, 5715-5725.

FESTOU, M. C., AND S. K. ATREYA (1982). Voyager ultraviolet stellar occultation measurements of the composition and thermal profiles of the Saturnian upper atmosphere. *Geophys. Res Lett.* **9**, 1147-1150.

GIERASCH (1989) personal communication.

HERBERT, F., B. R. SANDEL, R. V. YELLE, J. B. HOLBERG, A. L. BROADFOOT, AND D. E. SHEMANSKY (1987). The upper atmosphere of Uranus: EUV occultations observed by Voyager 2. *J. Geophys. Res.* **92**, 15093-15109

LINDAL, G. F., J. R. LYONS, D. N. SWEETNAM, V. R. ESHLEMAN, D. P. HINSON, AND G. L. TYLER (1987). The atmosphere of Uranus: Results of radio occultation measurements with Voyager 2. *J. Geophys. Res.* **92**, 14987-15001.

MCCARTY, R. D., J. HORD, H. M. RODER (1981). *Selected properties of hydrogen (Engineering Design Study).* U. S. Government Printing Office, Washington.

SICARDY, B., M. COMBES, J. LECACHEUX, P. BOUCHET, A. BRAHIC, P. LAQUES, C. PERRIER, L. VAPILLON, AND Y. ZEAU (1985). Variations of the stratospheric

temperature along the limb of Uranus: Results of the 22 April 1982 stellar occultation. *Icarus* **64**, 88-106.

SMITH, G. R., D. E. SHEMANSKY, J. B. HOLBERG, A. L. BROADFOOT, AND B. R. SANDEL (1983). Saturn's upper atmosphere from the Voyager 2 EUV solar and stellar occultations. *J. Geophys. Res.* **88**, 8667-8678.

SMITH, B. A., L. A. SODERBLOM, R. BEEBE, D. BLISS, J. M. BOYCE, A. BRAHIC, G. A. BRIGGS, R. H. BROWN, S. A. COLLINS, A. F. COOK II, S. K. KROFT, J. N. CUZZI, G. E. DANIELSON, M. E. DAVIES, T. E. DOWLING, D. GODFREY, C. J. HANSEN, C. HARRIS, G. E. HUNT, A. P. INGERSOLL, T.V. JOHNSON, R. J. KRAUSS, H. MASURSKY, D. MORRISON, T. OWEN, J. B. PLESCIA, J. B. POLLACK, C. C. PORCO, K. RAGES, C. SAGAN, E. M. SHOEMAKER, L.A. SROMOVSKY, C. STOKER, R. G. STROM, V. E. SUOMI, S. P. SYNNOTT, R.J. TERRILE, P. THOMAS, W. R. THOMPSON, AND J. VEVERKA (1986). Voyager 2 in the Uranian system: Imaging science results. *Science* **233**, 43-64.

STROBEL, F. D., J. P. APRUZESE, M.R. SCHOEBERL (1985). Energy balance constraints on gravity wave induced eddy diffusion in the mesosphere and lower thermosphere. *J. Geophys. Res.* **90**, 13067-13072.

VEVERKA,J., L. H. WASSERMAN, J. ELLIOT, AND CARL SAGAN, W. LILLER. (1974). The Occultation of β Scorpii by Jupiter I. The structure of the Jovian upper atmosphere. *Astron. J.* **79**, 73-84.

Appendix 1

Review of Inversion Method

Following Wasserman and Veverka (1973), the total bending of a light ray passing through a spherically symmetric atmosphere is given by

$$\theta(r_1) = \int_{-\infty}^{\infty} K(r)\, dx\ , \qquad \text{(A1-1)}$$

where r_1 is the distance of the ray at closest approach from the center of the planet (Figure A1-1), and K(r) is the curvature of the ray:

$$K(r) = \frac{1}{n}\frac{dn}{dr} = \frac{d}{dr}(\ln n). \qquad \text{(A1-2)}$$

The assumptions of Baum and Code (1953) for a stellar occultation are being adopted here. From the geometry of Figure A1-1 we have,

$$x^2 = r^2 - r_1^2\ . \qquad \text{(A1-3)}$$

If we take the total derivative we get,

$$dx = \frac{r\, dr}{(r^2 - r_1^2)^{1/2}}\ . \qquad \text{(A1-4)}$$

We may rewrite Equation A1-1 as:

Appendix 1

Figure A1-1 Basic occultation geometry. The distance 'D' is measured from the sky plane to the Earth or spacecraft. The ray indicated has been bent a total angle of θ and has passed within r_1 of the center of the planet.

Appendix 1

Figure A1-1

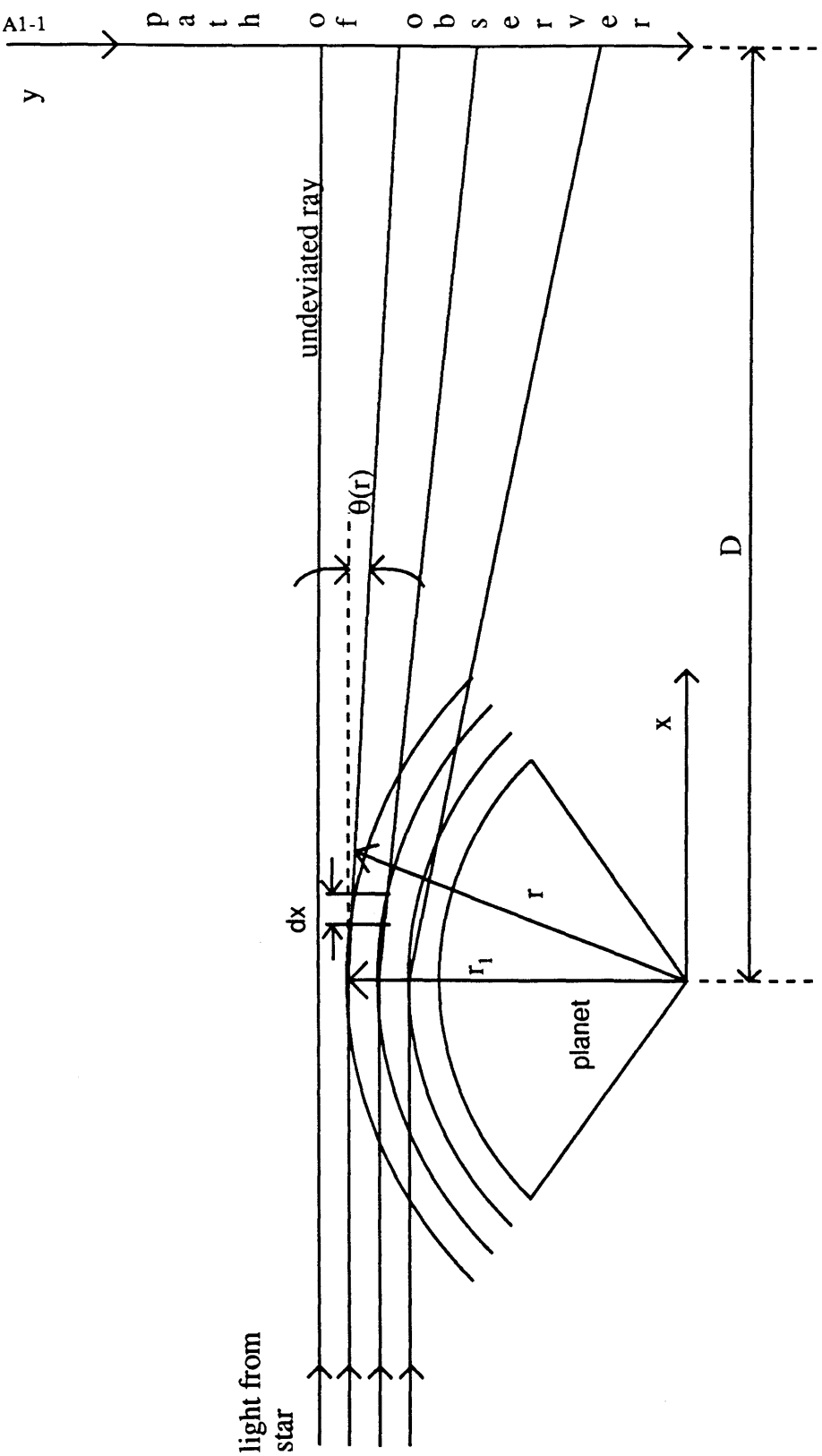

Appendix 1

$$\theta(r_1) = 2 \int_{r_1}^{\infty} \frac{r \frac{d}{dr}(\ln n)}{(r^2 - r_1{}^2)^{1/2}} dr \,. \qquad \text{(A1-5)}$$

Since the integral extends from r_1 to ∞ instead of from $-\infty$ to ∞ a factor of 2 is needed.

The denominator in the integral may be written as,

$$\left[\frac{r^2 r_1{}^2}{r r_1{}^2}\left(r^2 - r_1{}^2\right)\right]^{1/2} = \left[\frac{r^2 r_1{}^2}{1}\left(\frac{1}{r_1{}^2} - \frac{1}{r^2}\right)\right]^{1/2} . \qquad \text{(A1-6)}$$

If we now make the substitutions $r_1{}^2 = 1/s$ and $r^2 = 1/w$, we get for the denominator,

$$\left[\frac{r^2 r_1{}^2}{1}(s - w)\right]^{1/2} = r r_1 (s - w)^{1/2} \qquad \text{(A1-7)}$$

We now may write the integral as,

$$\theta(r_1) = 2 \int_{r_1}^{\infty} \frac{\frac{d}{dr}(\ln n)}{r_1 (s - w)^{1/2}} dr \,, \qquad \text{(A1-8)}$$

where the r previously in the numerator cancelled the r in Equation A1-7 above when substituted for the denominator. The derivative dr may be obtained in terms of w as follows:

Start with the definition of w in terms of r,

$$r = w^{-1/2} . \tag{A1-9}$$

Now take the total derivative to get

$$dr = -1/2\ w^{-3/2}\ dw . \tag{A1-10}$$

Substitute for r_1 in terms of s and for dr as in Equation A1-10 to get:

$$\theta(s) = -2\frac{1}{r_1}\int_0^s \frac{\frac{d}{dw}(\ln n)}{(s-w)^{1/2}}\,dw , \tag{A1-11}$$

and

$$\theta(s) = -2\frac{1}{r_1}\int_0^s \frac{\varphi'(w)}{(s-w)^{1/2}}\,dw , \tag{A1-12}$$

where $\varphi'(w) = \frac{d}{dw}(\ln n)$.

The next step is to use the Abel transform pair as written here:

$$f(x) = -K\int_0^x \frac{g'(y)}{(y-x)^{1/2}}\,dy \text{ , and } g(y) = \frac{1}{K\pi}\int_0^y \frac{f(x)}{(x-y)^{1/2}}\,dx . \tag{A1-13}$$

By inspection we can write:

Appendix 1

$$\varphi(s) = \ln n = \frac{r_1}{2\pi} \int_0^w \frac{\theta(s)}{(w - s)^{1/2}}\, ds, \qquad \text{(A1-14)}$$

where $K = \frac{2}{r_1}$.

Now express s and w in terms of r and r_1, to get,

$$\ln n = \frac{r_1}{2\pi} \int_r^\infty \frac{\theta(r_1)}{\frac{1}{r\, r_1}(r_1^2 - r^2)^{1/2}} -2\, r_1^{-3}\, dr_1, \qquad \text{(A1-15)}$$

where $s = r_1^{-2}$, upon taking the total derivative, we get,

$$ds = -2\, r_1^{-3}\, dr_1 .$$

At this point, the following approximations are made,

$$r + r_1 \approx 2\, r_1 \approx 2\, R_p \text{ and } K(r) = \frac{1}{n}\frac{dn}{dr} \approx \frac{dn}{dr} \qquad \text{(A1-16)}$$

where R_p is the Planet's radius. The first approximation is possible since the integration continues in practice only to the 'edge' of the atmosphere which is assumed only slightly greater than R_p.

The denominator may be manipulated as follows,

$$(r_1^2 - r^2)^{1/2} = \left[(r_1 - r)(r_1 + r)\right]^{1/2}. \qquad \text{(A1-17)}$$

This gives on substitution,

Appendix 1

$$\ln n = -\frac{1}{\pi\,(2\,R_p)^{1/2}} \int_r^\infty \frac{\theta(r_1)}{(r_1 - r)^{1/2}}\,dr_1 \quad . \tag{A1-18}$$

Take the derivative of Equation A1-18 with respect to r to get,

$$\frac{d}{dr}(\ln n) = -\frac{1}{\pi\,(2\,R_p)^{1/2}} \frac{d}{dr} \int_r^\infty \frac{\theta(r_1)}{(r_1 - r)^{1/2}}\,dr_1 \,. \tag{A1-19}$$

We may write the left-hand side of the above as $\frac{1}{n}\frac{dn}{dr}$ from Equation A1-2 and note that n is very nearly equal to 1, also $\nu = n - 1$ hence $dn = d\nu$. We now have upon integrating,

$$\nu(r) = \frac{1}{\pi\,(2\,R_p)^{1/2}} \int_\infty^r \frac{\theta(r')}{(r' - r)^{1/2}}\,dr' \,. \tag{A1-20}$$

Here r' is the dummy variable of integration.

For θ a positive angle we can evaluate $\theta(r)$ from the lightcurve data points $\phi(t)$. With reference to the occultation geometry, we have,

$$\frac{\phi^*}{\phi} = \frac{\Delta y}{\Delta r} = 1 - D\frac{\Delta\theta}{\Delta r} \text{ and } \Delta r = \Delta y + D\Delta\theta \,. \tag{A1-21}$$

These equations may be solved simultaneously as follows:

The first of Equations A1-21gives

$$1 - \frac{\phi^*}{\phi} = D\frac{\Delta\theta}{\Delta r}, \qquad \text{(A1-22)}$$

and the second gives

$$\Delta r - D\Delta\theta = \Delta y = v\,\Delta t\,. \qquad \text{(A1-23)}$$

If we divide by Δr, we get,

$$1 - D\frac{\Delta\theta}{\Delta r} = v\frac{\Delta t}{\Delta r}\,. \qquad \text{(A1-24)}$$

At this point, substitute for the second term with its equivalent from Equation A1-21 and divide by $\frac{\phi^*}{\phi}$, to get,

$$\Delta r = \frac{r\,\Delta t}{\frac{\phi^*}{\phi}}\,. \qquad \text{(A1-25)}$$

Substitute for Δr in Equation A1-23 and rewrite as,

$$1 - \frac{\phi^*}{\phi} = D\frac{\Delta\theta}{\frac{r\,\Delta t\,\phi}{\phi^*}}\,. \qquad \text{(A1-26)}$$

Now multiply by $\frac{\phi}{\phi^*}$ to get, upon rearranging,

Appendix 1

$$\Delta\theta = \left(\frac{\phi^*}{\phi} - 1\right)\frac{r\,\Delta t}{D} = -\left(1 - \frac{\phi^*}{\phi}\right)\frac{r\,\Delta t}{D} \quad . \tag{A1-27}$$

Equations A1-25 and A1-27 are the desired solution.

Referring to Figure A1-2, we set

$$\Delta t_i = t_{i+1} - t_i \text{ and } \bar{\phi}_i = (\phi_{i+1} + \phi_i)/2 \, . \tag{A1-28}$$

Arbitrarily start the integration at some value of θ such that $\frac{\phi}{\phi^*} \approx 1$ and $\Delta\theta \approx 0$. At each time increment compute $\Delta\theta_i$ and Δr_i. Then

$$\theta_i = \sum_i^N \Delta\theta_i \text{ and } r_i = \sum_i^N \Delta r_i \, . \tag{A1-29}$$

This evaluates θ on N spherical, concentric layers $r_1 > r_2 > r_3 > \ldots r_N$ with $\theta_i = \theta(r_i)$ such that $|\theta_1| < |\theta_2| < |\theta_3| < \ldots |\theta_N|$. Note that r_i now denotes the upper-most layer, rather than the level of closest approach of a ray.

Since integration to infinity is not possible for a real atmosphere and real data, Equation A1-20 must be approximated as,

$$\nu(r) \approx \frac{1}{\pi\,(2\,R_p)^{1/2}} \int_{r_1}^{r} \frac{\theta(r')}{(r' - r)^{1/2}}\, dr' \, . \tag{A1-30}$$

Since a singularity exists at the point deepest in the atmosphere (where $r' = r$), this equation

Figure A1-2 Planetary atmospheric layer, starlight ray and flux designations. The vector r is at the occulting planet. Phi 'ϕ' is the flux measured at the earth (after Wasserman and Veverka 1973).

Appendix 1

Figure A1-2

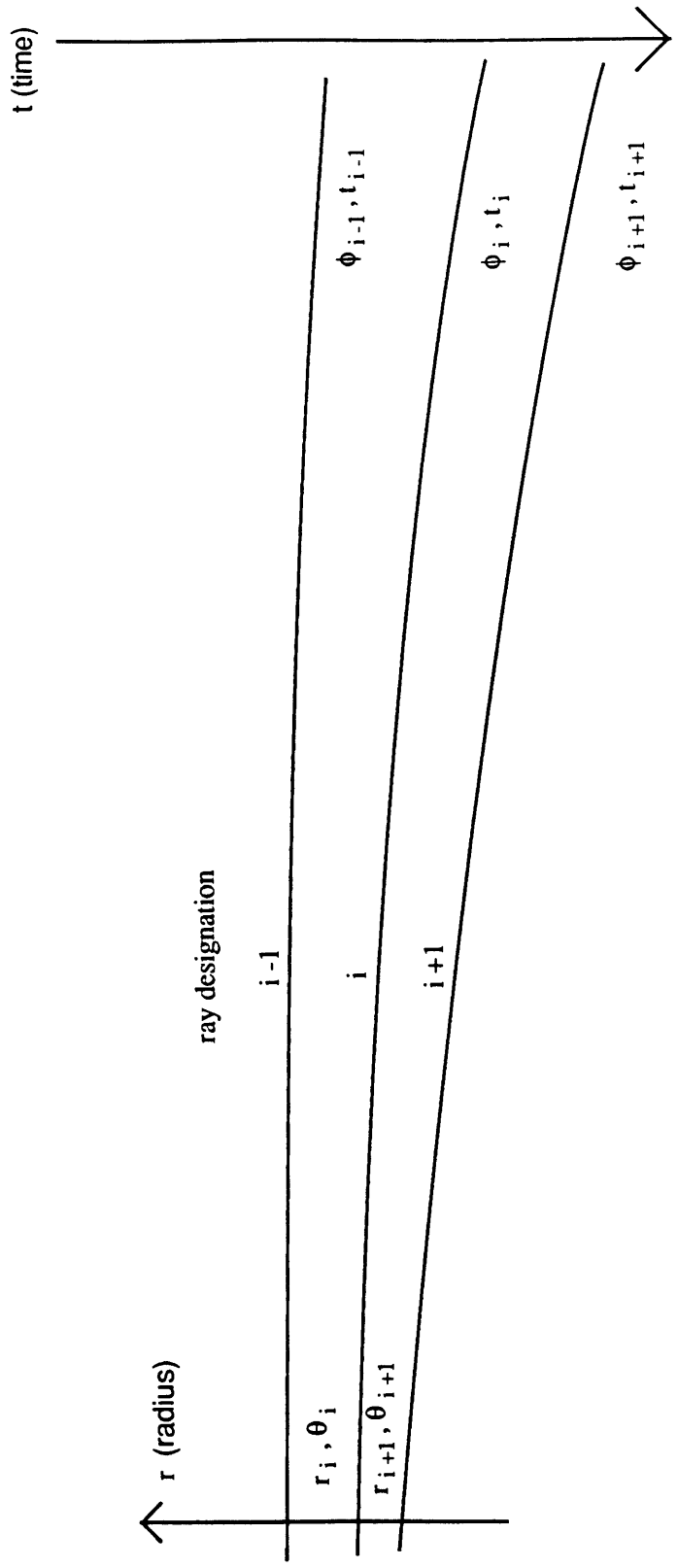

Appendix 1

is not suitable for numerical integration. Integration by parts ($v = \theta(r')$, $du = \frac{dr'}{(r' - r)^{1/2}}$) will however give the following useable form,

$$\nu(r) = -\frac{2(r_1 - r)^{1/2}\,\theta(r_1)}{\pi(2R_p)^{1/2}} - \frac{1}{\pi(2R_p)^{1/2}} \int_{\theta(r_1)}^{\theta(r)} 2(r' - r)^{1/2}\, d\theta \ . \quad \text{(A1-31)}$$

Note if $r_1 = \infty$ then the first term is equal to zero.

For the jth shell the refractivity is:

$$\nu_j = -\frac{2(r_1 - r_j)^{1/2}\,\theta_1}{\pi(2R_p)^{1/2}} - \frac{1}{\pi(2R_p)^{1/2}} \sum_{k=1}^{j} (r_k - r_j)^{1/2}\,(\theta_{k+1} - \theta_{k-1}). \quad \text{(A1-32)}$$

Where the factor of 2 inside the integral of Equation A1-31 is absorbed into the θ term within the summation in Equation A1-32. This is the form desired for numerical inversions.

Appendix 1

References

BAUM, W. A., AND A. D. CODE (1953). A photometric observation of the occultation of σ Arietis by Jupiter. *Astron. J.* **58**, 108-112.

WASSERMAN L., J. VEVERKA.(1973). On the reduction of occultation light curves. *Icarus* **20**, 322-345.

Appendix 2

Computation of high precision offsets between clocks

The time measurement offset circuit may be used in two modes. The first mode measures the offset between the leading (positive going) edges of an external pulse and the internal 1 second pulse. In this mode the offset is computed as

$$\Delta\_10khz = Count\_10khz * Period\_10khz \qquad (A2\text{-}1)$$

where Δ_10khz is the offset in seconds between the edges with a resolution of one period of a 10 khz signal, Count_10khz is the count on the 'offset' display after actuating the 'offset ckt' switch with the 'offset cnt spd' in the '10 khz' position, Period_10khz is the period of a 10 khz signal. The true offset (OFFSET) will be bounded such that

$$\Delta\_10khz - Period\_10khz < OFFSET < \Delta\_10khz \qquad (A2\text{-}2)$$

The second mode is used to obtain the offset in terms of the number of periods of the highest available frequency, FFAST (the input frequency to the clock circuit). To do this, the following procedure should be followed:

1. Obtain Δ_10khz as above.
2. Obtain the intermediate value δ_FFAST, this may be calculated similarly to the above where

$$\delta\_FFAST = Count\_FFAST * Period\_FFAST \qquad (A2\text{-}3)$$

the quantity Count_FFAST is the count on the display with the 'offset cnt spd' in the 'FFAST' position, Period_FFAST is the period of the FFAST signal.

3. Now calculate Δ_FFAST as

$$\Delta\_FFAST = \text{integer portion of}\left(\frac{\Delta\_10khz}{20{,}000 * Period\_FFAST}\right) + \delta\_FFAST$$

In this case the true offset (OFFSET) will be bounded such that

$$\Delta\_FFAST - Period\_FFAST < OFFSET < \Delta\_FFAST$$

Note: if in doubt about the frequency of FFAST, the input frequency of the clock circuit should be independently determined.